Dissertation

submitted to the
Combined Faculties for the Natural Sciences and for Mathematics
of the Ruperto-Carola University of Heidelberg, Germany
for the degree of

Doctor of Natural Sciences

presented by

Diplom-Physiker Frank Postberg
Born in Frankfurt (Main), Germany

Oral examination: December 19th, 2007

A New View on the Composition of Dust in the Solar System: Results from the Cassini Dust Detector

Referees: **Prof. Dr. Eberhard Grün**
Priv.- Doz. Dr. Mario Trieloff

Zusammenfassung.
Gegenstand der Arbeit ist die Auswertung und Interpretation von Flugzeit-Massenspektren der Kationen, die aus dem Einschlagsplasma von Hochgeschwindigkeitseinschlägen auf den Staub-Detektor der Raumsonde Cassini extrahiert werden. Die Zusammensetzung sechs verschiedener Staubarten wird abgeleitet.
Bereits auf dem Weg ins äußere Sonnensystem erhielt man Spektren eisenreichen interplanetaren Staubes. Weiterhin wurden zwei Arten extrem schneller Staubströme, die dem Jupiter- bzw. dem Saturnsystem entspringen, detektiert. Für die Jupiterströme wird Natriumchlorid, neben schwefel- und kaliumhaltigen Komponenten, als Hauptbestandteil identifiziert. Dies belegt den vulkanisch aktiven Jupitermond Io als Quelle für den Großteil der beobachteten Jupiter-Stromteilchen. Als Entstehungsmechanismus wird die Kondensation von Alkalisalzen aus Gasen vulkanischer Auswurffontänen vom Pele-Typ vorgeschlagen. Die Quellregion der Saturn–Stromteilchen ist das Ringsystem des Planeten. Silizium wird als Hauptbestandteil identifiziert. Dies weist darauf hin, dass der winzige Staub wahrscheinlich Überrest einst größerer Eispartikel ist, welche den äußeren dünnen Ring Saturns - den E-Ring - bevölkern.
Nach Cassinis Einschwenken in den Saturnorbit wurden bei Durchquerungen des E-Ringes drei weitere spektrale Typen identifiziert, die mit verschiedenen Staubpopulationen assoziiert werden. Der Hauptbestandteil von Typ I- und Typ II-Teilchen ist Wassereis, während Typ III-Staub eine mineralische Zusammensetzung aufweist. Im Gegensatz zu Typ I-Spektren, die reine Wassereiskristalle nahe legen, weisen Typ II-Spektren auf organische Komponenten und/oder silikatische Mineralien als Verunreinigungen in den Teilchen hin. Dies enthüllt die Eisvulkane des Mondes Enceladus als Quelle für Typ II-Teilchen, was eine dynamischen Wechselwirkung von Enceladus' Gesteinskern mit flüssigem Wasser nahe legt. Der wasserfreie Typ III-Staub weist eine eisenreiche Zusammensetzung, vermutlich in der Form von Pyrit, Oxiden und/oder Hydroxiden, auf. Eine magnesiumreiche silikatische Unterart ist wahrscheinlich. Retrograde oder ungebundene Teilchenbahnen ergeben die beste Übereinstimmung mit den Typ III-Beobachtungen.

Abstract.
In this work the time-of-flight mass spectra of cations, extracted from the plasma created by high-velocity particle impacts onto the Cassini dust detector, are evaluated. The composition of six different dust species is inferred.
During Cassini's cruise, spectra of iron-rich interplanetary dust were obtained. Subsequently two fast hypervelocity stream particle species, originating from the Jovian and Saturnian systems were detected. For the Jovian streams sodium chloride (NaCl) was identified as the major particle constituent, accompanied by sulfurous as well as potassium-bearing components. This implies that the vast majority of the observed Jovian stream particles originate from the volcanically active Jovian satellite Io. An alkali salt condensation of gases inside Pele-type volcanic plumes is proposed as the source mechanism. For the Saturnian stream species the source region is the planet's ring system. Silicon is identified as the main particle component, indicating that the tiny particles are probably remnants of once larger icy particles populating the outermost tenuous Saturnian ring, the E ring.
Following Cassini's Saturn orbit insertion, three further spectral types have been discovered (during crossings of the E ring), associated with different particle populations. The bulk material of Type I and Type II particles is water ice. In contrast Type III dust exhibits a mineral composition. Type I spectra imply pure water ice particles, whereas in Type II spectra organic compounds and/or silicate minerals are identified as impurities within the icy particles. This reveals the cryo-volcanic plumes of the moon Enceladus as the origin of Type II particles, which implies a dynamic interaction of Enceladus' rocky core with liquid water. The non-water Type III dust species exhibits an iron-rich composition, probably in the form of pyrite, oxides and/or hydroxides. A magnesium-rich siliceous subspecies is likely. Retrograde or unbound orbits are in best agreement with the Type III observations.

Preface

The work presented in this thesis was performed at the Max-Planck-Institut für Kernphysik under the supervision of Prof. Dr. Grün and Dr. Sascha Kempf.

Several chapters of the thesis are based on publications which have been published in refereed journals during the course of this work. In each of these publications the author of the thesis has significantly contributed either as leading author or coauthor. Most of the figures are taken from these original publications. However, the text has been thoroughly revised and adapted to recent findings.

In the following the publications and the respective chapters in this thesis are itemised:

- **Chapter 3**
  Hillier, J. K., Green, S. F., McBride, N., Postberg, F., Altobelli, N., Kempf, S., Schwanethal, J. P., Srama, R., McDonnel, J. A. M., and E. Grün, 2007
  Interplanetary dust detected by the Cassini CDA Chemical Analyser
  Icarus, vol. 190, p. 643–654.

- **Chapter 4**
  Postberg, F., Kempf, S., Srama, R., Green, S. F., Hillier, J. K., McBride, N., and E. Grün, 2006
  Composition of jovian dust stream particles
  Icarus, vol. 183, p. 122–134.

- **Chapter 5**
  Kempf, S., Srama, R., Postberg, F., Burton, M., Green, S. F., Helfert, S., Hillier, J. K., McBride, N., McDonnell, J. A. M., Moragas-Klostermeyer, G., Roy, M., and E. Grün, 2005
  Composition of Saturnian Stream Particles
  Science, vol. 307, p. 1274–127.

- **Chapter 6** (except sections 6.1.7 and 6.2.3)
  Postberg, F., Hillier, J. K., Kempf, S., Srama, R., Green, S. F., McBride, N. and E. Grün, 2007
  The E-ring in the vicinity of Enceladus II: Probing the moon's interior - the composition of E-ring particles
  Icarus, in press.

It has to be pointed out that this thesis also contains many yet unpublished results. This applies particularly to the target contamination analysis (chapter 2.3 and appendix B) and the analysis of the E ring Type III population (chapters 6.1.7 and 6.2.3).

If not noted otherwise the photographs displayed in this thesis are taken from the official NASA/JPL homepage (http://photojournal.jpl.nasa.gov/index.html).

Contents

Chapter 1

Introduction

Earth bound observations only allow the very poor investigation of dust in its various forms in the solar system. Often the medium is too tenuous to get much information from remote sensing, if any. Therefore *in situ* measurements using spacecraft have been carried out since the early seventies (Grün et al., 1980). Following investigations of a relatively dense dust medium at Halley's comet (Kissel et al., 1986a; Kissel et al., 1986b), large area dust detectors have been mounted on the interplanetary spacecraft Ulysses, Galileo and Cassini (Grün et al., 1992a; Grün et al., 1992b; Srama et al., 2004). Being the successor to the two other instruments, the Cassini dust detector is equipped with a time of flight mass spectrometer providing not only dynamic but also chemical information about the detected particles. These carry important information about their origin. Thus, the particle composition has the potential to reveal their actual source(s) and - furthermore - enable the study of the source's properties. This has successfully been achieved in multiple cases during the course of the Cassini mission, as is demonstrated in this work.

The focus of this thesis is on the chemical interpretation of the impact ionisation mass spectra produced by the Cosmic Dust Analyser (CDA) onboard the Cassini spacecraft. During its voyage, the Cassini spacecraft has encountered six different "dust families" so far. Each family shows typical spectral characteristics allowing the physical and chemical characterisation of the particles concerned. Besides the compositional analysis of the different species, planetological implications are derived where possible.

The thesis is organised as follows. In the first chapter the Cassini-Huygens mission and the spacecraft as the platform of the CDA are presented briefly. There then follows an introduction to the two environments this work is focussed on: The dust environments of Jupiter and Saturn. The latter is discussed with particular emphasis on the recently discovered ice-volcanism of the moon Enceladus where a subsurface reservoir of liquid water is a likely source of icy ring particles.
In chapter two the Cosmic Dust Analyser, and particulary the Chemical Analyser (CA) subsystem, is introduced. It includes a subsection (2.2) where the processing of the data used for this work is described and another subsection (2.3) which intensively discusses the instrument contamination issues and their possible influence on the results obtained in space.

Chapter three provides a summary of the compositional analysis of interplanetary particles which the CDA encountered in the early cruise phase.
In chapter four the measurements of the Chemical Analyser subsystem before and during the Jupiter flyby are presented. Here the composition of Jovian stream particles originating from giant volcanoes of the active moon Io is analysed. This in turn has implications for the modeling of such eruptions.
Chapter five discusses the composition of the Jovian stream particle counterpart in the Saturnian system. Here the origin of stream particles is the planets extensive ring system.
In Chapter six the dust population of the E-ring is analysed. During Cassini's numerous traversals through this outermost Saturnian ring, three different compositional particle species were identified, of which at least one is generated below the icy crust of the moon Enceladus.
The work concludes with chapter seven where all results are summarised.
Appendices provides useful additional information, supplementary tables and data.

1.1 The Cassini-Huygens Mission

Cassini is the fourth spacecraft to visit Saturn. In contrast to its predecessors Pioneer 11, Voyager 1, and Voyager 2, which only briefly traversed the Saturnian system on their cruise through the solar system, Cassini will orbit Saturn for at least six years. The spacecraft was named after the French-Italian astronomer Giovanni Domenico Cassini (1625–1712), who first noted the division between the Saturn's A and B ring (which now bears his name) and discovered the Saturnian moons Tethys, Dione, Rhea, and Iapetus. The scientific objectives of the Cassini mission are manifold – exploration of the planet itself, the ring system, Titan, the icy moons, and the magnetosphere. Beyond that, Cassini will help to reveal the complex interactions between the constituents of the Saturnian system. To achieve this, many parameters have to be measured simultaneously which in turn implies that many instruments have to operate simultaneously. To meet the mission objective, the orbiter is equipped with a suite of versatile instruments:

Cassini Plasma Spectrometer (CAPS) In situ study of plasma within and near Saturn's magnetic field.

Cosmic Dust Analyser (CDA) In situ study of dust grains in the Saturnian system.

Dual Technique Magnetometer (MAG) Study of Saturn's magnetic field and its interaction with the solar wind.

Ion and Neutral Mass Spectrometer (INMS) In situ study of the composition of neutral and charged particles within the magnetosphere.

Magnetospheric Imaging Instrument (MIMI) Global magnetospheric imaging and in situ measurements of Saturn's magnetosphere and solar Wind interactions.

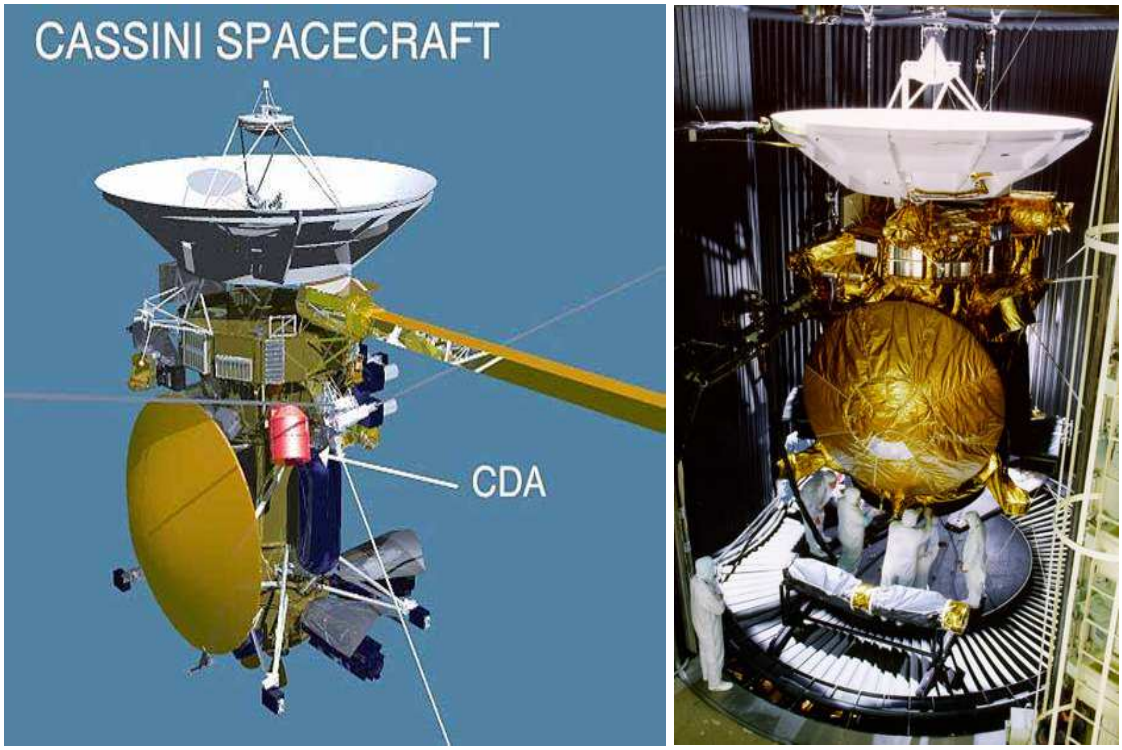

Figure 1.1: Left: Drawing of the Cassini-Huygens spacecraft. The position of the dust detector is indicated. Right: Cassini-Huygens during preflight-testing. The largest and most complex interplanetary spacecraft built to date, Cassini-Huygens is 4 m wide and 6.7 m high. Most of the instruments are already covered by thermal blankets (for protection against the aggressive space-environment) in this picture. The heat shield of the Huygens probe is clearly visible in both pictures.

Radio and Plasma Wave Science (RPWS) Measurement of electric and magnetic fields, and electron density and temperature in the interplanetary medium and within Saturn's magnetosphere.

Cassini Radar (RADAR) Radar imaging, altimetry, and passive radiometry of Titan's surface.

Composite Infrared Spectrometer (CIRS) Infrared studies of temperature and composition of surfaces, atmospheres, and rings within the Saturnian system.

Imaging Science Subsystem (ISS) Multispectral imaging of Saturn, Titan, rings, and icy satellites to observe their properties.

Radio Science Instrument (RSS) Study of atmospheric and ring structure, gravity fields, and gravity waves.

Ultraviolet Imaging Spectrograph (UVIS) Ultraviolet spectra and low-resolution imaging of atmospheres and rings for structure, chemistry, and composition.

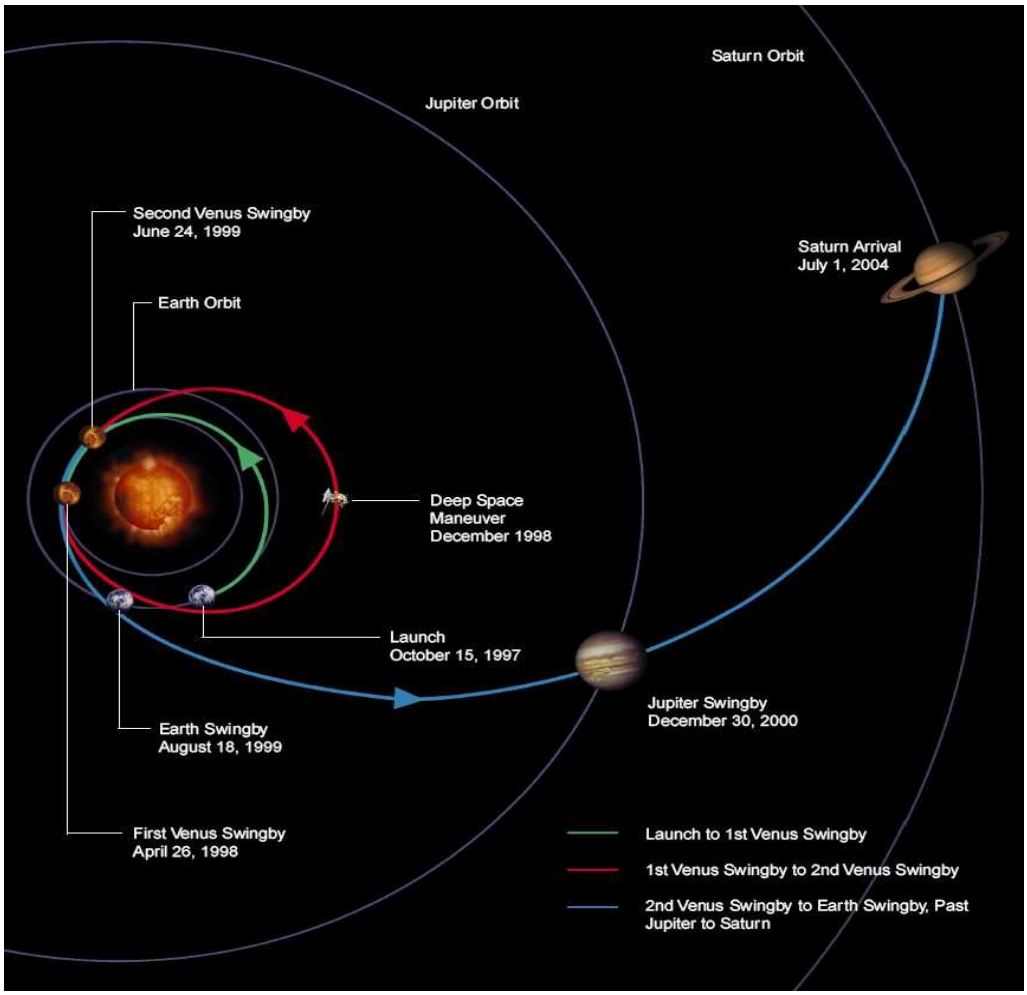

Figure 1.2: Cassini's path to Saturn.

Visible and Infrared Mapping Spectrometer (VIMS) Visible and infrared spectral mapping to study composition and structure of surfaces, atmospheres, and rings.

As well as those instruments, the spacecraft also carried the **Huygens Probe**, the main contribution of the European Space Agency (ESA). Its mission was to decent to the surface of Titan (the most prominent, planet sized moon of the system) and explore its atmosphere and surface.

Cassini is a 3-axis stabilised spacecraft. Most of the 12 instruments (Henry, 2002) are mounted on the body of the main spacecraft (Fig. 1.1). The spacecraft attitude is controlled either by reaction wheels or by thrusters. As a consequence of the body-fixed instrument mounting the spacecraft orientation needs to be changed frequently to adjust the instrument pointing. Clearly, this design is not optimal with respect to spacecraft and instrument operation. However, the eventual design was the only permissible concept within NASA's budgetary constraints.

Cassini was launched into an interplanetary trajectory on 15 October, 1997. The spacecraft performed two swingby manoeuvres at Venus and one at Earth before it flew past the Jovian System in late 2000 (see Fig.1.3). By firing the main engines for almost 100 minutes it entered into a Saturnian orbit on 1 July, 2004 (Saturn Orbit Insertion – SOI). Shortly before the SOI, on 11 June 2004, Cassini performed a close flyby of the icy moon Phoebe, which is moving in a retrograde orbit around Saturn. The four year prime mission phase of Cassini, including about 80 orbits started with the SOI and will end in mid 2008. The Huygens probe was released on the second orbit around Saturn in December 2004 and landed on Titan on January 14th 2005, operating for over 3 hours during the descent and on the surface. Cassini's nominal orbital tour contains 45 close flybys of Titan, 3 close flybys of the icy moon Enceladus, one each of the icy moons Hyperion, Dione, Rhea, and Tethys (Wolf, 2002). The large number of Titan flybys is not only due to the scientific importance of this moon but also due to the fact that Titan is the only Saturnian moon massive enough to perform gravity assist manoeuvres for modifying the spacecraft's orbit.

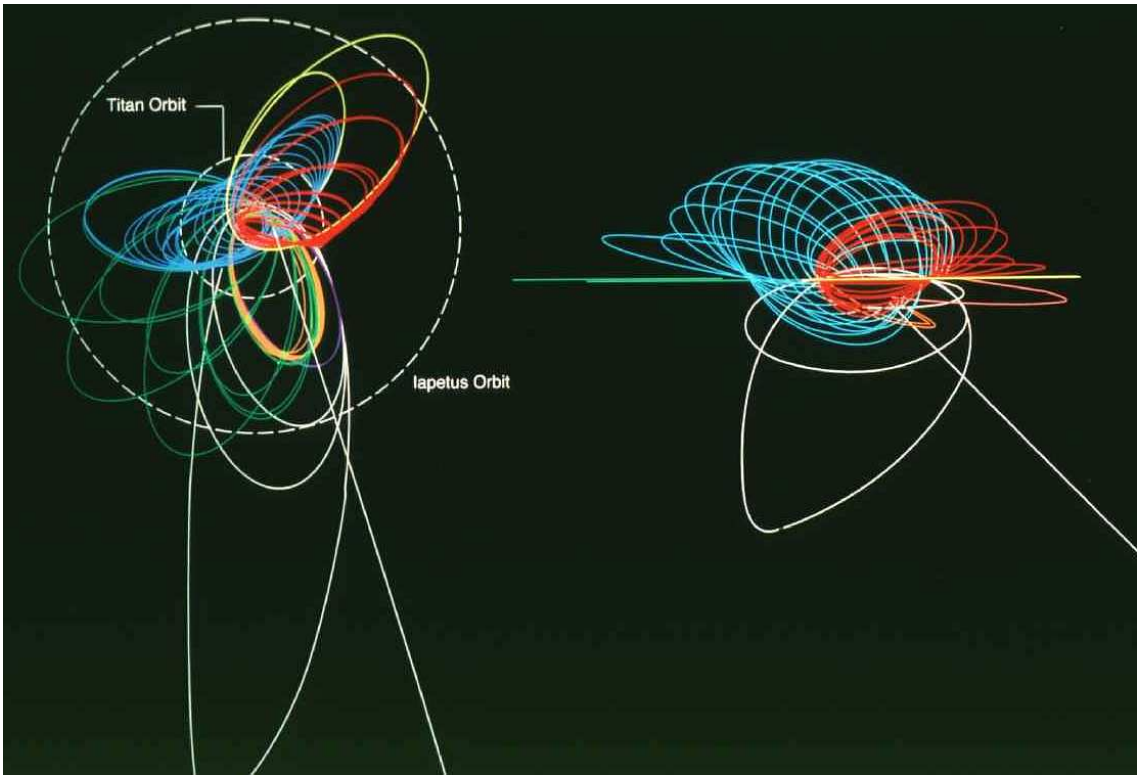

Figure 1.3: Cassini's tour trajectory around Saturn during the nominal mission.

An extended mission is scheduled from July 2008 onwards until June 2010. It is composed of approximately 55 orbits and is currently implemented by the Cassini navigation department. As well as more than 20 close Titan flybys it contains another 7 close Enceladus encounters and one flyby each to Rhea and Dione.

1.2 The Jovian System as a Dust Source

Figure 1.4: *The active moon Io in front of Jupiter's cloud bands. The Picture was taken by the Cassini cameras during the swingby manoeuvre on Dec. 30th, 2000.*

The Jovian system was first recognised as a source for dust particles during the encounter of the Ulysses spacecraft in 1991/1992 when high speed intermittent streams of tiny grains were discovered (Grün et al., 1993). The on-board dust detector registered several short impact bursts with a periodicity of 28 $\pm$ 3 days as well as of 14 $\pm$ 2 days. The radiants tended to lie close to the line-of-sight direction to Jupiter. Three years after Ulysses, the Galileo spacecraft approached the gas giant carrying an identical dust detector. Galileo again encountered the Jovian dust streams at a Jupiter distance of more than 1 AU. In 2004 the Ulysses Spacecraft again encountered Jupiter. This time the first streams were detected when the spacecraft was still 4 AU away from the planet. The evaluation of a large sample of 28 dust streams confirmed a periodicity of 26 days (closely matching the solar rotation period) with a subharmonic of 14 days, correlated with the pointing of the interplanetary magnetic field (IMF).(Krüger et al., 2006).

According to the current theories the basic mechanism for creating the dust streams is as follows: Once a grain is positively charged within the plasma environment of Jupiter's magnetosphere it will be accelerated by the outward pointing co-rotational electric field. Outside the magnetosphere, the dynamics of the grains are governed by the interaction with the IMF that eventually forms the dust stream(s). The intermittent nature of the stream detections is believed to be due to spacecraft traversals through layers of com-

pressed solar wind - e.g. so-called corotating interaction regions (CIRs)) - that enhances the dust flux, as observed in the vicinity of Saturn (Kempf et al., 2005a) and Jupiter (Krüger et al., 2006). Zook et al. (1996) simulated stream particle trajectories for the measured IMF throughout the Ulysses approach phase to Jupiter and demonstrated that only fast ($>$200 km s^{-1}) and tiny ($5-15$ nm) particles were able to reach the dust detector.

Although it was soon realised that if sub-micron charged particles exist within the Jovian magnetosphere they would be accelerated and ejected (Horányi et al., 1993a; Horányi et al., 1993b), there was some controversy about the dust's origin. The volcanoes of the Jovian moon Io (Fig. 1.4) (Grün et al., 1996) and Jupiter's gossamer rings (Fig. 1.5) (Hamilton and Burns, 1993) were proposed as potential dust sources. A periodogram analysis of impact rate data taken during two years of Galileo's orbit around Jupiter implies that Io is one important source of stream particles (Graps et al., 2000), emitting a continuous flux of nanometre-sized particles which form an oscillating sheet. The contri-

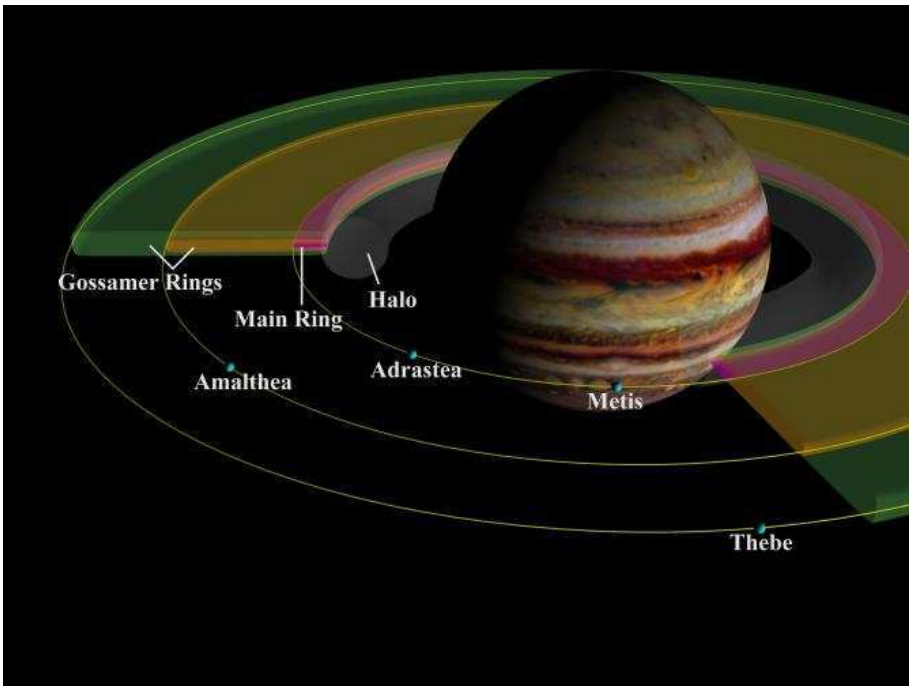

Figure 1.5: *The Jovian ring system.*

bution of Jupiter's rings to the dust flux is still discussed today. By means of the time-of-flight (TOF) mass spectrometer of the CDA onboard Cassini this question was answered. The spectra provided the ability to distinguish between the particle types from the two possible sources, which should leave different chemical fingerprints (chapter 4).

Jupiter's ring system consists of three components: the main ring, the halo, and the tenuous gossamer rings (Showalter et al., 1985). A significant fraction, if not all, of the dust forming the rings is supposed to be impactor-ejecta derived from the inner rocky moons Metis, Adrastea, Amalthea, and Thebe (Ockert-Bell et al., 1999; Burns et al., 1999;

Showalter et al., 2003), whose orbits are embedded in the ring system (Fig. 1.5). It has been shown that - unlike in Saturn's icy rings (Poulet et al., 2003; Hillier et al., 2007b) - rock forming minerals are predominant in the Jovian main rings (Wong et al., 2004). However, little is known about the composition of the gossamer rings and their primary sources Amalthea and Thebe. Those dark, narrow rings with low albedo are expected to consist mainly of rock fragments as well, but contributions from other components - such as water ice or organic material - cannot be ruled out. During Galileo's traversal through the gossamer ring in 2002, several thousand dust impacts were registered. The Galileo dust instrument wasn't equipped with a mass spectrometer, but the data revealed particle sizes in the micron as well as in the sub-micron range with the small grains dominating the number density (Krüger, 2003).

Figure 1.6: *Active volcanism pictured by the cameras of the Galileo spacecraft. As well as the volcanic plume at the top of the figure, a ring of volcanic ashes and a corresponding lava outflow can be seen at the bottom center.*

Volcanic ashes cover the surface of the moon Io (Fig. 1.6) whose interior is heated by Jupiter's tidal forces. The amazing variety of its colors indicate Sulfur in its various molecular structures (yellow, orange, red, brown, and black) as well as specific silicate minerals. Volcanically ejected dust particles can escape into Jupiter's co-rotating plasma torus where they almost instantly could become stream particles (Horányi et al., 1993a; Krüger et al., 2003; Flandes, 2004). It has to be pointed out that, while the composition of the Ionian gas and plasma environment has been extensively studied, there is no information about the composition of its dust environment. Furthermore, the genesis and

composition of particles in the volcanic plumes is still unclear (Geissler, 2005). Spectroscopic analysis of Io's atmosphere reveals SO_2 as the main component accompanied by smaller amounts of its subproducts SO, S and O as well as sodium chloride NaCl (Lellouch et al., 1996; Lellouch et al., 2003). The observation of emission lines in the Jovian plasma torus, which is supplied by Io's gas emission, gives a similar picture: S^+ and O^+ are the dominant components with S^{2+}, O^{2+}, SO_2^+ and the alkali-metal salt components Na^+, K^+, Cl^+, Cl^{2+} in smaller amounts (Küppers and Schneider, 2000; Schneider et al., 2000). The major part of the escaping gas which is not ionized forms neutral gas clouds around Io. Spectroscopy reveals this to be rich in Na, K, and O (Brown, 1974; Thomas, 1996). An abundant neutral S cloud is predicted but cannot be proved by optical line emission. Mendillo et al. (2004, 2007) clearly demonstrated that Io's volcanic activities have a controlling effect on the extent and brightness of the sodium cloud. Though silicate-type mineral components play a role in Io's volcanic system, so far there is no observational proof for their escape from Io's gravitation in any form (Na et al., 1998).

1.3 Dust at Saturn: The E Ring, Ice Volcanoes, and Streams

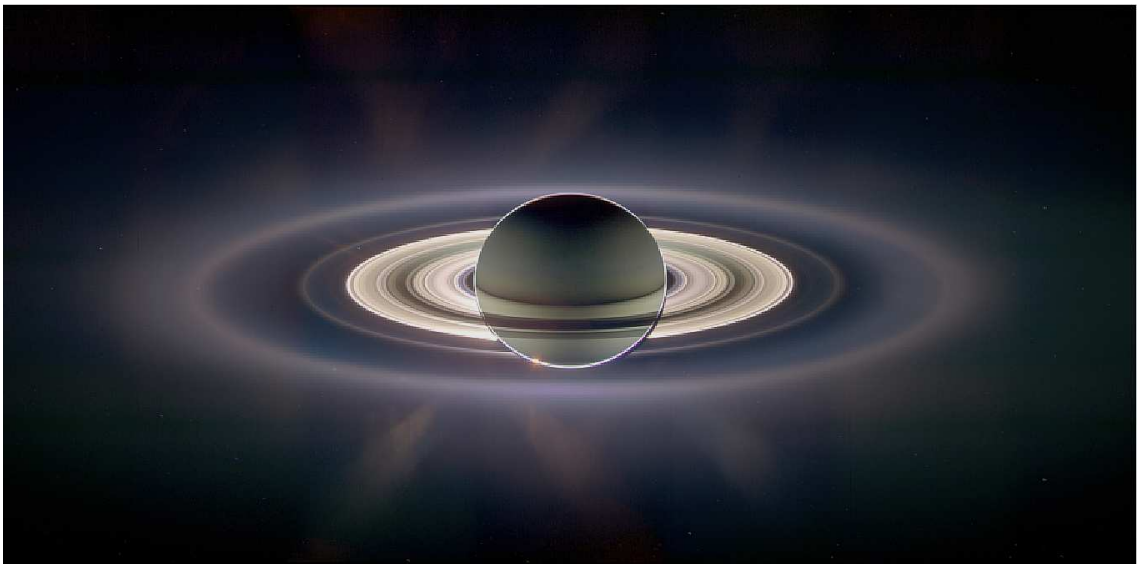

Figure 1.7: Saturn's ring system as seen by Cassini's cameras (contrast enhanced). The outermost ring is the inner part of the E ring. Its brightest region roughly marks the orbit of Enceladus and is called the "Enceladus torus". The Earth is visible as a faint spot, slightly inside the upper left segment of the thin G ring.

Saturn is famous for its huge ring system. The main ring system consists of the broad A and B rings separated by the Cassini Division and the optically thinner C and D rings (Figs. 1.8 and 1.7, parameters are given in Table A.3 in the appendix). James Maxwell

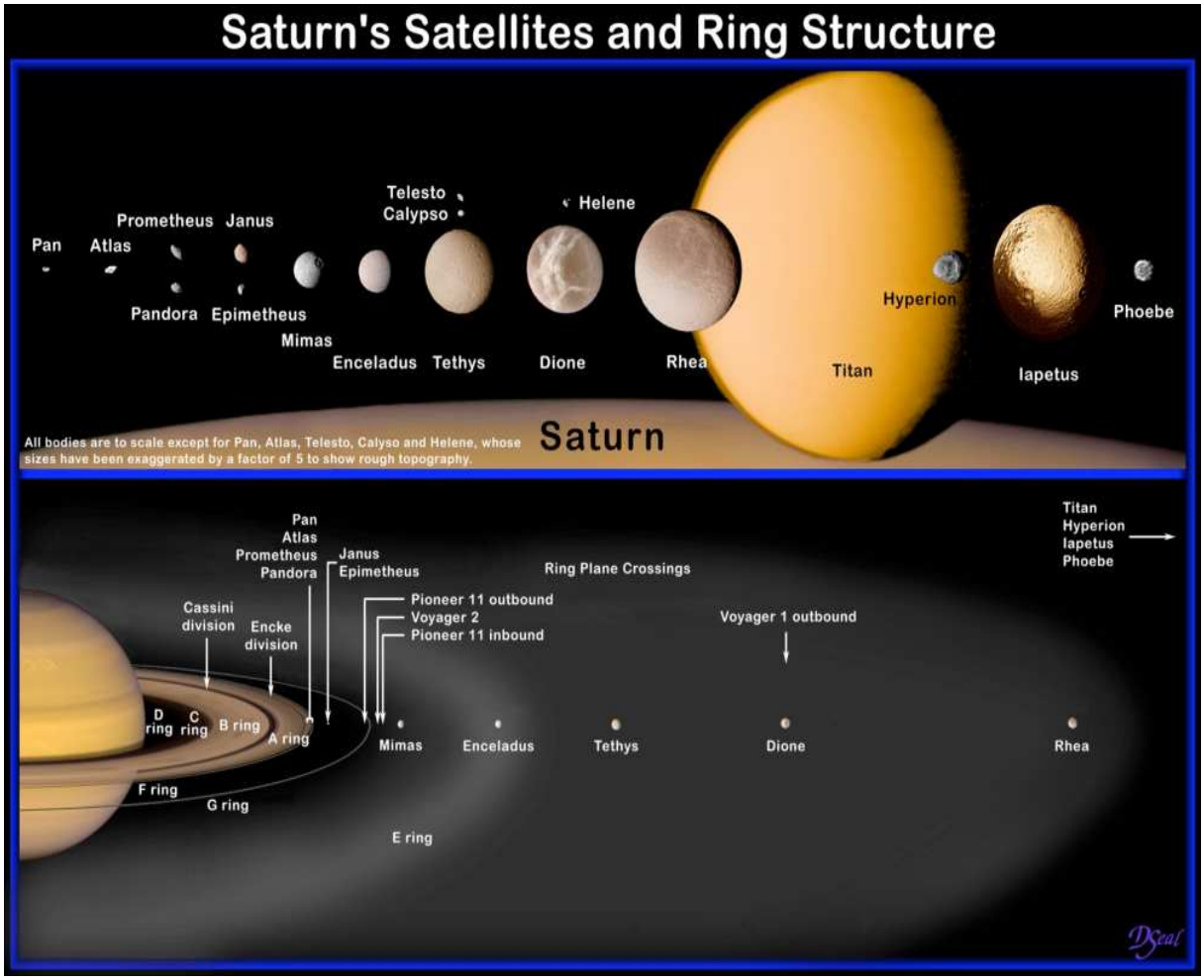

Figure 1.8: Rings and moons in the Saturnian system.

proved in 1857 that the rings are not solid but that they are composed of individual particles orbiting the planet. The next substantial revision of our view of the rings happened when the two Voyager spacecraft revealed the rich fine-structure of the main rings: spiral density and bending waves similar to those responsible for the galactic structure, sharp gaps with some of them containing elliptical ringlets or tiny moons, so-called spokes – shadows moving radially outwards, and many more interesting phenomena. The dynamics of the main rings are governed by collisions between the ring particles. Little is known about the long-term evolution of the main rings. The ring mass is sufficient to be self-sustaining on long time scales with the mass of the ring material being comparable to a 400 km diameter ice satellite (Murray and Dermott, 1999). However, close encounters between ring particles and external satellites slightly increase the particles' semi-major axes which may cause the system to slowly evolve outwards.

The outermost ring in the system is the vast E ring, the largest known planetary ring in the solar system (Figs. 1.8 and 1.7. The physics of this diffuse optically thin ring lying

exterior to the main rings is entirely different. The lifetimes of the approximately micron-sized ring particles are rather short due to the action of radiation pressure, electromagnetic forces and the plasma drag whilst collisions between the ring particles are of no relevance. The short lifetimes thus imply a recent source of fresh dust particles. For decades Saturn's icy moon Enceladus (Fig. 1.9) was suspected to be the major source of particles feeding the planet's outer E ring (Baum et al., 1981). Due to its low optical depth, the composition of the faint E ring could be only poorly investigated by remote sensing (reflectance spectroscopy) and, until Cassini's arrival, was basically inferred from the composition of the icy surfaces of its embedded moons (Showalter et al., 1991; Nicholson et al., 1996). In situ CDA measurements, obtained during Cassini's first E ring crossing in October 2004, confirmed that the particle composition in the outer E ring is dominated by water ice (Hillier et al., 2007b). A minor but significant contribution to the particle composition by other substances was also identified.

Figure 1.9: Enceladus' surface pictured by Cassini's cameras. It reveals different structures which hint at tectonic activity and other mechanisms that provide the amazing topographic variety. The active south polar region is marked by rifts called "tiger stripes" at the bottom of the picture.

Enceladus orbits Saturn at a mean distance of 3.95 Saturnian radii (Saturn's radius R_S = 60330 km) and is one of five satellites embedded in the huge diffuse E ring. The mean diameter of the moon is 504 km, and it has a surprisingly high average density of about

$1610\,\mathrm{kg\,m^{-3}}$ (Porco et al., 2006). In 2005, Cassini's instruments detected a major collimated particle and gas flow being emitted from Enceladus. During a close flyby the dust detector discovered a dust jet emerging from Enceladus' southern polar region (Spahn et al., 2006b); a site characterised by elongated cracks (Porco et al., 2006) - the so called "tiger stripes" (see Fig. 1.9) - significantly warmer than their surroundings (Spencer et al., 2006). The dust jet was accompanied by a neutral (predominantly water) gas cloud detected by both the Cassini magnetometer (MAG) (Dougherty et al., 2006) and the Ultra-Violet Imaging Spectrometer (UVIS)(Hansen et al., 2006). The density and composition of the neutral gas cloud was measured by the Ion and Neutral Mass Spectrometer (INMS) (Waite et al., 2006).

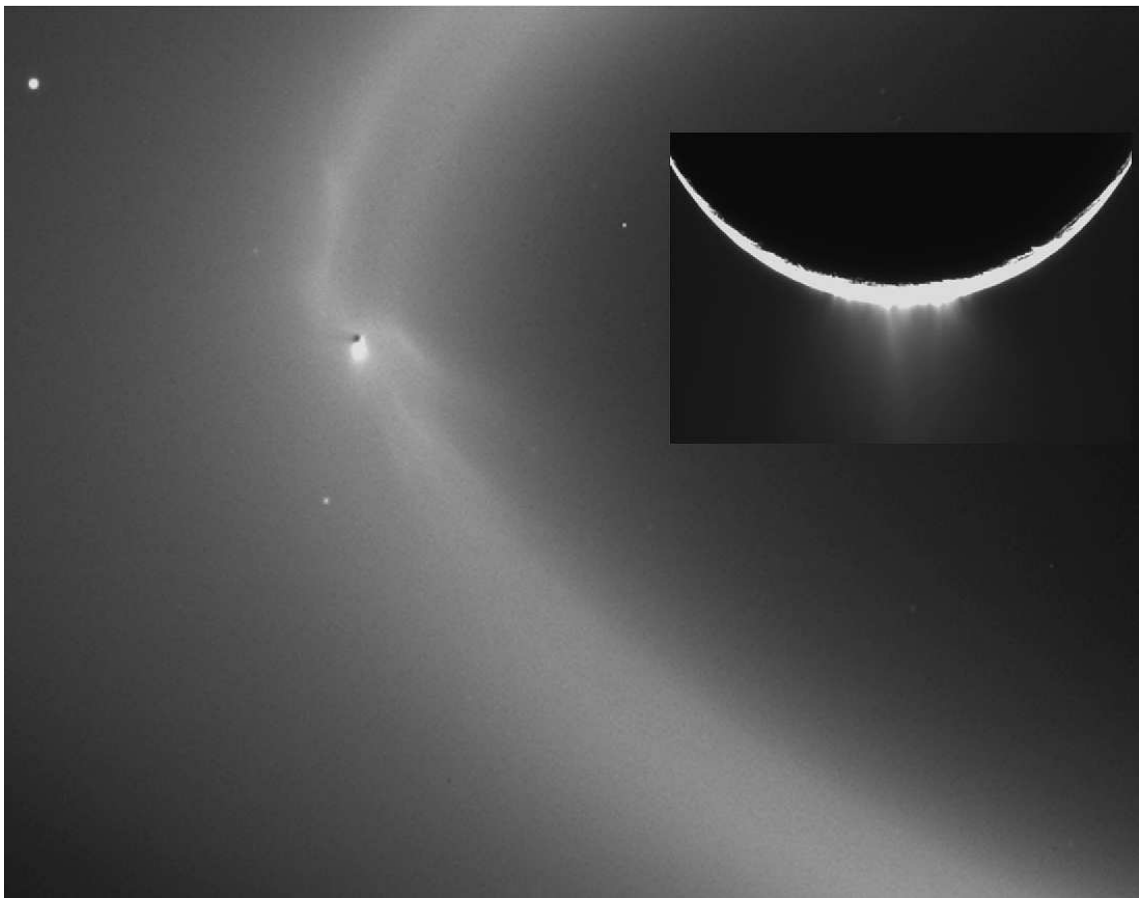

Figure 1.10: On this Cassini picture, Enceladus can be seen as a black dot embedded in the E ring. Towards the south, a bright particle stream marks the cryo-volcanic plumes. The inset shows the icy dust fountains emerging at different locations from the moon's surface. These pictures were taken several months after the discovery of the south polar gas and particle emission (see text).

Results of the close Enceladus flyby in June 2005 (E11) characterise the emissions from Enceladus' active source into the E ring as follows:

- There is a large confined neutral water vapour plume in the south polar region of

Enceladus (Hansen et al., 2006).

- There is also a strong particle flow which decouples from the gas flow soon after emission (Spahn et al., 2006b; Waite et al., 2006).
- The inferred column densities revealed a surprisingly high particle to gas ratio of less than 1:3 (Spahn et al., 2006b; Waite et al., 2006; Hansen et al., 2006).
- The neutral gas emission is dominated by H_2O ($\approx 91\%$), containing N_2 and/or CO ($\approx 4\%$), CO_2 ($\approx 3\%$), CH_4 ($\approx 1.5\%$) and possible traces of C_2H_2 and C_3H_8 (Waite et al., 2006).
- The moon's plasma environment consists mainly of water ions and water dissociation products H_3O^+, H_2O^+, OH^+, O^+ and H^+ as well as Nitrogen ions ${N_2}^+$ and N^+ (Tokar et al., 2006).
- The otherwise pure water ice surface of the moon is enriched with CO_2 and light organics in certain parts of the active south polar region (Brown et al., 2006).

Due to the presence of the active moon, the particle density of the E ring in the vicinity of Enceladus is significantly higher than in other regions (Figs. 1.7 and 1.10.) This region of enhanced density is now called the Enceladus torus. Since the radial density distribution appears to follow two power laws, peaked approximately around the Enceladus orbit (Kempf et al., 2007), the definition of the borders of the torus are somewhat arbitrary. In this work the torus is defined as the region of the E ring extending from 3.65 to 4.3 R_S.

Horányi (2000) proposed that, similarly to Jupiter, also Saturn's magnetosphere should also be able to generate dust streams. To try and discover possible Saturnian dust streams a CDA campaign dedicated for stream detection during Cassini's approach to Saturn was carefully designed. In agreement with model predictions for the interplanetary dust environment between Jupiter and Saturn the instrument registered almost no dust impacts during the late phase of Cassini's cruise to Saturn. However, by the beginning of 2004 when Cassini was closer to Saturn than 1 200 Rs, a couple of faint impact bursts by high-velocity grains were observed (Fig. 1.11).

Prior to Cassini's insertion into a Saturnian orbit 369 impacts were registered. All of them showed the characteristic features of a high velocity impact by a tiny (radii ≤ 10 nm (Kempf et al., 2005a)) dust particle. The intensity of the bursts seemed to grow with decreasing distance to Saturn, indicating a Saturnian origin of the impactors. Furthermore, interplanetary dust can be excluded as the source by examining the transmitted impact signals. From these an impact speed significantly exceeding 70 km s^{-1} was inferred (Kempf et al., 2005a), which excludes any contribution to the detected events from bound interplanetary grains. Furthermore, throughout the interval of analysis the CDA detector was geometrically insensitive to unbound interplanetary dust (the so-called β-metoroids, see Wehry & Mann (1999)). These observations initially supported the hypothesis that the Saturnian system is the origin of the observed particles.

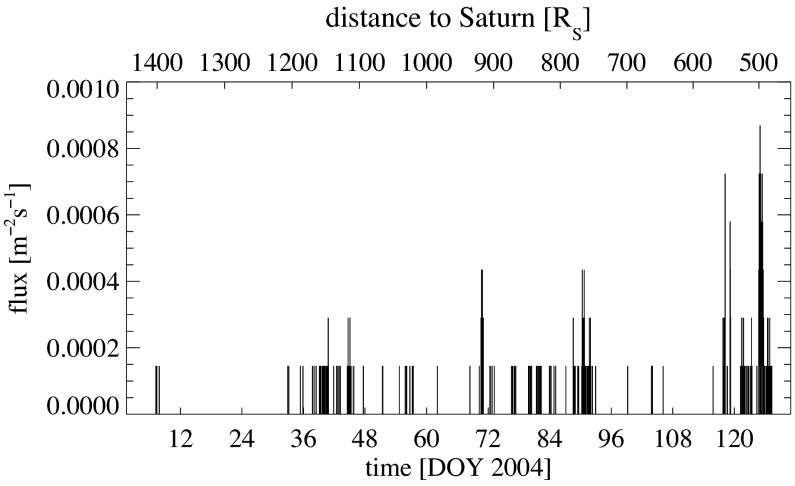

Figure 1.11: Flux of stream particles detected by the CDA at Cassini's approach towards Saturn. DOY = day of year. From Kempf et al (2005b).

With Cassini orbiting Saturn for several years now, the frequent detection of stream particles at almost every orbit clearly verified this initial assumption. The tiny particles are probably ejected into interplanetary space with about 80–100 km s^{-1}, where they - as their Jovian counterpart - can be further accelerated by traversals through layers of compressed solar wind (Kempf & Hsu (2007), personal communication).

Chapter 2

Instrument and Data

2.1 The Cosmic Dust Analyser

The Cosmic Dust Analyser (CDA) consists of two independent instruments (Fig. 2.1): the Dust Analyser (DA) and the High Rate Detector (HRD). The HRD was designed to monitor high impact rates (up to $10000\,s^{-1}$) in dust rich environments such as Saturn's ring plane and will not be discussed here. The DA has three different subsystems: the entrance grid, sensitive to the charge carried by the particle (QP detector), the classical Impact Ionisation Detector (IID), similar to Galileo-type instruments (Grün et al., 1992a; Grün et al., 1992b) and a time-of-flight (TOF) mass spectrometer, which is referred to as the Chemical Analyser (CA). Depending on the trajectory of the particle, it either hits the central Rhodium target (Chemical Analyser Target - CAT, diameter: 0.17 m), the surrounding Gold target (IIT, diameter: 0.41 m), the inner wall of the instrument, or one of the grids. This work only deals with impacts on the CAT because only these provide high resolution mass spectra. The other CDA components are described in e.g. Kempf et al. (2007) and in greater detail by Srama et al. (2004).

If a dust particle impacts onto the CAT with sufficient energy the particle is partly vaporised and ionised, forming an impact plasma of target and particle ions, together with electrons and neutral molecules and atoms. The instrument separates this plasma, the positive component of which is used to generate a time of flight (TOF) spectrum (see Fig. 2.2 for a more detailed explanation of the instrument operation).
Since TOF is proportional to the square root of the mass, the multiplier signal ideally represents a mass spectrum for identical ion-charges. In reality this equation is influenced by the broad distribution of the initial ion velocities Δv_0, varying flight paths Δs, and plasma shielding effects (Hillier et al., 2006).

The spectrum recording[1] can be triggered by exceeding charge thresholds on either the CAT or the multiplier (MP) itself (see Fig. 2.2). In the latter case, recording can be triggered up to several μs after the actual impact by the arrival of ions. Hypervelocity impacts, as in the case of stream particles, are often triggered by Hydrogen ions (H^+). For

[1] The high rate sampling mode of the multiplier.

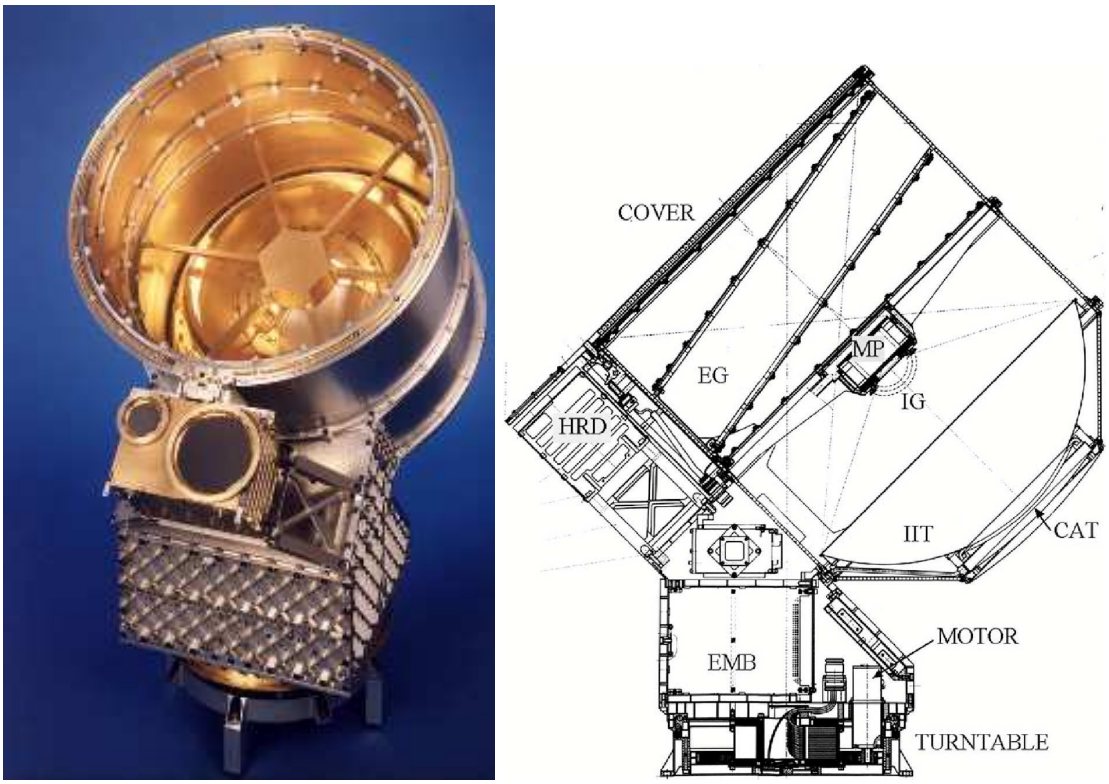

Figure 2.1: Photograph and schemetic of the Cosmic Dust Analyser (CDA). On the left picture the reverse of the multiplier housing (MP) can be seen in the center, behind which the inner (silvery) Rhodium target (CAT) and the outer Gold target (IIT) are visible. Below the DA unit are the two foil sensors of the High-Rate-Detector (HRD). The "IG" is the ion grid where the QI signal is sampled (Fig. 2.2). The entry grid (EG) is sensitive to the charge of the particle and forms the QP signal.

water dominated particles the "trigger ions" are, in most cases, Hydronium ions (H_3O^+). As a consequence, signatures of species with lower masses than e.g. H_3O^+ (19 amu), as well as the mass line of the triggering ion itself, do not appear in the fraction of spectra triggered by the multiplier, although Hydrogen or Hydronium ions are an abundant component of the impact plasma. Whether the recording of a spectrum is triggered by the impact on the CAT itself or by the arrival of ions at the multiplier strongly depends on the impact energy.

The spectra are logarithmically amplified, digitised at 8 bit resolution and sampled at 100 MHz for a period of 6.4 μs after triggering. Since the TOF is proportional to the square root of the mass to charge ratio of ions, this also represents a mass spectrum for a unit ion-charge. Unfortunately the TOF is also influenced by the broad distribution of initial ion velocities, varying flight paths, and plasma shielding effects (Hillier et al., 2006). The recording period of the high rate sampling mode enables the detection of ions with masses of up to approximately 190 atomic mass units (amu), assuming that the instrument recording is triggered by the impact itself and the ions are singly charged. During high

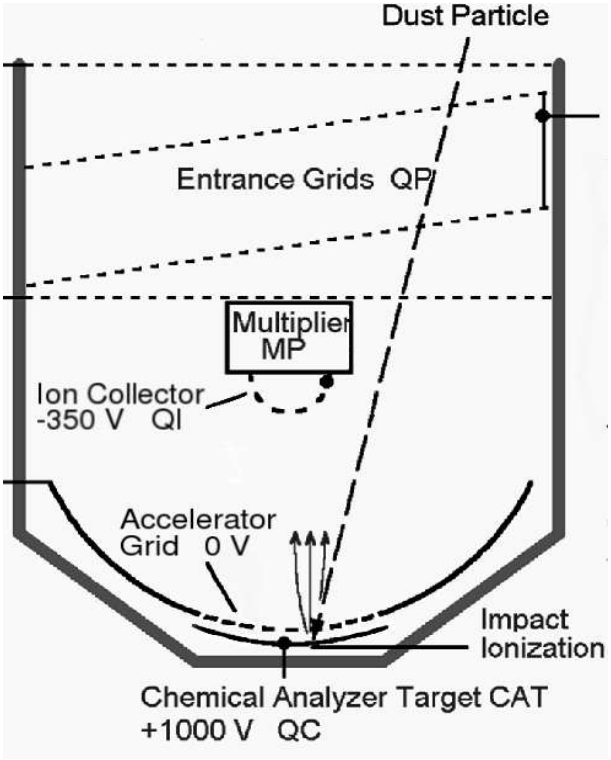

Figure 2.2: *A dust impact on the Chemical Analyser Target (CAT) creates a TOF spectrum. The CAT, which is composed of rhodium, is nominally held at a potential of about +1000 V. An electrically grounded grid is mounted 3 mm in front of it. Following the projectile impact, a plasma cloud expands from the target surface. The strong electric field (340 kV m^{-1}) separates the plasma: while the electrons and negative ions are collected at the CAT (QC signal), the positive ions are accelerated towards the grounded grid. After passage through this accelerator grid, the ions drift over a distance of 0.1924 m through a weak electric field (1.8 kV m^{-1}) towards the multiplier mounted in the centre of the instrument. About 50% of the incoming ions are collected by concentric grids in front of the multiplier where their integrated charge is registered by the QI channel. Behind these grids the passing ions enter a strong field region (100 kV m^{-1}) for final acceleration into the multiplier. Ion arrival time is proportional to the mass-to-charge (m/q) ratio of the ions. Their amplified signal (MP signal) is recorded as a positive ion TOF spectrum.*

particle fluxes, as may occur during crossings of the Saturnian ring plane, only a fraction of the detected events are transmitted (to reduce the space required for storage, as well as make best use of the limited data transmission time and bandwidth).

The spectrometer is sensitive to positive ions only. The mass resolution (m/Δm), derived from laboratory experiments with the instrument, depends on the atomic masses of the ions. At 1 amu, m/Δm is 10, increasing to 30 at 100 amu and up to 50 at 190 amu, although these values strongly vary with impact conditions (Stübig, 2002). In general this does not allow a detailed analysis of complex chemical structures and only very limited differentiation of isotopes. Nevertheless, the spectra allow the classification of different projectile types such as silicates, water ice, organic- or Fe/Ni-particles.

The limited instrument sampling rates, together with the short charge signal duration (due to the strong electric fields used to generate TOF spectra), mean that accurate particle speed and mass determination from CAT impacts cannot be done via signal risetimes (as with IIT or High Rate Detector impacts).

The aforementioned limitations of the detector were tolerated in order to produce a multi purpose instrument, capable of delivering high-quality results under varying conditions. Furthermore, CDA combines, for the first time, a large sensitive area with a time of flight mass spectrometer, allowing the chemical characterisation of a tenuous dust medium.

2.2 Datasets and Spectra Calibration

In this work, the term "occurrence of features" is used to refer to how many spectra contain a certain feature, whilst "abundance" refers to the number of ions of a certain species in a spectrum.

The impact charge yield[2] (Q) is classically described with a power law (e.g. Goeller and Grün (1989)) of the form:

$$Q = c \cdot m^{\alpha} \cdot v^{\beta} \tag{2.1}$$

c is a constant, m the particle mass and v the impact speed. Whereas α is generally assumed to be close to 1, CDA laboratory experiments yield values of between 2 and 6 for β (Stübig, 2002) depending on projetile material and impact speed regime.

The "total ion yield" or "total ion charge" given in this work is derived from the QI amplitude, which represents the positive ion charge of all particle and target species measured at the ion grids in front of the multiplier. Depending on their initial energy, approximately 30% of the ions produced at an impact are focussed here by the electric fields. 50% of those incoming ions are collected by the grids. Thus, the "total ion yield" is proportional to the number of ions produced by an impact and hence is a function of particle mass and speed (Reber, 1997; Srama, 2000; Stübig, 2002; Srama et al., 2004). The remaining ions that pass through the grids and impact the multiplier form the TOF spectrum.

The data of an individual impact consist of the TOF spectrum, the corresponding QC-amplitudes (number of collected electrons an anions at the CAT), the QI-amplitudes (number of positive charges at the multiplier entrance grid), and the impact times.

[2] negative charges collected at the target

The relation of TOF to ion mass is approximately given by:

$$t = b + a \cdot \sqrt{(m/q)} \tag{2.2}$$

q is the charge on the ions, and a is the so-called "stretch-parameter", which basically depends on the acceleration voltage. The "shift-parameter" b is the time offset $t - t_0$ and represents the shift between the time of triggering relative to the time of impact. To calibrate a spectrum a and b have to be determined.

The assignment of masses to this kind of TOF spectrum is not a simple task. Considering the target peak of Rhodium as an example, it can easily be seen that the ions of this species are distributed over a wide range of the TOF-scale (Fig. 4.1, 4.2). This is primarily due to their initial angular- and energy distribution in the impact plasma. Thus, in a strict sense the application of a mass scale to the abscissa is not correct. However, calibration experiments in the Heidelberg dust accelerator showed that the stretch parameter only varies by less than 1% around a value of $a = 4,8 \times 10^{-7}$ (Stübig, 2002; Lavila, 2002) if peak maxima positions are considered representative for the TOF of the respective ion species. Unless explicitly mentioned otherwise, this value is used for all spectra considered in this work. The determination of the shift parameter b is then accomplished by the assignment of ion masses to peaks of known species. This is described in more detail in the following sections for the individual datasets.

The data transfer from instrument to Earth is limited. To lower the data volume a wavelet compression method is occasionally used which reduces the number of datapoints in each spectrum by a factor of 2, 4, or 8. The compression is done by the instrument software. Compression factors of 4 and 8 in particular, lead to a substantial loss of mass resolution. Unless mentioned otherwise, no data compression was used for the data of this work.

2.2.1 Jovian Stream Particles

The dataset of Jovian stream particles consists of 458 TOF spectra recorded between September 4th 2000 and May 28th 2001. This corresponds to a Jupiter distance of 1.1 AU at the inbound trajectory and about 2 AU on the outbound trajectory. As Cassini is a platform for twelve instruments with a large number and diversity of requested operations, the pointing of the detector often didn't allow the detection of stream particles. Furthermore, it is important to understand that only a small fraction of the particles entering the CDA produce a mass spectrum (a total of more then ten thousand events were registered). During strong impact bursts only a fraction of the events were transmitted. The onboard software selected this fraction via the main criterion of "multiple distinct peak occurrence". A "by eye" revision of the data in 2007 showed that in fact over 700 spectra of Jovian stream particles were recorded. Thus, about 250 spectra have not been considered in the statistical analysis presented here. However, those mostly faint spectra were examined. They do not show any additional features and confirm the results of this work.

To provide a reliable statistical evaluation, similar impact conditions and a homogeneous data set have to be ensured. Thus, 287 spectra comprising the first two bursts registered on September 4th - 7th (stream 1) and October 1st - 4th 2000 (stream 2), are considered in the statistical analysis. Impacts detected afterwards were recorded under different and constantly varying impact conditions[3] and are of very limited use for the aim of this work. Additionally, streams 1 and 2 provide the highest impact rates and exhibited the best spectral quality. For stream 1 the minimum impact signal which triggers a "valid event" (the trigger threshold) was accidentally set too high. These events were thus all triggered "late" by the first ions reaching the multiplier (Fig. 2.2, chapter 2.1). However, the spectra of stream 2 (where the thresholds were set correctly) show no apparent difference from those of stream 1. From this we conclude that the higher thresholds during stream 1 had no influence on the detected particle composition types.

The calibration and analysis of the individual spectra was performed automatically using custom software, providing unbiased identification and integration of features. For this dataset, the determination of the shift parameter (b) necessary for the mass-calibration was performed using a cross-correlation method. The relative peak positions of four reference species usually present (C^+, Na^+, K^+, Rh^+) were used as a template. The mass resolution derived from laboratory experiments (as described in section 2.1) was achieved in many cases.

It is important to understand that neither the CDA nor its progenitors were designed for detecting stream particles. The CDA was built and calibrated for impactor masses greater than 10^{-18} kg with velocities below 70 km s^{-1}. This is very different from the properties of stream particles, which from simulations are believed to have masses around 10^{-21}kg (equivalent to a radius of about 10 nm) and impact velocities of more than 200 km s^{-1} (Zook et al., 1996), according to theoretical considerations probably over 400 km s^{-1}. Due to these extreme physical properties, dynamical information about an individual stream particle cannot be derived from the impact signals. However, some constraints for velocity and mass can be obtained. It is known that the rise time of the impact signal is dependent on the particle velocity (Eichhorn, 1976; Eichhorn, 1978). This is due to impact ejecta hitting the spherical target creating secondary impact ionisation events with a time delay dependent on the impact speed of the original particle. In fact the signal rise times of the stream particle impacts were smaller than the signal rise times of the fastest calibration impact measured in the Heidelberg dust accelerator facility of about $v_I \approx 70\,\mathrm{km\,s^{-1}}$. Due to their speed and size, the stream particles are likely to not produce any ejecta at all. In this case the rise time of the impact signal (QC) is a measure of the expansion time of the impact plasma, which is shorter than the time scale for possible ejecta impacts and again is an indicator of the particle's velocity. However, with this method the impact velocity cannot be constrained to better than setting a lower limit of about $v_I > 100\,\mathrm{km\,s^{-1}}$. The spacecraft's speed relative to the Jovian system was always

[3] As the spacecraft approached Jupiter the particle impact vectors changed significantly. Furthermore Cassini started to "roll" around a certain axis in October 2000, constantly changing the instrument boresight vector.

below 13 km s^{-1} and therefore had only limited influence on the impact vectors.

Many of the impact signals are just at - or even below - the nominal trigger threshold of the target signal. That is consistent with the very low particle masses predicted by simulations. If similar particle composition and speed are assumed, the masses of the impactors can be roughly compared using the amount of positive charge measured at the QI-channel.

The presence of H^+ is a known concomitant phenomenon of high velocity impacts due to target contamination (Krueger, 1996; Stübig, 2002; Kempf et al., 2005b) (see chapter 2.3 for details). As a positive side effect, all events whose impact charge at the target is insufficient to trigger the high rate sample mode still have a chance to produce a spectrum if the event is triggered by the ubiquitous H^+ ions arriving at the multiplier (see chapter 2.1). To maintain a large dataset, for a high statistical reliability, it is necessary to mix nominally (impact charge) triggered spectra, which show an H^+ feature, with those that are triggered by the multiplier and thus do not have this mass line. As a consequence, the H^+ features have not been taken into account for the total spectrum area (proportional to the number of ions contributing to a spectrum) when relative abundances were calculated. This has, however, no relevance for the data interpretation.

2.2.2 Saturnian Stream Particles

After the first detection of Saturnian stream particles in January 2004 (Fig. 1.11) until Cassini's arrival at Saturn at the end of June 2004 a total of 76 mass spectra were recorded. In addition, during the outbound leg of Cassini's first orbit about Saturn another 508 mass spectra were registered. Particles detected outside about 500 R_S caused relatively large impact charges, supporting an A ring origin, while particles registered after Cassini's orbit insertion generally produced only very little impact plasma, dynamically compatible with an E ring origin (Kempf et al., 2005a). With the exception of four particles detected closely after the SOI all stream particles were registered outside Saturn's magnetosphere, although their source lies within.

The Saturnian dust streams also consists of hypervelocity particles. As in the Jovian case, the transmitted impact signals (QC, QI) are much steeper than the fastest calibration impact of about 70 km s^{-1} recorded at the Heidelberg dust accelerator facility. Consequently, the impact speeds of the grains comprising the bursts considerably exceeds 70 km s^{-1}. Dynamical calculations hint at impact velocities between 80 and 200 km s^{-1} (Kempf & Hsu (2007), personal communication). Though the particle velocities are probably not as extreme as in the case of their Jovian counterpart, the mass of the grains appears to be even smaller. From theoretical considerations (Kempf et al., 2005a) most of the particles are expected to have radii well below 10 nm, in agreement with the mostly extremely faint impact signals.

All detected stream particle CAT impacts generated an H^+ line strong enough to trigger the event recording (see 2.1). In such a case, the offset times (shift parameter b) are

slightly above the TOF of H^+ ions (0.48 μs), which simplifies the mass calibration and allows the identification of the two dominant mass lines as C^+ (12 amu) and Rh^+ (103 amu) (Fig. 5.1). In some spectra only a single well-resolved line (C^+) is apparent.

For a reliable identification of other mass lines an iterative method was employed to magnify features too weak to be recognized easily in some of the individual spectra. This is described in detail in section 5.

2.2.3 Particles in Saturn's E ring

The E ring is a tenuous dust environment whose particles are, in general, dominated by water ice. During each orbit the Cassini spacecraft crosses the Saturnian ring plane, which in most cases is through the outermost of Saturn's rings. Almost 10 000 spectra have been recorded in 2005 alone, most of them during ring plane crossings. About 98% of all resolved spectra are dominated by water and water-cluster ions. These particles are considered to be the main population. Of those spectra that are not water dominated, less than 1% show mass lines primarily due to meteoritic metals and are investigated separately in the respective sections of this work (6.1.7 and 6.2.3). In a further 1% of spectra only ambiguous mass calibrations could be applied at best, due to difficulties in peak identification or indistinct peak shapes.

Water-rich E ring population

In this work a representative sample of about 2500 well-resolved spectra from over 5000 CAT impacts, obtained between February and November 2005 throughout the E ring, has been used. The data were recorded at ring plane crossings 3, 4, 7, 8, 9, 10, 11 and 20; the orbits are described in Kempf et al. (2007). The initial dataset is based on all transmitted data, which has been manually calibrated for the identification of CAT impacts. Additionally we selected spectra with a compression factor 2 or lower with at least two distinct mass lines. Whenever further restrictions apply to the dataset it is mentioned in the text.

The mass calibration of spectra is generally done by identifying the early water peaks. The analysis of the individual spectra is performed by a computer code, providing an unbiased identification of features. Only well shaped peaks with amplitudes of at least 2.5 times the root mean square (σ) level of the noise amplitude are considered. Due to the tendency of the dipolar water molecule to cluster with any other atomic or molecular species it encounters (see chapter 6.1.2), the calibration and interpretation of water ice spectra is quite challenging. While pure water ice spectra can easily be calibrated and identified by the code, spectra with significant contributions from water cluster with other species (especially alkali metals) of the form X_n-$(H_2O)_m{}^+$ are often confusing and misleading. In extreme cases water ice impacts may produce spectra completely dominated by alkali metal and alkali metal-water cluster signatures (see e.g. Fig.6.4). Those spectra need a careful "manual" calibration.

The accurate derivation of particle speeds and masses is much more difficult for impacts onto the CAT than onto the IIT (see chapter 2.1). For this reason we do not state individual dynamical particle properties for the majority of the measurements presented in this thesis. The size and velocity regime of the particle ensemble considered here is derived from the QI-rise time analysis in Kempf et al. (2007). The IIT impacts studied there stem from the same particle ensemble. Particle sizes are predominantly distributed between 0.1 and 1.0 μm, while impact velocities range between 8 and 25 km s^{-1} (see Kempf et al. (2007) for details).

During ring plane crossings the telemetry bandwidth only allows the transmission of a subset of the registered events. The selection is performed by the instrument software with varying criteria. To what extent this affects the selection (and subsequent transmission) of certain spectral types is only partly understood and currently under investigation. A preliminary analysis of the transmission statistics indicate that there is no strong bias in the transmission of mass spectra. However, we note that the returned dataset might be prone to unknown bias effects.

Non-water particles in the Saturnian ring-plane

Another dataset consists of spectra belonging to the small but significant non-water subpopulation. The CAT impacts between December 2004 and March 2006 have been scanned manually for this spectrum type. The criteria for identifying members of this dataset are the non detection of hydronium ions at 19 amu and their cluster at 37 amu, but the presence of a significant iron signature between 55 and 57 amu (see chapter 6.1.7). 93 events have been identified, which were then individually calibrated by using the Na, K, Fe and Rh mass lines.

Some of the impacts caused such high ion yields that severe disturbing effects - typical for high energy impacts - occurred. Besides deformed or "split" peaks (formed by a "slow" and "fast" ion species (Hillier et al., 2007a)), substantial peak shifting is observed. To correct for these effects is beyond the scope of this work. Thus, only 57 spectra with QI-amplitudes below 10^{-6} ions, required uncomplicated mass calibration, are used for the compositional analysis. The spectra of the dataset exhibit an excellent peak definition and sometimes exceed the mass resolution inferred from laboratory experiments (2.1). Only well shaped peaks with amplitudes of at least 2.5 σ of the noise amplitude level are considered.

As previously mentioned, the inference of particle speeds by QI-signal rise times is severely affected by the strong electric fields used to generate TOF spectra. Because the non water type is identified by its spectra, no conclusions regarding impact velocities can be drawn from the corresponding IIT-impacts as was possible for particles of the main E ring population. Although speeds for individual impacts can not be inferred, the statistics of QI rise times of the non-water dataset however, shows a clear tendency: On average their rise times are only half of the rise times of the water rich impactors. This hints at

substantially higher impact speeds. An alternative estimate of impact speeds derived from the spectral signatures is given in chapter 6.1.7 and also higher impacts speeds for these particles than for the water rich species (above 25 km s^{-1}).

2.3 Target Contamination

The generation of ions from contamination on metal targets has already been examined in the course of the development of the PIA / PUMA dust detectors by Knabe (1983) at the Heidelberg dust accelerator facility. Since then, contamination has been studied in association with impact ionisation measurements in the laboratory (Posner, 1995; Stübig, 2002) as well as in space (Brownlee and Kissel, 1990). The evaluation of the spectra of the Cassini mission obtained at the Jupiter swingby in late 2000 (Postberg et al., 2006) and during approach of the spacecraft towards Saturn in early 2004 (Kempf et al., 2005b) has revealed that a more detailed investigation of contamination phenomena is necessary. In the following three subsections we try to estimate the contamination status of the instrument at the time of the spacecraft launch and how it might effect the spectra obtained in space. In section 2.3.4 we summarise the results of stream particle data from Jupiter and Saturn where - due to the tiny hypervelocity impactors - the spectra are dominated by target material and associated contamination. Finally we compare the findings and deduce a plausible contamination status of the CDA target in 2.3.5.

2.3.1 Initial State of the Rhodium Target Plate

The Rhodium target plate used for the CDA's Chemical Analyser Target (CAT) was manufactured by the W. C. Heraeus GmbH and delivered in early 1992. Rhodium, a metal of the platinum group, is considered to be one of the most inert metals. The chemical analysis (Tack, 1992) of the material which was carried out by Hereaus certified a rhodium purity above 99.5 %. As main impurities Iridium (0.15 %) and Silicon (0.12 %) were stated.

The manufacturing and conditioning of the CAT was done by the Deutsches Zentrum für Luft- und Raumfahrt (DLR) in Berlin-Adlershof. Microanalysis of the material carried out by the DLR found that there were major Manganese (Mn) surface impurities over the whole plate. Furthermore, X-ray diffraction photography and Scanning Electron Microscopy showed rolled skin textures and a large number of cracks in which Nickel (Ni), Iron (Fe), Silicon (Si), Calcium (Ca) and Aluminium (Al) impurities could be found (Görlich et al., 1999). This required a Heat treatment, subsequent polishing, and Argon plasma sputtering of the surface was necessary to produce the required structure and cleanliness of the surface. The sputtering of the CAT was carried out twice, each time removing the upper 50 nm of the entire surface. These elaborate processes finally provided a satisfying condition of the buckled Rhodium plate in 1997 few months before Cassini's launch. Except the intrinsic Silicon impurities concentrated in "islands", a TOF-SIMS[4] analysis of the surface at the DLR proved that all impurities had been reduced to a sufficiently low level (Lura, 1997; Görlich et al., 1999). After an outgassing incident during spacecraft assembly in the United States, the instrument was sent back to Germany, where it was subject to another cleaning procedure. The target was heated up to 200°C in an UHV (Ultra-high vacuum) chamber for several hours to restore its previous state of cleanliness.

[4]Time-Of-Flight–Secondary-Ion-Mass-Spectrometry

Despite precautions to prevent recontamination, it was inevitable that the instrument was exposed to a certain amount of contaminants before it reached interplanetary space. Though otherwise constantly purged by a flow of nitrogen the target was exposed to open air for less than an hour at a final function test in Heidelberg. The purging stopped a few hours before the rocket launch; the remaining Nitrogen atmosphere within the closed instrument however, provided a certain protection. Special emphasis has to be put on the fact that an absolute pure metal surface - even of a noble metal like Rhodium - becomes polluted when exposed to even a very thin atmosphere. Within a few seconds, some monolayers of surrounding atoms and molecules are adsorbed onto the metal's surface. Thus, the clean state produced by the final heating procedure of the CAT at the DLR facilities could not be maintained.

2.3.2 TOF-SIMS Analysis of the Rhodium Target Plate

In 2003, a part of the Rhodium piece used to manufacture the CAT (which had been stored for over 9 years in a sealed plastic bag) was analysed extensively by TOF-SIMS to examine the state of any surface contamination. The TOF-SIMS is somewhat similar to the impact ionisation method used for the CDA time-of-flight spectra. Here the "projectiles" are Gallium ions at energies of 25 keV which hit the metal surface and transfer their kinetic energy via a collision cascade to the upper target layer of approximately 10 nm depth (Stephan, 2001) (Fig. 2.3). A small number of the surface atoms and molecules are emitted as secondary ions in a positive or negative charged state. The energy transferred to create the ions is roughly similar to that of a particle impact. It is thus expected that the abundance of emitted positive surface ions (cations) is applicable to CDA measurements. For a comprehensive introduction of the use of TOF-SIMS in cosmo-chemistry see Stephan (2001).

An untreated strip of about 1 cm^2 Rhodium cut from the CAT workpiece ("Sample 3") was examined at six different spots - with an area of 500 $\times$ 500 μm - for cation emission and two different spots for negative ion (anion) emission. Each of the spots was scanned for ions over a mass range of 1 to $\approx$ 250 amu in two stages. After the first analysis of the untreated material, a second analysis was carried out at two different spots, after cleaning 100 $\times$ 100 μm of the surface directly before the analysis through sputtering with 3 keV Argon ions. This again was done for positive and negative ion emission. In addition two other Rhodium plates ("Sample 1 and 2") were analysed at one location, first in their original states, and then again after sputter-cleaning for both positive and negative ion emission. All Samples are from the same workpiece used for the CDA target now operating in space. In contrast to Sample 3, Sample 1 and 2 have not been subject to the Argon sputter-cleaning treatment at the DLR described in section 2.3.1.

The complete set of TOF-SIMS images is shown in appendix B.

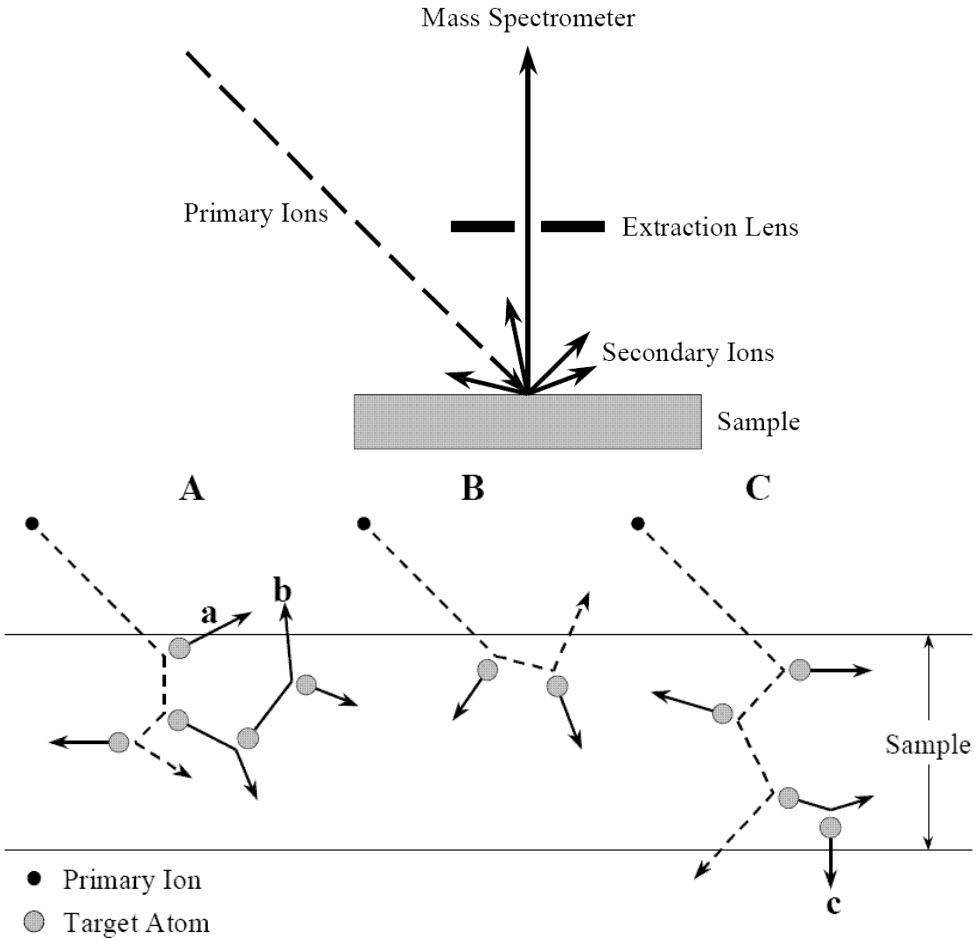

Figure 2.3: *The principle of secondary ion mass spectrometry: On the sample surface a primary ion beam generates secondary ions. The primary ions transfer energy in a collision cascade to the target atoms. Ion implantation (A), back-scattering (B) or forward scattering (C) may occur. Atoms from the target leave the sample after several collisions as secondary particles (a,b,c), a small proportion of which are ionised. The secondary ions are separated and detected within a mass spectrometer. From Stephan et al. (2001).*

Results

In Tables 2.1 and 2.2 the main results of the Sample 3 analysis are summarised. The measurements of the cleaned surface were carried out at a resolution of 256 $\times$ 256 pixel whereas the untreated surface was scanned at a resolution of 512 $\times$ 512 pixels. Thus, the intensities ("Yields") of the latter are *a priori* higher by a factor of 4. However, since the absolute values for ion emission depend on a number of factors (Stephan, 2001), a comparison of absolute values from different measurements - like the results for the cleaned and the uncleaned surface - has to be approached with care.

Cations: The untreated sample surfaces were all heavily contaminated. Of the elemental anions the alkali metals Caesium, Sodium, and Potassium are the dominant contaminant

Table 2.1: Summary of the TOF-SIMS surface analysis of Sample 3, cations. The "Y" row refers to the "Yield" as the total number of detected ions ($\times 10^4$) of the respective species. "P %" is the fraction of pixels, which show emission of the particular ion.

	Untreated Surface												
	Cs*	Na	K	Si	H	RhC	C_2H_x	Ca	RhH	Ni	C	RhOH	Al
Y	344	49	23	12	6.0	4.4	2.8	2.2	2.0	1.8	1.4	1.1	0.4
P %	81	45	33	32	18	14	5	6	5	6	8	14	4
	Cleaned Surface												
Y	0.3	1.4	1.4	0.1	0.3	3.0	0.1	0.6	0.3	n.d.	0.3	1.3	< 0.1
P %	4	20	15	1	6	18	< 1	4	4	0	4	10	< 1

Note: The values for the untreated sample surface are an average of six measurements. For the evaluation of the cleaned surface only one of the two measurements of Sample 3 could be used, since the sputtering procedure obviously didn't work properly for measurement DR0299 (see appendix B). Thus, for the average value of the cleaned surface the two measurements of Sample 1 and 2 are also taken into account.
* Caesium (Cs^+) is extremely abundant on Sample 3 only. In the analysis of Sample 1 and 2 Cs^+ emission only plays a subordinate role (see appendix B).

Table 2.2: Summary of the TOF-SIMS surface analysis of Sample 3, anions. The "Yield" row refers to the total number of detected ions of the respective species. "Pixel %" is the fraction of pixels, which show emission of the particular ion.

	Untreated Surface									
	F	C_xH_y	CN	H	C_2	Cl	O	C	48amu	Si
Yield ($\times 10^4$)	412	309	202	322	135	83	64	39	15	0.4
Pixel %	100	100	98	100	98	72	88	74	43	1
	Cleaned Surface									
Yield ($\times 10^4$)	116	2.4	15	0.4	1.6	1.7	1.0	< 0.1	0.3	n.d.
Pixel %	100	32	89	6	22	23	13	1	4	0

species, followed by Silicon, Hydrogen, Calcium, Nickel, Carbon and Aluminium at far lower abundancees[5]. Although TOF-SIMS is very sensitive to alkali metal ions, the abundance of Caesium on Sample 3 is unusual, and would be expected to be far below the Sodium and Potassium values. Since (Cs^+) emission from Sample 1 and 2 is much lower (see appendix B), Sample 3 probably was subject to an unusual Caesium contamination.
There are several molecular species present in small amounts. The $C_2H_x{}^+$ species (with x being 3,4 or 5) are likely to be fragment ions of hydrocarbons. RhH^+, RhC^+ and $RhOH^+$ are ions composed of the target material Rhodium and a contaminant species.
After the sputtering procedure the abundance of elemental contaminant ions decreased

[5]The surface analysis also shows an abundant emission of Gallium (Ga^+). Those ions are not considered here. The primary ion beam being Gallium ions, these of course are re-emitted to a certain extent.

substantially. Only ions of alkali metals, Calcium, Hydrogen and Carbon are still noticeable (Figs. 2.4, 2.5). It is quite interesting that the Rhodium cluster-ions RhC^+ and $RhOH^+$ are still detected in similar amounts than before the cleaning, indicating subsurface contamination.
There are obvious differences in the homogeneity of the distribution of the contaminants on the surface. While H^+, C^+, and $C_2H_x{}^+$ are almost equally distributed, the other listed contaminants have a more or less patchy appearance (Figs. 2.5 and 2.6). Na^+ and K^+ show the most irregular distribution but both alkali metals have clearly correlated locations (Fig. 2.4). Si^+ and Ni^+ also possess correlated locations. After sputtering, most of the cations show a much more homogenous emission (and hence surface distribution) except for Al^+, Ca^+, CaF^+ and Si^+ (Fig. 2.5), which are concentrated on a few tiny islands on the Rhodium surface[6].

Anions: The emission of secondary anions is even more abundant than cation emission. Of the elemental anions Fluorine, Hydrogen (Fig. 2.6), Chlorine, Carbon and Oxygen are dominant, very few Silicon anions are emitted. There is a rich coverage of $C_xH_y{}^-$ species (x = $1, 2$; y = $1, 2, 3$), which are fragment ions of hydrocarbons with C_2H^- and $C_2H_3{}^-$ as the most abundant species. CN^- is also emitted in great abundance. Since Nitrogen is not likely to form either anions nor cations, CN^- is a good tracer for Nitrogen adsorption on the sample surface. An unspecified anion with a mass of 48.01 amu (probably $C_4{}^-$) plays a minor role. It is unclear to what extent the Carbon ions are due to Hydrocarbon breakup or stem from a Carbon contamination layer.
After sputtering, the abundance of most of the contaminants is significantly reduced. However, the cleaning process is not as effective as for the positive species. Fluorine contamination, in particular, seems to be barely affected and CN^- indicates Nitrogen still to be present in significant amounts.
Although there are slight variations, the distribution of anions on the surface is in general more homogenous than the cation distribution. Chlorine and Fluorine have the patchiest appearance (Fig. 2.6). This hints at a refractory material origin, most likely alkali metal salts. As in the case of cations, the anions are more evenly distributed after the sputtering process.

Relevance of the TOF-SIMS analysis for CDA Spectra

After being exposed to air for more than 9 years, the examined Rhodium samples can be expected to be much more contaminated than the CDA target at Cassini's launch, whereas the argon sputtering provided a surface which probably was "too clean". After the thorough cleaning procedure, the CDA target was exposed to possible contaminants when it was installed in the vacuum chamber of the Heidelberg dust accelerator for a final test. Thus, the contamination status is likely to be in between the two states analysed above. However, we can conclude that contaminants that are not significant in the analysis of the untreated material do not play a role in the surface contamination of the CDA Rhodium

[6]For Si this behavior is only noticable on Sample 1 and 2, but is in perfect agreement with the findings of the DLR (Lura, 1997), see section 2.3.1.

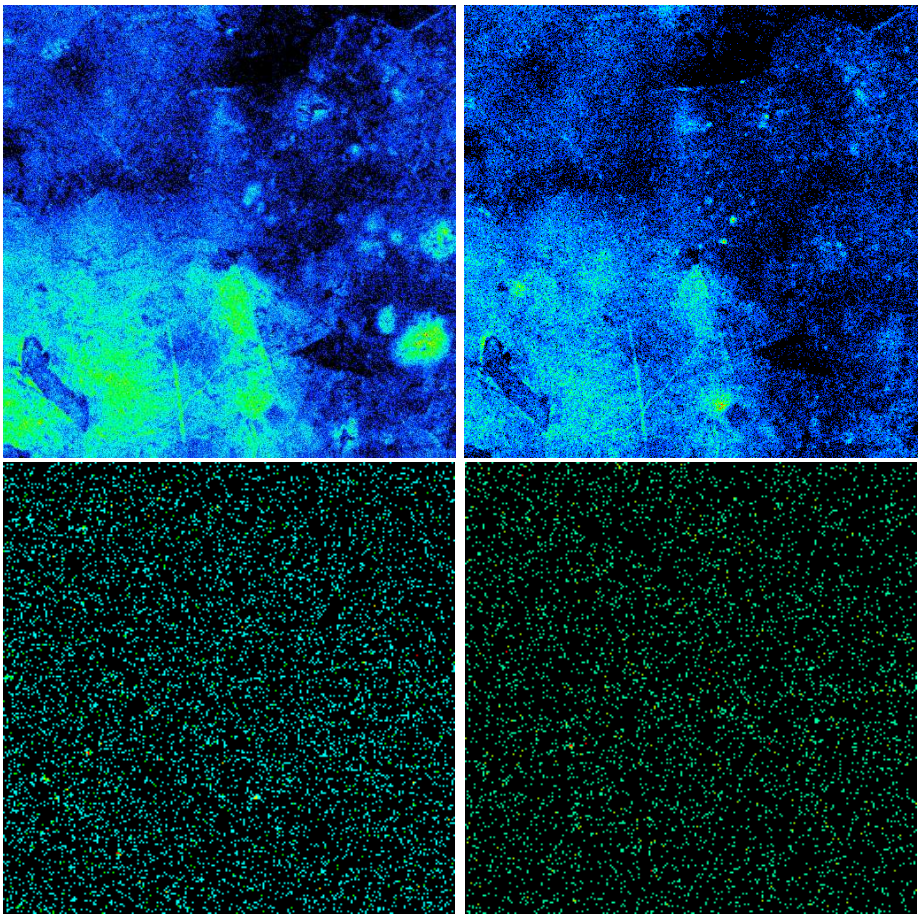

Figure 2.4: *Sample 3 TOF-SIMS analysis of Na^+ (left) and K^+ (right), before (above) and after (below) Argon sputtering. The untreated samples exhibits massive contamination which is highly concentrated in some places (green), whereas it is undetectable at other locations (black). On the sputtered sample the abundance is clearly reduced. However, a significant contamination remains. This is even more pronounced on sputtered samples 1 and 2 (see DR294 and DR2295 in the appendix).*

target.
Potential volatile contaminants present in the air (Nitrogen, Oxygen) and probably the vacuum chamber (Hydrogen and Hydrocarbons) are more likely to be adsorbed in the short period of exposure than more refractory material like metals or silicates. The analysis has shown that in contrast to refractory materials the surface adsorption of volatile materials like Hydrogen and Hydrocarbons does not depend that much on the structure of the metal surface.
Since the CDA is only sensitive to positive ions, the investigation of cation contaminants is generally of greater importance. However, at high impact speeds species with high ionisation energies, which preferably show up as negative ions in TOF-SIMS Spectra, can also form positive ions and thus be detected by the CDA.

From the results of the TOF-SIMS Analysis the abundant adsorption of Hydrogen, Oxy-

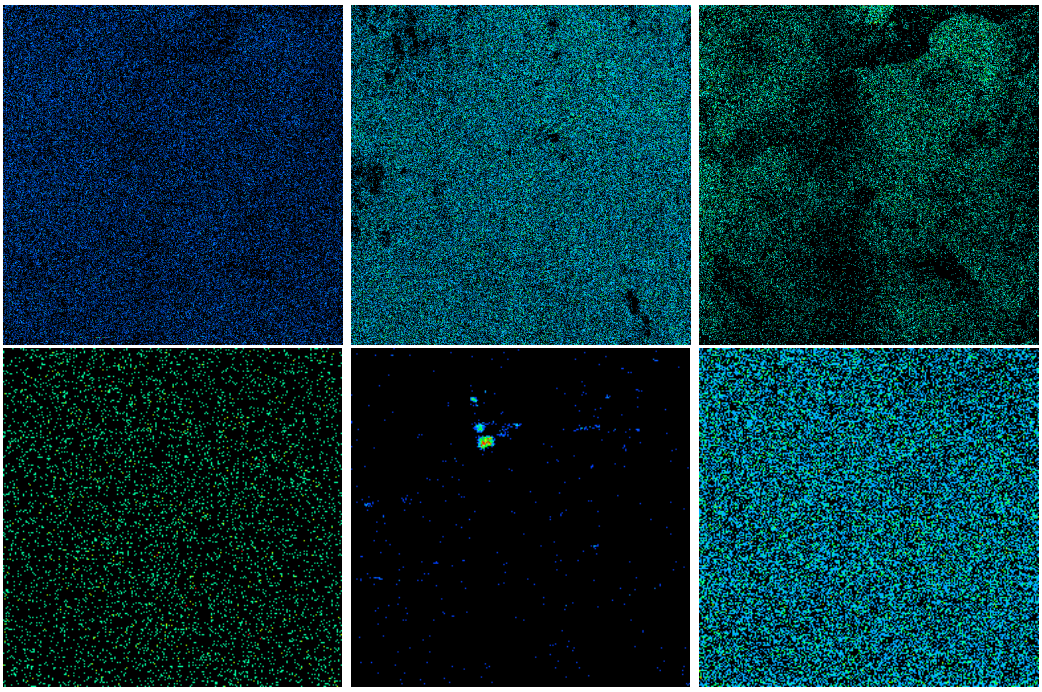

Figure 2.5: *Sample 3 TOF-SIMS analysis of H^+ (left) and Si^+ (middle) and RhC^+ (right), before (above) and after (below) Argon sputtering. In contrast to the metals, H^+ shows no patchy distribution. Though the total ion yield of Si^+ has significantly decreased on the sputtered sample (Table 2.1), tiny islands of high Si abundance appear. In contrast to all other cations shown, the RhC^+ abundance slightly increases after sputtering and exhibits a homogeneous distribution. $RhOH^+$ shows similar behaviour (see DR299 in the appendix). The example for Si^+ is taken from the Sample 2 analysis.*

gen, and Nitrogen onto the target surface is observed. Thus H^+, O^+, and possibly even N^+ signatures can be expected in spectra from high velocity impacts[7]. Volatile Hydrocarbons and Carbon might also be adsorbed at the target surface[8]. The extremely abundant Cs^+ in the Sample 3 analysis probably is of only minor relevance. Since it is not confirmed on the other investigated Rhodium surfaces, Sample 3 was probably subject to an unusual contamination event and is not indicative for the CAT. No precise conclusion can be drawn for Sodium and Potassium from the TOF-SIMS results alone. It is possible that a recontamination of the target during its short exposure to air occurred to an unknown extent. However, an abundant Sodium or Potassium contamination (as exhibited by the untreated samples) of the CAT is unlikely, but due to their low ionisation energies even traces might be relevant in CDA spectra obtained in space. Thus the values of the untreated surface in Table 2.1 are upper limits, whereas the values for the cleaned surfaces can be considered as rough indicators for their frequency of appearance in flight spectra. Of the other metals only Calcium and, less likely, Nickel might play a minor role as con-

[7]For H^+, O^+ this phenomenon is well known from impact ionisation experiments in the laboratory (see 2.3.3).

[8]However, the regular heating of the Rhodium plate in space (see 2.3.4) should induce a desorption of the majority of volatile species.

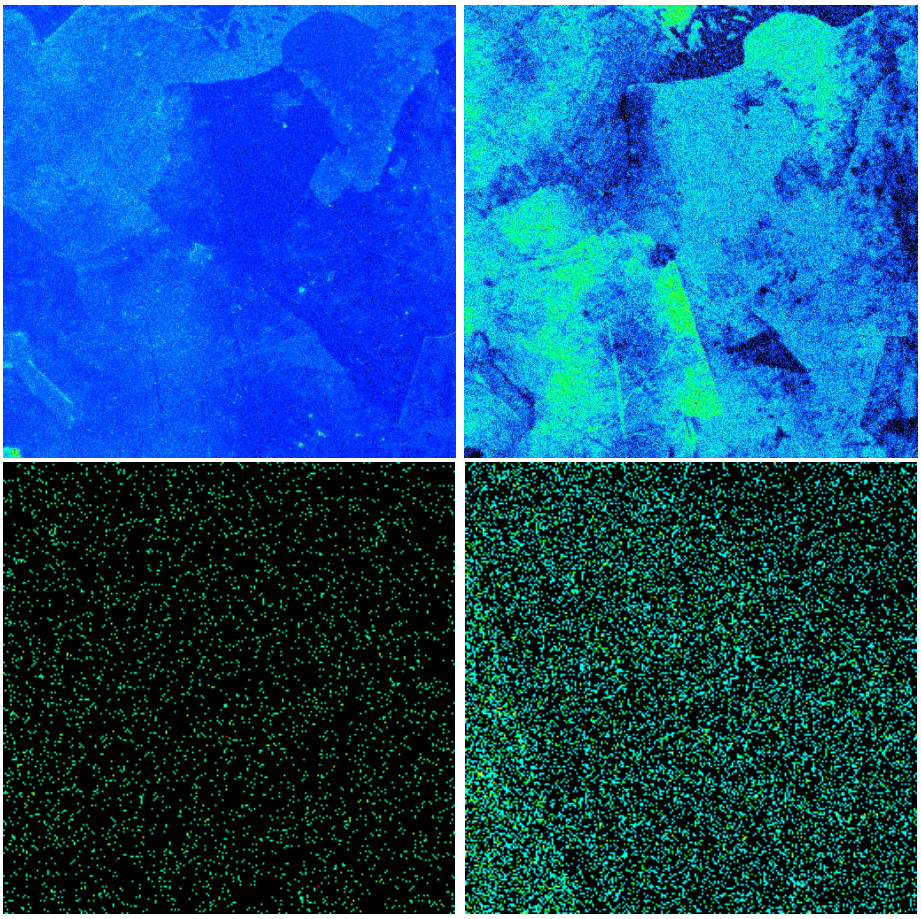

Figure 2.6: *Sample 3 TOF-SIMS analysis of H^- (left) and Cl^- (right), before (above) and after (below) Argon sputtering. The ion yield of the hydrogen contamination is much more abundant for cations than for anions. Still the distribution is almost homogeneous. Most of the Hydrogen is removed by the Argon sputtering. Cl^- shows a patchy distribution similar to Na^+ indicating NaCl to be the relevant surface contaminant. The sputter cleaning is obviously more effective for volatile substances (like Hydrogen) than for solids (like NaCl).*

taminant signatures. Though in the analysis of the untreated sample silicon is a surface contaminant of intermediate abundance, the rapid recontamination of the CDA target in the short period of air exposure after the sputter-cleaning is not expected. Thus, the status of the cleaned sample in the TOF-SIMS analysis in this regard gives a good estimate for CDA spectra and makes silicon contamination features above the level known from the intrinsic impurities of the Rhodium plate (see 2.3.1) unlikely. The resistance of RhC^+ and $RhOH^+$, and to a lesser extent RhH^+, to the sputter cleaning process implies that Carbon, Oxygen and Hydrogen have formed complexes or occludates within the target material which reach at least some nm below the surface (the thickness of the layer removed by the Argon sputter process). Because of their low abundance those cluster ions would be expected to show up only as small signatures in CDA spectra.

For a more precise estimation of the contamination state at the moment of Cassini's launch

into space it would be highly desirable to repeat a similar analysis with a sputtered sample which, following sputtering, has been exposed to the ambient environment for a few hours.

2.3.3 Contamination Signatures in CDA Laboratory Spectra

Several experiments and calibration campaigns with the CDA flight model and the flight spare model have been carried out in the Heidelberg dust accelerator facility. The van-der-Graaf accelerator is a high speed (1-70 km s^{-1}) dust source for particles with sizes ranging from about 0.1 μm to 100μm. The accelerator facility and the test setup is described in greater detail e.g. by Stübig (2002). Major calibration campaigns with the CDA Chemical Analyser subsystem were accomplished between 1994 and 2002 by Posner (1995), Srama (2000), Stübig (2002), Goldsworthy (2003), and Kuhn (2002). Here we summarise the results concerning the appearance of contamination signatures in the spectra obtained during those laboratory experiments, and also give some new interpretations.
Due to the special treatment of the CDA target before launch (see 2.3.1) the contamination status of the instruments used in the laboratory should be expected to be much worse. Thus, the contamination signatures observed in laboratory spectra can be treated as an upper limit. However, because of their rapid adsorption the contamination of the surface with gas molecules as a consequence of air exposure should be comparable in both cases.

At low impact speeds (1 - 10 km s^{-1}), the main contamination mass lines observed in all experiments were those of the alkali metals Lithium (Li^+, 7 amu), Sodium (Na^+, 23 amu) and Potassium (K^+, 39 amu), with Sodium being the most abundant species (Stübig, 2002; Kuhn, 2002; Goldsworthy et al., 2003). In fact, after impacts with $v_i \gtrsim 5$ km s^{-1} most spectra are dominated by Sodium and Potassium signatures. Those elements, emitted from a thin inhomogeneous surface contamination layer (see 2.3.2), have the lowest ionisation energies (see Table A.5) and often produce the only significant spectral features at impact speeds below 5 km s^{-1}. Besides that the occasional smaller amounts of probable molecular or cluster species at varying masses (e.g. at 72-73 amu), occur predominantly at low impact speeds. With increasing impact energies the proportion of alkali metal signatures decreases. This is due to three reasons:
a) Species with higher ionisation energies are contributing.
b) Deeper layers of target and particle are affected.
c) In accelerator experiments, fast particles are smaller than slow particles. The affected surface area becomes smaller.

At higher impact speeds peaks due to the target material (Rh^+, 103 amu) and of the contaminants Hydrogen (H_x^+, 1,2,3 amu), Carbon (H_x^+, 12 amu), and Oxygen (O^+, 16 amu) occur. A pronounced signature at 27-28 amu is also regularly recorded. There is a strong velocity dependence for the occurrence and abundance for most of these mass lines (see Table 2.3). Rh^+ appears at relatively low impact speeds and is roughly dependant on the density of the impactor. H^+ and C^+ appear at about the same velocities varying from

Table 2.3: Velocity thresholds for specific cation species in CDA laboratory experiments with differing projectile materials. The velocity refers to the speed above which the signature is generally present in spectra. Note, that small peaks are occasionally present at lower impact speeds. Above the stated value the ion abundance of the species was increasing with ever increasing particle velocity. The numbers are inferred from Stübig (2002), Kuhn (2002), and Goldsworthy et al. (2003).

Projectile	Rh^+ $km\,s^{-1}$	H^+ $km\,s^{-1}$	C^+ $km\,s^{-1}$	O^+ $km\,s^{-1}$
Iron	8	13	13	30
Aluminum	12	12	15	22
Carbon	8	10	9	>25*
Polystyrene	11	14	14	>25*
Aluminosilicate	8	13	13	25

*Those values have to be treated with reservation. For carbon and polystyrene projectiles very few spectra of impacts above 25km s^{-1} could be recorded. Furthermore the O^+ signature was of weak significance in those spectra.

about 10 to 15 $km\,s^{-1}$. The occurrence of the molecular Hydrogen lines H_2^+ and H_3^+ is occasional and - again - depends on impact speed. The probability that their signature is detectable as a companion of the H^+ peak is high at low impact speeds, whereas above $\approx 20\,km\,s^{-1}$ H_3^+ and above $\approx 35\,km\,s^{-1}$ H_2^+ disappear from CDA spectra (Goldsworthy et al., 2003). Oxygen only appears at the highest impact speeds achievable with the Heidelberg dust accelerator.

The velocity thresholds of different species depend on their ionisation energies. Although the total kinetic energy of the particle in the accelerator is slightly decreasing for faster (but smaller) particles, the maximum energy density at the impact location seems to increase. This allows the ionisation of species with ever higher ionisation potentials.

A mass line is occasionally observed at about 115 amu. Although not always attributed as such by the authors, this very likely is the signature of RhC^+. Although only observed occasionally and at low abundances, it was observed with all projectile materials (Stübig, 2002; Goldsworthy et al., 2003). The TOF-SIMS analysis (2.3.2) indicates carbon seems to be incorporated below the surface of the target. Thus, RhC^+ clusters are likely to be intrinsic impurity ions from the bulk material and not solely cluster ions formed from a carbonaceous surface contamination and the metal target in the plasma cloud.

The contaminant signature at 27-28 amu presents a special case. Although observed in CDA as well as CIDA and PIA/PUMA calibration experiments, the origin of this signature is unclear. In the early PIA/PUMA and CIDA experiments the mass line was thought to be $C_2H_3^+$ as a fragment ion of adsorbed volatile hydrocarbons, originated from oils used as a lubricant of the vacuum pumps. During the first CDA experiments in 1994, Posner found clear indications that the mass line was not due to target origin but to aluminium

contamination of the iron projectiles used for all previous laboratory experiments (Posner, 1995). Later in the course of the main CDA test campaign the position of the signature was found to be in better agreement with 28 amu and attributed as CO^+ contamination or Fe^{2+} projectile species (Stübig, 2002). Although using a similar setup Goldsworthy (2003) again reported 27 amu as the correct mass of the feature[9]. Whereas Stübig used the H^+ and Rh^+ lines for mass calibration of the TOF spectra, Goldsworthy used the omnipresent contamination lines of Na^+ and K^+ for calibration which in retrospect seems to be more reliable.
High resolution spectra from reflectron instruments with iron particles (Knabe, 1983; Srama, personal communication, 2007) clearly show that the position of the feature is at 27 amu. Although those experiments were carried out with the same Fe projectiles as the CDA experiments, the target material was different (Silver). However, this is considered to be of minor relevance for the nature of the contamination. Thus, candidates for the 27 amu feature are Al^+ and $C_2H_3^+$. While from the TOF-SIMS analysis of the Rhodium target (2.3.2) $C_2H_3^+$ is known to be a plausible candidate for surface contamination, Al^+ can only be due to the projectile (as suspected by Posner, 1995). There are a number of arguments that speak for and against either of the two candidates.

The reasons against $C_2H_3^+$ being of major importance, which thus favour Al^+ are as follows:

- From TOF-SIMS spectra the hydrocarbon contamination of the target surface is known to be basically homogenously distributed over the target surface (2.3.2). The occasional but significant appearance of the 27 amu feature is not in agreement with this observation.

- A closer examination of the CDA calibration data shows an occasional peak at 130 amu, the occurrence of which correlates with the abundance of the 27 amu peak. This is very likely a cluster of Rhodium with the 27 amu species. The likelihood for such a feature is much higher if the 27 amu species were of particle origin and not a surface contaminant of the target.

- The feature predominantly appears in experiments with iron projectiles. If the dust material is carbon the feature is very small if visible at all. Even with organic projectiles - where $C_2H_3^+$ is expected to be an abundant breakup ion of the particle material - the proportion of the 27 amu signature is lower than with iron projectiles (Stübig, 2002; Goldsworthy et al., 2003).

- The ratio of 27 amu ions to C^+ ions increases with the increasing impact speed of iron projectiles. Since at higher impact speeds the fragmentation of molecular species should occur this is not in agreement with $C_2H_3^+$ (Stübig, 2002).

- There are few indications for other fragment ions of hydrocarbons $C_{2+x}H_y^+$ known from TOF-SIMS spectra of hydrocarbon surface contamination as observed by e.g.

[9]This illustrates the problem of the mass calibration of an impact ionisation spectrometer without a reflectron (see Hillier et al. (2006) for details).

Neugebauer (2001). Furthermore there is hardly any evidence for $C_2H_4^+$ and $C_2H_5^+$ in our high resolution impact ionisation spectra with iron particles. Those ions always have a conjoint appearance with $C_2H_3^+$ when organic projectiles are used (see Fig 6.11).

- The asymmetric peak shape of the 27 amu feature in CDA spectra is in better agreement with a "bulk material" and not with a thin surface contaminant layer (Posner, 1995).

There are also findings which favour $C_2H_3^+$ over Al^+:

- In high resolution iron impact ionisation spectra of negative ions, a mass line at 25 amu clearly indicates C_2H^-. This confirms the suspected hydrocarbon contamination of the surface indicated by the TOF-SIMS analysis to be present (2.3.2). To which extent this can be treated as an indicator for an abundant positive ion emission is uncertain.

- A chemical analysis of the iron dust used for the accelerator shows that it contains only traces of aluminium ($< 0.5\%$). Consequently possible aluminium contamination must have occurred within the accelerator.

- Shots with aluminium projectiles yield a clear aluminium signature at impact speeds above $3\,\mathrm{km\,s^{-1}}$ (Stübig, 2002). In contrast when iron dust is used the 27 amu signature only becomes prominent above $10\,\mathrm{km\,s^{-1}}$.

The points above show that neither of the candidates is in complete agreement with the observations. The most likely solution is that both species play a role with varying contributions. $C_2H_3^+$ is likely to be a minor contaminant species which can e.g. be observed as a faint feature in the spectra after carbon particle impact. Since the CDA Rhodium plate is known to bear some silicon impurities (see 2.3.1) a respective ion feature at 28 amu could occasionally also contribute. The very distinct 27 amu signatures after high velocity iron impacts are only plausible if Aluminum is considered as a particle component as proposed by Posner (1995). However, since the peak only becomes prominent after impacts of fast particles, the aluminium must be concentrated predominantly in the small dust fraction, since those are accelerated at higher speeds. Since the original iron dust contains only minor aluminium impurities, a plausible scenario would be an *ex post* contamination inside the accelerator e.g. by abrasion of Al dust from the walls of the dust source container. A close investigation of this phenomenon is scheduled for 2008.

2.3.4 CDA Contamination Operating in Space

Possible Sources for a Contamination in Space

Even though it operates in "empty space", there are several contamination sources for an instrument situated on a spacecraft. The most prominent are rocket engine exhaust, outgassing of spacecraft components, and the interplanetary medium (with the solar wind as

the main contributor). The CDA target was subject to all those effects, especially after the instrument cover was removed in 1999. To reduce the impact of these threads the CDA is equipped with a heating device, which raises the temperature of the Rhodium target up to 370 K within 2 hours. In the standard procedure this temperature is maintained for another 8 hours. Those decontamination cycles were carried out regularly, executed in intervals of a couple of months, starting in September 2000 (DOY[10] 247) (see appendix A.1 for a list of the CDA decontaminations). Tests carried out by the DLR in Berlin-Adlershof demonstrated that within that period all volatile substances like atmospheric gases or Hydrocarbons were totally desorbed from the target surface. Nevertheless contamination in space is a critical parameter, as now discussed:

- Contamination by combustion products of the rocket engine:
  According to Guernsey (personal communication, 2006) the major combustion products are: N_2: 42%, H_2O: 29%, CO: 17%, CO_2: 9%, H_2+H: 2%. Considering the normal target temperature of about 210 K, H_2O and CO_2 are of particular relevance since those substances can condense on the CA target. However, there is no evidence for contamination from this source. First, there is no significant increase in the share of water signatures in stream particle spectra after the 98 min main engine burn during orbit insertion on 1 July 2004. Second, 8 hours heat-ups of the target on 21 March 2004 and 10 October 2004 (see appendix A.1) to remove possible contamination did not alter the frequency of those mass lines in stream particle spectra either.

- Interplanetary Medium:
  With a density of 5 ions per cm^3 at 1 AU solar distance the solar wind represents the main constituent of interplanetary space. It consists basically of ≈ 1 keV ions of H^+ ($\approx 95\%$) and He^{2+} ($\approx 4\%$). They are abundant enough to affect CDA measurements if accumulated on the Rhodium target over a long period. Cassini was subject to a flux of between $10^8\,cm^{-2}\,s^{-1}$ at Venus orbit decreasing to about $10^6\,cm^{-2}\,s^{-1}$ at Saturn. However, most of the time the pointing of the CDA was not favourable for exposure of the inner instrument towards the solar wind flux. The neutral interplanetary gas environment has a particle flux of up to a tenth of the ionic solar wind and consists primarily of Hydrogen atoms (Galli et al., 2006).

- Outgassing:
  Outgassing of volatile substances from spacecraft material is a well known but often poorly understood phenomenon. Due to the extremely low ambient pressure ($< 10^{-12}$ mbar), and the aggressive radiation environment in interplanetary space, all forms of non-metal components (especially lubricants and different kinds of synthetic material) are in principal a threat for instruments which are sensitive to pollution. The identification of outgassing products as a brownish layer on certain parts of the Genesis spacecraft (Burnett et al., 2005) demonstrated that the phenomenon is almost inevitable - even on spacecraft where the prevention of outgassing was of the highest priority. The layer occurred only on parts exposed to the sun, was about

[10] Day of year

5 nm thick and consisted basically of photopolymerised hydrocarbons, siloxane and a Fluorine bearing compound (Burnett et al., 2005; Calaway et al., 2007).

Contamination Features in CDA Spectra at Jupiter and Saturn

Most of the contamination features known from the CDA calibration experiments show up in space operation as well: Alkali metals, Hydrogen, Carbon, Oxygen and Silicon. However, in space the projectiles composition is unknown and thus it is unclear to what extent the features typically associated with contamination are due to particle ions.

It is possible to investigate this using the spectra due to the high velocity impacts of the tiny Jovian and Saturnian Stream particles ($v_i \gtrsim 100\,\mathrm{km\,s^{-1}}$, $r \lesssim 20\,\mathrm{nm}$). Under these conditions the proportion of generated ions, from the particle, is expected to be very small and the spectra should be dominated by target and thus contaminant ions. Furthermore, the impacts provide energy densities which should be high enough to form positive ions of almost every species present, thus making them "visible" for the CDA detector (see chapter 4 and 5). Note that particle sizes are far below, and the impact energies and velocities far above, the parameters accessible during calibration experiments. Thus, unexpected effects may occur.

Besides the target material Rhodium, Hydrogen and Carbon are the most abundant ion species observed in spectra of both stream particle types. In most cases those three signatures represent more than 95% of all detected ions. The amount of H^+ and C^+ in stream spectra far exceeds the number of ions which can be of particle origin. This observation proves that at least a bigger fraction of Hydrogen and Carbon ions result from contamination. The clear anti-correlation of C^+ and the target ions Rh^+ (Fig 2.7) and decreasing ion proportion with increasing impact energy (Fig 2.8) is in excellent agreement with C^+ coming from a layer on top of the Rhodium plate. The fact that the weakest impact of Saturnian stream particles only created a C^+ but no Rh^+ signal is also difficult to explain without the assumption of an abundant carbonaceous surface contamination.

In both Jovian and Saturnian stream particle spectra features of Sodium and Potassium are observed. It can be demonstrated that in the Jovian case those species actually are particle compounds (section 4.1). Thus, the Saturnian counterpart delivered better data for estimating the alkali metal contamination of the target. Here, a - mostly faint - Sodium signature could be identified in 45 % of spectra, and a Potassium signature in 15 % of spectra. Since it is unknown to what extent these features are due to particle compounds[11] this can be considered an upper limit for the contaminated target area.

Oxygen ions were observed in spectra of Jovian as well as Saturnian stream particles. Although the signatures might be partly due to particle ions the relatively high proportion even in faint spectra (see Fig. 2.8) hint at a dominant contribution from target contaminants.

[11] Although even small amounts of alkali metals are easy to detect by some of Cassini's instruments, no indication for them to be apparent in the Saturnian system has been reported so far.

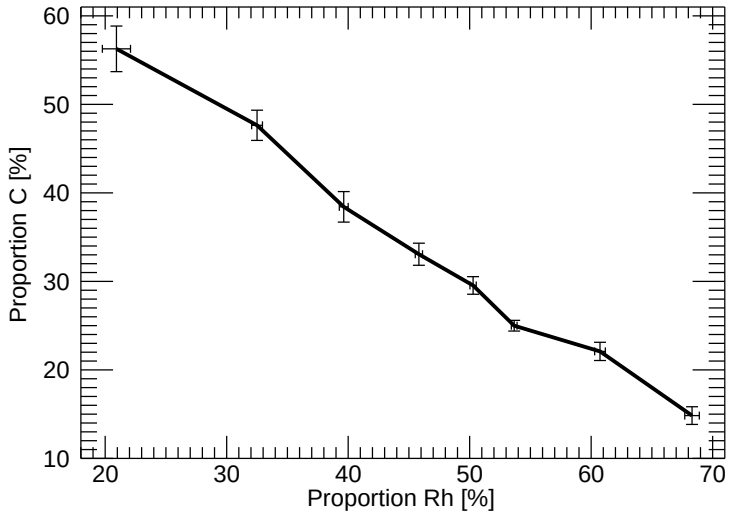

Figure 2.7: *Anti-correlation of C^+ and Rh^+ ion abundance in spectra of Jovian stream particles. The percentage given represents the proportion of the peak integral with respect to the total spectrum area. The standard error of the samples of each data point are given as error bars.*

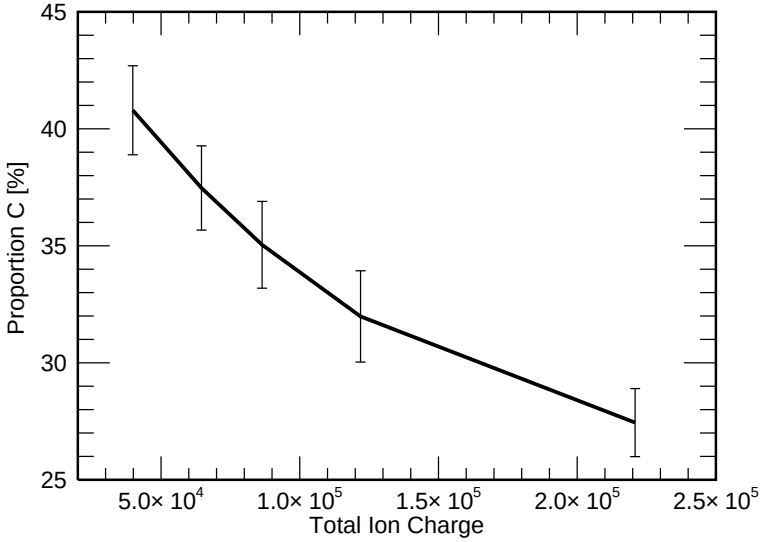

Figure 2.8: *The proportion of Carbon ions decreases with increasing total ion yield (a good indicator for the impact energy). This trend is characteristic for ions stemming from a surface contaminant.*

The feature observed at 28 amu which in both spectrum types is attributed to Silicon, is in principle also in agreement with fragment ions ($C_2H_3^+$, $C_2H_4^+$, $C_2H_5^+$) from hydrocarbon surface contamination. However, this is unlikely for several reasons as described in the following section. It is inevitable that the intrinsic Silicon impurity islands (see 2.3.1) of the rhodium target occasionally cause a signature in CDA spectra. Since those islands are rare (2.1) they cannot cause the feature observed in about two thirds of the stream particle spectra.

The faint signatures at 19 amu occasionally observed in both Jovian and Saturnian stream particle spectra - attributed as H_3O^+ in the original analysis (Kempf et al., 2005b; Postberg et al., 2006) - could also be due to F^+ contamination.
Especially in the case of Saturnian dust stream impacts there is evidence for occasional weak signatures in agreement with N^+. However, it is unclear to which extent those features are of particle origin.

2.3.5 Conclusion

In the following a conclusive summary for all potential contaminants of the CAT is given. All substances not mentioned in this section are considered irrelevant for CDA contamination issues. The most prominent of these absent species are: B, Mg, P, S, Ti, Cr, Mn, Fe, Cu, Zn, Pb and all molecular species except Hydrocarbons and the Rhodium cluster ions mentioned below.

Alkali metals

After sputtering of the entire target, removing two times a layer of 50 nm deep, only traces of these metals remained at best. This was proven by TOF-SIMS analysis carried out by the DLR and the University of Münster. Only a minor recontamination of the target before or after Cassini's launch is plausible. The proportion of the Na^+ and K^+ contaminated area of 20% and 15% respectively, observed in on the cleaned samples in section 2.3.2, can be taken as indicative values. The values on the untreated TOF-SIMS samples (45% and 33%) are upper limits. The spectra of Saturnian stream particle impacts confirmed the overall alkali metal contamination to be low. Upper limits of about 45% (Sodium) and 15% (Potassium) of the target area contaminated with a detectable amount of the respective alkali metal[12] could be derived. Since trace amounts of alkali metals in Saturnian dust streams cannot be ruled out, these values could be lower. However, since CDA is extremely sensitive to alkali metals, even traces leave a significant signal in the spectra, especially at low impact velocities. Impacts of larger particles do effect a larger target surface area than stream particles which are mostly smaller than 10 nm. Thus, with large projectiles a greater proportion of impacts than observed in the case of stream particles may ionise enough alkali metals to reach the detection limit of about 200 ions.

Although Lithium occasionally plays a role in laboratory spectra, there is no indication for contamination of the CDA target. Caesium was found to be abundant in the TOF-SIMS analysis of one of the samples. However, neither the analysis performed by the DLR nor stream particle spectra show any hint of Cs^+.

[12] with occasional spots of high concentrations located probably at surface micro-structures.

Other metals

Other metals than alkali metals are not to be expected to play a significant role in CDA spectra. Rare and weak signals of Calcium, aluminium, and Nickel can not be ruled out. The accelerator grid mounted 3 mm in front of the target (see 2.1) is composed of a Copper-Beryllium alloy. Since the grid is subject to bombardment by impactors small amounts of these metals might be deposited on an initially small proportion of the target area increasing with the age of the instrument.

Silicon

The surface contamination of silicon bearing compounds was removed by the sputter-cleaning procedure. A recontamination during the short period of air exposure is very unlikely. The intrinsic silicon impurity of 0.12 %, implemented as islands in the rhodium bulk material, certainly may occasionally contribute to the ion yield observed in CDA spectra. However, the TOF-SIMS analysis implies that the occurrence of such an event is below 5%.

Nitrogen, Oxygen and Carbon dioxide

Since the CDA interior was purged with Nitrogen after the cleaning process of the Rhodium target, and subsequently exposed to Earth's atmosphere for a short period, these gases were adsorbed at the surface. Although the heating of the target should have induced a desorption of these substances, it has to be noted that the first of the decontamination cycles was carried out almost a year after the spacecraft launch.
The emission of $RhOH^+$ from deeper layers in the TOF-SIMS analysis demonstrated that Oxygen could be incorporated subsurface within a Rhodium plate which has been exposed to air for about 10 years. The frequent and abundant appearance of Oxygen signatures in stream particle spectra hints that this occurred to the CDA target as well, probably before and after the sputter cleaning procedure. However, in contrast to H^+ and C^+, O^+ does not appear in every one of those hypervelocity impacts and is far less abundant (see Table 4.1 and Fig. 4.2). To what extent this is due to the slightly higher ionisation energy or a different origin is unclear. In any case, a detectable amount of O^+ should only be expected at high impact velocities.
Nitrogen was definitely adsorbed onto the target surface before launch. In contrast to Hydrogen, Carbon, and Oxygen the TOF-SIMS analysis does not hint at a subsurface absorption by the sample. The occasional and weak signatures in agreement with N^+ after stream particle impacts demonstrate that it has no apparent relevance in CDA spectra, even at impacts in principal providing sufficient energy densities to form Nitrogen cations.
CO_2^+ has not been observed as a significant contaminant at any stage, neither in the TOF-SIMS analysis nor in CDA laboratory or space flight operation.

Halogens

Chlorine and Fluorine have been identified as surface contaminants in the TOF-SIMS analysis of the untreated Rhodium sample. The latter was still abundant after the sputter cleaning procedure. Since both species are unlikely to appear as cations (Fluorine has the highest ionisation energies of all non noble gases) they are unlikely to play a significant role in CDA mass spectra and have never been observed in laboratory experiments. However, the extreme energy density of stream particle impacts has never been simulated on Earth and Cl^+ was indeed identified in Jovian dust stream spectra. In this case the ions were attributed as particle compound and since there is no evidence for Cl^+ in the Saturnian counterpart this is plausible. Based on the TOF-SIMS analysis, Fluorine can be expected to be far more abundant and in contrast to Chlorine located even below the Rhodium target surface. The occasional identification of faint 19 amu signatures in Jovian and Saturnian stream particle spectra can be interpreted as F^+. The homogenous distribution revealed in TOF-SIMS however, is not reflected by the uncommon appearance of those features.

Hydrocarbons

Hydrocarbons have been entirely removed from the target during the cleaning process in 1997 and a recontamination through the short exposure to air is not likely. However, for a final function test the instrument was mounted inside the vacuum chamber of the dust accelerator in Heidelberg. Thus, the instrument was inside a thin atmosphere probably containing residuals oil from the vacuum pumps. During the calibration campaigns when the instrument was exposed to this atmosphere for much longer periods, signatures of $C_2H_3^+$ (27 amu), though mostly weak, were observed. In the case of the CDA operating in space the regular heating of the target should produce a complete desorption of hydrocarbons. However, in both Jovian and Saturnian stream particle spectra distinct features of a species with masses of about 28 amu were detected. There the 28 amu signature was attributed as Si^+ (28 amu). The signature is however, in principal also in agreement with fragment ions of a hydrocarbons ($C_2H_3^+$, $C_2H_4^+$, $C_2H_5^+$). Since the energy density at the impact location of stream particle impacts is too high for the survival of any chemical bonds, these molecular species may stem from a surface location further away from the impact crater where the energy density has dropped sufficiently (Neugebauer, 2001). Moreover, the very rich presence of H^+ and C^+ would be in excellent agreement with residuals of hydrocarbons after a high energy impact. Nevertheless, abundant hydrocarbon signatures are considered implausible for following reasons:

- The case of hydrocarbon fragment ionisation after high energy impacts in remote regions of lower energy density has been described by Neugebauer (2001). There the ionisaton of $C_3H_x^+$ - $C_5H_x^+$ species was always observed, and in principal is inevitable due to the cracking of long chained hydrocarbons. Similar observations were made with impact ionisation experiments using organic impactors in Heidelberg with CDA (Stübig, 2002; Goldsworthy et al., 2003) and a next generation high resolution spectrometer (Srama & Woiwode, personal communication, 2006). There are no hints for $C_{(2+n)}$ species in stream particle spectra.

- In the case of Saturnian stream particles Rhodium cluster peaks with the 28 amu species are observed at about 131 amu. This is extremely unlikely with a surface contaminant which is ionised far from the actual impact crater. In contrast, a target-projectile cluster is a common phenomenon and has already been observed in the laboratory at 131 amu with silicon (28 amu) containing projectiles (Kuhn, 2002).

- Possible hydrocarbon contamination is expected to be homogenously distributed over the whole surface (see 2.2) as in the case of hydrogen or carbon which appear in every stream particle spectrum. In contrast, the 28 amu feature only occurs in about two thirds of the spectra, although the ionisation energies for the formation of $C_2H_x^+$ were provided by each impact.

- In Type III spectra observed within Saturn's E ring (see chapter 6.1.7) the impact conditions are much more favorable for a release of possible hydrocarbon contaminant ions than with stream particles. However, in that case only a few, mostly faint, signatures can be observed between 27 and 29 amu.

Target contamination by hydrocarbons however, can not be ruled out entirely. Due to the outgassing of volatile organic substances by the spacecraft it is possible that this material condenses on the target surface in between CDA decontamination cycles. If such a contamination layer is present it does not appear to have left any significant trace of hydrocarbon ions in CDA spectra up to now.

Hydrogen

The phenomenon of proton release after high velocity impacts has been frequently observed (Knabe, 1983; Krueger, 1996; Stübig, 2002). All metals can adsorb Hydrogen on the surface or even solve Hydrogen (such that it occupies interstitial sites or vacancies in the host metal's lattice). A comprehensive introduction to this topic is given by Fukai (2005). From the sheer abundance of H^+ in spectra obtained at Jupiter (Fig. 4.2), it is clear that these ions cannot stem from the particle alone. In fact there are so many ions, that the abundant solution of Hydrogen gas within the metal lattice has to be considered. The appearance of RhH^+ in deeper layers of the Rhodium target detected by TOF-SIMS (2.3.2) supports this assumption. However, due to the negative enthalpy of solution Rhodium cannot solve large amounts of Hydrogen atoms in an equilibrium state at low ambient pressure (Wipf, 2001).
It is currently unclear where the Hydrogen actually comes from. A possible explanation would be an entry of protons from the solar wind when the target is not shielded by a planetary magnetic field or the spacecraft. With impact speeds of several hundred km s^{-1} the protons are implanted about 50 nm below the surface. Due to the low target temperature ($\approx$ 210–220 K) the diffusion coefficient of Hydrogen in the metal lattice is very small. This might lead to an accumulation close to the surface where protons can be released through a high velocity impact. However, since Rhodium has a much lower ionisation energy the ratio of Rhodium to Hydrogen observed in spectra should be much higher if a considerable amount originates from the bulk material. This favours an impact mechanism which leads to hydrogen surface ionisation over an area which is many times larger

than the area directly hit by the impactor. As well as the accumulation of hydrogen from the interplanetary medium, a further possible source of surface contamination would be outgassing from spacecraft components. In addition to adsorbed elemental or molecular hydrogen, adsorbed hydrocarbons could be the reason for the abundant H^+ detection. However, those species should be desorbed by the heating of the target. Thus, there must be an immediate re-adsorption of the Hydrogen bearing compounds to explain the H^+ signals soon after (a few hours) decontamination (e.g. on DOY 247 in 2000).
A detectable amount of H^+ is not expected at low impact velocities.

Carbon

The phenomenon of C^+ contaminant ions is known from high velocity impacts at the CDA calibration experiments performed at the Heidelberg dust accelerator facility (see 2.3.3). However, the abundance of C^+ in stream particle spectra obtained at Jupiter and Saturn is above all expectations and C^+ is the least understood of all contaminant species. In the spectra of Saturnian stream particles (see chapter 5.1), C^+ is the dominant feature especially at the lowest total ion charges (see Fig. 4.1). In these faint spectra the amount of C^+ often is significantly higher than 50% of all detected ions, representing many times more atoms than the particles were likely to contain. Also Jovian stream particle data provide clear evidence that C bearing compounds are an abundant surface contaminant (see 2.3.4). As the TOF-SIMS analysis (2.3.2) indicates, Carbon also seems to be incorporated within the target. Thus, RhC^+ which is detected not only at TOF-SIMS but also in spectra obtained in the laboratory (2.3.3) and space (see sections 3.1, 4.1, 5.1, 6.1.7) is probably an intrinsic impurity ion from the bulk material close to the surface and not a cluster ion of a carbonaceous surface contamination and the metal target. In contrast to C^+, which can not be expected at low impact velocities, RhC^+ forms at much lower energy densities.
The source for surface contamination of C-bearing compounds in space is currently not clearly identified. In laboratory spectra the signature was usually attributed as a fragment ion of organic contamination from lubricant oil originating from the vacuum pumps. Since this is not applicable in space and Carbon is not known to be an abundant element in the interplanetary environment a more likely source is the outgassing of carbon bearing compounds from the spacecraft. However, there are only weak indications of hydrocarbon fragment ions (see the respective section above). Furthermore, there is only weak indication for $C_{(2+n)}{}^+$ carbon cluster ions such as appear in CDA spectra with fast hydrocarbon projectiles in the laboratory (Srama & Woiwode, 2006, personal communication; Goldsworthy et al., 2003 ; Stübig, 2002).
The most plausible explanation is a Carbon-bearing contamination that for some reason appears basically as C^+ and H^+ in the spectra. For example, an amorphous, Carbon-rich contaminant probably does not allow the abundant formation of $C_xH_y^+$ ions. Such materials can be generated if Hydrocarbons are exposed to UV radiation and degenerate as the C-C and C-H bonds are cracked. This results in a short-chained and Carbon-rich amorphous layer which cannot be removed by heating (Göhrlich, personal communication, 2007; Palumbo et al., 2004). However, the layer must have been established prior to September 2000 when the first stream particle spectra were encountered (Postberg et al.,

2006) if not before the recording of the IDP spectra in 1999 (Hillier et al., 2007a).

Summary

To summarise the contamination chapter, all possible contaminants with decreasing relevance for CDA spectra are listed below.

- Carbon and Hydrogen are the most abundant contaminant species. Their relevance increases with increasing impact speed. They form dominant signatures in all fast hypervelocity impacts. At low impact speeds (below approximately 10 km s^{-1}) they might not show up at all.
- Sodium and Potassium are contaminants which are inhomogeneously distributed over the target surface. The more abundant Na compounds cover less than 45%, Potassium compounds less than 15% of the target area. Their relevance increases with decreasing impact speed and increasing particle size. Occasionally Na^+ signatures (23 amu) can be dominant at low impact speeds (below approximately 10 km s^{-1}).
- Oxygen is a likely target contaminant. However, it only shows up at high impact speeds (above approximately 30 km s^{-1}). Even then it is not always detectable and if present it is clearly less abundant than Carbon and Hydrogen.
- Molecular contaminant ions of RhC^+ (115 amu) and, less abundant, $RhOH^+$ (120 amu) are likely to cause occasional small signatures.
- Hydrocarbon contamination due to spacecraft outgassing is likely. Their relevance as molecular ions in CDA spectra however, appears to be negligible. There might be an occasional minor signature at 27 and 29 amu.
- There are intrinsic Silicon impurities within the target material which cause detectable signals at 28 amu in 0.5–5% of spectra.
- Rare and weak contamination signatures cannot be ruled out for Fluorine, Calcium, Nickel, Nitrogen, Water, Copper and Beryllium.

Chapter 3

Interplanetary Particles in Cassini's Early Cruise Phase

3.1 Spectra Analysis

During the early cruise phase CDA obtained two spectra of interplanetary dust particles which hit the Chemical Analyser Target (CAT). The spectra were recorded on 27th May 1999 (impact 1) and 10th November 1999 (impact 2) not far from earth orbit at solar distances of 0.89 and 1.87 AU, respectively. Cassini was close to the ecliptic plane for both detections. As full science operation was not intended during such an early phase of the mission, transmission bandwidth was limited and the spectra were denoised and wavelet compressed before being sent to Earth. This reduced the sampling rate by a factor of 4 for impact 1 and 2 for impact 2. Particularly in the case of impact 1, the nominal mass resolution was therefore significantly reduced.

Fig. 3.1 shows the two spectra, the appearance of which - except for the sampling rate - is very similar. The identified mass lines are listed in Table 3.1.

The interpretation of signatures given in Tab. 3.1 differs slightly from the original publication by Hillier et al. (2007b):

- Here the possibility of Calcium being the responsible species for 1f / 2d is emphasized. Potassium (K^+, 39 amu) and Calcium (Ca^+, 40 amu) cannot be separated by the CDA, especially in compressed spectra. Since K^+ is expected to be a minor surface contaminant (see 2.3), this would in general be the more plausible assumption. In the case of the absence of Sodium (Na^+, 23 amu) however, this is different. The examination of the target surface (2.3.2) as well as of all other recorded spectra (2.3.3, 2.3.4) suggest a conjoint appearance of K^+ with its more abundant "sister ion" Na^+. Since there is no evidence for the latter in both spectra, Ca^+ becomes a possible candidate, too, though not as a contaminant, but as a particle component.

- The features 1k and 2i are attributed as RhC^+. Previously Fe_2^+ was considered an equivalent alternative. The investigation presented in 2.3.2 shows RhC^+ as a minor subsurface contaminant. Furthermore, the position of the peak and the absence of Fe_2^+ in laboratory experiments with iron projectiles (Posner, 1995; Stübig, 2002)

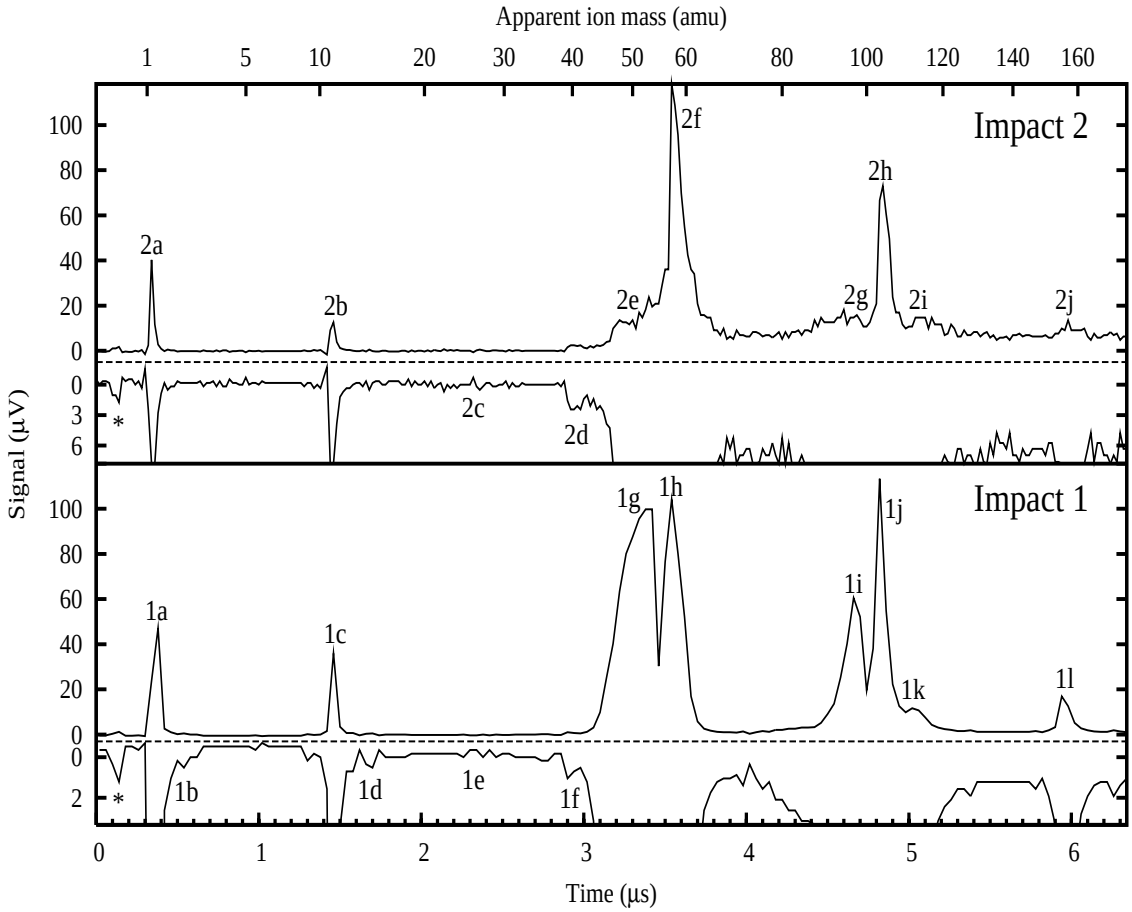

Figure 3.1: *IDP mass spectra obtained during the early Cassini cruise phase. In each panel, below the dashed line, the spectrum is shown inverted and magnified by a factor of 10. The mass scale is calibrated by* $t_p = 0.492\sqrt{m} - 0.20\mu s$ *(impact 1) and* $t_p = 0.492\sqrt{m} - 0.18\mu s$ *(impact 2).*

confirm RhC^+ as the more likely option. Nevertheless, it is possible that Carbon stemming from the particle forms a target-projectile cluster ion, and contributes to the comparatively distinct RhC^+ signatures.

3.2 Composition of Particles

It is quite striking that the apparent composition of both particles, detected at different locations, is very similar. This is even more relevant when the unexpected composition is taken into account. In fact, without a second similar spectrum, the chemical interpretation would have been rated untrustworthy.

Clearly Iron is a major component and by far the most abundant metal in both particles. Of other metals, minor amounts of Calcium are possible; Titanium, Vanadium, Chromium,

Table 3.1: Identified quantifiable mass lines for both impacts. The keys refer to Fig. 3.1. Besides the listed species, minor but unquantifiable amounts of Ni, Cr, Mn, Co, Ti, and V are possible for impact 2.

Species	Key		Ions		Comment
	I 1	I 2	I 1	I 2	
$H^+, {H_2}^+$	1a,b	2a	52 200	44 700	solar Wind
C^+	1c	2b	42 800	19 300	mostly CAT contaminant
O^+	1d	-	600	-	possible CAT contaminant
Si^+? / Fe^{2+}?	1e	2c	< 500	< 500	weakly significant
K^+ / Ca^+	1f	2d	2 100	10,700	possible CAT contaminant
Fe^+*	1g,h	2e,f	742 600	745 200	main projectile component
Rh^+*	1i,j	2g,h	395 600	513 700	target material
RhC^+, Fe_2^+?	1k	2i	37 000	105 600	contaminant or target-projectile cluster
$RhFe^+$	1l	2j	34 100	74 900	target-projectile cluster
Total			1 307 000	1 514 000	

*Here both peaks - "slow" and "fast" species - are included (see Hillier et al (2007b) for details).

Manganese, Cobalt and Nickel cannot be ruled out. Neither Silicon or Sulphur are a significant non-metallic particle component. The distinct mass lines of Hydrogen and Carbon indicate that energy densities at the impact site are more than sufficient to form cations of both species (Si and S) if present (see A.5). This is surprising since silicates are assumed to be the most abundant IDP material and Sulphur is commonly expected in Fe-rich IDPs (forming e.g. pyrites). Moreover, the total absence of Magnesium - a component of the most likely silicate, olivine - supports the identification of a silicate poor particle.
Carbon and, less likely, Oxygen are the only non-metal compounds found in the spectra which are possibly of particle origin. Furthermore, species which are not likely to form cations at the given energy densities (thus remaining invisible for the CDA) Nitrogen, Fluorine, and probably Chlorine can not be ruled out.

The most likely interpretation of both spectra is a basically metallic Iron/Nickel rich particles. A certain contribution of Carbides, Carbonates, Oxides and trace amounts of Calcium halogenides however, is in agreement with the recorded spectra.
It has to be pointed out that - especially for the bigger particle in impact 1 - it is quite possible that only the outer part of the grain contributed to the cation component of the impact plasma. Thus, in the case of an inhomogeneous particle, the core composition may not show up at all.

3.3 Particle Velocities and Masses

The inference of impact velocities from QI risetimes commonly used for IIT impacts (Srama et al., 2004; Kempf et al., 2007) is only of limited value for CAT impacts, because of the signal is strongly compressed by the strong E-field created by the accel-

erator grid. Therefore the utilisation of the QC to QI signal ratio (Srama, 2000) was attempted by Hillier et al. (2007a). The derived values are 18 ± 10 and $7.7 \pm 4.6\,\mathrm{km\,s^{-1}}$ for impact 1 and 2, respectively. Using this values particle masses are deduced, yielding $9\,^{+55}_{-8} \times 10^{-14}\,\mathrm{kg}$ (impact 1) and $1.4\,^{+1.9}_{-0.8} \times 10^{-12}\,\mathrm{kg}$ (impact 2). The calibration relation used by Hillier (2007a) however, is only reliable for laboratory impacts, since this relation is strongly biased by the characteristics of the van der Graf accelerator used in Heidelberg. Therefore, an alternative method to derive impact velocities by spectral signatures is presented here. The energy densities of an impact determine the threshold for the ionisation of species depending on their ionisation energies. Laboratory experiments confirm that this effect depends much more on the particle's velocity than on its mass (2.3.3).

Impact 1 clearly provided higher energy densities than impact 2. This is indicated by the greater abundance of species with high ionisation energies, namely the ubiquitous surface contaminants H^+, C^+, and especially O^+, which is not detectable for impact 2. On the other hand, the cluster ions (RhC^+ and $RhFe^+$) have a far higher relative abundance in impact 2, characteristic of lower energy densities.
In laboratory experiments with Iron projectiles, H^+ and C^+ regularly appear in spectra at impact speeds exceeding $13\,\mathrm{km\,s^{-1}}$, whereas the velocity threshold for O^+ is about $30\,\mathrm{km\,s^{-1}}$ (see Table 2.3). Since the stronger impact signals of IDPs imply higher particle masses than in the laboratory, those values have to be treated as upper limits here. $10\,\mathrm{km\,s^{-1}}$ (H^+ and C^+) and $25\,\mathrm{km\,s^{-1}}$ (O^+) are assumed to be more realistic values in this case.
The abundances of H^+ and C^+ in impact 2 imply an impact speed substantially faster than the minimum speed thresholds, whereas the few O^+ ions in impact 1 line are in agreement with a velocity closer to the respective upper threshold. From that we conclude impact speeds of $25-35\ \mathrm{km\,s^{-1}}$ (impact 1) and $13-25\ \mathrm{km\,s^{-1}}$ (impact 2) to be the most likely energy regimes. There is the additional constraint that impact 1 has to be considerably faster (in the order of $10\,\mathrm{km\,s^{-1}}$) than impact 2. These values are close to or even exceed the upper limits given by Hillier et al. (2007a). However, the derived speed for impact 1 is in good agreement with orbital elements of impact 1 calculated by Altobelly et al. (2003), where the most likely impact speed is found to be $33\,\mathrm{km\,s^{-1}}$. For impact 2, a speed estimate of $11\,\mathrm{km\,s^{-1}}$ using the signal rise time method is given by Kempf et al. (2004). However, this method turned out to be not applicable to CAT impacts as discussed above.

With significantly higher speed estimates, the particle masses can be assumed to be much lower than those given in the original publication. The finding that the particle mass for impact 1 was lower than for impact 2 however, can be confirmed. Impact 2 occurred at a clearly lower speed but yielded more ions than impact 1, which - with the given similar composition - can only be explained with a substantially higher particle mass.

Chapter 4

Jovian Stream Particles

4.1 Results

4.1.1 Identification of Ion Species

In Fig. 4.1 two representative examples of the impact spectra of Jovian stream particles are shown. Table 4.1 lists the properties of the 9 most distinct spectral features. In general only the 4 most abundant features (F1, F3, F5, F9) and F8 show a well defined shape. The weaker features are often irregular or barely separable from background noise in individual spectra. This can be improved by co-adding and creating sum spectra. As can be seen in Fig. 4.2 this leads to improved peak definition and better signal-to-noise ratio at the price of a decreased mass resolution.

Table 4.1: Dominant spectral features

Feature	$\langle t_{max} \rangle$ [μs]	$\frac{\langle \Delta t \rangle}{\langle t_{max} \rangle}$	Occurrence	Extent [amu]	Origin
F1	0.52	2.1%	287 (100%)*	0.9 - 1.3	H^+
F2	1.09	5.0%	109 (38%)	4.2 - 6.0	C^{2+}(?)
F3	1.66	0.5%	287 (100%)	9.0 - 14.5	C^+
F4	1.89	1.2%	228 (79%)	14.5 - 16.5	O^+
F5	2.32	0.3%	281 (98%)	20 - 25	Na^+
F6	2.56	1.6%	190 (66%)	26 - 30.5	Si^+
F7	2.77	2.5%	168 (59%)	30.5 - 37	S^+ / Cl^+
F8	3.01	0.6%	225 (78%)	38 - 41	K^+
F9	4.84	0.5%	287 (100%)	70 - 110	Rh^+

Note: The second column refers to the average position of the feature's maximum and column 3 list its relative variation. Column 5 shows the common extent of the feature as indicated by the arrows in Fig. 4.2 with respect to an ideal atomic mass scale.

** = Only a fraction of the spectra show a H^+ feature (F1), with the recording of the others triggered by H^+ (see 2.1), so an occurrence of 100 % is stated.

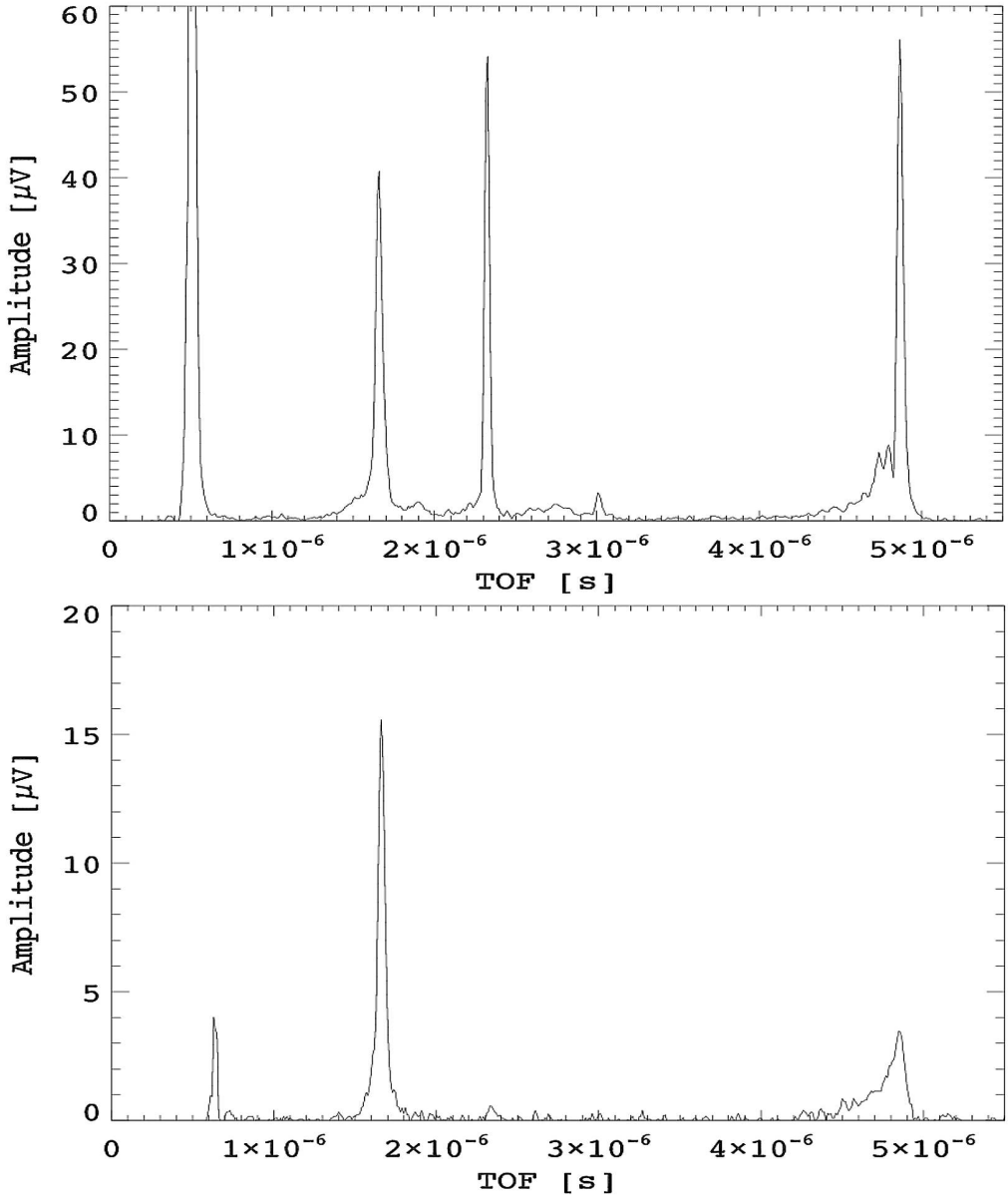

Figure 4.1: *Examples of two spectra obtained on 2nd October 2000 which have been filtered smoothed and calibrated. The upper spectrum is due to a strong impact (QI Amplitude ≈ 280,000 ions), the lower spectrum reflects a weak impact (QI Amplitude ≈ 40,000 ions). While the upper spectrum shows most of the typical features as described in Table 4.1, the weaker spectrum only shows features of carbon (F3), sodium (F5), and the target material rhodium (F9). This event was triggered by the multiplier (see section 2.1)and thus does not show a hydrogen feature. Note, that in contrast to the upper spectrum the first peak in the lower spectrum is an artefact which indicates the start of the high sample rate mode of the multiplier and not a hydrogen peak.*

Except for the broad features F2 and F7, the atomic mass lines shown in Table 4.1 could be identified by the position of the peak maximum. The average position of the maximum of the F2 feature corresponds to a mass of 5.2 amu. Since no isotope with a mass of 5 amu exists, F2 is likely to represent a multiply charged species. Doubly

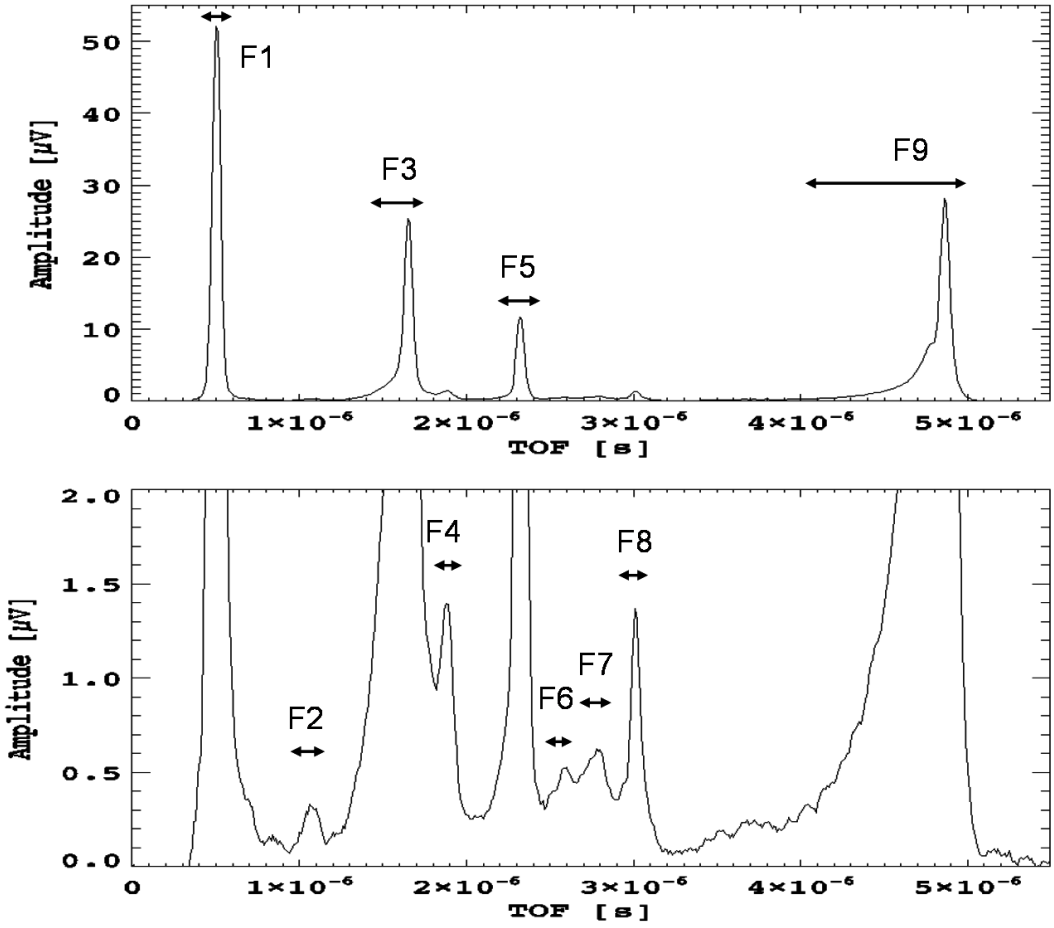

Figure 4.2: *Sum spectrum of 30 typical TOF spectra. Nine major peak features can be identified (see Table 4.1). The lower spectrum shows a stretched y-scale. The arrows show the common extent of the feature (Table 4.1, column 5).*

charged ions are expected to appear at a TOF equivalent of half the mass of the singly charged species. There is no clear evidence for B^+ (isotopes with 10 and 11 amu) in the spectra, thus a strongly shifted C^{2+} mass line is the best candidate. This assumption is supported by the fact that there is a clear anti-correlation between the abundance of C^+ ions (F3) and F2. Doubly ionised atoms apparently don't stay long enough inside the plasma to recombine. Favored by their high charge to mass ratio C^{2+} ions probably leave the impact plasma earlier than the singly charged ions used for mass calibration. This makes a substantial shift towards lower TOF plausible (see also next paragraph).

Especially in strong spectra, a broad feature with a varying and irregular shape extending from 2.65 to 2.9 μs appears (F7). In other spectra there are one or more small and narrow peaks which extend over only part of the TOF-range stated above. The well defined shape of F7 displayed in Fig. 4.2 can only be achieved by adding a number of spectra. An analysis of the positions of peak maxima within F7 reveals that it is composed of more than one mass line (Fig. 4.3). The maxima are most frequent at $t_{max} \approx 2.70\,\mu$s , $t_{max} \approx 2.80\,\mu$s and $t_{max} \approx 2.87\,\mu$s. Those times are consistent with the mass lines of sulfur ions (S^+, 32 amu)

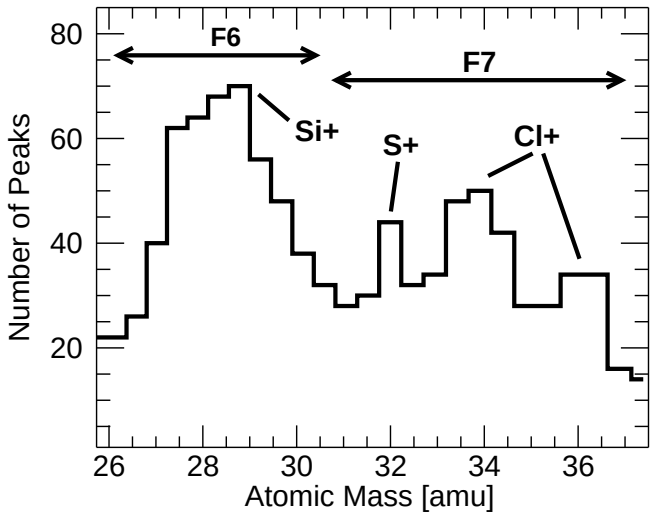

Figure 4.3: *Distribution of peak occurrences in the TOF-range of F6 and F7. Both features cover a relatively broad range of possible atomic masses. In contrast to F6, the peak maxima of F7 cluster at certain positions. As described in the text this leads to the identification of sulfur and two, slightly shifted, chlorine isotopes represented by F7. Though F6 might represent more than one mass line as well, they cannot be resolved.*

and slightly shifted mass lines of chlorine ions (Cl^+, isotopes with 35 amu (75%) and 37 amu (25%)). Apart from Cl^+ isotopes, a shift towards lower TOF can be observed for the possible C^{2+} feature (F2) and the O^+ mass line (F4). These three features represent the ions with the highest ionisation energies of all observed species (Table A.5). Ions with high ionisation energies have a greater chance of recombining with electrons, favouring the survival of those that can escape the impact plasma very quickly. This causes a shift of the maximum towards a shorter TOF relative to the ions used for mass calibration. In most cases, the shifted Cl^+ main isotope at about 2.80 μs ($\approx$ 34 amu) dominates F7. In contrast to its less abundant neighbours it can often be integrated with an acceptable error and is used for quantitative correlation tests (see section 4.2).

Four main species familiar from calibration experiments can be found in almost every spectrum and on average represent about 95% of the detected ions. Along with the target ions Rh^+ (F9), the spectra are dominated by the H^+ (F1) and C^+ line (F3), which both are believed to be due to target contamination (see chapter 2.3), and the alkali metal species Na^+ (F5).

As a consequence of the high energy densities after the impact, the formation of molecular or cluster ions is unlikely. Thus, all the distinct features shown in Table 4.1 and Fig. 4.2 are considered to be of atomic origin. Apart from F2, there is little indication of multiple charged ions as well. This is a little surprising considering the energy densities involved, but in good agreement with previous results from impact ionisation instruments at comet Halley (Brownlee and Kissel, 1990) which had a relative impact speed of 60–80 km s^{-1}.

It appears that only a small fraction of the kinetic energy is used for ionization while most of the energy is used for excavation and vaporization. Furthermore most of the initially multiply charged ions obviously recombine with electrons inside the impact plasma before they are accelerated towards the multiplier. There is also only a weak indication of cluster ions, which are investigated in chapter 4.1.2.

Many more small features than shown in Table 4.1 can be observed, but except for a few signatures they do not show a statistical accumulation at a specific region and disappear when a number of spectra are added to form a sum-spectrum. However, some of them show up more or less regularly and are worth mentioning. A tiny feature occasionally appears at 2.10 μs which is consistent with the hydronium ion (H_3O^+, 19 amu) indicating the presence of traces of water or Fluorine cations (F^+, 19 amu). Another region where small, often irregularly formed features are sometimes present is on or preceding the leading flank of the rhodium feature (F9). Between 3.45 μs and 3.8 μs they might be associated with the doubly charged target species Rh^{2+} (51.5 amu) or other metal ions such as Cr^+ (52, 53 amu), Mn^+ (55 amu) , Fe^+ (56 amu) Ni^+ (58, 60 amu). Note that, in this work, it cannot be determined whether these low significance features are artefacts, contamination, or particle components. At about 5.15 μs an occasional small feature extends the trailing flank of the rhodium peak. This is likely to be due to RhC^+ (115 amu), a known contaminant ion (see 2.3).

Fig. 4.4 shows how the occurrence of peaks of different species depends on the total ion charge (which is a good indicator of impact energy).

4.1.2 Identification of Particle Ions

Impacts with high energy densities typical of those due to the tiny, high velocity stream particles can neither be reproduced in the laboratory nor have they been simulated on computers. It is expected that for an impact of nanometre-sized particles with speeds above $50\,\mathrm{km\,s^{-1}}$ only a small fraction of the produced ions are in fact particle material (Hornung and Kissel, 1994; Hornung et al., 2000). The majority of the plasma ions originate from the target material Rhodium (F9) which contains impurities and surface contamination (see 2.3). Due to the small number of particle atoms, species with low abundance or high ionisation energies might be hidden by background noise. So, particularly with small total ion charges, a species that is present in the particles might not be visible in the spectra at all. Another aspect known from impact experiments is that even with similar composition, velocity, and mass of the projectiles, the resulting spectra often appear quite different because of varying local impact conditions on the target. As a consequence, the identification of features associated with the particle is difficult. Only statistical considerations based on a large sample of impacts can provide a reliable insight into the particles' composition.

H^+ appeared as a very abundant feature (F1) in our spectra. The large features observed represent far too many ions to be solely of particle origin. H^+ is considered to be primar-

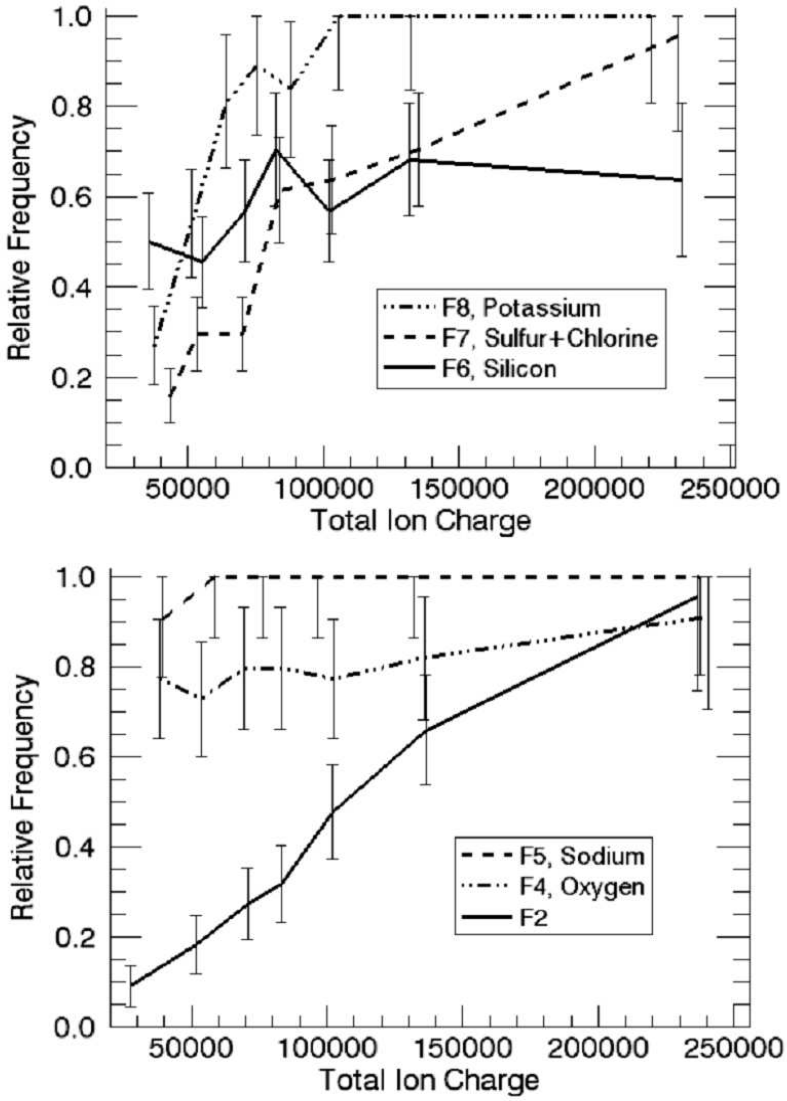

Figure 4.4: *The occurrence of mass lines as a function of the total ion charge (QI amplitude). Carbon and rhodium features (F3, F9) can be observed in every spectrum. The occurrence of some features clearly depends on the total ion charge, while others (F6 and F4) do not show a correlation. It has to be pointed out that the overall signal-to-noise ratio of a spectrum depends on the total ion charge. Thus, the assumption that the occurrence decrease of F2, F7, and F8 features is due to an overlay of background noise is appropriate.*

ily due to a release of protons from the Rhodium target after an impact. The phenomenon is examined in further detail in chapter 2.3.

When discussing the C^+ feature, the impactors are considered to be high velocity particles with a mass of about 10^{-21}kg. These tiny particles, with radii of about 10 nm, are composed of too few atoms to create a peak area of the size of the observed C^+ feature (F3), thus - as with H^+ - the C^+ ions cannot be solely of particle origin. The details of

this and other contamination phenomena of the CA target are discussed in chapter 2.3.

Alkali metals like sodium and potassium are well known surface contaminants, too. But the high ion abundance and the high occurrence of the alkali metal features (F5, F8) is unusual. These signatures can be identified in 98% of the spectra. Analysis of the surface of the rhodium plate which was used for the CA target shows that the surface is not homogeneously covered with alkali metals and not more than 45% (Na) or 33% (K) of the area is affected (see chapter 2.3). This is clearly contradictory to the interpretation that all Na and K originate as contaminants in impact spectra measured at Jupiter. Measurements of stream particles originating from Saturn with similar impact properties show an alkali metal feature in less than 50% of all spectra (Kempf et al. (2005b), see also chapter 5). Furthermore, the latter show very weak signatures of Na^+ and K^+: the average proportion of alkali metal ions in the Saturnian dust stream spectra is more than a magnitude lower than in spectra recorded at Jupiter (see chapter 4.1). The tiny alkali metal features seen in Saturnian stream spectra probably represent the alkali metal surface contamination which clearly favours sodium to be a substantial particle component of the Jovian dust streams.

An useful method for identifying major particle components is through target-projectile cluster ions. For decades laboratory experiments have demonstrated that the most abundant particle ions may form clusters with the target material (Knabe, 1983). Unfortunately, this is only effective at low energies, so in the case of Jovian stream particles these types of mass lines cannot be expected to be very noticeable. Nevertheless, even the identification of faint target-cluster mass lines is a strong indicator for a major particle component, provided that the corresponding projectile mass line shows up in the spectrum as well.

Peaks consistent with target-projectile ions and exceeding a 3-σ significance of the noise amplitude can barely be found. The most significant post-Rhodium feature sometimes indicates RhC^+ (115 amu), which is a known contaminant ion (see 2.3). However, when certain spectra are co-added, the sum spectrum reveals some weak features of cluster ions. Adding all stream 1 spectra that show clear F7 features (30 to 37 amu) reveals two new peaks as can be seen in Fig. 4.5. They occur between 0.45 and 0.55 μs (F10), and between 0.65 and 0.85 μs (F11) after the rhodium peak maximum. F11 corresponds to a target-projectile cluster-ion of the form RhX^+, with X being the projectile species of a mass between 30 and 37 amu. With these target-projectile features of 3-5σ significance, a correlation can be proved: If only the subset of the spectra with F7 signatures that show peak maxima between 31 and 33 amu are used for the sum spectrum, the corresponding RhX^+ feature gets narrower with a maximum at 0.69 μs ($\approx$ 31 amu) after the target feature (Fig. 4.6, grey spectrum). The sum of spectra with maxima between 33.5 and 37 amu shows an equivalent local maximum 0.8 μs ($\approx$ 36 amu) behind the rhodium peak (Fig. 4.6, black spectrum). So the species that form the small, broad F7 signature all have "mirror peaks" as target-projectile ions. This implies that those ions, namely Cl^+ and S^+, originated from major particle components. It is remarkable that F10 is not apparent in the grey spectrum of Fig. 4.6, while it is pronounced in the black spectrum of Fig. 4.6 with a maximum at 0.51 μs ($\approx$ 23 amu) after the Rh^+ peak, which is consistent with a $RhNa^+$

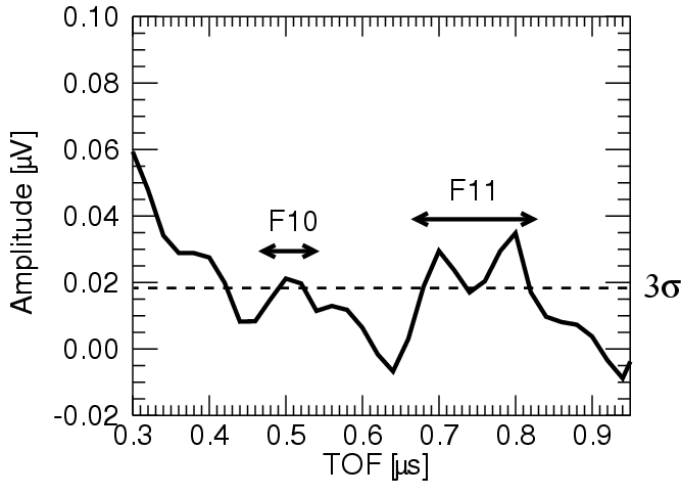

Figure 4.5: *Detailed view of the part of a coadded spectrum after the rhodium peak. If spectra with a distinct F7 signature (31 amu - 37 amu) are co-added, features of significance (F10 and F11) appear in that area. The TOF is with respect to the maximum of the rhodium signature. The trailing flank seen on the left is due to RhC^+, a known contaminant ion.*

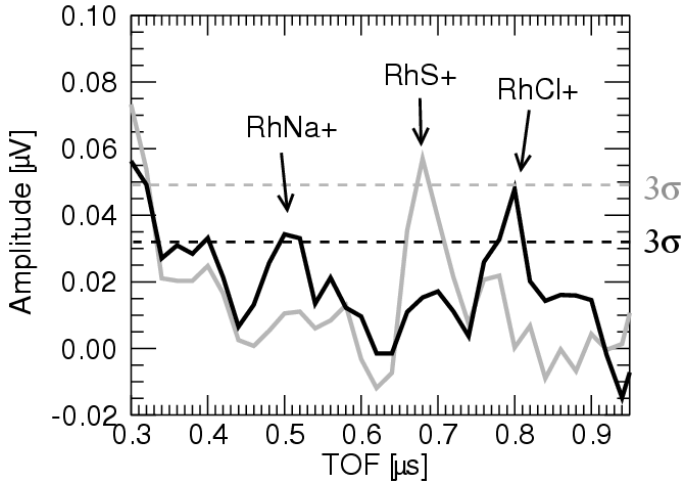

Figure 4.6: *Here only a fraction of the spectra of which Fig. 4.5 is composed are co-added. Grey line = peak maxima between 31 amu and 33 amu. Black line = peak maxima between 33.5 amu and 37 amu. Only fractions of F10 and F11 show up. Those features are likely to represent different target-projectile cluster-ions. The variation in the 3-σ line is due to the different number of co-added spectra.*

cluster-ion. The possible conjoint appearance of $RhCl^+$ and $RhNa^+$ cluster-ions indicate a correlation of the alkali metal with chlorine in the particle.

Qualitative and quantitative correlations between mass lines are an indicator for a common source. For that reason, correlation analysis has been a major field of research during the statistical examination of the data. As shown in Fig. 4.7 there are clear quantitative

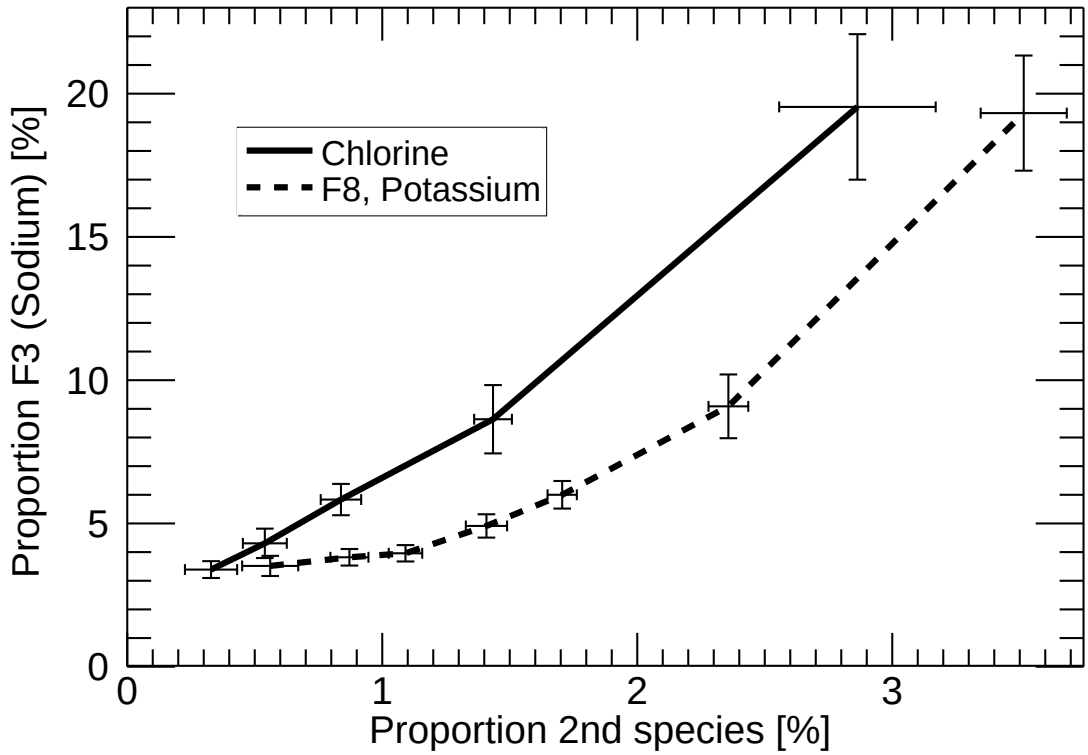

Figure 4.7: *Correlation between the abundances (as a percentage of the total spectrum area) of the species responsible for F3 (sodium) and F8 (potassium; broken line) and chlorine (solid line). For the latter, only the part of F7 features which are dominated by Cl^+ ions are taken into account (maximum between a TOF of 2.75 µs and 2,85 µs, equivalent 33 to 35.5 amu).*

correlations between $Na^+$and K^+ as well as Na^+ and Cl^+. If both elements are present the extremely reactive sodium and chlorine immediately form NaCl, which supports the assumption of NaCl being the common parent molecule of Na^+ and Cl^+. The correlation between $Na^+$and K^+ strongly indicates that potassium is part of the particle, too.

Calibration experiments with the CDA flight spare at the Heidelberg dust accelerator facility demonstrate that at high velocities the contribution of surface contaminants to the resulting mass spectra decreases with increasing particle mass (Stübig, 2002). This is due to the fact that the amount of surface contamination scales with the projected grain area while the total charge scales with the grain volume (in a regime where the particle becomes completely ionised). The same applies to target material: while the amount of particle ions increases linearly with particle mass m_p the generated target ions only increase proportionally to $m_p^{2/3}$ (Krueger, 1996). This leads to a steadily increasing particle proportion with increasing particle mass for a given velocity. As can be seen in Fig. 4.8, the relative abundance of Na^+ in the spectra quadruples from less than 3% at low total ion charges to 11.5% at the highest total ion charges. Such a distinct increase of a particle-species indicates that for the observed impacts the varying total ion charges depend on

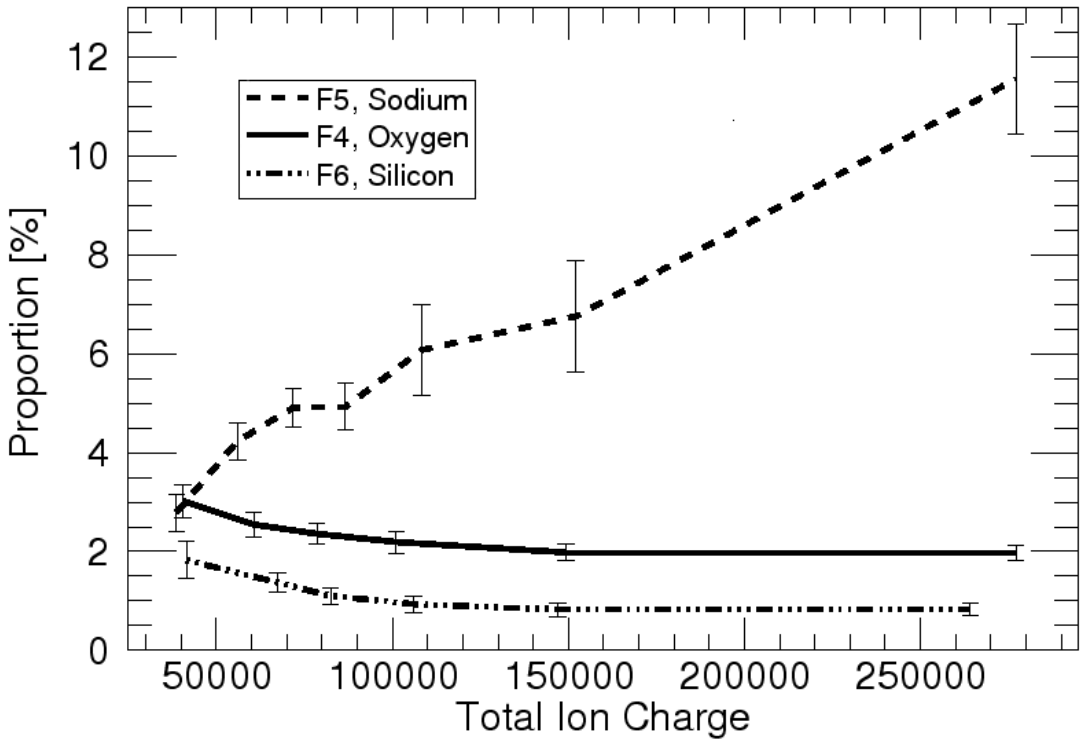

Figure 4.8: *Relative abundance (as a percentage of the total spectrum area) of the ion yield of sodium, oxygen and silicon features as a function of the total ion charge (QI amplitude). Only spectra where a distinct peak of the species is observed are considered. It is obvious that the proportion of Na^+ increases while the proportion of Si^+ and O^+ decreases.*

variations in the impacting particles' masses. If the particles' velocities were responsible for the variations in total ion charge, this would lead to a relative decrease of particle ions with increasing total ion charge.

Despite the frequent observation of O^+ and Si^+ mass lines - which could imply the presence of silicates - there is little indication that those ions represent particle material. O^+ and Si^+ show neither a significant mutual correlation as should be expected for silicates nor a correlation with any of the other possible particle materials identified above. Furthermore, Si^+ does not have an associated target-cluster ion $RhSi^+$, as in the case of the Saturnian stream particles (Kempf et al., 2005b) (see chapter 5.1). Additionally, the relative abundance of Si^+ and O^+ in the spectra decreases with increasing total ion charge as can be seen in Fig. 4.8. For low total ion charges the features of Si^+ and Na^+ on average are of about the same magnitude, whereas for the highest ion charges the Na^+ projectile ions are over ten times more abundant than the Si^+ ions. Finally, there is only weak evidence for the mass lines of metals that are expected to accompany rocky minerals (Fe, Mg, Ca, Al, Ni), which in general are more likely to be detected as positive ions than Si or O. Silicon is a known impurity of the Rhodium plate material (Tack, 1992) and tends

to accumulate in "islands" on and below the Rhodium surface (see chapter 2.3). This is in agreement with the fact that the occurrence of Si^+ signatures is independent of the total ion charge. Nevertheless, TOF-SIMS analysis of the rhodium target surface indicates that less than 5% of its volume shows Silicon impurities (see chapter 2.3), which is certainly not enough to explain the occurrence of the mass line. However, if silicates are part of the particle then their abundance appears to be quite independent of the projectile masses.

O^+ is a known contaminant ion from high speed laboratory impacts (see 2.3.3. However, in many spectra the feature appears to be too big to be solely caused by a thin contamination layer. As in the case of Si^+ the great abundance of O^+ could be explained if a fraction of the ions were of particle origin.

The rare occurrence of a weak feature consistent with water or Fluorine could be due to contamination (see 2.3) or a rare particle component.

4.2 Discussion

The following section is divided into four parts. In the first subsection mainly qualitative aspects of particle components are considered, to derive the source of the stream particles. Quantitative estimates (associated with greater uncertainties) are discussed in subsection 2. In subsection 3 an estimate for the particle masses from the number of ions in the spectra is derived. Thus far the particle composition has been discussed based solely on the spectra analysis. The final subsection is about the implications of those results for particle formation in volcanic plumes on Io. Findings from research into Io's atmospheric chemistry are combined with our results and a particle formation process, as well as a refined picture of the particle composition, are suggested.

4.2.1 Composition and Source of Particles

As a consequence of the results presented above Sodium Chloride (NaCl) is identified as an important particle component. Because of the quantitative correlations $Na^+ \Leftrightarrow K^+$, NaCl is accompanied by K^+. As an extremely reactive element Potassium has to be bound in a compound (KXy), possibly KCl. Except for some of the faintest signals Sodium and Potassium ions are observed in every spectrum, indicating that the vast majority of the particles are of the NaCl/KXy composition-type. The fact that the Cl^+ mass line occurs in fewer spectra than the alkali metals doesn't necessarily mean that Cl^- isn't their associated anion in the particle. Its high ionisation energy (Table A.5 in the appendix) allows for an immediate recombination of many generated Cl^+ ions. Thus, especially for small total ion charges it is quite reasonable that a Cl^+ line could be hidden by background noise. It is not surprising, that there is a weaker indication for target-projectile ions of the type $RhNa^+$ and RhK^+ than for RhS^+ and $RhCl^+$. For alkali metal ions it is energetically

much more favourable to "stay alone" than for elements with high ionisation energies (see Table A.5).

The occurrence and area of mass lines consistent with S^+ is quite low. Nevertheless, in laboratory experiments target cluster ions have only been observed with major particle and target components. Thus the presence of corresponding cluster ions indicates that sulfur plays an important role in the elemental composition of at least some particles. S can either be present in its elemental form or, considering the other possible particle elements, probably in an alkali metal compound or in SO_x.

Whilst the signatures of Si^+ and O^+ are consistent with target contamination as a source of these ions, the abundance and frequent occurrence of both species is difficult to explain solely with impurities. This leads to the conclusion that these species are probably present in the particles themselves.

As a consequence of C^+ and H^+ being an abundant target contaminant (see section 2.3), carbon and hydrogen can neither be excluded nor confirmed as part of the elemental composition of Jovian stream particles.

The strong indication for sulfur being part of many of the particles confirms Io as a source for the dust streams. NaCl is a known component of Io's volcanic ejecta as well. It is evident that it does escape from the moon's gravitational influence, forming the major source for Na and Cl species in the Ionian system (Fegley and Zolotov, 2000; Küppers and Schneider, 2000; Schneider et al., 2000; Moses et al., 2002a; Lellouch et al., 2003; Mendillo et al., 2004; Mendillo et al., 2007). Since sodium and especially the highly volatile chlorine are supposed to be only minor components of interplanetary minerals (Küppers and Schneider, 2000), it is unlikely they are major components of the Jovian ring particles. Thus, our results support Io being the source for the vast majority, maybe all the stream particles detected far outside the Jovian magnetosphere. However, a minor contribution from Jupiter's gossamer rings, with an upper limit of about 5 % of the observed impacts (mainly contributing to the smallest of the observed stream particles), is consistent with our data. This estimate is made under the assumption that gossamer ring particles would not have an abundant alkali metal or sulfur component and mainly consist of rock forming minerals.

4.2.2 Quantitative Estimations of the Particle Composition

All previous applications of impact ionisation have shown that many unknown parameters may influence the relative ion yield of the different species in an impact plasma. This reflects the complexity of the impact process. Thus, derivation of quantitative statements about the particle's composition is associated with major uncertainties. However, the task gets less complicated if we assume that all particle atoms are ionised in the impact plasma. As a matter of fact, with the impact velocities and particle masses of the Jovian streams stated above, the energy densities are high enough for complete ionisation. We have reason to assume that the entire particle material was initially converted into mainly positive

atomic ions and electrons (Hornung, personal communication 2004). Consequently, the influence of the various ionisation efficiencies of atomic species is reduced. In an environment with such energy densities, matrix effects, which reflect the interaction of different molecular or atomic species, are suppressed as well. But still it has to be pointed out that the quantitative considerations made in the following have a speculative component.

Although with reduced emphasis (in the case of Jovian stream particles), the ionisation energy of atoms (Table A.5) is still one key parameter for the relative ion yields (Kissel and Krüger, 1987). It is an important indicator for the formation and recombination probability of ions and electrons within the impact plasma.

The influence of this parameter on the relative ion yields of Jovian stream particles can be observed by comparing the ion yields of Na^+ and Cl^+. If we consider NaCl as the parent molecule, the abundance of both species in the particles can be assumed to be roughly similar. This assumption is supported by the finding that volcanically emitted NaCl is the dominant source for Na and Cl ions in the gas of Io's upper atmosphere, the plasma torus and the neutral cloud (Fegley and Zolotov, 2000; Küppers and Schneider, 2000; Schneider et al., 2000; Moses et al., 2002a; Lellouch et al., 2003; Mendillo et al., 2007)[1]. In the spectra about 6 - 10 times more Na^+ than Cl^+ appears (Fig. 4.7). Considering the extreme difference of ionisation energies between the alkali metal and halogen species, this ratio is surprisingly low. Previous calculations for high velocity impacts would imply $Na^+ : Cl^+$ ratios of 50 : 1 or more (Krueger, 1996). This is due to the fact that in all previous cases much lower energy densities were considered, where the ionisation efficiencies clearly favour the formation of Na^+. In contrast, all Jovian stream particles are assumed to be initially ionised regardless of their ionisation energy, which in this case only influences the recombination of ions.

On average Na^+ is about 5 times more abundant than K^+ in the spectra (Fig. 4.7). As the latter has the lowest tendency to recombine (Table A.5), this ratio is likely to be exceeded in the particle, indicating K bearing components to be only a minor companion of NaCl.

The results imply that the proportion of sulfur is less than the proportion of chlorine for the observed particles. Cl has a higher ionisation energy than S, nevertheless the F7 feature in general represents more Cl^+ than S^+ and the maxima consistent with Cl^+ occur more frequently (Fig. 4.3). Although unknown matrix effects might have an unfavourable influence on the release of S^+, it is unlikely that they could compensate for the considerable difference on ionisation energies. This finding is in contrast to the estimated gas emission into Io's atmosphere where sulfuric components - especially SO_2 - are clearly dominant (Lellouch et al., 2003). This phenomenon is extensively discussed in chapter 4.2.4.

A part of the observed Si^+ and O^+ might be of particle origin. However, the absence

[1] All other Na-bearing compounds are assumed to play a minor role here.

of $RhSi^+$ target-projectile ions and appropriate metals implies that silicate minerals represent only a minor component. The yield of Na^+, K^+ and Cl^+ clearly increases with increasing total ion charge. In contrast, the occurrence and the abundance of the Si^+ and O^+ features shows only a minor dependence on the total ion charge (Figs. 4.4 and 4.8). Thus, if silicate signatures are not exclusively due to contamination, their contribution to the particle seems to be independent of its mass. This interpretation would be consistent with a silicate rich condensation nucleus in the particle.

Due to the omnipresent strong contaminant signatures of Carbon and Hydrogen in the spectra, it cannot be ruled out that they play a role in the particles' elemental composition in some proportion. Molecules composed of those elements (e.g. water or organic compounds) are not known to play a relevant role in Io's volcanic activities, its atmosphere or exosphere (Zolotov and Fegley, 2000; Schaefer and Fegley, 2005b). Thus, it may be expected that their contribution to the dust streams is small or negligible.

The final picture from the quantitative estimates inferred from the spectra is as follows: NaCl is the main constituent of the observed Jovian stream particles, while potassium bearing components play a minor role. Sulfur or sulfurous components are other important constituents. No definite conclusion can be drawn regarding the presence of water ice or fluorine components. Silicates or rocky minerals could be a particle component, representing a minor contribution, possibly located in the grain cores. A more refined estimation can be given when considerations about condensation mechanisms in volcanic plumes are taken into account in chapter 4.2.4.

4.2.3 Estimation of Particle Masses

Assuming that the vast majority of the observed Na^+ is of particle origin and the recombination of alkali metals is negligible, a lower limit for the number of Sodium atoms in the particle can be estimated. Depending on their initial energy, about 15 % of the ions released by the impact plasma are detected by the ion collector grid (QI channel) (Srama, 2000; Stübig, 2002). This is almost equivalent to the number of ions reaching the multiplier. An average QI signal represents about 100 000 ions. After correcting for the abundance of H^+ ions (Reber, 1997; Stübig, 2002) a mean value of about 2500 Na^+ ions in the spectra is obtained. This corresponds to 16 000 Na atoms in an average dust grain. Furthermore it can be assumed that the Na atoms are basically bound in NaCl molecules as the most abundant particle constituent by far. Thus one obtains a good estimate of particle masses. The NaCl molecules (with a mass of 58 amu each), represent a total mass of about 1.5×10^{-21} kg in an average dust grain. Varying with the area of the Na^+ peak, the variation of the mass is about one order of magnitude up and down, equivalent to particle radii ranging from 5 to 25 nm (assuming a density of 2200 kg m^{-3}). This is in very good agreement with the particle masses derived from simulations based on Ulysses data. (Zook et al., 1996)

4.2.4 Implications for Dust Formation in Io's Atmosphere

In contrast to the gaseous components, the knowledge about dust formation and composition in Io's atmosphere and exosphere is basically speculative. NaCl is the parent molecule for the vast majority of the Na and Cl species detected in Io's gas and plasma environment (Fegley and Zolotov, 2000; Küppers and Schneider, 2000; Schneider et al., 2000; Moses et al., 2002a; Lellouch et al., 2003). Furthermore, its abundance is dependent on the volcanic activity on the moon (Lellouch et al., 2003; Mendillo et al., 2004; Mendillo et al., 2007). However, it is less abundant than species derived from SO_2 gas, the main component of the ionian atmosphere. The current estimation for the disc averaged proportion of NaCl in the atmosphere is 0.3%, though higher concentrations probably occur in volcanic plumes (Lellouch et al., 2003). The Na^+ and Cl^+ concentration in the plasma torus amounts to 2 - 6% each (Küppers and Schneider, 2000; Schneider et al., 2000). So obviously the finding that NaCl is more abundant than sulfur in stream particles needs a mechanism that explains the inversion of these proportions. To understand what affects the particles' composition one has to understand the dust formation and escape mechanisms on Io.

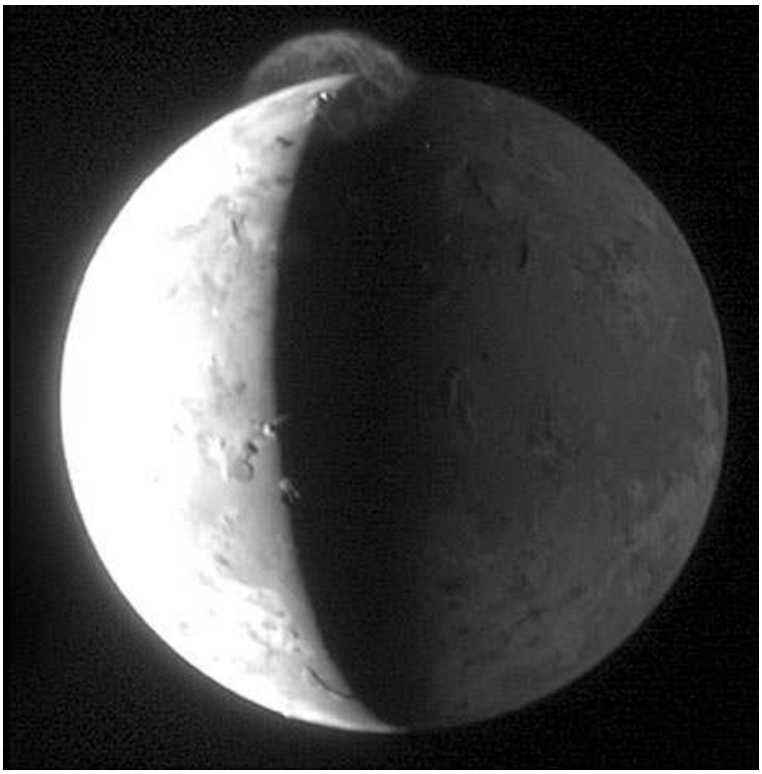

Figure 4.9: Dust plume of a Pele-type volcano observed in February 2007 by the New Horizons spacecraft. The plume height is estimated to be approximately 350 km (Spencer et al. (2007))

.

Krüger et al. (2003) showed a correlation between the occurrence of the high plumes of the Pele-type volcanoes (named after the largest Ionian volcano) and dust stream impacts

on the Galileo dust detector. Dust particles in the plume, reaching a sufficient altitude, are charged by the capture of ionospheric electrons and subsequently accelerated through the magnetosphere. Only particles which reach the top of the plumes at an altitude of almost 400 km have a chance to escape (Flandes, 2004). The flight time from the vent to this height is about 15 - 20 min. Thus the CDA spectra imply NaCl to be the most abundant component in nanometer-sized particles at the top of Pele-type plumes 20 min after the ejection from the vent(s).

In smoothed ultraviolet Voyager images of the Pele plume a bright top appears (Strom and Schneider, 1982). The authors suggested that this top is caused by a concentration of particles at the shock front. Recent observations by the New Horizons spacecraft (Spencer et al., 2007) also show this phenomenon in impressive particle plumes (Fig.4.9). Simulations of Pele-type plumes with entrained particles demonstrated that only particles with sizes below 10 nm[2] track the volcanic gas flow (Zhang et al., 2004). Furthermore it was shown that those particles could reach the shock and concentrate there (Moore et al., 2003). The condensation of particles on refractory nuclei inside the plume is likely. Due to their fluffy structure they can track the gas flow much better than compact spherical particles. Thus particularly those condensed particles can reach high altitudes even if their size exceeds 10 nm (Zhang et al., 2004). Like most authors, Zhang et al. (2004) assumed the possible particles in the plume consist mainly of condensed or liquid SO_2 because of its great abundance in the atmosphere and on the surface. This assumption however, is neither required to explain current observations nor a thermochemical necessity.

Considering condensed and gas phases, the swiftly changing equilibria in a volcanic plume are not easy to model. Moses et al. (2002a; 2002b) considered chemical kinetics, photolysis, diffusion and condensation of volatiles outgassed from a Pele-type vent with a temperature of 1440 K in a one dimensional model. They showed that due to their high condensation temperatures NaCl and KCl are abundant condensates 20 min after outgassing from the vent. About 5 % of the initial amount of NaCl and KCl in the gas phase form stable condensates with low vapour pressure. Under these ambient conditions sulfuric components (except a minor contribution from Na_2SO_4) are still far from condensation. In their simplified model Moses et al. assumed the vapour condensed around the pre-existing condensation nuclei of refractory materials, present in proportion to the atmospheric pressure. Thermochemical equilibrium considerations of the alkali metals and halogen species in volcanic gases from silicate magmas on Io at 1760 K were accomplished by Schaefer and Fegley (2005). They show that below 1000 K NaCl and KCl are by far the most abundant condensates for a wide range of pressures and temperatures. Na_2SO_4 and NaF condense as minor components. The solid KCl converts to K_2SO_4 in a SO_2 atmosphere below 620 K. When temperature drops below 500 K sulfur condenses as S_8, still far above the condensation temperature of SO_2 which is about 115 K depending on the atmospheric pressure. However, in the model of Moses et al. (2002a) S_8 contributes to only a negligible proportion of the condensed phase. So the alkali metal sulfates Na_2SO_4 and K_2SO_4 could represent the main sulfuric components observed in the TOF spectra

[2]assuming a compact and spherical shape

with the latter being the main potassium bearing component. Fegley & Zolotov (2000), Moses et al. (2002a), Lellouch et al. (2003), and Schaefer and Fegley (2005) consider a Sodium / Potassium ratio in volcanic ejecta of about 10/1. This ratio is in good agreement with our estimates for stream particles. The declining proportion of O^+ with increasing total ion yield in our spectra (Fig. 4.8) can be explained with the finding that a part of the observed O^+ is due to target contamination and / or a silicate core. It also indicates that alkali metal sulfates cannot be a very abundant particle component.

In general the results of the thermochemical modelling by Schaefer and Fegeley (2005) are qualitatively and quantitatively in good agreement with our findings. A speculative picture of the particle, considering both results, can be given as follows. The main constituent is NaCl. Na_2SO_4 and K_2SO_4 are minor constituents each representing 5 - 10 % of the NaCl mass. A minor proportion of NaF ($< 5\%$ of the NaCl mass) is also possible. Depending on the condensation temperatures, sulfur molecules might have a small contribution on the surface. The particle is probably condensed around a silicate core whose mass has only a limited dependency on the total particle mass.

Recent observations by the New Horizons spacecraft confirm the hypothesis of this work that most plume particles condense from the gas phase close to the shock front rather than being ejected from the source (Spencer et al., 2007). The spectra analysis furthermore implies that there are probably no pure SO_2 condensates with a size of 5 - 25 nm present in Pele-type plume tops and thus these condensates do not appear to play an important role within the first minutes after outgassing from the volcano's vent. Sulfur species like SO_2 or SO definitely condense upon contact with Io's cold surface. Condensation probably also occurs in shocks or colder regions of the plume at greater horizontal distances from the vent. An alternative scenario would be that SO_2 condenses on particle surfaces as the final layer of the condensation cascade. Subsequent sputtering of the stream particles' surfaces on their voyage through the ionosphere and the plasma torus of Io would lead to dissociation and evaporation of the highly volatile SO_2 frost.

Chapter 5

Saturnian Stream Particles

5.1 Results

5.1.1 Identification of Ion Species

All Saturnian stream mass spectra show distinct mass lines of mostly atomic ions in the lower mass range ($m < 150\,amu$), indicative of high impact energies. Most of the spectra are composed of less than about 30 000 ions. For these impact types, however, the recording of the event is not triggered by the target signals but by the H^+ line exceeding the multiplier threshold (see 2.1). The H^+ comes from the Rh target (see 2.3). Even impacts by tiny particles can generate an H^+ line strong enough to trigger the event recording. In such cases, the offset times (the shift parameter b) are slightly above the TOF of H^+ ions (0.48 μs) which makes the mass calibration less complicated and allowes the identification of the two dominant mass lines as C^+ (12 amu) and Rh^+ (103 amu) (Fig. 5.1). In some spectra only a single well-resolved line (C^+) is apparent.

The reliable identification of further mass lines within the faint noisy spectra is a challenging task. For that reason an iterative method was employed to magnify features too weak to be easily recognized in some of the individual spectra. Apart from C^+ and Rh^+, the most prevalent mass lines, 16 amu (O^+), 23 amu (Na^+), 39 amu (K^+), and 56 amu (Fe^+) were identified by co-adding spectra of similar strength and with similar features. Then, each individual spectrum was scanned for these lines to improve the mass scale calibration. This procedure was repeated until the resolution of the spectral lines of the sum spectrum showed no further improvement. In this way a consistent dataset of calibrated individual mass spectra was obtained.

As well as the aforementioned ions, clear evidence for a species at 19 amu (H_3O^+), which is characteristic for water ice, and/or F^+ was found. There is no indication, however, of water cluster ions $(H_2O)_xH_3O^+$, with $x = 1, 2, \ldots$ such as are typically found at impacts by water ice grains at low impact energies. Likely candidates for the frequent strong line at 28 amu are CO^+ and Si^+. With the given high impact speeds molecular species like CO^+ are initially disintegrated and far less likely to form a significant feature than an elemental species. This favours Si^+ over CO^+. Furthermore there is evidence for Fe^+ in the data

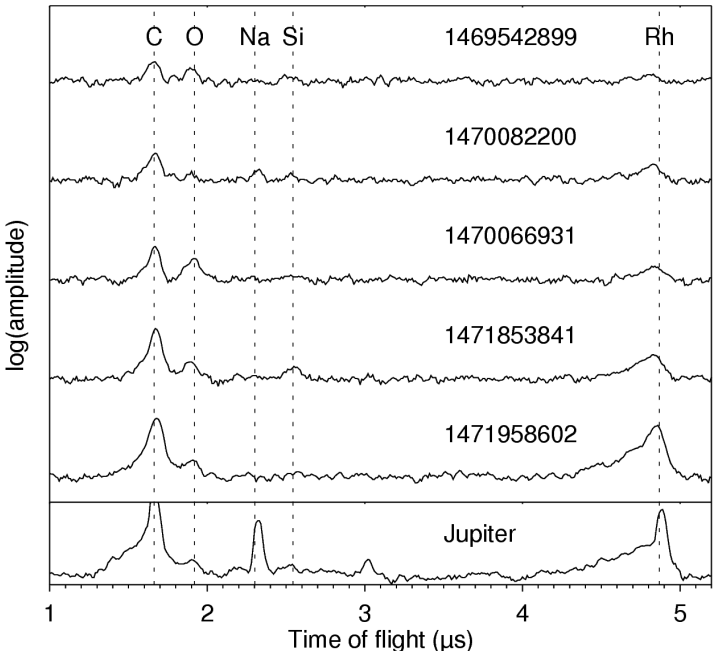

Figure 5.1: Examples of mass spectra displayed in order of increasing strength of the target electron (QC) signal (top to buttom). The uppermost spectrum (spacecraft clock (SCLK) 1469542899) is composed of less than 18000 ions while about 180000 ions contributed to the lowermost Saturnian spectrum (SCLK 1471958602). The dotted lines indicate the masses of C, O, Na, Si, and the target material Rh. The dominant ions are C and Rh. The relative shift of the Rh peak with increasing ion signal is a phenomenon also known from laboratory experiments. For comparison the bottom panel shows a typical spectrum from a Jovian stream particle, dominated by C^+, Na^+, K^+, and Rh^+. From Kempf et al. (2005b).

which is a component of typical silicate minerals such as olivine $(Mg,Fe)_2SiO_4{}^+$. Thus, assigning the 28 amu line in the Saturnian stream particle mass spectra to Si^+ seems to be the more reliable assumption. A small percentage of the spectra showed faint features at 14 amu (N^+) and 18 amu which may be $NH_4{}^+$ or H_2O^+. In the initial analysis by Kempf et al. (2005b) these features of low significance were attributed to nitrogen compounds which retrospectively is a quite speculative assumption.

At least two post-Rhodium features can be identified occasionally at 115 amu and 131 amu. Those are attributed to Rhodium cluster ions RhC^+ and $RhSi^+$.

5.1.2 Identification of Particle Ions

All spectra are dominated by a C^+ line. As in the case of Jovian stream particles, we consider the impactors to be high velocity particles with a mass of about 10^{-21}kg or even less. Particles with radii below 10 nm (Kempf et al., 2005a) are composed of too few atoms to create a peak area of the size of the observed C^+ feature. Thus the C^+ ions

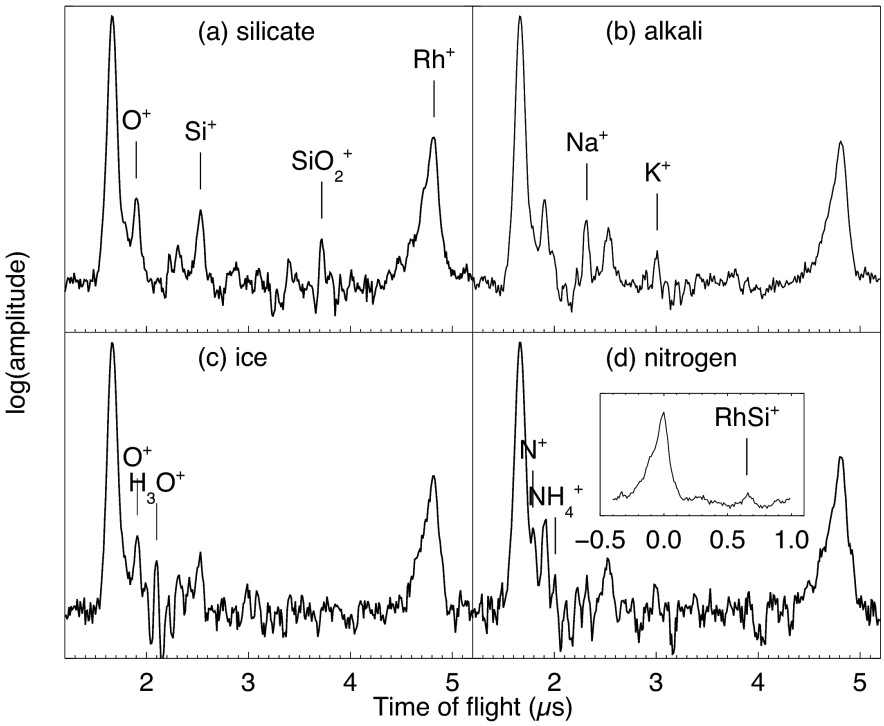

Figure 5.2: Co-added spectra of the four spectrum types produced by selecting indivdual spectra with $q_e < 15$ fC and showing Si^+, $SiO_2{}^+$, or Fe^+ (a - silicate), Na^+ or K^+ (b - alkali metal), O^+ and H_3O^+ (c - ice), and possible N^+(?) and $NH_4{}^+$(?) (d - nitrogen). In each case features of the other types are still apparent. The inset shows the $RhSi^+$ cluster-ion line obtained by co-adding all spectra with a clear Si^+ line and $q_e < 15$ fC relative to the Rh^+ peak position (in μs). From Kempf et al. (2005b).

cannot be solely of particle origin. This implies an abundant Carbon contamination of the target (for more details see section 2.3). However, it is unclear whether there is a particle contribution and, if so, to what extend. In principle the same applies to H^+ ions: Though known to be an abundant contaminant, it cannot be ruled out that a part might be of particle origin.

To characterise the spectra qualitatively up to four "composition types"[1] were assigned to each individual spectrum according to its identified lines (Fig. 5.2): a *silicate* type to spectra showing at least a Si^+, $SiO_2{}^+$, or Fe^+ line, an *alkali metal* type to spectra showing at least a Na^+ or K^+ line, an *water ice* type to spectra showing both an O^+ and H_3O^+ line, and an *ammonium* type to spectra showing both an N^+ and a possible $NH_3{}^+$ line. About 12% of the spectra could not be associated with one of the composition types, 74% of the spectra are of the silicate type (32% of them simultaneously belong to the ice type),

[1]Here, composition refers to the composition of the impact plasma and not the particles' composition!

but only about 7% of the spectra are of the ice type but show no silicate lines.

Nearly 50% of the spectra show at least one alkali metal line (Fig. 5.3). A TOF-SIMS

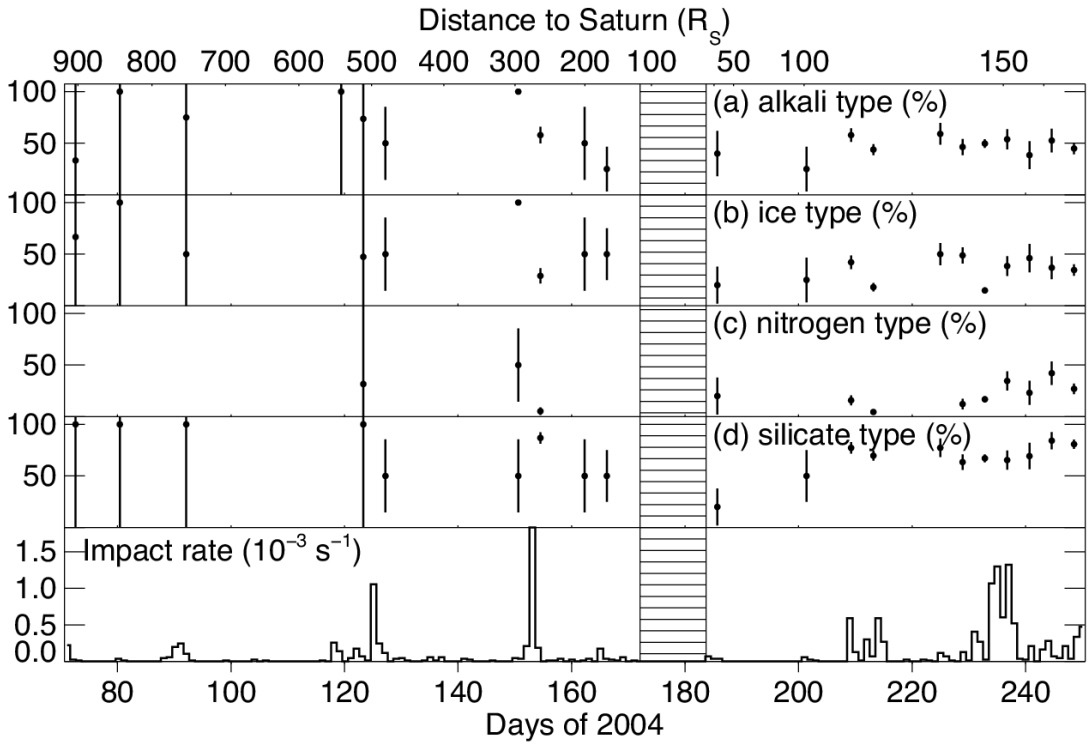

Figure 5.3: Stream particle impact rates registered by CDA during Cassini's approach to Saturn and during the outbound leg of Cassini's first orbit around Saturn (lower panel). Between 20 June 2004 (day 172) and 1 July 2004 (day 183) the CDA detector was powered off (marked by the outlined area). Cassini entered Saturn's magnetosphere on 28 June (day 180) and left the magnetosphere on 5 July 2004 (day 187). Note that CDA was not continuously geometrically sensitive to stream particles. After Cassini's orbit insertion most of the stream particles were detected during the daily 9 hour data transmission to Earth when Cassini slowly rotated about its antenna axis. The sequence of data transmissions was almost evenly distributed so that the detected impacts reproduce the stream particle flux on time scales longer than 12 hours. For Cassini's approach phase this was unfortunately not the case (Kempf et al., 2005a). The upper panels display the percentage of spectra showing lines typical for alkali metals (a), ice (b), putative nitrogen compounds (c), and silicates (d) as function of time. The vertical bars indicate the uncertainty associated with counting statistics. From Kempf et al. (2005b).

analysis of a CDA Rhodium target sample shows that there are stochastically distributed tiny patches of Na and K impurities on the surface (see 2.3 and appendix B). These are roughly estimated to cover 20% of the target surface, probably more. Moreover, the surface contamination exhibits a correlation between the detection probabilities for Na^+ and for K^+. This implies that the greater part, if not all alkali metals stem from the target.

A remarkable finding is the presence of lines at approximately 115 amu and 131 amu,

which are heavier than the target material Rh (103 amu) by 12 amu, and 28 amu, respectively. Low energy impacts are known to often form target-projectile clusters built up of the target atom and of the most-abundant projectile atom or molecule (Knabe, 1983; Stübig, 2002). Even target-projectile compounds which are difficult to form such as $RhAl^+$ or $RhFe^+$ apppear in mass spectra produced in laboratory impact experiments (Stübig, 2002). Thus, target-projectile ions are indicators of prominent projectile substances provided the corresponding projectile ion shows up in the spectrum as well. At higher impact energies target-projectile ions are less likely to be formed and will produce only faint lines, if any. However, in the case of the - similarly high energy - impacts of Jovian stream particles Rhodium cluster ions, though at the verge of the detection limit, were present. There $RhNa^+$, RhS^+, $RhCl^+$ and RhC^+ could be identified (see 4.1). In Saturnian stream spectra an enlarged peak at 131 amu occurs if spectra with a clear 28 amu peak are co-added (see inset in Fig. 5.2). This implies that Silicon is a major particle component. The less frequent Fe^+ signatures seem to be an accompanying component of a rock forming mineral.

A peak at 115 amu which implies RhC^+ can be observed for all types of CDA data recorded in the Jovian system, the Saturnian System and in interplanetary space (see the respective chapters). This is likely to stem from the contamination also detected by TOF-SIMS analysis of the Rhodium target (see 2.3). Again, a C contribution from the particle can not be ruled out.

The water peaks of H_3O^+ and possibly H_2O^+, could in principle be target contamination as well since there is no indication for target-projectile ions as in the case of E ring particles (see 6.1). However, the H_3O^+ features are very faint and possible Rh-H_3O^+ features therefore might be hidden in the background noise. Furthermore, in order to prevent contamination by icy substances the CDA target is regularly heated up to over 90 °C. Thus, water ice - at least occasionally - might be a particle component. Alternatively, the 19 amu feature could be identified as F^+, which has found to be a possible contaminant of the Rhodium target by TOF-SIMS analysis (see 2.3).

Although a known contaminant (see 2.3), O^+ is likely to be of particle origin to a certain extent. With water ice and silicates as presumed particle components the O^+ ions are probably fragments of the respective parent molecules.

The presumed nitrogen type features are an even more difficult case. As mentioned in the previous chapter, it is currently not clear if the 18 amu peak can be attributed to NH_4^+ or H_2O^+. This is currently under investigation. If one rules out the contamination by combustion exhaust of the rocket engine (see 2.3), the weak and rare N^+ signature is likely to be of particle origin. But since the temperatures at the the given solar distances are too high for nitrogen ice it is probably a fragment ion of larger molecules.

In summary, only Silicon has been unambiguously identified as particle component.

5.2 Discussion

The likelihood of finding a line in an individual spectrum depends on the signal-to-noise ratio, which itself is related to the amount of plasma q_e generated by the impact. Fluctuations in the occurrence of the less abundant composition types (ice and nitrogen) correlate with periods during which only faint impacts were registered. However, the dominant silicate and alkali metal composition types show no pronounced time dependence (no variation with Saturnian distance). This suggests that the time dependence of the ice and nitrogen type is at least partially due to the data processing. Taking this into account, one can conclude that the source of the Saturnian stream particles needs to be fairly homogeneous. Particles originating from different locations within the A ring and E ring are made of similar material.

The preponderance of spectra with silicate lines and the significant $RhSi^+$ target-projectile feature suggest that the majority of the detected grains consists of a silicate material. If the water ice lines are not due to target contaminations or Fluorine then about a third of the silicate grains had ice mantles, whereas solid ice grains are rare. Due to the low occurrence and significance of the possible nitrogen type features no definite statement can be made. However, they indicate that Nitrogen might be a particle compound. Since solid N_2 ice can be disregarded, CN bonds or clathrate hydrates embedded in water ice would be the most likely form. As a consequence of C^+ and H^+ being an abundant target contaminant (see section 2.3), carbon and hydrogen can not be ruled out to be part of the elemental composition of Saturnian stream particles. The same in principle applies to Na^+ and K^+. However, since CDA is extremely sensitive to alkali metals the (generally tiny) features are only in agreement with a minor particle component.

The data do not provide clear evidence for solid ice grains smaller than about 10 nm. Furthermore, the homogeneity of the mass spectra data set implies that the composition at least of the particles smaller than approximately 10 nm is homogeneous as well. The reservoir of stream particles capable of escaping from the Saturnian system essentially consists of the silicate impurities from the ring material.

Saturn's main ring is thought to be primarily made of water ice, possibly containing clathrate hydrates of ammonia or methane and a minor amount of impurities – most probably iron-bearing silicate compounds (Esposito et al., 1984). E ring particles predominantly consist of water ice. Ring particles originating from the Enceladus plumes contain impurities – probably tiny inclusions made of a silicate or of an organic compound (see chapter 6). If the plume particle inclusions are silicates than the Enceladus plumes may be an important source of Saturnian stream particles. Since dust is subject to plasma sputtering in the aggressive environment of Saturn (Jurac et al., 1998) stream particles might be the remains of a once larger particle created below the surface of Enceladus. To answer the question whether the streams originating from the E ring are composed of silicates ejected by the Enceladus plumes may require advances in the theory of the Enceladus cryo-volcanism and the E ring particle dynamics as well as high-resolution mass spectra of plume particles.

It has to be pointed out that the vast majority of thousands of stream particle spectra recorded following the first orbit have not been evaluated yet. Together with ongoing studies of stream particle dynamics, this might allow for further findings regarding their sources.

Chapter 6

Populations of Saturn's E Ring

6.1 Results

The sections 6.1.1 to 6.1.6 deal exclusively with the dataset of the water rich main population of the E-ring (see 2.2.3). Section 6.1.7 contains the analysis of the dataset of the non-water population.

In all spectra shown in this chapter the spectrum amplitude is shown on a linear scale. The x-axis is, however, non-linear in time of flight and scales with the ion mass.

6.1.1 Appearance of Water in CDA TOF Mass Spectra

The vast majority of registered events are due to impacts of water ice particles. A good understanding of the appearance of this bulk material in our spectra is vital for the identification of particle impurities. The CDA spectra of water ice are typically dominated by cluster-peaks (Fig. 6.1) and are similar to spectra obtained in laboratory experiments (Timmerman, 1989; Timmermann and Grün, 1991). The size of the water clusters ($H(H_2O)_x^+$) in spectra can vary from $x = 1$ (no cluster formation) up to $x > 15$ (Fig. 6.1, Fig. 6.3). The relative amplitudes change as well - many showing an exponential decrease with increasing cluster length, others following an envelope; maxima generally varying from $x = 1$ to $x = 4$.

In some spectra a peak at the left flank of the far bigger Hydronium peak can be identified. This may be H_2O^+ at 18 amu as observed by Timmermann (1989), but it has to be noted that this signature, to an unknown extent, could be due to NH_4^+ with an identical molecular mass.

6.1.2 Clustering Mechanisms

Since the study of clustering phenomena is not within the scope of this work, only a brief introduction is given here. The clustering of water molecules after ionisation in the gas phase is a well investigated phenomenon (e.g. Shi et al. (1993), Wang et al. (2003)). The

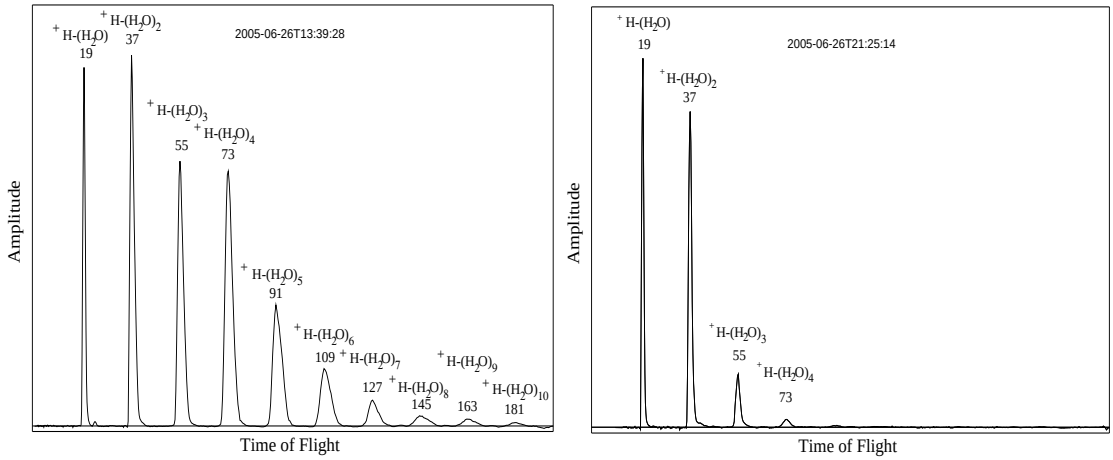

Figure 6.1: Examples of E-ring water ice spectra. All labelled peaks are due to ions formed from water molecules. The mass in atomic mass units (amu) is given below the molecular species. The Hydronium ion (H_3O^+) with a mass of 19 amu is followed by a sequence of cluster ions of the form (H-$(H_2O)_x{}^+$) with 18 amu gaps in between. Both impacts have similar total ion yields (QI amplitudes). Different impact conditions lead to a different appearance of water clusters - e.g. high energy densities preferably lead to short clusters (see section 3.2). The spectrum amplitude has been slightly smoothed.

only reliable investigation of water clustering inside impact plasmas is that by Timmermann (1989) and Timmermann and Grün (1991). These laboratory and our E-ring spectra are similar in appearance to those examined extensively with other ionisation methods (e.g. Shi et al. (1993), Wang et al. (2003)). Thus the clustering mechanisms seem to be comparable.

Within the initial impact cloud, neutral species are likely to be dominant: H_2O and to a minor extent H and O. However, ions are formed as well: basically H_2O^+, H^+ and OH^-. The negative species are removed, collected at the target and cannot be observed with the CDA (as mass spectra). From this initial mixture the formation of Hydronium ions (H_3O^+) occurs very rapidly - yielding an enthalpy of $\Delta H = 7.2\,\mathrm{eV}$ per molecule - before the plasma can be penetrated by the electric field (after about 10 - 100 ns). Within this time frame the energetic state of the molecule ensemble can be further optimised by clustering (Fig. 6.2). Since the energy gain from repeated clustering decreases, the process gets slower with increasing cluster size.

Clusters are formed when molecules interact and their relative kinetic energy is lower than the cluster energy. Thus the final size distribution of cluster ions depends on:

- the number density of ions, molecules and atoms in the plasma cloud
- the kinetic energy of species (temperature)
- the time interval before the plasma cloud is disrupted by the electric field

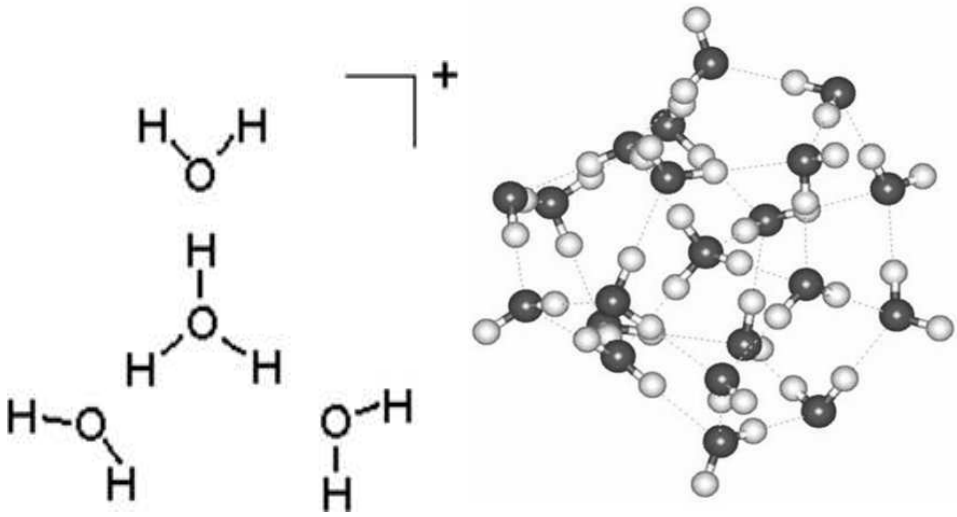

Figure 6.2: Neutral water molecules cluster with Hydronium ions. Oxygen - as the electron rich part of the water dipole - establishes a loose bond with the Hydrogen atoms of the neighboring molecule. In this way large cluster ions can be generated. (right figure from http://www.lsbu.ac.uk/water)

- the ion / neutrals ratio

In Fig. 6.3, a spectrum is shown where water molecules cluster with the target material Rhodium. This is one example of water molecules clustering with other species. The abundance of water molecules in the impact plasma and their strong dipole moments encourage the formation of clusters with any type of ions present.

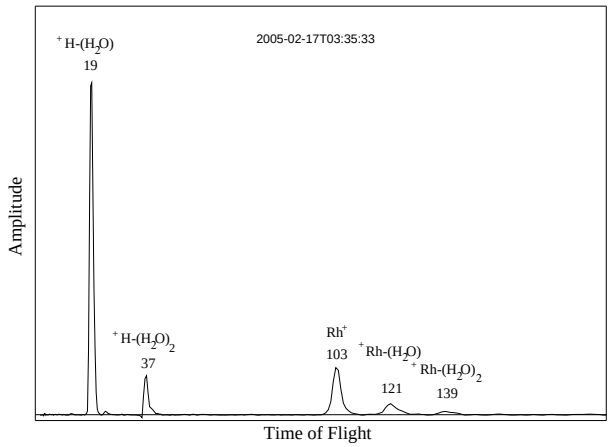

Figure 6.3: Example of a water ice spectrum with little water-water clustering. Neutral water molecules cluster with other ion species as well: At higher masses the target material Rhodium (103 amu) is apparent as Rh^+, with a target-projectile cluster of the form Rh-$(H_2O)^+$ (121 amu) and Rh-$(H_2O)_2{}^+$ (139 amu). The spectrum amplitudes have been slightly smoothed.

As well as with Rhodium, water clusters with the target contaminant Sodium are frequently observed when Sodium ions (Na^+) are present in great abundance within the plasma (see section 6.1.3). Thus a high Sodium peak is, in general, accompanied by distinct Sodium water cluster peaks at higher masses. There are - fortunately rare - examples where Sodium water clusters dominate the whole range of the spectrum (Fig. 6.4).

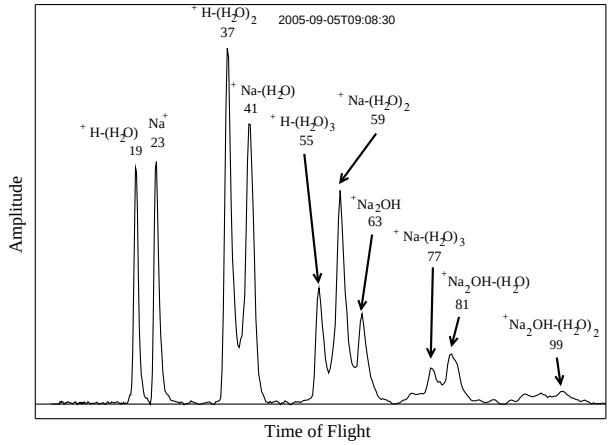

Figure 6.4: This spectrum shows peaks occurring due to Sodium ions clustering with water molecules. With a large enough proportion of Na^+ not only a species of the type Na-$(H_2O)_x{}^+$ is formed but also (Na_2OH)-$(H_2O)_x{}^+$. Sodium is a surface contaminant on the impact target and unlikely to play a role in the particle's composition. The spectrum amplitude has been slightly smoothed.

6.1.3 Non-Water Spectral Features in Water-Rich Spectra

In the water-rich E ring spectra obtained in the torus, a number of mostly small, non-water signatures show up occasionally (Fig. 6.5). Several of these features appear frequently at a specific TOF and these are described in this section.

The distinctive peaks of the alkali metals Sodium (23 amu) and Potassium (39 amu) can be identified in many spectra, although the latter may often be swamped with ions from the second water cluster (37 amu). Both species are likely to be due to the well investigated target contamination (see chapter 2.3 for details). Because of their very low ionisation energies, alkali metals show up in spectra each time the impact plasma affects one or more of the "alkali metal islands" on the target. The resulting increase in the observed alkali metal occurrence (found to be about 65% of the ring spectra) is in good agreement with numerical simulation based on the expected target contamination and the area affected by submicron impacts.

Other small peaks which are occasionally present are attributed to Hydrogen in the form of H^+, $H_2{}^+$ and $H_3{}^+$ (1, 2, 3 amu), and Carbon (12 amu). Both species are homogeneously distributed at, or slightly below, the entire target surface (see chapter 2.3). As a

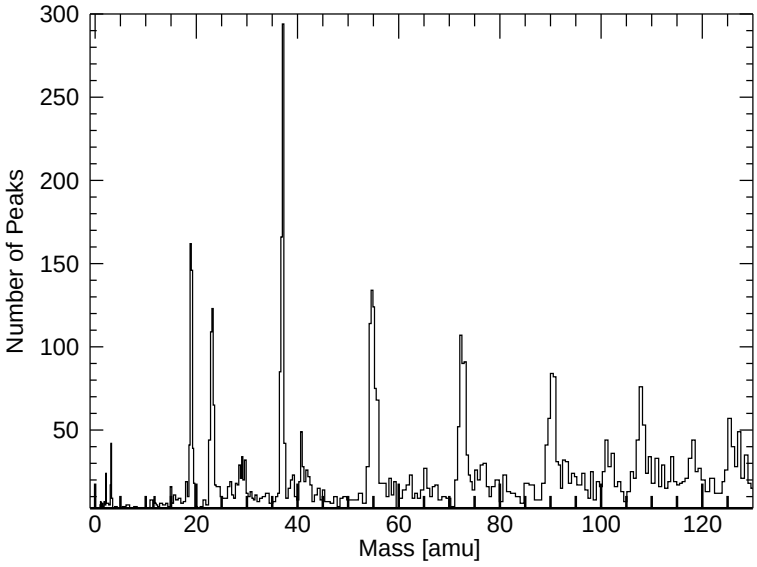

Figure 6.5: Histogram of peak maxima detected in a representative sample of 672 spectra obtained in the Enceladus torus. Many of the smaller impact signals have been triggered late by H_3O^+ ions (see section 2). Mass lines with m$\leq$ 19 amu are therefore under-represented.

consequence Carbon and Hydrogen ions can neither be excluded or confirmed to be of particle origin. In the hypervelocity (100–400 km s^{-1}) impacts of Jovian and Saturnian dust stream particles, Carbon and Hydrogen - which both have quite high ionisation energies (Table A.5) - were be observed in every spectrum. In the E ring spectra of water ice particles, C^+ and Hydrogen ion peaks reached the 2.5 σ detection limit each time the energy densities were high enough to ionise a sufficient amount of neutral species. Thus, the observed correlated appearance of C^+ and $H_x{}^+$ with water clusters of small size ((H-$(H_2O)_x{}^+$) with low x) is a plausible indicator for high energy densities.

At a position in the spectra corresponding to 15 amu or slightly higher, a small peak can occasionally be identified. It might represent $CH_3{}^+$(15 amu). A contribution from Oxygen ions (16 amu) which, typically for species which prefer to form negative ions, are known to appear "too early" (see chapter 4.1) is also possible. However, laboratory experiments (Timmerman, 1989; Stübig, 2002; Goldsworthy et al., 2003) indicate that the given impact speeds of 8-25 km s^{-1} are possibly not high enough for O^+ formation. In his laboratory experiments Timmermann (1989) only observed O^+ peaks at impact speeds above 30 km s^{-1} (also see 2.3.3). Thus $CH_3{}^+$, a fragment ion of organic compounds, appears to be more likely. If present, O^+ may be due to surface contamination or particle origin. This will be further discussed in section 6.2.

As previously discussed in section 6.1.1, an occasional peak at a time of flight corresponding to 18 amu can not only be interpreted as H_2O^+ but also as $NH_4{}^+$. Thus, the presence of the latter cannot be excluded. Statistical investigations are currently in progress to determine the likelihood of $NH_4{}^+$ in E ring spectra.

There is one obvious, frequently occurring larger spectral signature, which is not attributable to water-, target- or target contamination ions and their respective clusters. It mostly shows up as a broad, low peak with a maximum corresponding to a mass between 28 and 29.5 amu. With few exceptions, its amplitude is far below those of the dominant water peaks. Sometimes barely resolved small peaks in this mass region indicate that the broad feature actually represents several overlapping species. An analysis of peak-maxima positions for a couple of hundred distinct spectra with this signature reveals that there are indeed at least two or three mass lines present between a time of flight of 2.45 and 2.67 μs (26 - 31 amu) (Fig. 6.6). One mass line occurs at a TOF equivalent to about 27 amu and is distributed between 2.45 and 2.51 μs (26 - 27.5 amu). In most spectra, however, the signature peaks at between 2.54 and 2.61 μs (28 - 29.5 amu), which indicates at least one other species within this range. A third mass line might lie at about 30 amu. The whole resolved or unresolved complex, within a time of flight ranging from 2.45 to 2.67 μs, described in this paragraph, will be addressed henceforth as the "29 amu signature".

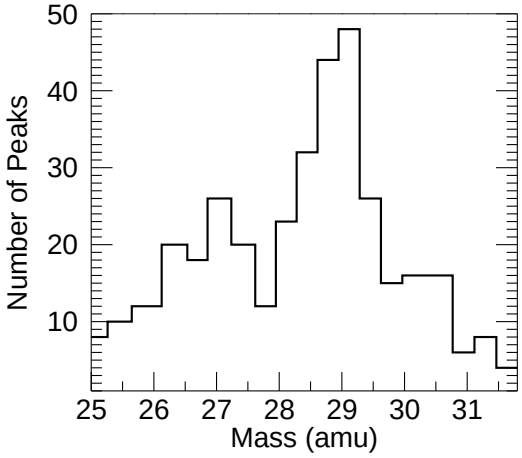

Figure 6.6: Distribution of peak maxima between 25 and 32 amu. Only uncompressed spectra with strong signals are considered here. At least two, probably more, mass lines are present between 26 and 31 amu.

Unfortunately there are many atomic and molecular ions which have compatible masses within this range. The obvious candidates are listed in Table 6.1.

A closer look at the plausibility of each of the candidates and the consequent implications for the particle composition will be given in sections 6.1.6 and 6.2. Other spectral features, that in general have a concomitant appearance with the 29 amu signature, will be discussed in section 6.1.5.

Table 6.1: Obvious candidates for ions forming the 29 amu signature

Ion Mass	Ion Species
26 amu	-
27 amu	Al^+, $C_2H_3{}^+$, HCN^+
28 amu	Si^+, CO^+, $N_2{}^+$
29 amu	$C_2H_5{}^+$
30 amu	$C\text{-}H_2O^+$
31 amu	$C\text{-}H_3O^+$, CH_3O^+*

*Methanol-like methoxy ion

6.1.4 Classification of Spectra

It is striking that in most cases the overall appearance of the spectra changes if a 29 amu signature is present (Figs. 6.7, 6.8 and 6.9). It seems to be the characterising peak for a whole class of spectra, which is defined in this section.

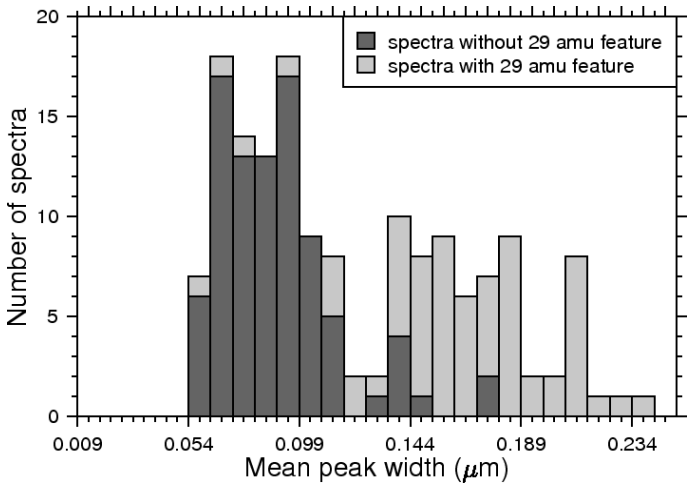

Figure 6.7: Bipolar distribution of peaks' mean width (FWHM). In most of the wide type spectra a 29 amu signature could be identified (light grey), while the narrow type mostly does not have a mass line there (dark grey). In contrast to a similar plot shown in Hillier et al. (2007), this sample of the first E ring crossing in late 2004 is restricted to a narrow regime of total ion yields.

An analysis of the mean peak width (the full width half maximum, FWHM) of all peaks in each spectrum from the first sample of E ring spectra collected in 2004, has already revealed a bipolar distribution of "wide and narrow type" spectra (Hillier et al., 2007b). This bipolarity becomes more pronounced when the influence of the "natural" peak broadening towards higher total ion yields is reduced (Fig. 6.7), by binning the sample over a series of impact charge ranges. Though this method is still subject to bias effects which tend to smooth out any contours in such a distribution, the bimodality is

apparent in each of those narrow "impact charge groups". About 85 % of the "wide type" spectra in a sample of intermediate impact charges show a 29 amu signature (Fig. 6.7). Furthermore the broadening of peaks is correlated with a substantial increase in "noisy" oscillations overlying the spectrum (Fig. 6.8). This cannot be interpreted as an increase of overall spectrum noise because the baseline in the low mass region of the spectrum shows the same low noise levels common in CDA spectra. Here maybe the particle structure (e.g. lower bulk density), morphology or impact characteristics affect the disintegration of the particle. This could lead to plasma conditions which favour interactions that result in peak broadening and the fuzzy appearance of those spectra at longer TOF.[1]

Pure water ice spectra hardly ever show such oscillations and wide peaks only appear at the highest total ion yields. Here Debye shielding and possibly delayed ionisation within the large impact plasma clouds may be responsible for the widening of peaks and this can be observed in all CDA mass spectra with increasing frequency at higher total ion yields.

Another typical difference between the two spectrum types is the pattern of the water cluster peaks (Figs. 6.8 and 6.9). While in pure water ice spectra the highest signature is usually the hydronium peak at 19 amu, the probability of the second or third water cluster peak (37 or 55 amu) being the most abundant is increased in spectra showing a 29 amu signature.

As is shown in 6.1.5, several other common as well as 'exotic' unidentified peaks accompany a 29 amu signature. Together with broad peaks and large amplitude oscillations these characteristics (Figs. 6.8 and 6.9) imply that rather complex chemistry is present in the impact plasma.

Definition:

From our initial examination of the spectra two main types of water ice spectra are identified: without (henceforth Type I) and with a 29 amu signature (henceforth Type II)[2]. Type I spectra show hardly any traces of ions other than the E ring bulk material - water, and occasionally target or target contamination. In contrast, Type II spectra exhibit a significant contribution from other particle components and, as for Type I, sometimes signatures of the target or known target contaminants.

[1] Another interpretation could be many tiny barely resolved mass lines which appear as oscillations of the spectrum amplitude (see 6.1.6).

[2] Many of the exceptions where a spectrum of narrow peaks appear together with a peak between 26 and 31 amu don't show the usual broad feature here, but only a narrow peak between 30 and 31 amu. From this it is deduced that the Carbon water clusters (C-H_2O^+ and/or C-H_3O^+ see Table 6.1) forming that peak are mostly not linked to the water peak broadening. Therefore spectra with a single narrow peak in the range of 30 and 31 amu are not considered to be Type II spectra.

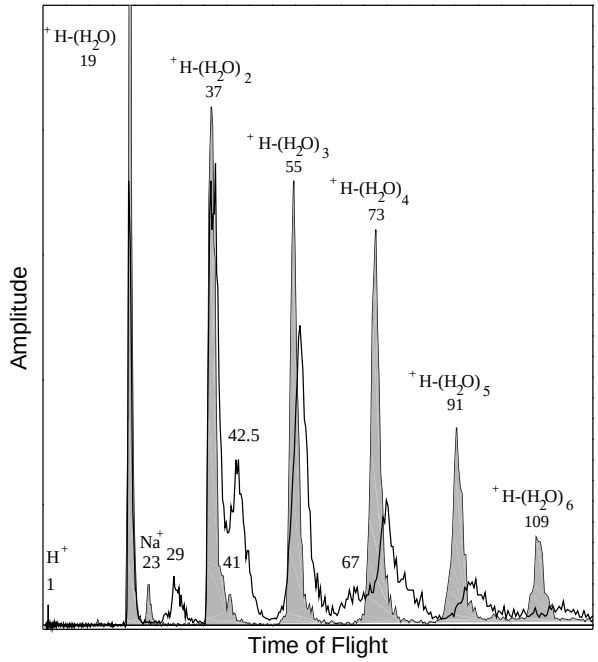

Figure 6.8: Comparison between a Type I (grey) and a Type II (bright) spectrum. The only non-water features observed in Type I spectra are due to target material (Rh) or known target contaminants. Here Hydrogen (1 amu), Sodium (23 amu) and its first water cluster Na-H_2O^+ (41 amu) are clearly visible. Apart from the defining multiple-component peak at 29 amu, Type II spectra often show another wide feature peaking between 42 and 43 amu and a bulge at a time of flight corresponding to 65–68 amu. The FWHM of Type II peaks are wider and in the second half of the spectrum "noisy" oscillations with amplitudes far above the baseline noise level can be observed. While the first two water peaks (19 and 37 amu) are at identical positions in both spectra, there is an increasing shift towards longer times of flight for the larger water clusters in the Type II spectrum.

6.1.5 Statistics and Correlations

To aid the identification of species forming the 29 amu signature and help interpret Type II spectra, it is helpful to look for coincident features. The most obvious coincidence is within the 29 amu peak itself. Its extent indicates the presence of at least two ion species with masses between 27 and 29 amu. But there are other peaks - mostly small or quite broad - as well as other spectrum characteristics correlated with this feature (Figs. 6.8, 6.9, 6.10 and Table 6.2).

Small features may seem to correlate simply because they are not likely to be found in faint or compressed spectra. To reduce this effect only uncompressed spectra with a total ion yield of over 90 000 ions for the statistics in Fig. 6.10 and Table 6.2 are used. Above this level even small features become statistically (at the 2.5σ level) significant above the noise amplitude. Furthermore, at high ion yields the impact is normally triggered by the impact signal (see 2.1) and therefore unknown selection effects are reduced. To increase the statistical significance further, the reproducibility of the features (repet-

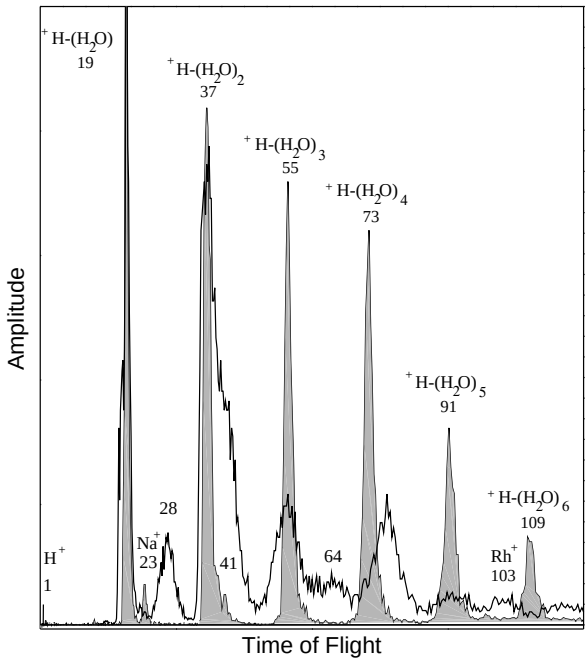

Figure 6.9: The same Type I spectrum (grey) as in Fig. 6.8 with a different typical Type II spectrum (white). Here, the widening of peaks in Type II is even more apparent. The species with a mass of about 42 amu is not resolved any more. The bulge between the third and fourth water clusters is present, although at slightly shorter TOF than in Fig. 6.8. Here, the typical case is shown where only the H-$(H_2O)_4{}^+$ cluster (F6) seems to be shifted, while the other water cluster peaks appear at the same times as in Type I. In this example the largest water cluster of the Type II spectrum is H-$(H_2O)_2{}^+$; the spectrum shows a Rhodium signature and a mass line at 18 amu directly in front of the Hydronium peak. Note: In contrast to Fig. 6.1 - 6.4, the spectra shown here are raw data and have not been subject to any smoothing.

itive occurrence) over a large set of E ring spectra is considered. For this purpose data from outside Enceladus' torus was also considered. Thus, the statistical significance of the features (Fx) attributed below (Fig. 6.10, Table 6.2) is above 99 % .

The attribution of typical Type II signatures, "Fx", (Table 6.2) becomes even more pronounced if only spectra with large 29 amu signatures are taken into account. F6 and F8 mostly appear "instead of" and not "together with" the adjacent water cluster peak. This is reflected by the reduced occurrence of H-$(H_2O)_4$ and H-$(H_2O)_5$ in Type II spectra. Thus F6 and F8 could be seen as water cluster features shifted towards longer TOF (Fig. 6.8 and 6.9). F6 and F8 are exemplary cases for all larger water cluster (H-$(H_2O)_4$ and higher) peaks, where this phenomenon is frequent. F6 is particularly striking, since in many Type II spectra it appears as the only shifted water cluster (see Fig. 6.9). In contrast F1, F2, F3, F5, and F7 appear as additional peaks. F4 is a special case. It is sometimes clearly separated from the second water peak (Fig. 6.8), while other times it seems to merge with it (Fig. 6.9). In rare cases F4 even appears to dominate H-$(H_2O)_2$, which leads to an apparent shift of the 37 amu water peak towards higher masses. Whether this

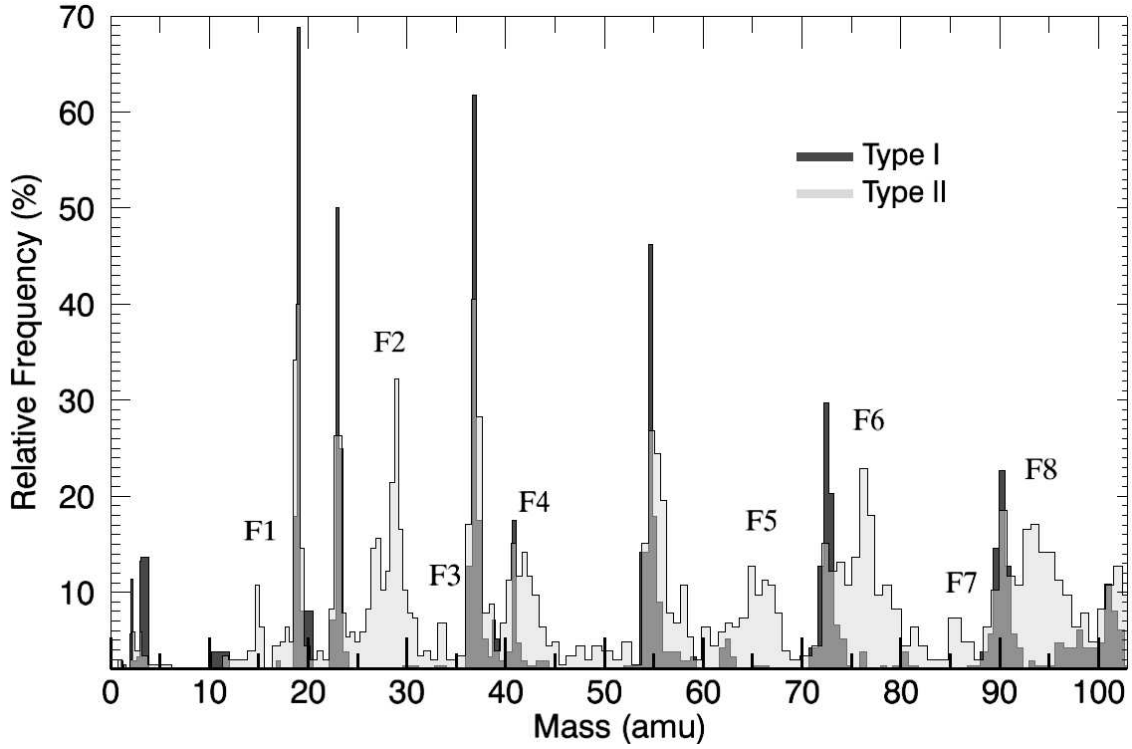

Figure 6.10: Occurrence of peak positions for Type I (dark grey) and Type II (light grey) spectra. The y-axis is relative to all spectra of the respective spectrum type. The typical Type II spectrum features are labeled (Fx). The histogram is extensively discussed in the text.

is also the mechanism which leads to the shifting phenomenon observed with F6 and F8 is currently unclear. It has to be pointed out that F4 (42-43 amu) is not a slightly shifted Sodium cluster Na-H_2O (41 amu), which is also present in Type I spectra (Fig. 6.10, Table 6.2). While Na-H_2O correlates - qualitatively and quantitatively - with Na^+, F4 does not and often appears in spectra in which no Sodium ions are present (e.g. the Type II spectrum in Fig. 6.8).

Though rare, F1, F3 and in most cases F7 are well-defined narrow peaks. In contrast, all other "Fx" features are broader and could consist of multiple mass lines. This is especially evident for F5, the peak with the widest FWHM of all regularly appearing spectral features.

Possible candidates for F1 - F8 are discussed in 6.1.6.

Type II spectra have been detected in abundance everywhere in the E ring: From $3\,R_S$ to outside Rhea's orbit ($8.7\,R_s$), both within and far above (or below) the ringplane. The occurrence of Type II spectra varies little between different ring plane crossings. Between 20 % and 80 % of spectra show particle impurities with a slightly increasing probability

Table 6.2: Appearance of selected features in E ring spectra. All unnamed features (Fx) are much more frequent in Type II spectra. The spectra considered are identical to those used for Fig. 6.10. The total number of spectra in the sample is 417 of which 205 (48.5 %) are of Type II. The total number of mass lines in all Type II spectra is 4270 and 2736 in Type I (ratio 1.6 : 1). The percentages given, refer to the distribution of the respective feature between Type I and Type II spectra (sum of both values is always 100%).

Feature	TOF [μs]	Mass range [amu]	Total #	Type II spectra	Type I spectra	Ratio T II : T I
Hydrogen	0.45-0.86	0.9-3.2	110	36 (33 %)	74 (67 %)	0.49 : 1
Carbon	1.59-1.70	11.0-12.5	33	15 (45 %)	18 (55 %)	0.83 : 1
F1	1.84-1.89	14.8-15.5	41	38 (93 %)	3 (7 %)	12.7 : 1
Sodium	2.27-2.33	22.4-23.6	280	108 (39 %)	172 (61 %)	0.63 : 1
F2	2.45-2.67	26.0-31.0	209	205 (98 %)	4 (2 %)	50 : 1
F3	2.72-2.80	32.1-34.0	27	23 (85 %)	4 (15 %)	5.8 : 1
Na-(H_2O)	3.06-3.09	40.6-41.4	90	44 (49 %)	46 (51 %)	0.96 : 1
F4	3.09-3.17	41.5-43.5	84	74 (88 %)	10 (12 %)	7.4 : 1
F5	3.84-3.96	64.0-68.0	126	103 (82 %)	23 (18 %)	7.9 : 1
H-(H_2O)$_4$	4.04-4.12	71.0-74.0	230	74 (32 %)	156 (68 %)	0.47 : 1
F6	4.16-4.24	75.0-78.0	135	116 (86 %)	19 (14 %)	6.1 : 1
F7	4.40-4.48	84.0-87.0	30	25 (83 %)	5 (17 %)	5 : 1
H-(H_2O)$_5$	4.53-4.60	89.0-92.0	229	97 (42 %)	132 (58 %)	0.73 : 1
F8	4.40-4.48	93.0-96.0	138	113 (82 %)	25 (18 %)	4.5 : 1
Rhodium	4.80-4.90	100-104	142	74 (52 %)	68 (48 %)	1.09 : 1

Note: Because of the exception in the definition of Type II spectra (see footnote in 6.1.4), F2, on rare occasions, can be found in Type I spectra as well.

with higher total ion yields[3]. A more detailed analysis of the spatial distribution of both types within the Saturnian ring system, using a bigger data ensemble is a high priority for future work.

6.1.6 Type II Spectra

Type II spectra exhibit a significant contribution from non-water particle components. In this section it is evaluated which ion species can be assigned to the 29 amu signature and other possible non-water features in those spectra. This is done without making any assumptions about their physical origin. The compositional implications of Enceladus' plumes as a source are taken into account in the discussion section.

[3]However, during ring plane crossings, the transmission bandwidth only allows the transmission of data from a selection of impact events (see section 1). Therefore it is noted that the returned dataset might be prone to unknown - though probably not very significant - bias effects. A more precise evaluation of the spatial occurrence of Type II spectra in the E ring is in progress.

The 29 amu signature is likely to be formed by the superposition of at least two or three mass lines (Fig. 6.6). A list of appropriate ions is given in Table 6.1.

Carbon water clusters C-H_2O^+ and/or C-H_3O^+ form ions between 30 and 31 amu. In some rare cases a single peak not embedded in a wider 29 amu signature appears in the 30–31 amu region (see footnote 6.1.4). This peak is correlated with a C^+ signature (12 amu), which implies that the respective mass line(s) is (are) indeed due to Carbon water clusters. The Carbon in the cluster probably originates from the known Carbon contamination which covers the whole target homogeneously (see 2.3). CH_3O^+ can not only be interpreted as a Carbon water cluster but also as a Methoxy ion, an ion fragment of alcohols. It is possible that this species is sometimes present within the 29 amu signature broadening it towards longer TOF.

This leaves at least two further species between 26 and 29 amu which appear conjointly and form the majority of ions within the 29 amu signature. Most of the peak maxima contributing to the 29 amu signature are distributed between a TOF corresponding to 28.5 and 29 amu (Fig. 6.6) with an average of 28.8 amu. Nonetheless, there are reasons to justify the consideration of 28 amu ions, too. The mass calibration is done with the early water peaks. A small relative shift of the other mass lines is not unreasonable and has been observed on several other occasions in CDA mass spectra (Stübig, 2002; Postberg et al., 2006; Hillier et al., 2007a). The other plausible possibility is the hydrogenation of 28 amu species. In principle all 28 amu candidates (Si^+, CO^+, $N_2{}^+$) form protonated cluster ions (SiH^+, COH^+, N_2H^+ or even $XH_2{}^+$ and $XH_3{}^+$) if there is sufficient Hydrogen. The ratio of hydrogenated species strongly depends on the amount of Hydrogen present. With water as the bulk material of the particles, Hydrogen is an abundant constituent of the impact cloud[4]. Furthermore, the Rhodium target is another Hydrogen source (see 2.3).

The ionisation energies, and to some extent their electron affinities (Table A.5), are key parameters for the relative cation yields (Kissel and Krüger, 1987). They are an important indicator for the formation and recombination probability of ions and electrons inside the impact plasma before they can be accelerated by the external electric field. The relative abundance of cations for a given energy density decreases exponentially with increasing ionisation energy (Krueger, 1996).

Carbon oxide and Nitrogen compounds

On the first glance conjointly appearing $N_2{}^+$ and HCN^+ seem to be a pair of ions which could explain the 29 amu signature. However, molecular Nitrogen has a substantial higher ionisation energy than water and Hydrogen (Table A.5). Furthermore, the ionisation energy far exceeds the dissociation energy of the N_2 molecule ($D_0(N_2) = 9.8$ eV). Thus the appearance of N_2 as positive ions in CDA mass spectra is highly improbable. The formation of N_2H^+ would be a more energetically favorable ionisation path than direct

[4]Together with ions (H^+), one can expect neutral molecules (H_2) and neutral elemental radicals (H·), probably the most abundant water breakup product for the given energy regime.

ionisation. But this would require the presence of enough H^+ ions for an abundant charge transfer to a cluster ion. Since only occasionally the presence of H^+ ions is observed, which do not correlate with the appearance of the 29 amu signature, this is an unlikely mechanism. Similarly the high ionisation potential of HCN also does not favour abundant cation formation.

CO^+ and COH^+ are other species which could be responsible for the majority of ions forming the 29 amu signature. The ionisation energy again does not favour the formation of CO^+, although it is not as extreme as for the case of N_2. On one hand, the correlation with a small signature which can be attributed to O^+ (F1) is as expected. On the other hand, C^+ would be expected to correlate as well, which is not the case (Table 6.2). As with N_2, it would furthermore be difficult to explain the other typical Type II peaks[5]. Carbon dioxide ions (CO_2, 44 amu) might contribute a little to the right flank of F4, but probably do not play a major role either.

The probability of Carbon oxides and inorganic Nitrogen compounds being an important impurity observed in E ring particle spectra is very low. Nevertheless, the presence of CO or HCN in particlular as minor constituents, cannot be excluded.

Organic compounds

The simplest interpretation of the 29 amu feature is as unresolved mass lines of Vinyl- or Ethyl radical ions $(C_2H_3)^+$ (27 amu), $(C_2H_5)^+$ (29 amu) and maybe $(C_2H_4)^+$ (28 amu) as the sought-after ions[6]. These probable breakup fragments of larger hydrocarbons, with quite low ionisation energies (≈ 8.5 eV), would perfectly explain the two or more species between 27 and 29 amu. The assumption seems tempting that those organic molecules are of the same origin as the occasionally observed Carbon ions, which are probably due to an homogeneous target contamination (see 2.3). However, this is unlikely for several reasons. (1) There is clearly no correlation between the occurrence of Carbon ions and the 29 amu signature (Table 6.2). (2) A target coverage of organic material would release vinyl- or ethyl-like ions on every impact which produced a sufficiently high energy density. The release of Hydrogen and Carbon cations are a good example for this threshold effect. In contrast to those ions, there is no indication that impacts leading to a 29 amu signature are subject to a special energy density regime. The irregular (in this regard) occurrence of the feature is not in agreement with homogeneously distributed organic contamination.

If $C_2H_3{}^+$ and $C_2H_5{}^+$ play a role, they are likely to be of particle origin. Considering the impact velocities, which are in general above 8 km s^{-1} (Kempf et al., 2007), it

[5]With the exception of F5, which could be a water cluster of the form CO-$(H_2O)_2{}^+$ or COH-$(H_2O)_2{}^+$, respectively N_2H-$(H_2O)_2{}^+$, none of the other frequent signatures in Type II spectra can be linked to Carbon oxides or obvious inorganic Nitrogen species.

[6]For linear hydrocarbons ion species with odd numbers of H atoms are always more abundant (as can be seen in Fig. 6.11).

is unlikely that many large hydrocarbon fragments survive (Srama & Woiwode, 2006, personal communications; Goldsworthy et al., 2003). Larger organic molecules are disrupted into smaller C_xH_y fragments, with x and y depending on the impact conditions and the organic substances. CDA calibration experiments with polystyrene particles yielded unsaturated hydrocarbon fragment ions dominating the spectrum at speeds below 17 km s^{-1} (Goldsworthy et al., 2003). Recent laboratory experiments with two types of aromatic long-chain hydrocarbon projectiles (Srama & Woiwode, 2006, personal communications), demonstrated that for certain impact speeds the most abundant resulting positive ions are C_2 and C_3 species of the form $C_2H_3^+$ (27 amu) and $C_2H_5^+$ (29 amu), and $C_3H_5^+$ (41 amu) and $C_3H_7^+$ (43 amu) respectively (see Fig 6.11). The C_2 species can

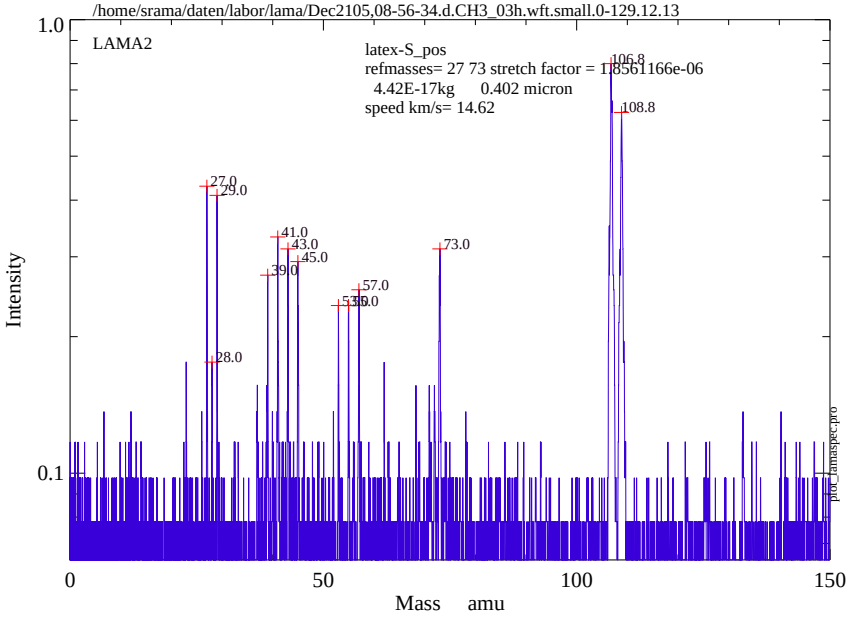

Figure 6.11: High resolution positive ion spectrum of an organic particle impact obtained in the laboratory. The particle consists of an aromatic polymer (Poly-[bis(4-vinylthiophenyl)sulfide]) 0.4 μm in size. The impact speed was 14.6 km s^{-1}. The large organic molecules decompose to only three major positively charged impact fragment groups: 27+29 amu, 41+43+45 amu and 53+55+57 amu which represent C_2H_x, C_3H_x and C_4H_x breakup ions of the aromatic structure. These signatures are in good agreement with the major non-water components observed in Type II spectra. The C_4 component would be hidden by dominant water cluster signatures. The peaks at 107 and 109 amu are ions of the target material silver, the peaks at 23, 39 and 73 amu are due to contamination.

be attributed as the main constituents of the 29 amu signature (F2) and the correlating F4 feature could be attributed to the expected propyl analogues, with $C_3H_7^+$ being the dominant species[7]. The observed correlation with a mass line at about 15 amu could imply

[7]It is known from laboratory experiments (Stübig, 2002; Goldsworthy et al., 2003; Srama & Woiwode, 2006, personal communications) that, of the possible fragments of aromatic polymers, $C_2H_3^+$ (27 amu) is the most abundant ion of the C_2 species in many cases. In contrast, our results (Fig. 6.6) would indi-

CH_3^+ as another smaller hydrocarbon fragment also known from laboratory experiments.

There are few candidates for F3, which must be the signature of an ion species with a mass of about 33 amu. Since there is no atomic ion of that mass, molecular or cluster ions have to be considered, of which CH_3-H_2O (33 amu) is the most probable when considering organic species. F5 is in agreement with C_5H_x organic fragment ions also observed in the laboratory (Srama & Woiwode, 2006, personal communications). The "missing" C_4 fragment is expected at about 55 amu and would therefore be hidden by water ions. F5 can also be interpreted as a water cluster, in this case of the 29 amu signature ions with two water molecules (65 amu). F6 and F7 can again be attributed to larger - purely organic - cluster ions known from laboratory experiments. However, this to be treated with reservation, since in principle every atomic mass above 50 amu can be assigned to an organic ion fragment or cluster ion, especially when hetero atoms like N, O or S are considered. Nevertheless, the pattern of non-water species observed in Type II spectra matches the results of high resolution accelerator experiments with organic projectiles (Srama & Woiwode, 2006, personal communications) surprisingly well (see Fig. 6.11).

The nature of F6 and F8, which are good examples of the possible shift of larger water peaks towards longer TOF (see Fig. 6.8), cannot be as easily explained with organic material. Of course one could think of certain organic cluster species with the required masses, but that would not justify the "replacement" of the adjacent water cluster peak. A more plausible explanation would be to assume a matrix effect (reflecting the interaction of different molecular or atomic species after impact). This sometimes seems to cause a delayed release of large water cluster ions from the impact plasma. However, this is implausible in cases where this shift applies to F6 but does not occur with ions of the target material rhodium and other large water clusters (Fig. 6.9). Thus, at least for the latter type of spectra a general plasma shielding effect as the exclusive reason for water peak shifting can be ruled out.

There are two more characteristics in Type II spectra that are in good agreement with organic ions: (1) The strong oscillations in Type II spectra typically start at a time of flight equivalent to about 25-50 amu and continue up to the end of the spectrum recording at about 200 amu. The low mass part of the spectrum only shows the noise oscillations common for CDA spectra. (2) The same applies to the peak broadening: In contrast to the rest of the spectrum, the low mass part (at least up to the H_3O^+ peak) usually shows narrow features (Fig. 6.8 and 6.9). Both observations are in agreement with unresolved multiple mass line spectra typical for complex organic materials (Stübig, 2002).

We conclude that many effects frequently occurring in Type II spectra are in good agreement with organic impurities embedded in water ice particles.

cate $C_2H_5^+$ (29 amu) to be the dominant ion. However, impact ionisation spectra of other than aromatic polymers have not yet been experimentally investigated.

Silicates

Cations of Silicon are also good candidates for the 29 amu feature. In contrast to N_2 and CO, the relatively low ionisation potential favours the abundant formation of positive ions in a water environment, even with only traces of Si present[8]. In addition Si^+ is known to hydrogenate with neutral H species even at low Hydrogen concentrations (e.g. Tardy et al. (1981)), which would explain the shift of the peak towards 29 amu due to SiH^+. Other hydrogenated species ($SiH_2{}^+$ and/or $SiH_3{}^+$ (Tardy et al., 1981)) could be responsible for further peak broadening towards higher masses. Note that in contrast to e.g. N_2 the formation of hydrogenated ions occurs not only with H^+, but with more abundant neutral hydrogen species as well. Silicate fragment ions SiO^+ (44 amu) could be a minor contributor to the right flank of F4.

Since pure quartz (SiO_2) is quite rare, Si cations would most probably originate from metal bearing Silicate minerals. The most abundant metals generally present in minerals are Magnesium and Iron followed by Calcium and Aluminium. Despite their ionisation energies being lower than that of Silicon, none of these species has a regularly appearing distinct elemental mass line in the E ring spectra. Recent high resolution impact ionisation experiments indicate that - in contrast to silicon ions - in many minerals the formation of atomic metal ions is suppressed (Mocker, 2006, personal communications). This might be due to matrix effects, but a total absence of metal mass lines seems to be unlikely. However, though subtle, in most cases signatures which can be attributed to metals were identified, as will be explained in the following.

Al^+ can be assigned to the observed 27 amu mass line broadening the 29 amu signature to the left. In some cases two matching peaks are resolved. Its low abundance in comparison to Silicon could be explained by an Aluminium-poor mineral. But in contrast to Aluminium, many minerals like Olivine and Pyroxene are expected to be Magnesium-rich. In rare cases, small mass lines which are in agreement with Mg^+ (24 amu) can be observed accompanying the 29 amu signature. Of course this observation alone is not sufficient to indicate Mg-rich silicates. However, the positions of the correlating signatures F4, F6, F8 are in good agreement with Magnesium water clusters Mg-$(H_2O)^+$ (42 amu), Mg-$(H_2O)_3{}^+$ (78 amu) and Mg-$(H_2O)_4{}^+$ (96 amu). This matches the relatively high cluster energy liberated when forming such clusters ($Mg^+ + (H_2O) \rightarrow$ Mg-$(H_2O)^+ + 1.3$ eV, compared to: $Na^+ + (H_2O) \rightarrow$ Na-$(H_2O)^+ + 0.9$ eV). Thus, the tendency of Magnesium ions to "hide" in water clusters could be justified. Iron, the other expected abundant metal in minerals, would be masked: With water clusters dominating the spectra, the presence of minor contributions of Fe^+ (56 amu) and its water clusters can never be detected with the CDA due to the generally large overlying H-$(H_2O)_3{}^+$ feature (55 amu). A similar

[8]Because of the strong bonds within minerals, the direct formation of Si^+ from silicates requires more than just the ionisation energy of Silicon (8.2 eV). The more probable mechanism here is a two step ionisation. After an impact the particle will be totally vapourised and silicon from possible mineral compounds will likely be present in the form of SiO (Atterer, 1959). Through collisions with fast components of the impact plasma, a fraction of the SiO is partly dissociated (D_0 (SiO) = 7.8 eV). In a subsequent step the ionisation of neutral Si occurs. Since the ionisation energy of SiO (11.5 eV) is above its dissociation energy, SiO will always yield a small fraction of Si^+ in an environment of sufficient energy density.

problem is found with possible Calcium peaks and the dominant H-$(H_2O)_2^+$ signature (37 amu). As in the case of Magnesium, a Ca^+ (40 amu) line, as well as its water clusters, could be responsible for the observed peak broadening and shifting of pure water clusters.

F3 cannot be attributed to a metallic silicate species. Its rare occurrence and general low abundance characterises it as a rather subordinate feature. The most plausible inorganic ion is hydrogenated Sulfur, SH^+, which would indicate occasional traces of Sulfur in the mineral. F5 and F7 more or less match clusters of Silicon with two and three water molecules respectively, and F1 can be attributed to O^+ as an expected minor mass line accompanying silicates at high energy densities.

The identification of F6 and F8 with Mg-$(H_2O)_3^+$ (78 amu) and Mg-$(H_2O)_4^+$ (96 amu) could explain the putative shift of respective pure water clusters: at large masses neutral water molecules clustering with Hydronium ions and with - 5 amu heavier - Magnesium ions would create two overlying, unresolved broad peaks with the maximum shifted between the two extreme cases. If this assumption is true, the statistics of Type II spectra imply very abundant Mg^+ in the impact plasma. Due to the much lower ionisation potential of Magnesium compared to water, this however might be plausible even with minor silicate impurities.

In addition to the very rare occurrence of Mg^+- compatible peaks, this coherent picture is somewhat spoiled by the fact that there is hardly any indication of a cluster of the form Mg-$(H_2O)_2^+$ (60 amu). Considering the presence of the smaller and bigger Magnesium water clusters, it is presently unclear why this cluster in particular should be suppressed. The same applies in principle to the observation of possible Si-$(H_2O)_2^+$ (F5) without an apparent signature of Si-$(H_2O)^+$ (46 amu). Nevertheless, all frequent peaks in Type II spectra can be explained satisfactorily.
Besides organic compounds, silicate minerals are another plausible source of non-water cations in Type II spectra.

6.1.7 Type III Spectra

Identification of ion species

A histogram of the peak frequency of the dataset is given in Fig. 6.12. All spectra of the dataset are co-added to produce the spectrum shown in Fig. 6.13. The former gives a good impression of the occurrence, the latter of the ion abundance, of the signatures. All relevant signatures are summarised in Table 6.3.
All Type III spectra show the mass lines of Hydrogen[9] (H^+, H_2^+) Carbon, Rhodium, and a species which is at flight times equivalent to about 56 amu. Often the latter is the largest feature of the spectrum and - given the high energy densities indicated by the abundance of H^+ and C^+ - it is unlikely to be a molecular or cluster species. This clearly hints at iron

[9] or are triggered by H^+.

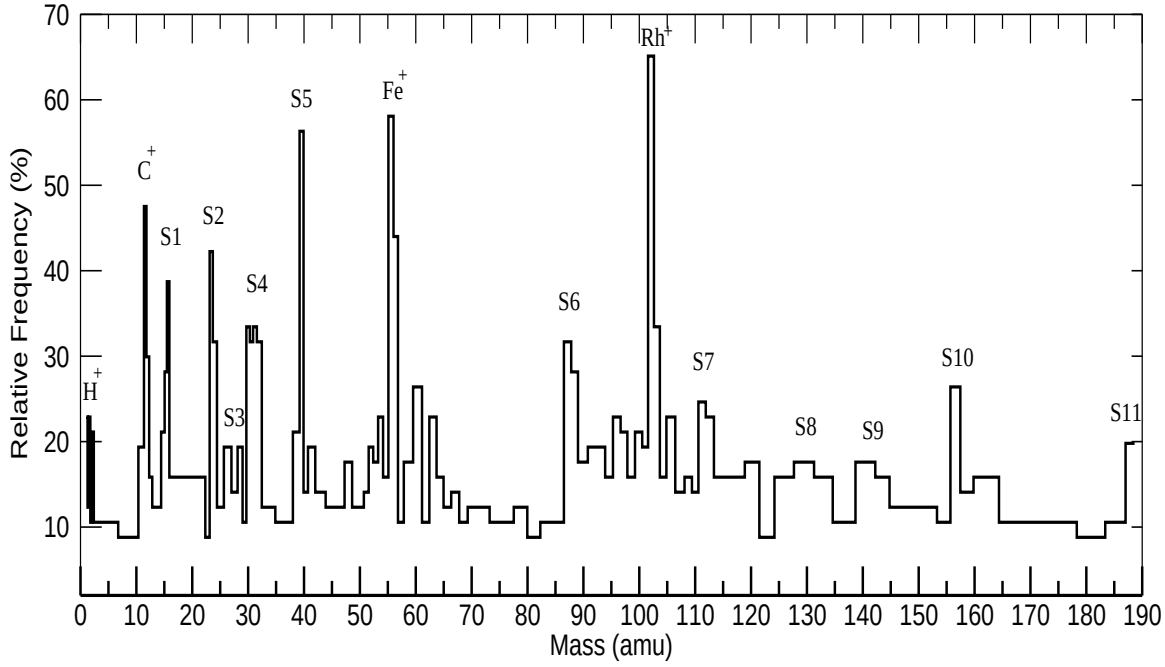

Figure 6.12: Occurrence of peak positions for Type III spectra. Possible ion species for all non attributed signatures (Sx) are given in Table 6.3 an are extensively discussed in the text. Many of the smaller impact signals have been triggered late by H^+ ions. Hydrogen mass lines are therefore under-represented.

ions as the origin of the 56 amu feature, which is confirmed by the occasional observation of a conjoint minor peak at 54 amu in good agreement with the expected isotopic ratio of iron (56 amu: 92%; 54 amu: 6%) (see Fig. 6.14). Since the separation of iron isotopes is at the limit of the instrument capabilities, it is no surprise that this can be achieved only in some spectra with optimal peak definition[10].

Other abundant mass lines which are mostly present occur at flight times corresponding to 14.5–16 amu (S1), 23–24.5 amu (S2), 30–32 amu (S4), and 39–40.5 amu (S5). Further frequent peaks of lower amplitude can be found at flight times equivalent to 86–89 amu (S6), 110–113 amu (S7), 156–158 amu (S10) and less frequently at 26.5–28.5 amu (S3), 125–128 amu (S8), 141–144 amu (S9) and 186–190 amu (S11).

The only plausible candidate for S1 is O^+. The mass line is often shifted towards lower TOF, an observation known from laboratory (Stübig, 2002) and space (4.1.2). The shifting strongly depends on the QI-amplitude: At a low total ion yield the position of the peak is nearly as expected for O^+ (1.192 μs $\sim$ 16 amu), with an ever increasing shift towards lower TOF as the QI-amplitude increases (Fig. 6.17). Sometimes an accompanying

[10]In fact, an unambiguous iron isotope separation is not reported from CDA calibration experiments, which demonstrates the extraordinary good peak definition (and thus mass resolution) of some Type III spectra.

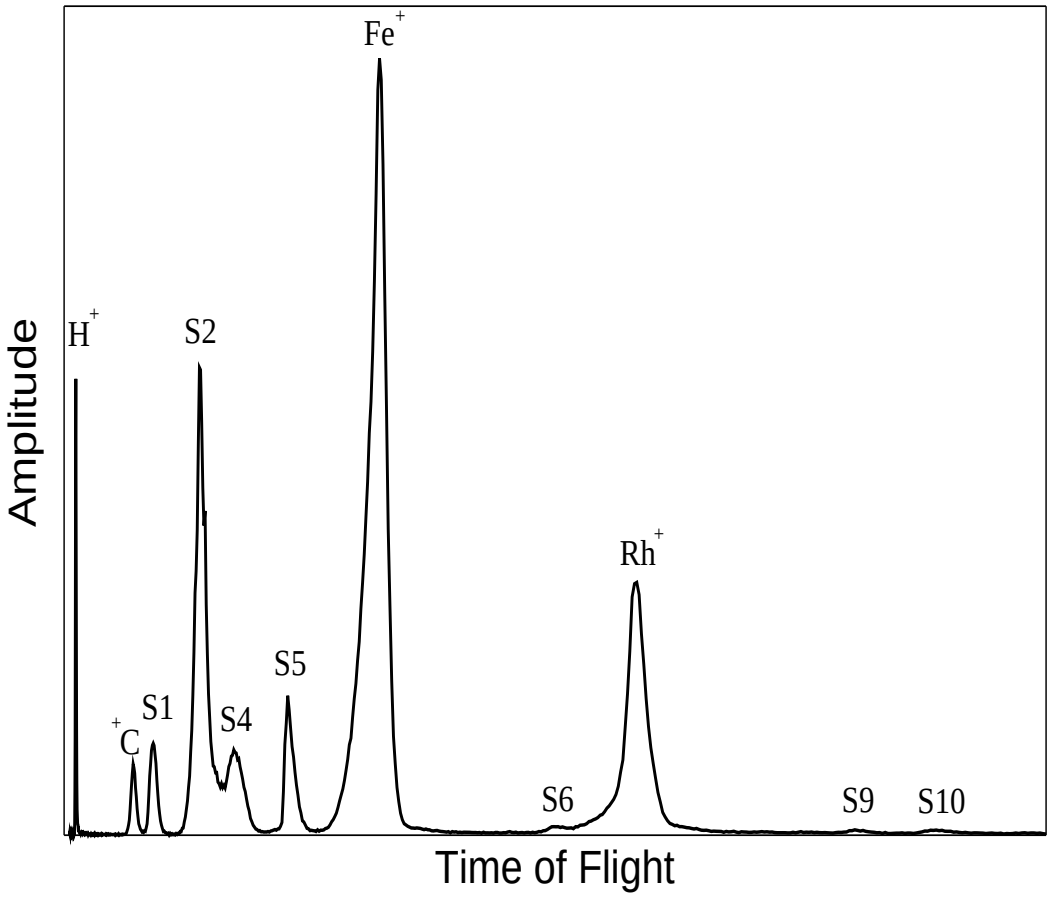

Figure 6.13: Co-added spectrum of all 57 spectra used for the Type III spectra analysis. Possible ion species for all unassigned signatures (Sx) are given in Table 6.3 and are extensively discussed in the text. Many of the smaller impact signals have been triggered late by H^+ ions. Hydrogen mass lines are therefore under-represented. Some signatures visible in Fig. 6.12 can not be seen here: S3 and S8 are "swamped" by larger neighbouring signatures, whereas the amplitude of S8 is too low to form a noticeable signature.

minor peak can be identified at slightly higher TOF which is in agreement with OH^+.

S2 and S5 can be attributed to the alkali metal ions of Sodium (23 amu) and Potassium (39 amu), but are also in agreement with Magnesium (24 amu) and Calcium (40 amu) ions. Both alkali metals are expected to show up in a certain number of spectra as surface contaminant signatures (see 2.3) and have been observed in most CDA datasets in laboratory and space. The occasional observation of an accompanying mass line at about 41 amu, perfectly matching the expected isotopic ratio of Potassium (39 amu: 93%; 41 amu: 7%), confirms the presence of the alkali metal (see Fig. 6.15). However, in most cases only a single S5-peak is present. Since it is often unclear if such a single peak is formed only by not separated Potassium isotopes (e.g. in Fig. 6.16), Calcium cannot be ruled out as a S5-species in all cases.
For S2, there are several indicators for a significant contribution from Magnesium (be-

Table 6.3: Regular signatures in Type III dataset (57 spectra).

Signature	Ion TOF [μs]	Occurrence	Equiv. ion mass [amu]	Possible ions
H	0.48–0.54	57 (100%)*	1.0 - 1.3	H^+
C	1.59–1.68	57 (100%)	11.0 - 12.3	C^+
S1	1.84–1.93	50 (88%)	14.6 - 16.2	O^+
S2	2.29–2.37	40 (70%)	23.0 - 24.4	Na^+, Mg^+
S3	2.46–2.57	21 (36%)	26.3 - 28.6	Al^+, Si^+, $C_2H_3^+$
S4	2.62–2,72	51 (89%)	29.8 - 32.0	P^+, S^+, SiH_x^+(?)
S5	2.99–3.05	46 (81%)	38.9 - 40.3	K^+, Ca^+
Fe	3.56–3.61	57 (100%)	55.0 - 56.7	Fe^+
S6	4.46–4.52	34 (60%)	86.2 - 88.8	FeS^+, FeP^+, $?^+$
Rh	4.81–4.89	57 (100%)	100.5 - 103.8	Rh^+
S7	5.04–5.10	28 (49%)	110.2 - 113.0	Fe_2^+, RhC^+
S8	5.37–5.42	13 (23%)	125.0 - 127.5	$RhNa^+$, $RhMg^+$, $?^+$
S9	5.71–5.76	15 (26%)	141.5 - 144.0	Fe_2S^+, RhK^+(?), $RhCa^+$(?), $?^+$
S10	5.99–6.04	20 (35%)	155.7 - 158.5	$RhFe^+$
S11	6.55–6.61	11 (19%)	186.0 - 189.5	$RhFeS^+$, $RhFeP^+$, $?^+$

Note: The TOF and the ion mass given refer to the position of the maximum of the signature. The possible ions are extensively discussed in the text. Unlikely ion species are marked with "(?)". If further, currently unspecified ion species are feasible, a $?^+$ is added.

* = Only a fraction of the spectra show a H^+ feature, but the recording of the others is triggered by H^+ (see 2.1), so an occurrence of 100 % is stated.

sides Sodium) in some spectra. The reproducibility of the peak position of Na^+ is known to be very high (see Tables 4.1, 6.2 and Fig. 6.10). In the case of Type III spectra however, Fig. 6.12 indicates a distribution over a broader mass range in agreement with both Na^+ and Mg^+ signatures being present in the Type III dataset. Furthermore, in at least three spectra, the appearance of S2 is in good agreement with the isotopic abundances of Magnesium (24 amu: 79%; 25 amu: 10%; 26 amu: 11%), (see Fig. 6.16).

The unambiguous attribution of S4 to a particular species is not possible. As in the case of the Oxygen feature (S1), its position varies with the total ion yield (Fig. 6.17). The TOF ranges from a mass equivalent to 32 amu at low QI-amplitudes to less than 30 amu at the highest QI-amplitudes. The signature usually extends over a comparatively wide range of TOFs. Considering the otherwise excellent peak definition in Type III spectra, this indicates two or more unresolved mass lines forming S5 in most of the spectra. The elemental species in this mass range are Phosphorus (31 amu) and Sulfur (32 amu). With O^+ being an abundant ion, O_2^+ would be another species with a matching mass for S4. However, the distinct presence of molecular oxygen ions has never been observed in impact ionisation spectra and is considered to be unlikely. As in the case of Type II particles, hydrogenated Silicon of the form SiH_x^+ cannot be ruled out. But in comparison to the water-rich Type II spectra, neutral Hydrogen species within the impact plasma are much less abundant.

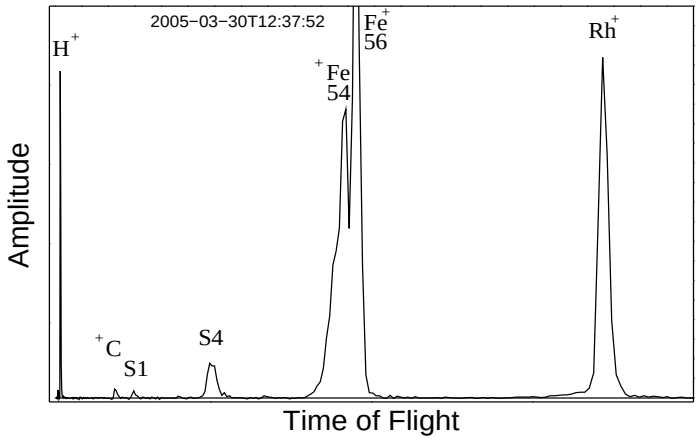

Figure 6.14: Iron isotopes. Note that the iron double peak is not due to a plasma effect as observed occasionally at large total ion yields (Goldsworthy et al., 2003; Hillier et al. 2007a).

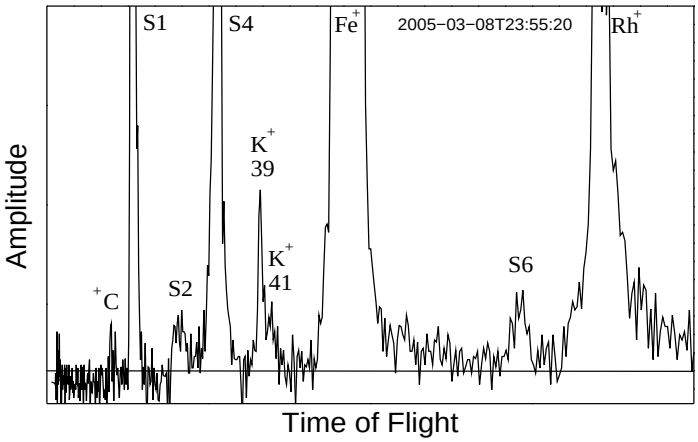

Figure 6.15: Potassium isotopes. This relatively weak spectrum has been triggered by H^+ ions (see 2.1), thus showing no respective mass line.

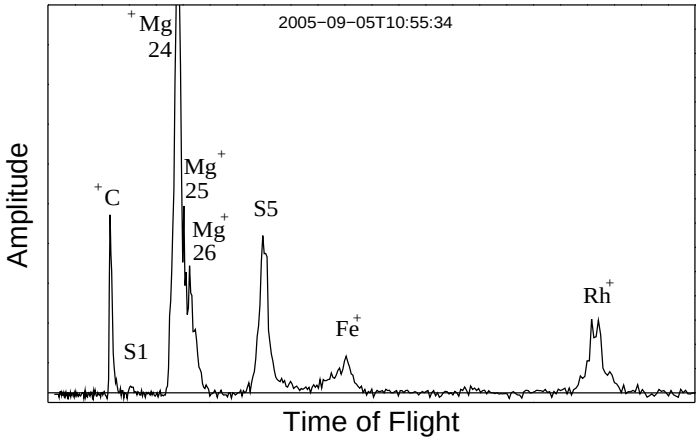

Figure 6.16: Magnesium isotopes. This spectrum has been triggered by H^+ ions (see 2.1).

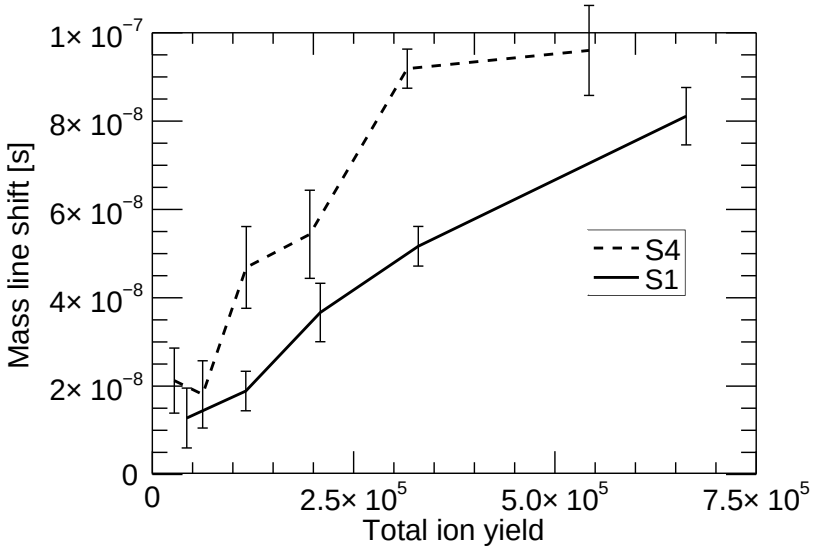

Figure 6.17: Increasing TOF-shift of S1 and S4 with increasing total ion yield (which is inferred from the QI-amplitude). The shift is given relative to a TOF of 1.192 μs ($\sim$ 16 amu) for S1 and 2.715 μs ($\sim$ 32 amu) for S2. The TOF-shift is equivalent to a (seemingly) mass shift relative to the peaks used for spectra calibration.

Moreover, there are only a few weak signatures in agreement with Si^+ which also reinforces the idea that hydrogenated Silicon is not important in Type III spectra. Thus, P^+ and S^+ are the most plausible candidates for S4.

The frequent low amplitude peaks S6, S7, and S10 can all be attributed to cluster ions. With Iron and Rhodium as abundant constituents of the impact plasma, S10 obviously is the mass line of $RhFe^+$. Typical for cluster ions, it is sometimes shifted towards lower TOF. S6 is likely to be another Iron cluster ion, where the metal is associated with the species forming S4 (e.g. FeS^+). The most plausible candidate for S7 is Fe_2^+. Although the TOF of the peak is slightly too low, RhC^+ has to be considered as an alternative S7-species. This ion has been observed on several other occasions in the laboratory (Goldsworthy et al., 2003) and in space (4.1, 5.1). It probably is exclusively due to target contamination (2.3).

Of the less frequent low amplitude features, S3 can be attributed to Al^+, Si^+ or $C_2H_3^+$.
S8 is only detectable in a few spectra, mostly in conjoint appearance with a strong S2-peak. This hints at a cluster ion of the form $RhNa^+$ or $RhMg^+$, respectively.
With a TOF equivalent to 141–144 amu, S9 in principle matches a Rhodium cluster ion, where the target material clusters with a species of about 40 amu, indicating RhK^+. However, in this case the cluster ion shows no correlation with the K^+ peak S5. As Fig. 6.19 indicates S9 is most abundant in Iron-rich spectra. Since an elemental mass line of 140–145 amu would be due to the very unlikely presence of rare earth metals (lanthanides) in detectable amounts, other molecular or cluster ions have to be considered for S9. The most plausible candidate is a cluster consisting of two Iron atoms and the S4-species (e.g.

Fe_2S^+), the total mass of which is in good agreement with the position of the signature. This interpretation of S8 is supported by the observation of S6, which already indicates a cluster of the S4 species with one Iron atom.
The most plausible explanation for S11, present as a minor peak in a few spectra is a cluster of S6 and Rhodium (e.g. $RhFeS^+$).

Identification of particle ions

Hydrogen and Carbon are known to be abundant target contaminant ions (2.3). There is no specific indication to consider Hydrogen and Carbon to be of particle origin. However, a particle contribution cannot be ruled out.

Iron clearly is a major particle constituent in many Type III impactors. As Fig. 6.13 shows, it is the most abundant signature in the dataset. The frequent $RhFe^+$ target-projectile-cluster (S9) underline the significance of Iron.

Although not unambiguously attributed, S4 also represents particle constituents. Compounds of S4 and Iron occasionally seem to "survive" the impact as intact fragment ions (S6 and S8) of the particle's molecular structure.

Although Oxygen ions are a known contaminant species, there is strong indication that S1 is, to a certain degree, of particle origin. The abundance of O^+ is extraordinarily high. In all previous observations in laboratory and space, O^+ was always clearly less abundant than its conjoint appearing contaminant signature C^+ (see 2.3). In contrast, Type III spectra on average show more O^+ than C^+ (Fig. 6.13). This is particulary remarkable if the high ionisation energy of Oxygen is taken into account (Table A.5). Thus, Oxygen - at least occasionally - has to be a major particle component.

As was the case for S1, S2 is a signature of a potential target contaminant (Sodium). However, there are indicators for a particle origin in Type III spectra. The variation in the S2 abundance is extreme: Sometimes it dominates the spectrum, whereas it is not detectable at all in other spectra. This characteristic is only in agreement with a Sodium target contamination for impacts with relatively low energy densities. At high energy impacts, as in the case of Type III particles (see next subsection), Na^+ from surface contamination is not expected to be a dominating signature. Thus, S2 is likely to stem from the particle to a certain amount. It has already been pointed out that besides Na^+, in some cases Mg^+ is a plausible species for S2. Since Magnesium has never been observed as a contaminant, the amount of Mg^+ in the respective spectra implies Magnesium to be a major component of some particles.

Interestingly the abundance of S2 is in clear anti-correlation with the amount of Iron ions (see Fig. 6.18). Furthermore, spectra with an abundant S2 feature show less S4 ions than spectra with abundant Iron signatures (Fig. 6.19). This hints at two different composition types within the Type III dataset and will be further discussed in 6.2.3.

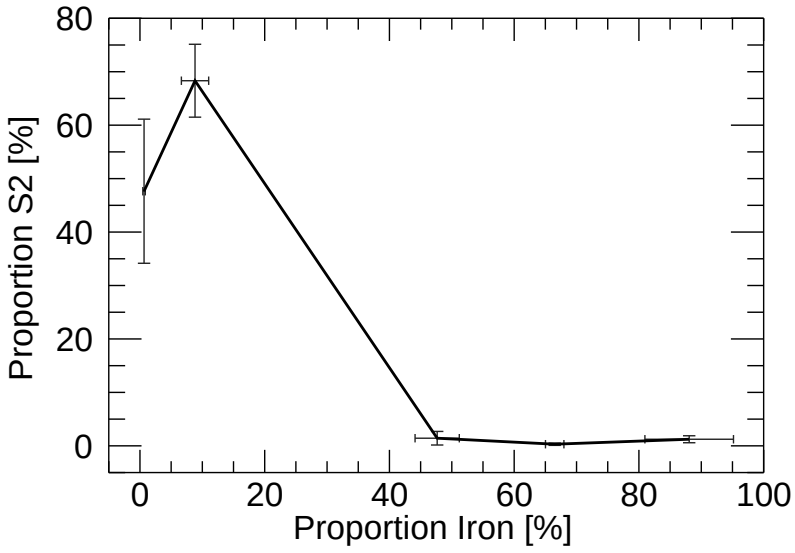

Figure 6.18: Anticorrelation of Fe and S2 abundance. The curve indicates two composition types. One with a relative Iron ion abundance above 40% but less than 5% S2-ions. The other comprises more than 40% S2-ions but less than 10% Iron ions.

S3 indicates that minor amounts of Aluminum or Silicon could sometimes play a role in the particles' composition. If $C_2H_3^+$ is responsible for S3, these ions are likely to stem from contamination of the target surface (2.3).

Particle dynamics

Although the focus of this thesis is on particle composition, some basic dynamical considerations are helpful to derive the "nature" of the Type III particle family.

The abundant O^+ detection alone is proof for much higher impact energy densities than for Type I or Type II particles. There oxygen ions can be detected only in minor quantities, if at all[11]. Since even Type III impacts with the smallest total ion yields show distinct O^+ signatures, sufficient energy densities are already provided by small (but fast) particles. In laboratory experiments an O^+ detection by CDA requires impact speeds above 25 km s^{-1} (see Table 2.3). Inferred from the abundance of Oxygen and Hydrogen ions, the impact speeds in most cases are in agreement with speeds above 30 km s^{-1}. As mentioned in 2.2.3, the average rise time of the Type III QI-signals (3.6 μs) is only about half of the rise time of water-rich CAT impacts (7.6μs), which also hints at substantially higher impact speeds.

Also the amplitudes of the QI-signals, as well as those of the QC-signals, are on aver-

[11]Type I spectra in general do not show an O^+ signature. In Type II spectra the identification of the respective small feature is ambiguous, since it can also be attributed as CH_3^+.

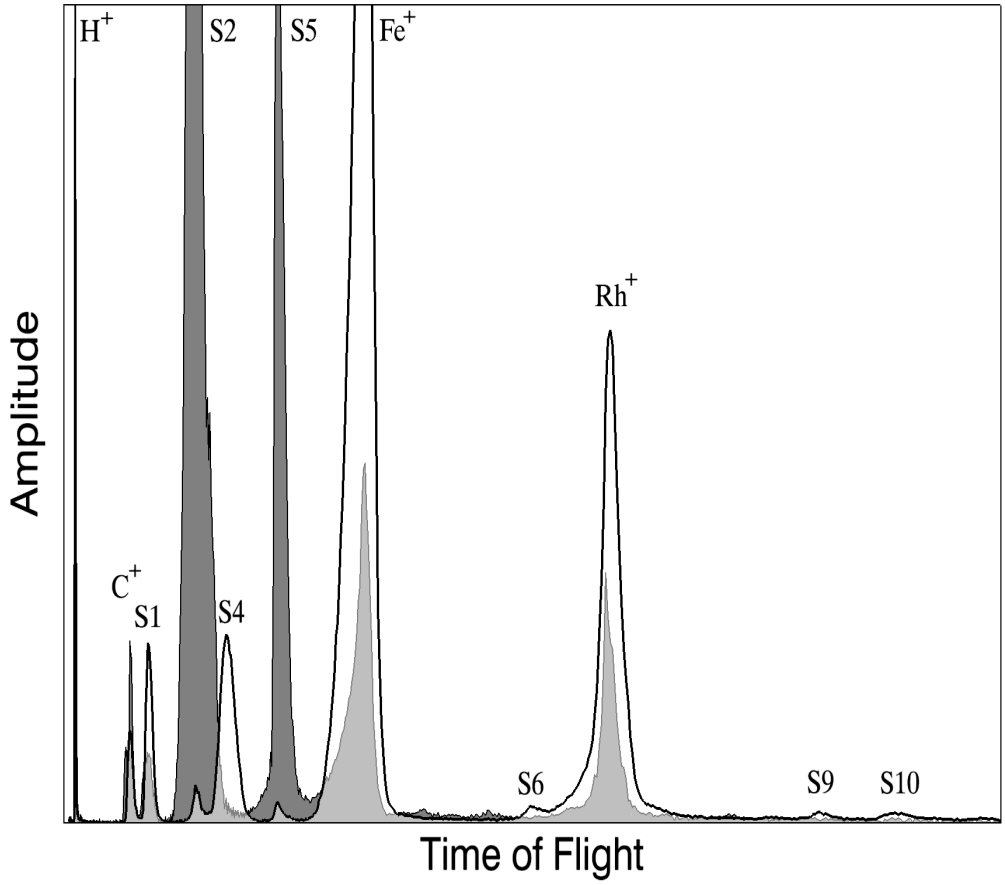

Figure 6.19: Two co-added spectra of spectrum subsets. In the white sum-spectrum all of the 35 spectra with a relative Iron abundance above 40% have been co-added (Type IIIa). The grey spectrum is composed of all of the 8 spectra with an S2-ion abundance above 40% (Type IIIb). Besides variations in the two characterising peaks (S2 and Iron), there are several other differences: Type IIIb spectra show no S4 and less S1 and Rhodium ions than Type IIIa. S5 is bigger than in Type IIIa spectra. Only the Type IIIa sum spectrum exhibits small amounts of the cluster ions S6, S9 and S10.

age considerably higher than those of the water rich impactors. Since only a lower limit for the impact speed can be given at best, the derivation of particle masses is likewise not precise. It is currently unclear if the stronger impact signals are only due to the higher impact speed of Type III particles or if the masses deviate as well.

An examination of the instrument boresight vector at the recording time of Type III spectra shows that most of the possible particle trajectories are not in agreement with dust in prograde Keplerian orbits in the Saturnian ring-plane. A first analysis by U. Beckmann (2007, personal communication) - an example of which can be seen in Fig. 6.20 - demonstrates that all detected particles are in fact in better agreement with retrograde orbits. This could be an explanation for the observed high impact speeds, which otherwise hint at particles unbound to Saturn. It is likewise noteworthy, that all particles have been observed

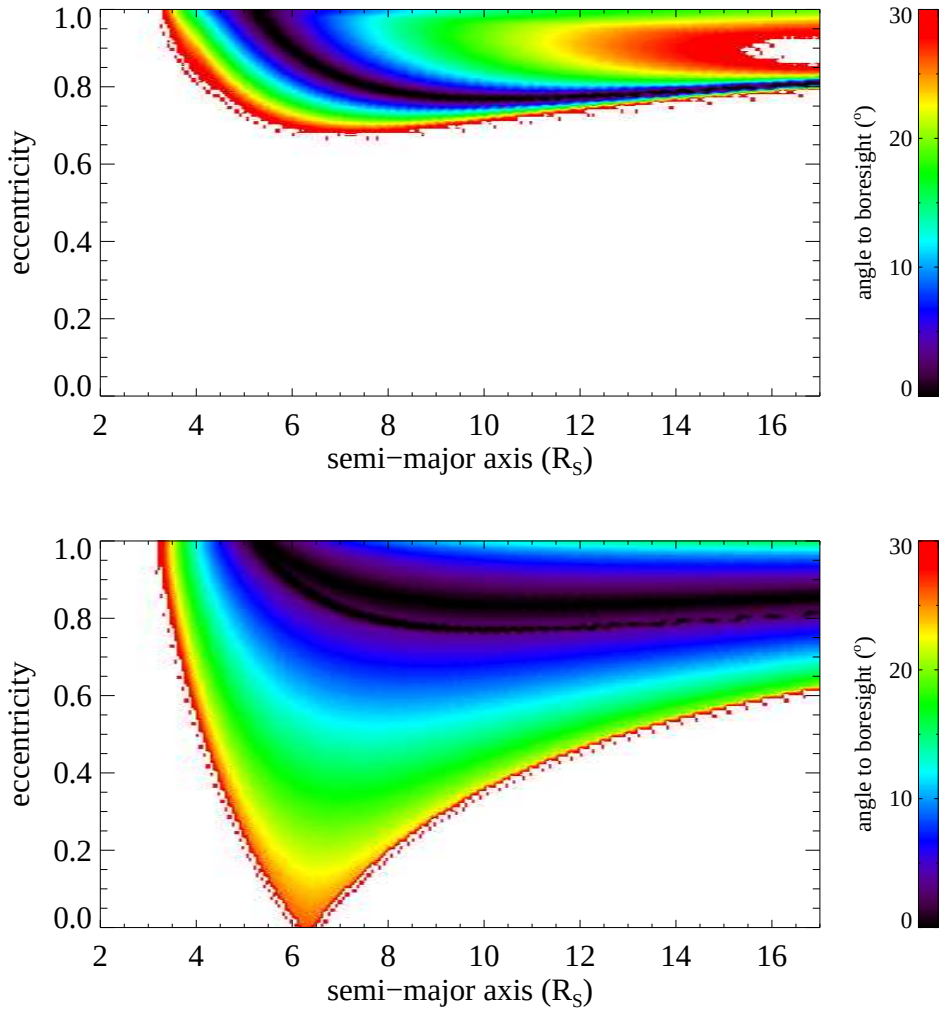

Figure 6.20: Typical possible eccentricities inferred from the CDA pointing geometry of a Type III particle detected at a Saturnian distance of 6.2 R_S in the plane of the E ring. The upper figure shows possible prograde orbits, whereas the lower plot also includes retrograde orbits. The color-code refers to the possible angles of the particle trajectory relative to the CDA boresight (the maximum apex angle for a CAT impact is 29°). Only prograde orbits with extreme eccentricities are feasible, whereas retrograde orbits allow for much lower (and more realistic) orbital elements. This is applicable to nearly all Type III particles. Plot by Uwe Beckmann.

close to the Saturnian ring plane (at a Saturnian distance between 3 to 12 R_S). Although the CDA data of some inclined orbits has been extensively searched for Type III spectra, none so far could be found at Cassini positions significantly above or below the ring plane.

Interestingly the detection of Type III spectra often occurs in clusters: Of the 93 particles recorded between March 2005 and March 2006, 79 occurred as 7 almost consecutive series of 4 to 23 events within a few hours. It is no surprise that very few detections of Type I or Type II spectra interfered with those Type III series, since due to the pointing of

the instrument it was not sensitive to the water-rich main population.
It has to be pointed out that it is currently unclear to what extend the non-detection of Type III particles at an instrument pointing favourable for particles of low eccentricity, is biased by the overwhelming presence of the water-rich population. A more detailed analysis has to be accomplished before final conclusions about Type III particle dynamics can be drawn.

6.2 Discussion

6.2.1 Two Water Spectrum Types - Two Populations - Two Sources?

The existence of two different types of water-rich spectra has been demonstrated: one showing hardly any traces of ions other than those from the E ring bulk material - water, and occasionally target material and target contamination (Type I); the other with a significant contribution of other particle components (Type II). Besides determining the composition of those impurities the further question of whether the spectral types can be assigned to different populations from different sources, in particular Enceladus' cryovolcanoes, is of great interest.

On the one hand, the multiple differences between Type I and Type II spectra (see 6.1.4) imply two particle types of different chemical composition (see 6.1.6) and perhaps structure populating the E ring. On the other hand the possibility has to be considered that Type I and Type II are the spectral appearance of the same particle species for different regimes of impact speeds or particle masses[12]. Within the limits of the mass and velocity determination of CAT impacts (see 2.1) there is no significant indication for different impact speeds or mass regimes. The more frequent occurrence of H^+ in Type I spectra - the formation of which requires high energy density impacts (see Appendix 2.3.3) - possibly hint towards slightly higher average impact speeds for particles creating Type I spectra. Furthermore characteristics of the water cluster pattern in Type I spectra (see 6.1.4) possibly indicate more frequent high energy impacts (Timmerman, 1989). However, we observe a quite clear separation of two spectral types which can hardly solely be justified by a slight statistical difference in impact speeds. Furthermore there are hardly any indications for a continuous transition from one type to another due to changing impact parameters. This fact alone favours the theory that the two spectral types do indeed represent two particle populations (Type I and Type II) which both contribute to the observed particle size and speed distributions (see 2.2).

Though the age of the surface of Enceladus varies a lot, the reflectance spectra are, in all

[12]If the 29 amu signature is caused by elemental ions - such as in the case of silicate impurities - higher impact speeds would not significantly alter the appearance of that feature and this possibility can be discarded. Impact energy can only play a role for the categorisation of Type I or Type II spectra in the case of molecular impurity signatures, which would probably disintegrate at higher energy densities. That in turn could be used as a tool to give further insights into the nature of the impurities in future Enceladus flybys (see Outlook section.)

regions except for the tiger stripes (see 1.3), practically identical to those due to pure water ice at both infrared and optical wavelengths (Brown et al., 2006; Porco et al., 2006). This is unique among the known celestial bodies. Currently the vents produce $> 150\mathrm{kg\,s^{-1}}$ of gas (Hansen et al., 2006), a part of which condenses on the cold surface of the moon. Whereas observations (Porco et al., 2006) indicate that the dust flux is pretty collimated and settles down mostly in the tiger stripe region, it is likely that the entire surface is covered with condensed vent gases. The bulk of the moon's surface is thus subject to an ongoing resurfacing process and is likely to consist of pure water ice and probably minor amounts of CO_2 frost (Brown et al., 2006). The other components detected by the neutral gas spectrometer (Waite et al., 2006) will not condense on the surface under the temperatures given. Calculations show that external sources - like surface gardening by interplanetary dust particles (IDPs) - are totally dominated by the water deposition. Slight deviations from a pure water ice surface can only be measured at the tiger stripes where the surface is more influenced by sedimenting vent particles. Here significant contributions of CO_2 and organics have been found by Cassini's Ultraviolet Imaging Spectrograph (Hansen et al., 2006).

The pure water ice surfaces of Saturn's inner moons are a self-suggesting candidate for Type I particles. A so-called impactor ejecta process has been proposed as a source of particles replenishing the E ring. Here, impacts of interplanetary dust or E ring particles onto the icy surfaces of the moons release smaller particles and feed the E ring (Spahn et al., 2006a; Spahn et al., 1999; Hamilton and Burns, 1994) [13].

Although a minor contribution cannot be excluded, it is very improbable that the impurities observed in Type II spectra could be the result of an impactor ejecta process. Thus we state the hypothesis that Type II particles are almost entirely generated by Enceladus' cryovolcanoes, while Type I particles are also in agreement with impactor ejecta. This of course does not exclude the possibility that an unknown fraction of the pure water Type I particles are generated by Enceladus' eruptions as well. It has to be pointed out that even if the two spectral types are due to the same compositional particle type and source, the chemical fingerprints found in the spectra would still be difficult to explain with an origin other than Enceladus' plumes. Future flybys will clarify the origin of Type I and Type II particles (see section 6.2.4).

The occurrence of Type I and Type II spectra is similar and seems to vary only little within the E ring (see section 3.5). This finding indicates that an efficient dispersal of Enceladus' plume particles occurs within the E ring.

6.2.2 Chemical Fingerprints of Enceladus

It is known from numerical modelling that the observed dust phenomena can only be explained satisfactorily by a nucleation process occurring below the moon's surface (Schmidt

[13] The contribution of these processes to the dust flux feeding the E ring is not well known but is supposed to be small compared to the vent emissions (Spahn et al., 2006b).

et al., 2007). Thus far the particle composition has been discussed based solely on spectra analysis. If Type II particles are produced in Enceladus' cryo-volcanoes, we can combine current knowledge of the active moon with our results. This leads to a refined picture of particle composition, which in turn has implications for the particle production process inside Enceladus.

Most possible candidates for the 29 amu signature in Type II spectra are suspected to be present under the moon's surface (Silicates, Carbon monoxide, Nitrogen and simple organics (Kargel, 2006; Waite et al., 2006; Brown et al., 2006) - see also 1.3). As was shown in 6.1.6 the most plausible candidates for explaining the spectral appearance are organic material and/or Silicates. This becomes even more justified when Enceladus' plumes as the probable origin are taken into account.

Carbon oxide and Nitrogen species

Nitrogen and/or Carbon monoxide molecules are known to be highly enriched in the vicinity of Enceladus (Waite et al., 2006). However, it is almost impossible for both species to exist as solid pure ices in the Saturnian system. Thus, it seems to be an attractive possibility to consider the CO^+ forming the characterising peak as a fragment of less volatile CO_2 ice in the particle. But, for energetic reasons and from experiments (Adamczyk et al., 1988; Velotta et al., 1994), it is evident that if CO_2 is the parent molecule of CO^+, the mass line of ${CO_2}^+$ (44 amu) should be more abundant than that of CO^+. Although ${CO_2}^+$ may contribute a little to the F4 signature it clearly represents only a minor part of the non-water components, if any. Thus CO_2 can be excluded from playing a major role here.

N_2 or CO clathrate hydrates, with the volatile molecules embedded in a water ice lattice, might be a more realistic assumption. If however, clathrates pass through low pressure - high temperature phases (Porco et al., 2006; Tian et al., 2007) as proposed for Enceladus' vents, such volatile components are likely to outgas completely from liquid water. Thus, the presence of those molecules in a freshly ejected particle is unlikely. But there is another process which could lead to the embedding of gas molecules into water ice after ejection. If water condenses below 120 K it forms an amorphous structure which can trap volatile gases (Bar-Nun et al., 1987). This process could be effective directly after the preformed water ice particles have been ejected by the vents into a cool environment (radiation temperature 80 K), whilst still in contact with a dense gas flow. Depending on several parameters, which are currently unclear, a thin outer layer of gas-laden amorphous ice could be formed around μm sized particles. However, there are reasons why this, too, might not be an important process:

- CO_2 is only a minor fraction of the non-water particle compounds, if present at all. Since CO_2 is quite a significant compound in Enceladus' gas environment (Waite et al., 2006) and by far the least volatile (after water), this finding places constraints on the other gas components, too. It indicates that the particle production conditions were not favourable for the absorption and embedding of any of the other

detected gas compounds (CO, N_2, CH_4, C_2H_2, C_3H_8) into plume particles, whether as clathrate hydrates or as inclusions in amorphous ice.

- If we consider Type II particles as originating from Enceladus, then they have been subject to plasma sputtering for several decades whilst reaching the outer E ring. That would have removed at least 0.1 μm of the outer layer of the particle (Jurac et al., 1998; Jurac, 2001; Juhász and Horányi, 2002). Even if the newest plasma models are applied (Beckmann, 2006, personal communications), this picture does not change significantly. Thus a thin amorphous ice layer around particles as described above is unlikely for particles populating the outer E ring. However, Type II spectra are detected in abundance even outside Rhea's orbit (Hillier et al., 2007b).

Consequently, volatile compounds, as detected by Cassini's Ion and Neutral Mass Spectrometer in the plumes' gas phase (Waite et al., 2006) (see section 1.3), are not considered to be an abundant impurity in Type II particles. Following the analysis of spectra in 6.1.6, this is especially true for CO and N_2. However, a minor contribution from volatiles cannot be ruled out until refined vent models are available.

Organic compounds

Though some of the mass lines found by the Ion and Neutral Mass spectrometer and attributed to organics (15, 28 and 44 amu) are similar to mass lines in CDA spectra, the arguments against volatile compounds (see 6.2.2) apply to these organic compounds, too. Nevertheless, these volatile organics identified in the gas phase can be taken as indicators for refractory organic components which can be detected in the solid state. Ionic fragments of refractory organics would be in good agreement with many of the signatures found in the impact plasma of Type II particles (see 6.1.6).

This possibility is of particular importance since Matson et al. (2007) strongly suggested chemical processes at a hot (> 500 K) rock-water interface inside Enceladus may be occurring. They predict complex organic compounds to be present in a "rich, warm aqueous organic soup below the surface". If this is the case, it would indeed be no surprise to find them condensed in the particles as well. The quantity of putative organic ions present in some spectra would indicate that particles occasionally contain organic material at concentrations of up to several percent. The most likely candidates for those refractory organics are either aromatic, long-chained or polar hydrocarbons. Their vapour pressure can be similar to water and they would not out-gas easily at high temperatures or low pressure and could even function as condensation cores. Furthermore polar hydrocarbons (such as alcohols, acids or nitriles) - in contrast to e.g. CO, N_2 or CO_2 - are very soluble in water, reducing the boiling and melting temperature. Therefore those organic compounds are more likely to "survive" the particle production process in sufficient concentrations and freeze out as an alloy with the more abundant water ice.

Silicates

Type II spectra are also in agreement with a contribution from Magnesium-rich, Aluminium-poor minerals embedded in water ice particles. The incorporation of such silicates into Enceladus' plume particles would not be unexpected. Enceladus is believed to have an amazingly large silicate core (Porco et al., 2006). It is plausible that water oceans under the ice crust of the moon could contain a small proportion of undifferentiated submicron silicate particles. In particular, with water cycling material into and out of regions of a rocky core surface of serpentinized silicates (Matson et al., 2007), clay minerals could be detached. Tiny silicate grains with sizes probably far below 0.1 μm, floating in a liquid environment, would be incorporated in the ice or even function as condensation cores for the plume particle production in active vents. That would help to explain the extraordinarily large particle production rate observed (Schmidt 2007, personal communications). The primary compounds of silicates (metals and silicon) have very low ionisation energies compared to water. Thus, only minor silicate inclusions in water ice (probably in the order of 1 %) would be enough to explain most Type II spectra.

As an alternative or parallel scenario, silicates could be debris from interplanetary impactors (dating back to a time before the plumes were active), now incorporated in an upper subsurface ice layer of the moon. However, a mass fraction of about 1% silicates from IDPs in the whole volume of the upper ice crust is not very likely. Nevertheless, the incorporation of IDPs during the formation of vent particles may, in principle, occur for a certain fraction of vent particles.

It has to be noted that CDA has previously detected Silicon in Saturnian dust as a major constituent of Saturnian stream particles (Kempf et al., 2005b) (see respective chapters in this work). There the extremely energetic impact conditions made the survival of a molecular species with a mass of 28 amu very unlikely; thus, the corresponding mass line could only be attributed as Si^+. Furthermore it was shown that those tiny particles originate from the E ring (Kempf et al., 2005a). In fact, the fate of E ring particles is either to collide with an embedded moon, to collide with the main rings, or to end up in a dust stream accelerated out of the Saturnian system. Therefore, this Si-rich nano dust could be the sputtered remnants of larger icy E ring particles created in the interior of Enceladus.

6.2.3 The Non-Water Dust Population (Type III)

Particle composition

There are no indications for water or other icy components in Type III spectra. Most of the particles contain a substantial amount of Iron and/or Magnesium. The majority of these metals is generally assumed to be bound as the metallic compound of silicates (e.g. olivine or pyroxene). Thus, it is unexpected that in Type III spectra only a few, mostly low abundant, signatures which are in agreement with a silicon component can be found. Instead, the non-metallic particle component identified in section 6.1.7 comprises of Oxygen and the S4–species which probably are mostly Phosphorus and/or Sulfur.

Figs. 6.18 and 6.19 hint at two compositional subtypes to be present. However, it has to be pointed out that at least for spectra with large total ion yields a homogenous particle composition is not necessarily the case. The particle sizes of the stronger impacts are likely to exceed 1 μm, which is a typical diameter of volumes with homogenous composition in cometary grains or IDPs (Zolensky et al., 2006; Keller et al., 2006; Brownlee et al., 2006).

The majority of the detected particles ($\approx$ 65%) are Iron-rich and Magnesium-poor (Type IIIa, white spectrum in Fig. 6.19). Plausible iron-rich minerals composed of the detected ions are Iron-Sulfur minerals like pyrite and Iron oxides or hydroxides. S6 and S8 would mark fragment ions of a pyrite lattice of the form FeS^+ (S6) and Fe_2S^+ (S8). The wideness of S4 implies Phosphorus in conjoint appearance with the Sulfur species. Iron ions are on average about 10 times more abundant than the S4-species in Type III spectra (Fig. 6.13). Considering the much higher ionisation energy of Sulfur and Phosphorus, this is consistent with an Iron to Sulfur (Phosphorus) ratio of about 2:1 to 1:2. Especially in Type IIIa spectra the O^+ abundance is extreme (e.g. S1 in Fig. 6.15). Besides Iron oxides this, together with the presence of S4, is also in agreement with sulfates. Hydroxides are indicated by the occasional presence of a putative OH^+ mass line. Within the iron-rich type, S2 probably represents mainly the Sodium contamination of the target (as indicated in 6.19) and not Sodium or Magnesium particle ions.

There appears to be a less numerous ($\approx$15%) subspecies (Type IIIb), which contains less iron and more Magnesium (Fig. 6.19). Here, the presence of S4 (Sulfur, Phosphorus) is less likely and less abundant. In contrast to the Iron-rich Magnesium-poor Type IIIa, Silicon features (28 amu) are occasionally present. This is indicated in Fig. 6.19 by a substantially broadened right flank of S2. This putative flanking peak has a time of flight which is equivalent to 28 amu. Thus, those particles probably contain a certain amount of a Magnesium-rich silicate compound like olivine. The increased S5 indicates Potassium or Calcium to be further relevant but minor compounds[14].

About 20% of the spectra show characteristics of both compositional types discussed made above. Occasional minor amounts of Calcium and Aluminum in Type III particles are in agreement with the spectra analysis in both types. Due to their presence as contaminants Carbon, Hydrogen, Sodium and Potassium cannot ruled out as being, to be to a certain extent, of particle origin.

Particle origin

The origin of Type III dust is currently unclear. It is even possible that Type III particles, which sometimes appear in streams, have several different origins. However, the homogeneity within the spectra of the dataset imply only two sources at most.
In contrast to Type I and II particles, the compositional analysis excludes Saturn's icy moons as a source. The abundant formation of ion species with high ionisation energies,

[14]Due to their low ionisation energy, even minor amounts of these elements create major signatures.

hint at impact velocities of at least 25 km s^{-1} for most of the events. On the one hand Cassini's position at the moment of detection hint at a source close to Saturn's ring plane, on the other hand the instrument pointing indicates that many of Type III particles are not in prograde orbits of low eccentricity (like the icy main population of the ring).

The aforementioned constraints exclude some but leave many options for possible sources. Nevertheless, it is an amazing result that a somehow coherent mineral particle population in retrograde orbits is in good agreement with the data. They could be impact ejecta from - maybe still undetected - objects with retrograde orbits around Saturn.
Although the high frequency of detection (up to 21 within 7 hours on March 8 and 9, 2005) speaks against unbound particles (or would at least be highly unexpected), IDPs or interstellar dust are in principle possible Type III particles. In this context the two Cassini spectra of IDPs described in chapter 3.1 should be mentioned: as in the case of Type III spectra they show a surprisingly abundant iron component.
Within the period relevant for the Type III dataset, the flux of interstellar particles was from the direction of the sun. Therefore for small interstellar grains with a β–value (Burns et al., 1979; Landgraf, 2000) above 1.4 (corresponding to about 0.1 μm particle size) it might have been impossible to reach the spacecraft during 2005 (S. Kempf, personal communication, 2007).

A detailed dynamical analysis has not been done yet. Together with a thorough compositional analysis of a greater dataset than used for this work, the source(s) of Type III particles might be revealed in the near future.

6.2.4 Outlook

The identification of organics and/or silicates in otherwise water rich particles is considered to be significant. However, there still are some inconsistencies in the interpretation of Type II spectra (see 6.1.6). Furthermore, some rarely occurring peaks indicate that other components might be present in particles escaping Enceladus' plumes. Experiments with several different organic species are currently in progress at the Heidelberg dust accelerator facility. Advanced experiments with silicate projectiles (late 2007) and specifically doped water ice (2009) are in preparation. This will lead to a better understanding of Type II spectra and the nature of Enceladus' particles.

Most importantly, our team hopes to acquire high resolution spectra of freshly ejected plume particles during the next close Enceladus flybys. The flyby geometries in March 2008 (Orbit 61), and those of Cassini's extended mission will allow to the theory that Type II spectra can in general be attributed to vent particles whereas impactor ejecta appear as Type I spectra. In orbit 61, Cassini's closest approach will be at the moon's equatorial plane, outside the influence of cryo-volcanic activity, and thus the dust environment should be dominated by impactor ejecta. As the spacecraft moves away from the moon, it will cross the plumes and freshly ejected plume particles will be dominant. Furthermore, CDA will be able to acquire vent particle spectra at different relative speeds during different flybys (6.8 to 17.7 km s^{-1}). These are likely to reveal further details of

the non-water component in Type II spectra and allow us to distinguish between organic and silicate compounds.

The examination of Type III particles given in this work is only preliminary. A more detailed investigation of the compositional as well as the dynamical aspects of a larger dataset than used for this work is in progress. This will help to reveal the source(s) of the dust particles of pure mineral composition.

Chapter 7

Summary

The compositional analysis of six different dust "families" discovered by the dust detector onboard the Cassini spacecraft is presented in this work. The base data are time-of-flight mass spectra of cations extracted from the plasma created by high-velocity dust impacts onto the target of the instrument.

Three dust species have been encountered in interplanetary space (IDPs and two stream particle populations). The other three were detected in the ring plane of Saturn after Cassini's orbit insertion[1]. In Tables 7.1 and 7.2 the basic characteristics of the particles and the spectra are summarised.

Table 7.1: Parameters for the dust species investigated in this thesis. The number of spectra given refers to the number of spectra used for this work. With the exception of the IDPs the total number of recorded spectra is considerably larger.

Dust species	Period of detection	Spectra in dataset	Impact speeds ($km\,s^{-1}$)	Dominant particle size
IDP	May and Nov 1999	2	10–30	0.5–5 μm
Jovian stream	Sep 2000–July 2001	458	200–500	5–25 nm
Saturnian stream	since Jan 2004	584	80–200	2–10 nm
E ring, Type I	since Oct 2004	$\approx$2500 *	8–25	0.1–1 μm
E ring, Type II	since Oct 2004	$\approx$2500 *	8–25	0.1–1 μm
E ring, Type III	since March 2005	57	$>$25	0.2–5 μm **

*The spectra of Type I and Type II are within a single dataset. Of this initial dataset, subsets have been created for a detailed characterisation of the two spectrum types.
**These values are merely speculative and have to be treated with reservation.

[1]Though the Saturnian stream particles were initially revealed in interplanetary space, they subsequently are also detected frequently during Cassini' orbital tour.

Table 7.2: Spectrum characteristics and inferred particle composition for the dust species investigated in this thesis.

Dust species	Spectra characteristics	Inferred particle composition
IDP	- Fe^+, Rh^+ dominant - H^+, C^+, O^+ - clear $RhFe^+$ cluster - Fe^+ and Rh^+ "peak splitting"*	- Iron-rich mineral - little or few silicate and pyrite - Pure Iron/Nickel or Iron-rich carbonaceous mineral or oxides
Jovian stream	- H^+, C^+, Rh^+, Na^+ dominant - O^+, Si^+, K^+, S^+, Cl^+ - weak $RhCl^+$, RhS^+, $RhNa^+$ cluster - spectra often triggered by H^+	- Sodium chloride main compound - further alkali metal salts likely - minor sulfurous compounds - silicate core possible
Saturnian stream	- faint spectra; C^+, Rh^+ dominant - O^+, Si^+ - occasional Na^+, K^+ - weak $RhSi^+$ cluster, H_3O^+, N^+(?) - spectra always triggered by H^+	- siliceous main compound - occasional water ice mantle possible
E ring, Type I	- water cluster dominant - frequent Na^+, K^+, Rh^+ - frequent Na-water, Rh-water cluster - occasional H^+, C^+ - spectra often triggered by H_3O^+	- pure water ice particle
E ring, Type II	- All characteristics of Type I - Si^+, Al^+ or $C_2H_x^+$ - further organic ions or Mg-water cluster - bad peak definition, "noisy" spectra	- water ice main compound - impurities of organic or siliceous material - yet unspecified compounds likely
E ring, Type III	- either Fe^+ or Na^+/Mg^+ dominant - H^+, Rh^+, S^+/P^+, O^+, K^+/Ca^+, C^+ - minor Si^+, Al^+ - clear $RhFe^+$ cluster - cluster ions of Fe with S/P - occasional isotopes of Fe^+, Mg^+, K^+, due to good peak definition - spectra occasionally triggered by H^+	- Iron-rich mineral dominant (Type IIIa), pyrite and Iron oxides/hydroxides, phosphorous compound likely - Magnesium-rich subspecies (Type IIIb) with possible siliceous mineralogy (e.g. olivine)

*see Hillier et al. (2007a) for details.

The *in-situ* studies of the CDA allow the investigation of material which is not accessible by other means. Furthermore, with the dust being a messenger of their parent bodies, the spectra provide insight into the properties of the particles' sources. These are summarised in the following.

- From the chemical fingerprint Io's volcanoes are identified as the source for the vast majority of, and possibly all, Jovian stream particles detected. Concluding NaCl as the most abundant particle component contrasts with (rather than contradicts) observations of gaseous components in the Ionian atmosphere, the plasma torus and

the neutral cloud where sulfur species are dominant while alkali metal and halogen species are minor components.
The results suggest that particles are formed in a condensation cascade inside erupting volcanic gases, a finding which has been recently confirmed by observations of the New Horizons spacecraft (Spencer et al., 2007). The condensation probably occurs around pyroclastic silicate cores. Due to their high condensation temperatures sodium and potassium salts condense prior to sulfuric compounds. The resulting particles escape from the top of Pele-type plumes probably before the abundant SO_2 could condense. If alternatively the conditions allow SO_2 to become solid on the particles' surface, subsequent sputtering or heating in the ionosphere and the plasma torus yields dissociation and evaporation of the highly volatile SO_2 frost.

- The composition of nano-dust escaping the Saturnian ring system as stream particles to be basically siliceous, is an unexpected finding. The spectra obtained during the approach towards the giant planet, before Cassini's orbit insertion, are likely to be probes of Saturn's main rings. The stream particle spectra obtained whilst the spacecraft was in orbit predominately represent the remnants of E ring particles, probably once ejected by Enceladus' plumes. The as yet unaccomplished statistical evaluation of most of the thousands of stream particle spectra obtained during Cassini's orbital tour might deliver further information about the dust sources.

- The clear separation of two different water dominated spectrum types is best explained by the existence of two different icy particle species within the E ring main populations. The impurities observed in Type II spectra favour Enceladus' cryovolcanic vents as their source. The pure water ice Type I spectra could also be the result of an impactor ejecta process where micro impacts onto the clean water ice surfaces of Saturn's inner moons release smaller particles feeding the E-ring. Both particle types can be found in abundance everywhere in the E-ring, which indicates a rapid dispersal of Enceladus' plume particles within the entire ring.
  Type II spectra imply a complex chemistry and perhaps particle structure. The signatures of impurities in Type II spectra are best matched by organic fragments and/or magnesium-rich, aluminum-poor silicates. This implies one or both of those species are present in particles escaping Enceladus' plumes. Generation mechanisms for organic compounds at a hot rock-water interface far below the moons surface already have been suggested by Matson et al. (2007). Silicate particle components, which were once submicron particles floating in a liquid environment below the icy surface of Enceladus, were then incorporated as the water froze. They might be clay minerals detached from the moon's large rocky core due to water cycling through cracks at a core-water interface, as suggested by Matson et al. (2007). Functioning as condensation cores, submicron-sized silicate or refractory organic grains would increase the particle production rate inside Enceladus' vents.
  Both possible impurities - organic and silicate - within water ice particles place constraints on geophysical modelling which hint at an interface of rock with liquid water below Enceladus' icy surface.

- A minor but significant non-water dust particle population with different orbital elements than the icy main population can be found in the outer Saturnian ring plane. The likely pure mineral composition of Type III dust, excludes Saturn's icy moons as an origin. Since there appear to be two main compositional Type III subtypes, different sources might play a role.
  The dust might stem from, probably still undetected, objects orbiting Saturn in retrograde direction. However, an external origin is also possible.

Appendix A

Data tables

A.1 CDA Decontamination Schedule

CDA decontamination cycles until October 5, 2007 taken from the original instrument output. On the dates indicated, the heating was switched “on” or “off”. The format of the date is: year-DOY-time.

2000-110T14:00:00 79PS DECON HTR ON;
2000-110T23:00:00 79PS DECON HTR OFF;
2001-130T00:06:20 79PS DECON HTR ON;
2001-130T10:06:20 79PS DECON HTR OFF;
2001-258T04:08:20 79PS DECON HTR ON;
2001-258T14:08:20 79PS DECON HTR OFF;
2001-258T05:07:20 79PS DECON HTR ON;
2001-258T15:07:20 79PS DECON HTR OFF;
2002-132T21:07:20 79PS DECON HTR ON;
2002-133T17:07:20 79PS DECON HTR OFF;
2003-200T01:51:40 79PS DECON HTR ON;
2003-200T13:50:00 79PS DECON HTR OFF;
2003-290T05:51:40 79PS DECON HTR ON;
2003-290T18:00:00 79PS DECON HTR OFF;
2003-352T15:21:50 79PS DECON HTR ON;
2003-353T02:25:00 79PS DECON HTR OFF;
2004-284T08:46:40 79PS DECON HTR ON;
2004-284T14:39:00 79PS DECON HTR OFF;
2005-039T21:23:30 79PS DECON HTR ON;
2005-040T09:37:00 79PS DECON HTR OFF;
2005-130T21:34:15 79PS DECON HTR ON;
2005-131T07:43:54 79PS DECON HTR OFF;
2005-146T04:19:00 79PS DECON HTR ON;
2005-146T12:19:00 79PS DECON HTR OFF;
2005-224T01:28:35 79PS DECON HTR ON;
2005-224T09:28:35 79PS DECON HTR OFF;

2005-295T12:28:50 79PS DECON HTR ON;
2005-295T12:31:00 79PS DECON HTR OFF;
2005-295T19:29:00 79PS DECON HTR OFF;
2005-334T20:00:04 79PS DECON HTR ON;
2005-335T03:17:53 79PS DECON HTR OFF;
2005-365T15:45:55 79PS DECON HTR ON;
2005-365T15:47:00 79PS DECON HTR OFF;
2006-001T00:34:55 79PS DECON HTR OFF;
2006-034T12:36:10 79PS DECON HTR ON;
2006-034T19:53:00 79PS DECON HTR OFF;
2006-092T08:26:20 79PS DECON HTR ON;
2006-092T15:48:00 79PS DECON HTR OFF;
2006-128T23:06:20 79PS DECON HTR ON;
2006-129T14:13:00 79PS DECON HTR OFF;
2006-196T01:59:20 79PS DECON HTR ON;
2006-196T09:56:00 79PS DECON HTR OFF;
2006-262T13:53:20 79PS DECON HTR ON;
2006-263T04:35:00 79PS DECON HTR OFF;
2006-304T20:33:20 79PS DECON HTR ON;
2006-305T04:05:00 79PS DECON HTR OFF;
2006-341T19:08:21 79PS DECON HTR ON;
2006-342T02:40:01 79PS DECON HTR OFF;
2007-008T16:08:21 79PS DECON HTR ON;
2007-008T23:40:01 79PS DECON HTR OFF;
2007-108T03:55:36 79PS DECON HTR ON;
2007-108T14:52:01 79PS DECON HTR OFF;
2007-167T05:47:35 79PS DECON HTR ON;
2007-167T10:44:00 79PS DECON HTR OFF;
2007-292T20:46:35 79PS DECON HTR ON;
2007-293T06:23:00 79PS DECON HTR OFF;

A.2 Jovian System

perihelion distance:	740 520 000 km
aphelion distance:	816 620 000 km
semi-major axis:	778 300 000 km
eccentricity:	0.04839266 km
inclination:	1.30530°
sidereal period:	11.862 y
mass:	$1.8986 \cdot 10^{27}$ kg
mean density:	1326 kg m^{-3}
polar radius:	66 854 km
equatorial radius:	71 492 km

axial tilt:	3.13°
sidereal rotation period:	9.9250 h
escape speed:	$59.5\,\mathrm{km\,s^{-1}}$

Table A.1: Orbital and physical data on some of the Jovian moons.

name	a		e	i	T_m	M_m[1]	R_m[1]
	(10^3 km)	(R_J)		(°)	(d)	(kg)	(km)
Adrastea[2]	129	1.81	0.0018	0.054	0.29826	$7.493 \cdot 10^{15}$	8
Amalthea[2]	181	2.54	0.0032	0.380	0.498179	$2.068 \cdot 10^{18}$	83
Thebe[2]	221	3.11	0.0176	1.080	0.6745	$1.499 \cdot 10^{18}$	49
Io[2]	421	5.90	0.0041	0.036	1.769138	$8.932 \cdot 10^{22}$	1821
Europa[2]	671	9.40	0.0094	0.466	3.551810	$4.800 \cdot 10^{22}$	1561
Ganymede[2]	1 070	14.99	0.0013	0.177	7.154533	$1.482 \cdot 10^{23}$	2632
Callisto[2]	1 883	26.37	0.0074	0.192	16.689018	$1.076 \cdot 10^{23}$	2409
Leda[3]	11 165	155.38	0.1636	27.457	238.72	$1.094 \cdot 10^{16}$	3
Himalia[3]	11 461	160.79	0.1623	27.496	250.5662	$6.744 \cdot 10^{18}$	85
Lysithea[3]	11 717	164.15	0.1124	28.302	259.22	$6.294 \cdot 10^{16}$	3
Elara[3]	11 741	164.39	0.2174	26.627	259.6528	$8.692 \cdot 10^{17}$	40
Ananke[3]	21 276	269.93	0.2435	148.889	-631	$2.997 \cdot 10^{16}$	10
Carme[3]	23 404	316.54	0.2533	164.907	-692	$1.319 \cdot 10^{17}$	15
Pasiphae[3]	23 624	329.14	0.4090	151.431	-735	$2.997 \cdot 10^{17}$	18
Sinope[3]	23 939	331.94	0.2495	158.109	-758	$7.493 \cdot 10^{16}$	14

Notes:

[1] Data from Seidelmann et al. (2002)

[2] Orbital data from Jacobson (2003) UP230 - JPL satellite ephemeris

[3] Orbital data from Jacobson (2000)

Table A.2: Data on the Jovian rings.

name	boundaries				thickness	optical
	(km)	(R_S)	(km)	(R_S)	(km)	depth
halo[1]	89 400	1.25	123 000	1.72	33 600	$3 \cdot 10^{-6}$
main ring[1]	123 000	1.72	128 940	1.81	5 940	$5 \cdot 10^{-6}$
Gossamer ring (Amalthea)[2]	128 940	1.81	181 350	2.54	2 600	10^{-7}
Gossamer ring (Thebe)[2]	128 940	1.81	221 900	3.11	8 800	10^{-7}
Thebe ring (extension)[2]	221 900	3.11	280 000	3.92	8 800	10^{-8}

Notes:

[1] Data from Murray & Dermott (1999)

[2] Burns et al. (1999)

A.3 Saturnian System

perihelion distance:	1 349 467 375 km
aphelion distance:	1 503 983 449 km
semi-major axis:	1 426 725 413 km
eccentricity:	0.054 150 60
inclination:	2.484 46°
siderial period:	29.46 y
mass:	$5.6846 \cdot 10^{26}$ kg
mean density:	687.3 kg m^{-3}
polar radius[1]:	54 364 km
equatorial radius[1]:	60 268 km
reference radius[2]:	60 330 km = 1 R_S
axial tilt:	26.73°
sidereal rotation period:	10.785 h
escape speed:	35.49 km s^{-1}

Notes:
[1] corresponds to 1 bar surface
[2] models Saturn as sphere corresponding to a 100 mbar surface

Table A.3: Data on Saturn's rings.

	boundaries				thickness		optical
	(km)	(R_S)	(km)	(R_S)	(km)		depth
D ring[1]	66970	1.11	74510	1.23	0.1	0.1	10^{-5}
C ring[1]	74510	1.23	92000	1.52	0.1	0.1	10^{-1}
B ring[1]	92000	1.52	117580	1.95	0.1	0.1	1.5
A ring[1]	122170	2.02	136780	2.27	0.1	0.1	$5 \cdot 10^{-1}$
F ring[2]	140180	2.32	140270	2.32	6.5	6.5	10^{-1}
G ring[3]	165000	2.73	176000	2.92	280	280	10^{-6}
E ring[1]	189870	3.15	256900	4.26	9000	9000	$3 \cdot 10^{-6}$
	256900	4.25	420000	6.96	9000	17000	$3 \cdot 10^{-6}$

Notes:
[1] Data from Cuzzi et al. (1984)
[2] Data from Bosh et al. (2002)
[3] Data Lissauer et al. (2000)

Table A.4: Orbital and physical data on some of Saturn's moons.

	a [1] (km)	(R_S)	e [1]	i[1] (°)	T_m (d)	M_m [2] (kg)	M_m [3] (km)	R_hill (km)
Mimas	186038	3.08	0.022	1.53	0.947	$3.750 \cdot 10^{19}$	199	521
Enceladus	238410	3.95	0.004	0.02	1.374	$1.080 \cdot 10^{20}$	252	950
Tethys	294974	4.89	0.001	1.09	1.892	$6.176 \cdot 10^{20}$	536	2102
Dione	377647	6.26	0.002	0.02	2.740	$1.096 \cdot 10^{21}$	562	3259
Rhea	527231	8.74	0.001	0.35	4.520	$2.307 \cdot 10^{21}$	764	5831
Titan	1222265	20.26	0.029	0.33	15.954	$1.345 \cdot 10^{23}$	2575	52419
Hyperion	1478604	24.51	0.112	0.43	21.230	$5.583 \cdot 10^{18}$	133	2196
Iapetus	3560488	59.02	0.028	7.52	79.329	$1.806 \cdot 10^{21}$	734	36292
Phoebe	12998651	215.46	0.152	175.3	553.370	$8.294 \cdot 10^{18}$	107[4]	22023

Notes:

[1] Data from Murray & Dermott (1999)

[2] Data from Seidelmann et al. (2002)

[3] Data from Roatsch et al. (2006)

[4] Data from Giese et al. (2006)

A.4 Ionisation Energies and Electron Affinities of Elements and Molecules

Table A.5: Atomic masses, ionisation energies and electron affinities* of some relevant elements and molecules.

Species	Main isotope	$E^0 \longrightarrow E^+$	$E^0 \longrightarrow E^-$
Hydrogen	1 amu	13.60 eV	- 0.76 eV
Lithium	7 amu	5.39 eV	- 0.62 eV
Carbon	12 amu	11.25 eV	- 1.60 eV
Nitrogen (N)	14 amu	14.53 eV	$>$ 0.00 eV
Oxygen	16 amu	13.62 eV	- 1.46 eV
Water (H_2O)	18 amu	12.62 eV	$>$ 0.00 eV
Fluorine	19 amu	17.42 eV	- 3.40 eV
Sodium	23 amu	5.14 eV	- 0.55 eV
Magnesium	24 amu	7.65 eV	$>$ 0.00 eV
Aluminum	27 amu	5.99 eV	- 0.43 eV
HCN	27 amu	13.61 eV	$<$ - 1.00 eV
Nitrogen (N_2)	28 amu	15.58 eV	$>$ 0.00 eV
Carbon monoxide (CO)	28 amu	14.01 eV	- 1.33 eV
Silicon	28 amu	8.16 eV	- 1.39 eV
C_2H_5	29 amu	8.40 eV	-
Phosphorus	31 amu	10.49 eV	- 0.75 eV
Sulfur	32 amu	10.36 eV	- 2.07 eV
Chlorine	35 amu	12.97 eV	- 3.62 eV
Potassium	39 amu	4.34 eV	- 0.50 eV
Calcium	40 amu	6.11 eV	- 0.02 eV
C_3H_5	41 amu	8.10 eV	-
C_3H_7	43 amu	7.80 eV	-
Silicon monoxide (SiO)	44 amu	11.49 eV	-
Carbon dioxide (CO_2)	44 amu	13.78 eV	$>$ 0.00 eV
Iron	56 amu	7.91 eV	- 0.16 eV
Rhodium	103 amu	7.46 eV	- 1.14 eV

*Electron affinity is the energy required to add an electron to the neutral. Thus, negative numbers mean that energy is liberated. Species with high (negative) electron affinity and high (positive) ionisation energy (e.g. Oxygen) tend to form negative ions. In the cases where energy is needed to form the negative species the value is set to $>$ 0.00. For certain species no data is available.
Data from "Handbook of Chemistry and Physics, 85th Edition" (2002).

Appendix B

TOF-SIMS Data of the Target Contamination Analysis

In this appendix the term “Target” (e.g. Target 2) is used to address the different Rhodium samples. This is equivalent to the term “Sample” used in chapter 2.3.2 (e.g. Sample 2).

For each set of scans the Target (Sample) number, and in case of Target 3 a position index, is given at the top of the page. Each set of the 22 scans contains one or two pages and is identified with a label of the form “Dr0♯♯♯c1” with ♯♯♯ ranging from 280 to 301. If the target was subject to Argon sputtering before the analysis it is indicated by the phrase “after sputtering”.

The individual scans are labelled with either the name or the mass of the respective ion species and its charge (“+” or “-”). The number below each scan is the total number of ions detected (ion yield). On the lower right corner another number marks the maximum intensity measured for a single pixel of the scan. The intensity of each pixel is given as a color code spanning the colours of the visible light spectrum, with blue representing the lowest intensity and red the highest.

Note that CN^- was accidentally attributed as $C_2H_2^-$ in some of the anion scans. In chapter 2.3.2 the cation scans labelled with masses of about 104, 115, and 120 are attributed to RhH^+, RhC^+, and $RhOh^+$ respectively.

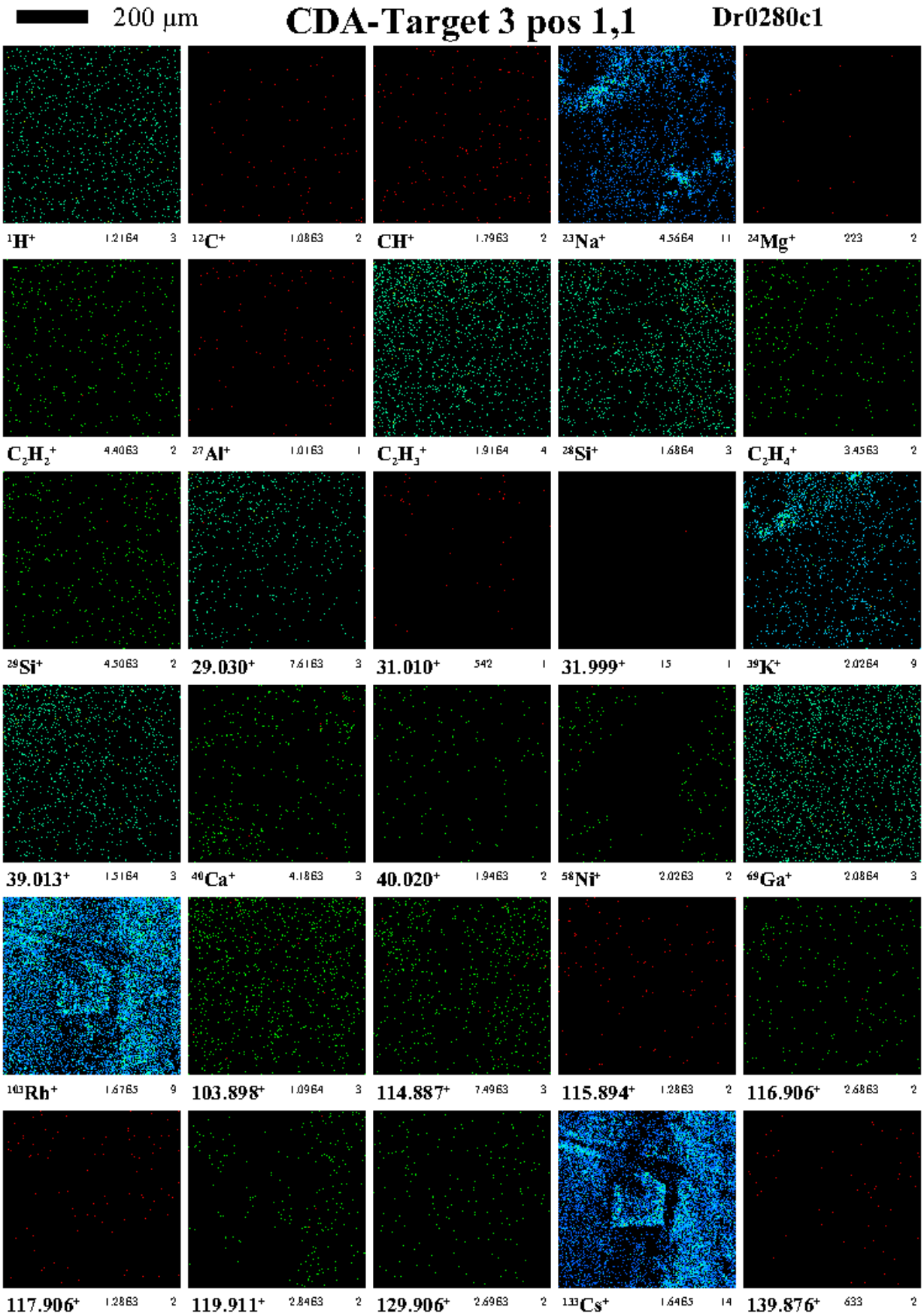
200 µm
CDA-Target 3 pos 1,1
Dr0280c1
$^{1}H^{+}$ 1.2164 3
$^{12}C^{+}$ 1.0863 2
CH^{+} 1.7963 2
$^{23}Na^{+}$ 4.5664 11
$^{24}Mg^{+}$ 223 2
$C_2H_2^{+}$ 4.4063 2
$^{27}Al^{+}$ 1.0163 1
$C_2H_3^{+}$ 1.9164 4
$^{28}Si^{+}$ 1.6864 3
$C_2H_4^{+}$ 3.4563 2
$^{29}Si^{+}$ 4.5063 2
29.030^{+} 7.6163 3
31.010^{+} 542 1
31.999^{+} 15 1
$^{39}K^{+}$ 2.0264 9
39.013^{+} 1.5164 3
$^{40}Ca^{+}$ 4.1863 3
40.020^{+} 1.9463 2
$^{58}Ni^{+}$ 2.0263 2
$^{69}Ga^{+}$ 2.0864 3
$^{103}Rh^{+}$ 1.6765 9
103.898^{+} 1.0964 3
114.887^{+} 7.4963 3
115.894^{+} 1.2863 2
116.906^{+} 2.6863 2
117.906^{+} 1.2863 2
119.911^{+} 2.8463 2
129.906^{+} 2.6963 2
$^{133}Cs^{+}$ 1.6465 14
139.876^{+} 633 2

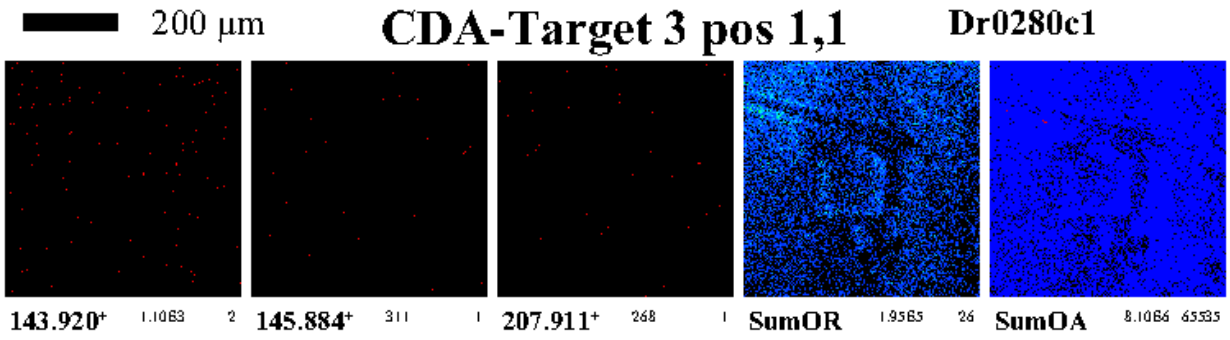
200 µm
CDA-Target 3 pos 1,1
Dr0280c1
143.920+ 1.1083 2
145.884+ 311 1
207.911+ 268 1
SumOR 1.9585 26
SumOA 8.1086 65535

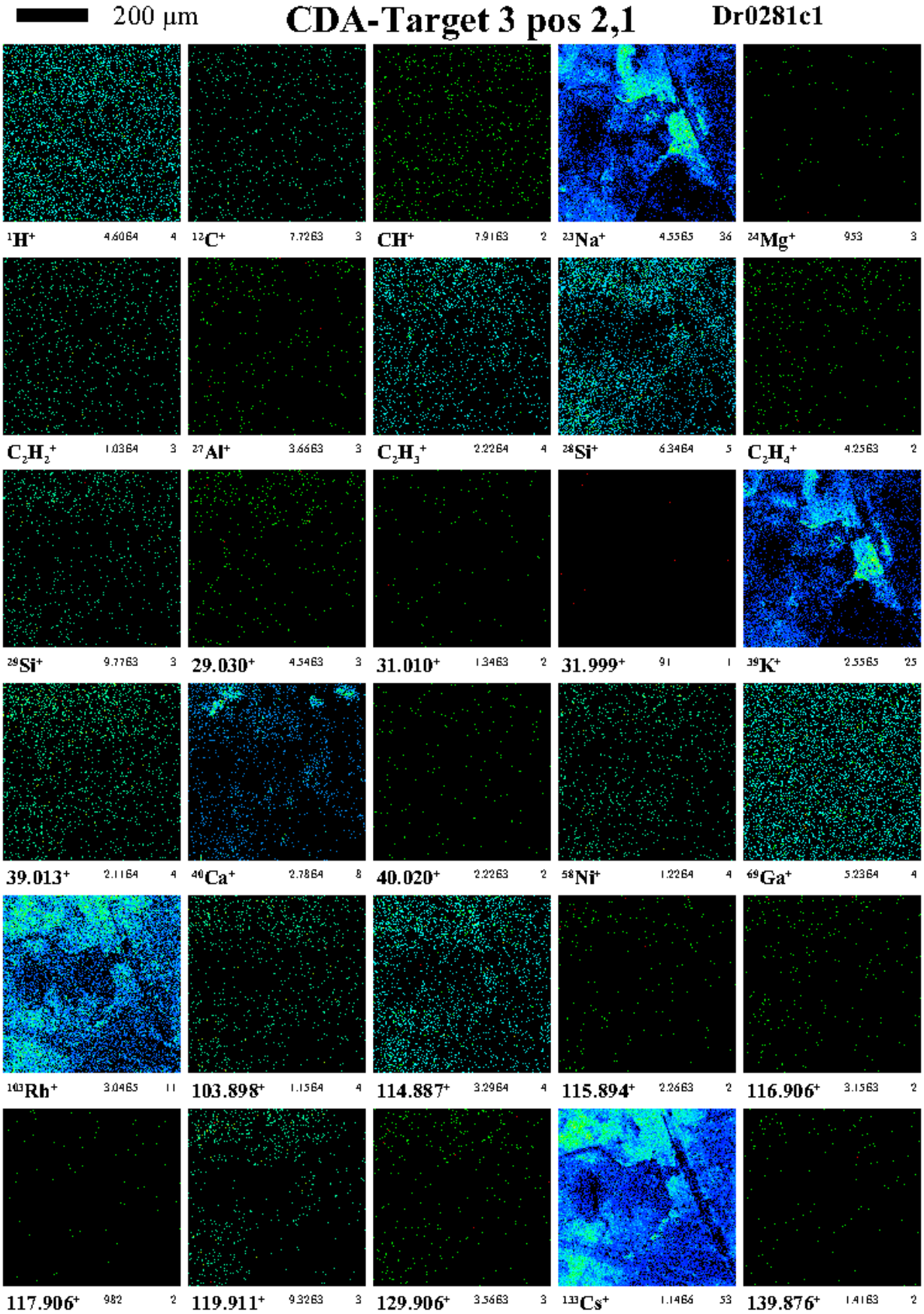
200 µm
CDA-Target 3 pos 2,1
Dr0281c1
$^{1}H^{+}$ 4.6064 4
$^{12}C^{+}$ 7.7263 3
CH^{+} 7.9163 2
$^{23}Na^{+}$ 4.5565 36
$^{24}Mg^{+}$ 953 3
$C_2H_2^{+}$ 1.0364 3
$^{27}Al^{+}$ 3.6663 3
$C_2H_3^{+}$ 2.2264 4
$^{28}Si^{+}$ 6.3464 5
$C_2H_4^{+}$ 4.2563 2
$^{29}Si^{+}$ 9.7763 3
29.030^{+} 4.5463 3
31.010^{+} 1.3463 2
31.999^{+} 91 1
$^{39}K^{+}$ 2.5565 25
39.013^{+} 2.1164 4
$^{40}Ca^{+}$ 2.7864 8
40.020^{+} 2.2263 2
$^{58}Ni^{+}$ 1.2264 4
$^{69}Ga^{+}$ 5.2364 4
$^{103}Rh^{+}$ 3.0465 11
103.898^{+} 1.1564 4
114.887^{+} 3.2964 4
115.894^{+} 2.2663 2
116.906^{+} 3.1563 2
117.906^{+} 982 2
119.911^{+} 9.3263 3
129.906^{+} 3.5663 3
$^{133}Cs^{+}$ 1.1464 53
139.876^{+} 1.4163 2

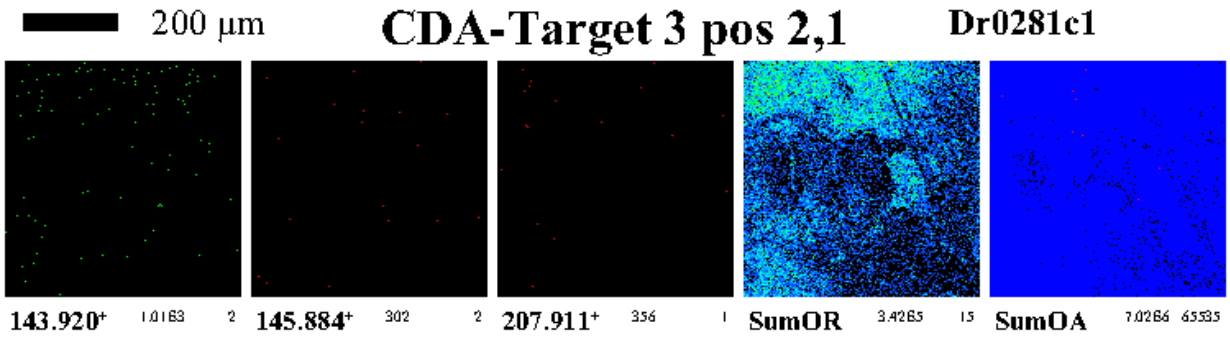
200 µm
CDA-Target 3 pos 2,1
Dr0281c1
143.920+ 1.0183 2
145.884+ 302 2
207.911+ 356 1
SumOR 3.4265 15
SumOA 7.0286 65535

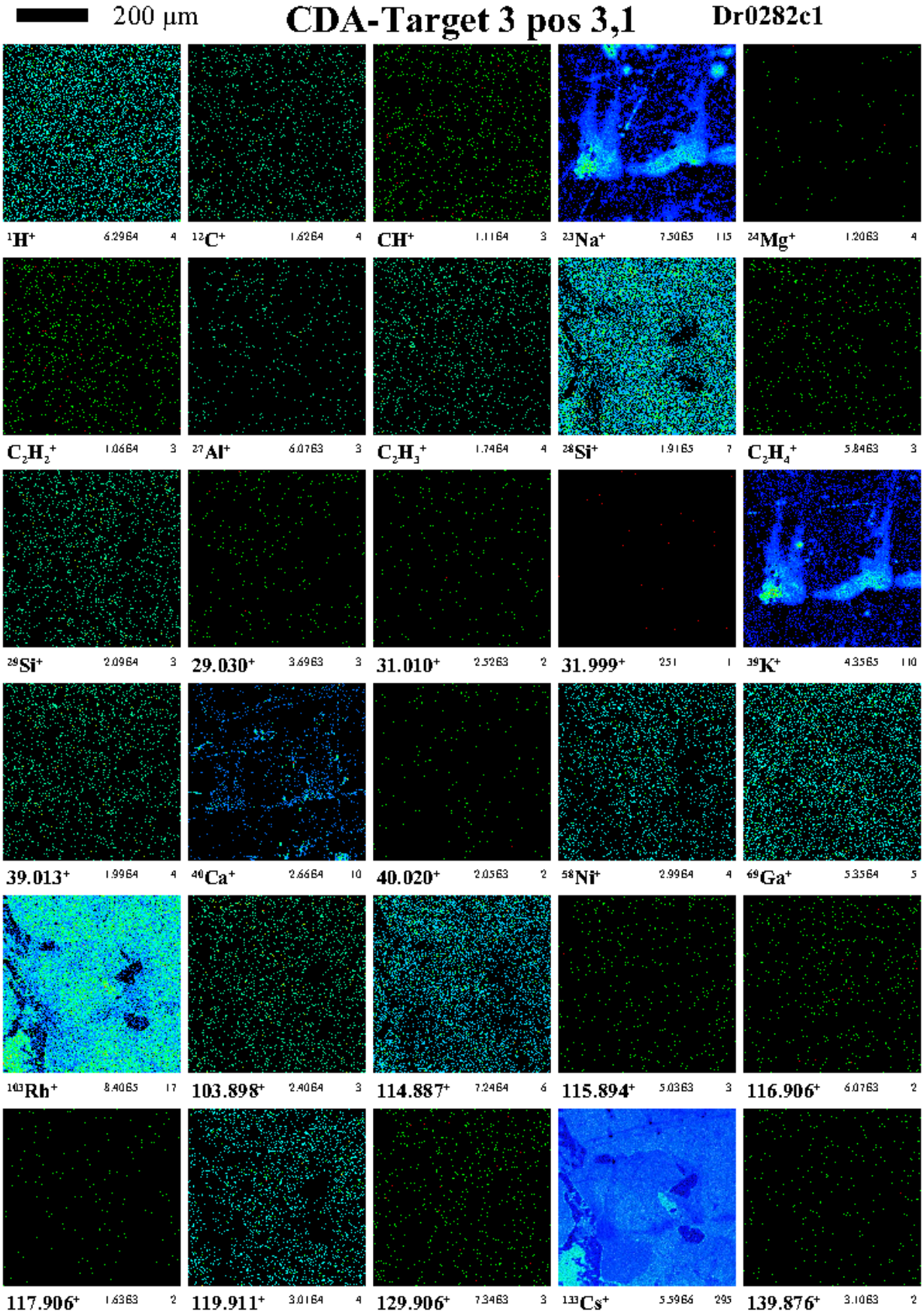
200 µm
CDA-Target 3 pos 3,1
Dr0282c1
$^{1}H^{+}$ 6.29E4 4
$^{12}C^{+}$ 1.62E4 4
CH^{+} 1.11E4 3
$^{23}Na^{+}$ 7.50E3 115
$^{24}Mg^{+}$ 1.20E3 4
$C_2H_2^{+}$ 1.06E4 3
$^{27}Al^{+}$ 6.07E3 3
$C_2H_3^{+}$ 1.74E4 4
$^{28}Si^{+}$ 1.91E5 7
$C_2H_4^{+}$ 5.84E3 3
$^{29}Si^{+}$ 2.09E4 3
29.030^{+} 3.69E3 3
31.010^{+} 2.52E3 2
31.999^{+} 251 1
$^{39}K^{+}$ 4.35E5 110
39.013^{+} 1.99E4 4
$^{40}Ca^{+}$ 2.66E4 10
40.020^{+} 2.05E3 2
$^{58}Ni^{+}$ 2.99E4 4
$^{69}Ga^{+}$ 5.35E4 5
$^{103}Rh^{+}$ 8.40E5 17
103.898^{+} 2.40E4 3
114.887^{+} 7.24E4 6
115.894^{+} 5.03E3 3
116.906^{+} 6.07E3 2
117.906^{+} 1.63E3 2
119.911^{+} 3.01E4 4
129.906^{+} 7.34E3 3
$^{133}Cs^{+}$ 5.59E6 295
139.876^{+} 3.10E3 2

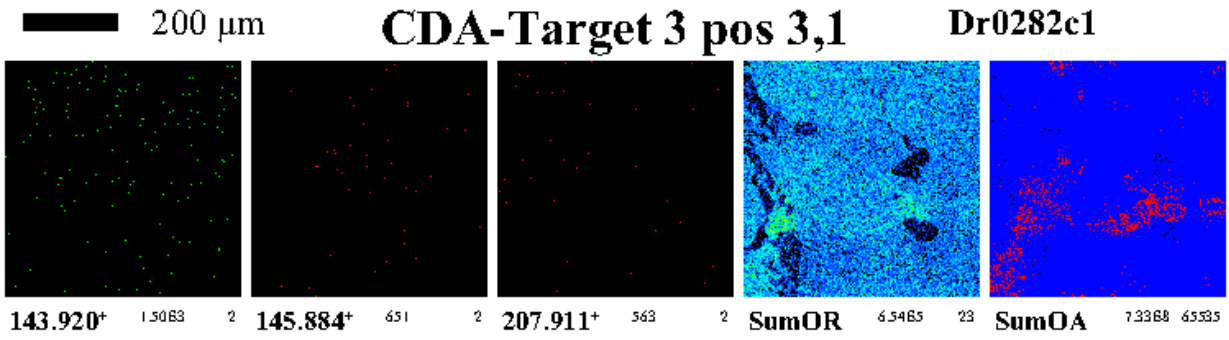
200 µm
CDA-Target 3 pos 3,1
Dr0282c1
143.920+ 15083 2
145.884+ 651 2
207.911+ 563 2
SumOR 65485 23
SumOA 73388 65535

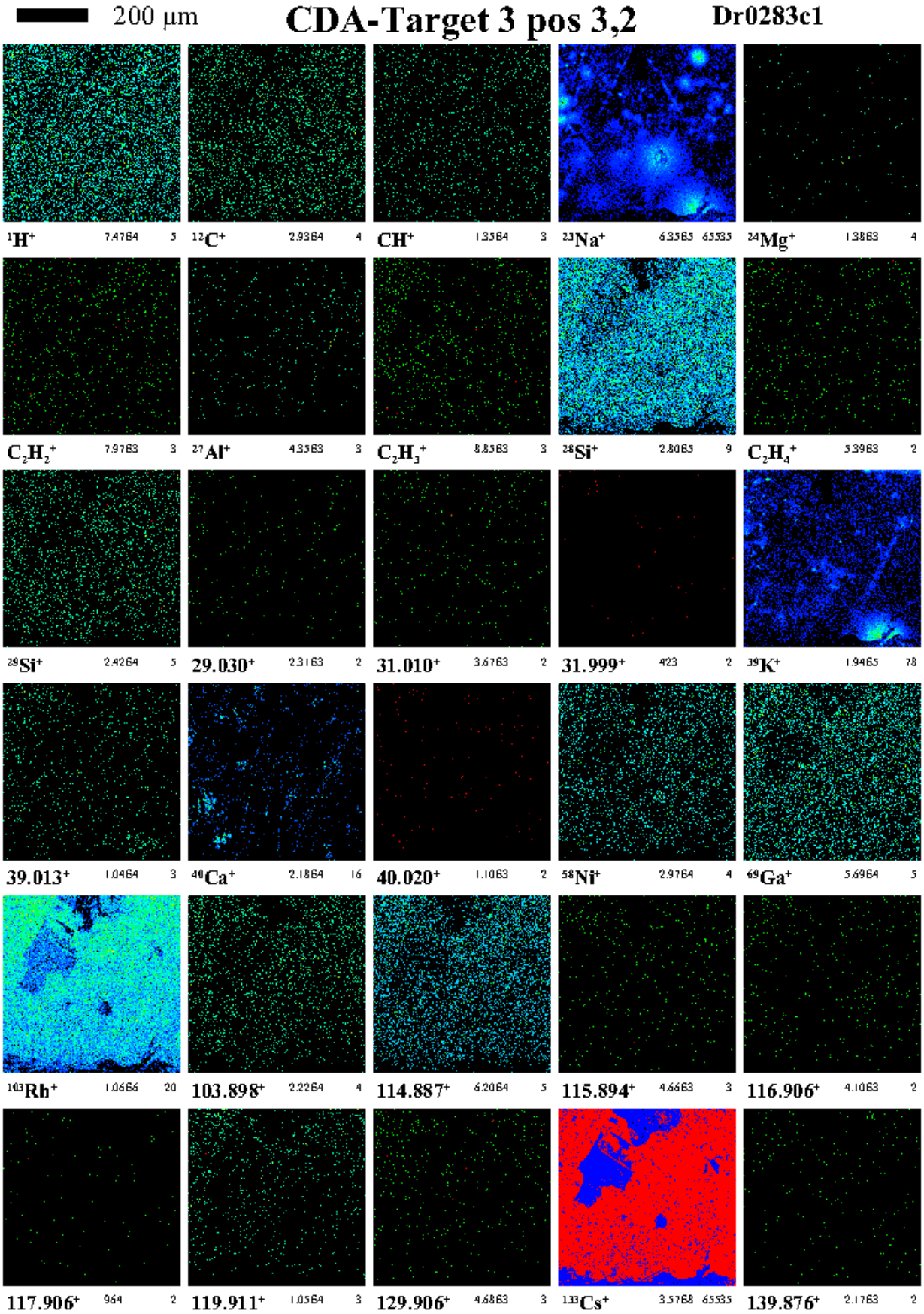
200 µm
CDA-Target 3 pos 3,2
Dr0283c1
$^{1}H^{+}$ 7.47E4 5
$^{12}C^{+}$ 2.93E4 4
CH^{+} 1.35E4 3
$^{23}Na^{+}$ 6.35E5 65535
$^{24}Mg^{+}$ 1.38E3 4
$C_2H_2^{+}$ 7.97E3 3
$^{27}Al^{+}$ 4.35E3 3
$C_2H_3^{+}$ 8.85E3 3
$^{28}Si^{+}$ 2.80E5 9
$C_2H_4^{+}$ 5.39E3 2
$^{29}Si^{+}$ 2.42E4 5
29.030^{+} 2.31E3 2
31.010^{+} 3.67E3 2
31.999^{+} 423 2
$^{39}K^{+}$ 1.94E5 78
39.013^{+} 1.04E4 3
$^{40}Ca^{+}$ 2.18E4 16
40.020^{+} 1.10E3 2
$^{58}Ni^{+}$ 2.97E4 4
$^{69}Ga^{+}$ 5.69E4 5
$^{103}Rh^{+}$ 1.06E6 20
103.898^{+} 2.22E4 4
114.887^{+} 6.20E4 5
115.894^{+} 4.66E3 3
116.906^{+} 4.10E3 2
117.906^{+} 964 2
119.911^{+} 1.05E4 3
129.906^{+} 4.68E3 3
$^{133}Cs^{+}$ 3.57E8 65535
139.876^{+} 2.17E3 2

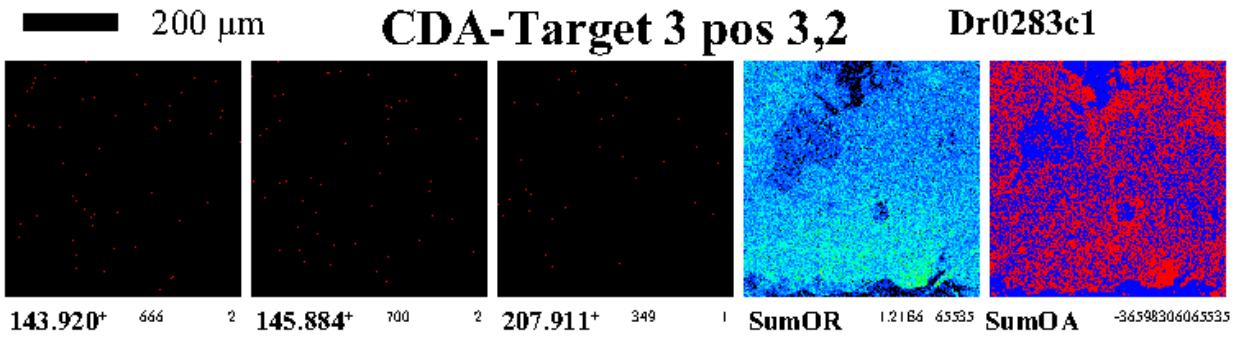
200 µm
CDA-Target 3 pos 3,2
Dr0283c1
143.920+ 666 2
145.884+ 700 2
207.911+ 349 1
SumOR 1.2166 65535
SumOA -365983060655535

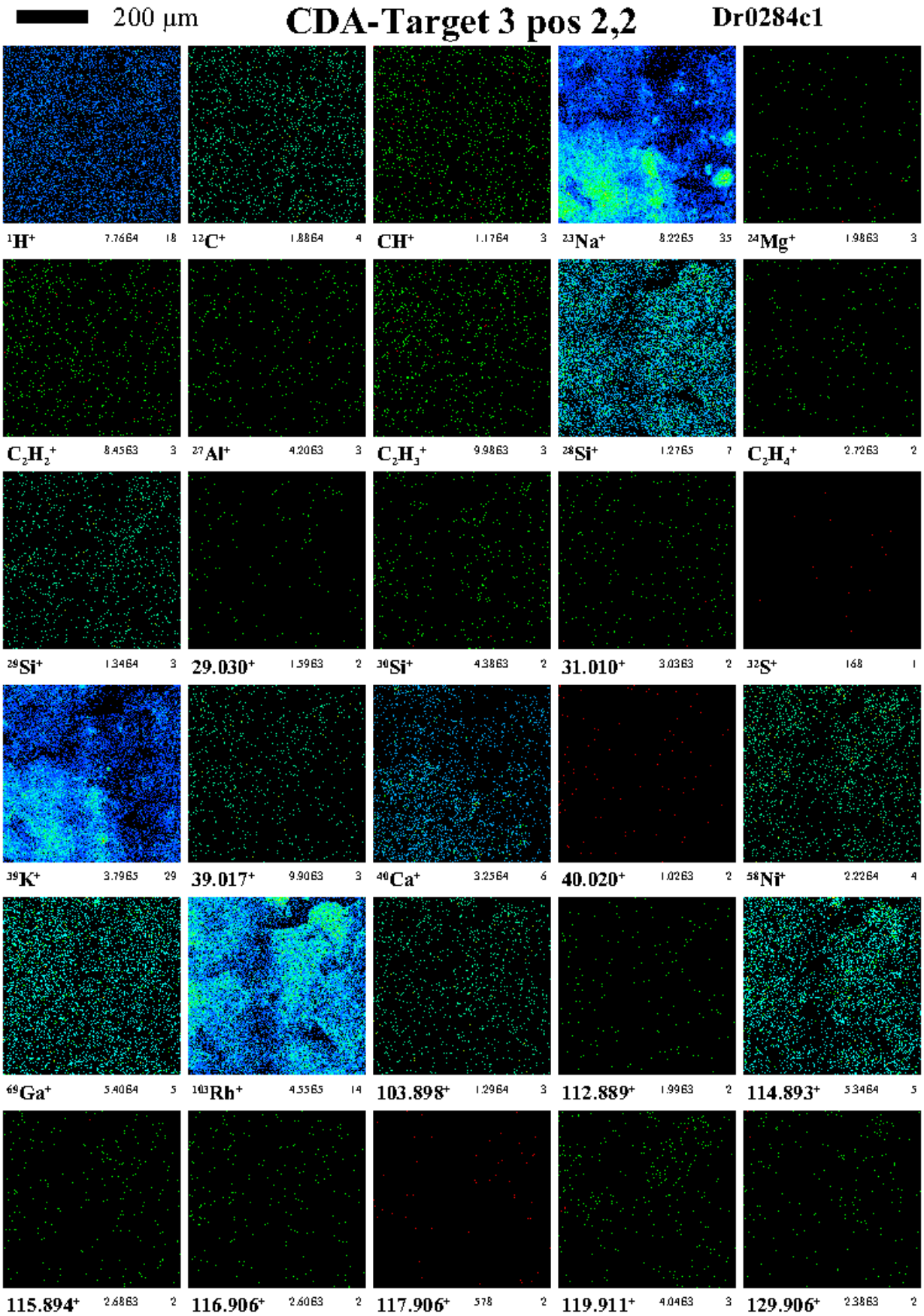
200 µm
CDA-Target 3 pos 2,2
Dr0284c1
$^{1}H^{+}$ 7.76E4 18
$^{12}C^{+}$ 1.88E4 4
CH^{+} 1.17E4 3
$^{23}Na^{+}$ 8.22E5 35
$^{24}Mg^{+}$ 1.98E3 3
$C_2H_2^{+}$ 8.45E3 3
$^{27}Al^{+}$ 4.20E3 3
$C_2H_3^{+}$ 9.98E3 3
$^{28}Si^{+}$ 1.27E5 7
$C_2H_4^{+}$ 2.72E3 2
$^{29}Si^{+}$ 1.34E4 3
29.030^{+} 1.59E3 2
$^{30}Si^{+}$ 4.38E3 2
31.010^{+} 3.03E3 2
$^{32}S^{+}$ 168 1
$^{39}K^{+}$ 3.79E5 29
39.017^{+} 9.90E3 3
$^{40}Ca^{+}$ 3.25E4 6
40.020^{+} 1.02E3 2
$^{58}Ni^{+}$ 2.22E4 4
$^{69}Ga^{+}$ 5.40E4 5
$^{103}Rh^{+}$ 4.55E5 14
103.898^{+} 1.29E4 3
112.889^{+} 1.99E3 2
114.893^{+} 5.34E4 5
115.894^{+} 2.68E3 2
116.906^{+} 2.60E3 2
117.906^{+} 578 2
119.911^{+} 4.04E3 3
129.906^{+} 2.38E3 2

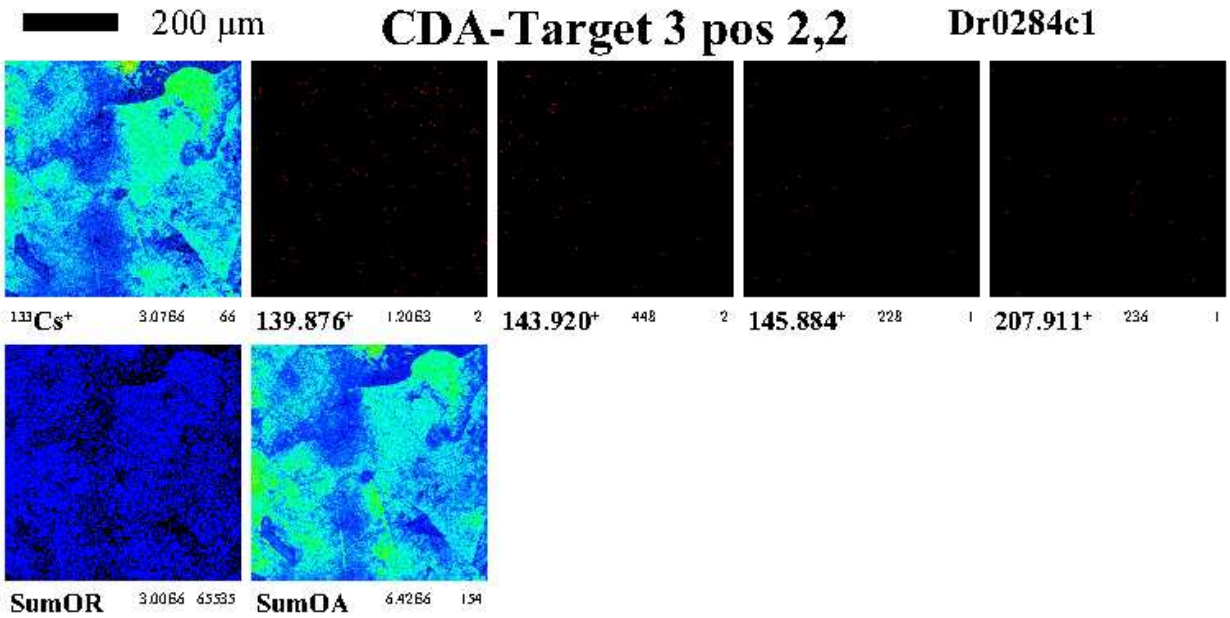
200 µm
CDA-Target 3 pos 2,2
Dr0284c1
133Cs+ 3.0786 66
139.876+ 1.2063 2
143.920+ 448 2
145.884+ 228 1
207.911+ 236 1
SumOR 3.0086 65535
SumOA 6.4286 154

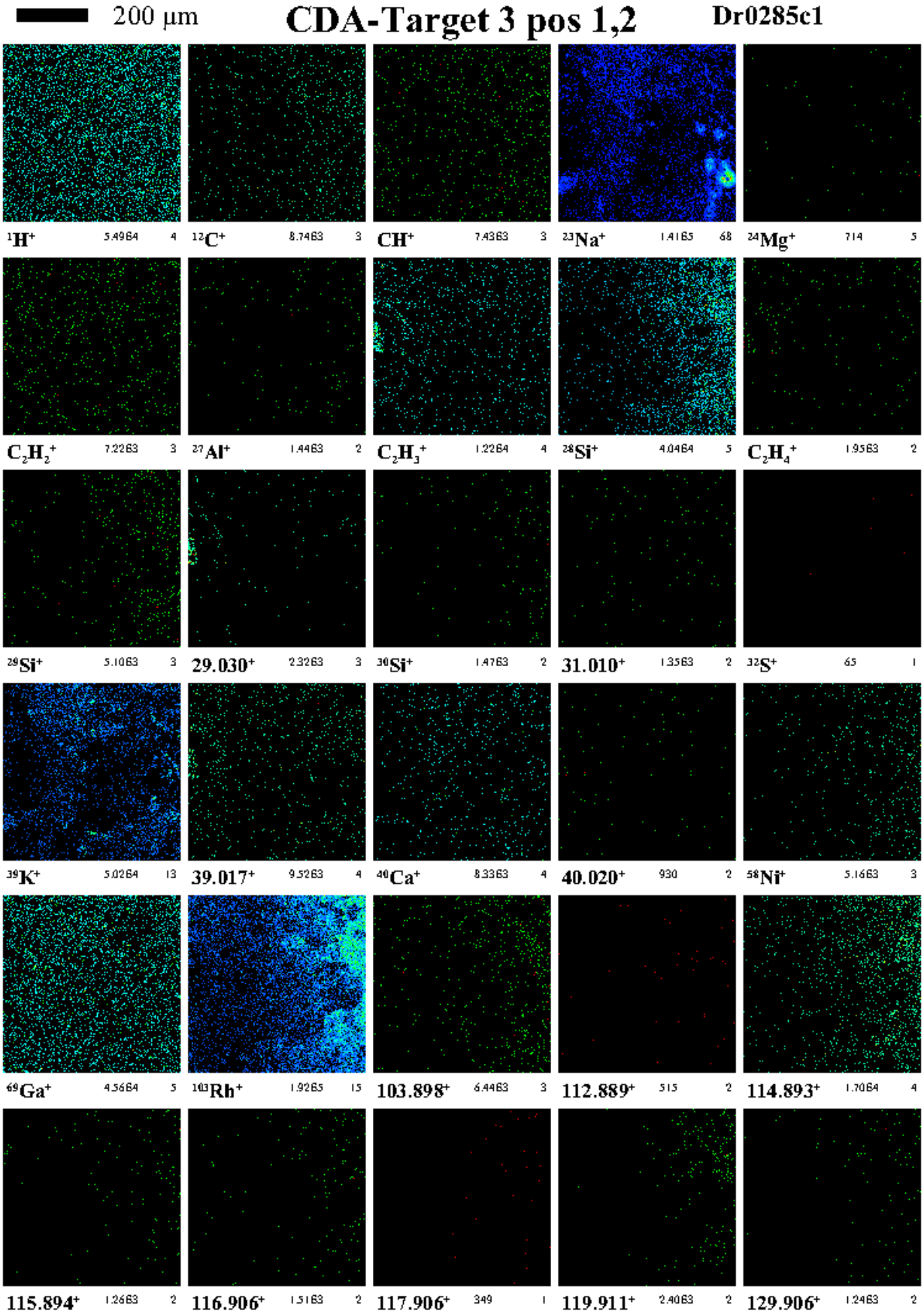
200 µm
CDA-Target 3 pos 1,2
Dr0285c1
$^{1}H^{+}$ 5.49E4 4
$^{12}C^{+}$ 8.74E3 3
CH^{+} 7.43E3 3
$^{23}Na^{+}$ 1.41E5 68
$^{24}Mg^{+}$ 714 5
$C_2H_2^{+}$ 7.22E3 3
$^{27}Al^{+}$ 1.44E3 2
$C_2H_3^{+}$ 1.22E4 4
$^{28}Si^{+}$ 4.04E4 5
$C_2H_4^{+}$ 1.95E3 2
$^{29}Si^{+}$ 5.10E3 3
29.030^{+} 2.32E3 3
$^{30}Si^{+}$ 1.47E3 2
31.010^{+} 1.35E3 2
$^{32}S^{+}$ 65 1
$^{39}K^{+}$ 5.02E4 13
39.017^{+} 9.52E3 4
$^{40}Ca^{+}$ 8.33E3 4
40.020^{+} 930 2
$^{58}Ni^{+}$ 5.16E3 3
$^{69}Ga^{+}$ 4.56E4 5
$^{103}Rh^{+}$ 1.92E5 15
103.898^{+} 6.44E3 3
112.889^{+} 515 2
114.893^{+} 1.70E4 4
115.894^{+} 1.26E3 2
116.906^{+} 1.51E3 2
117.906^{+} 349 1
119.911^{+} 2.40E3 2
129.906^{+} 1.24E3 2

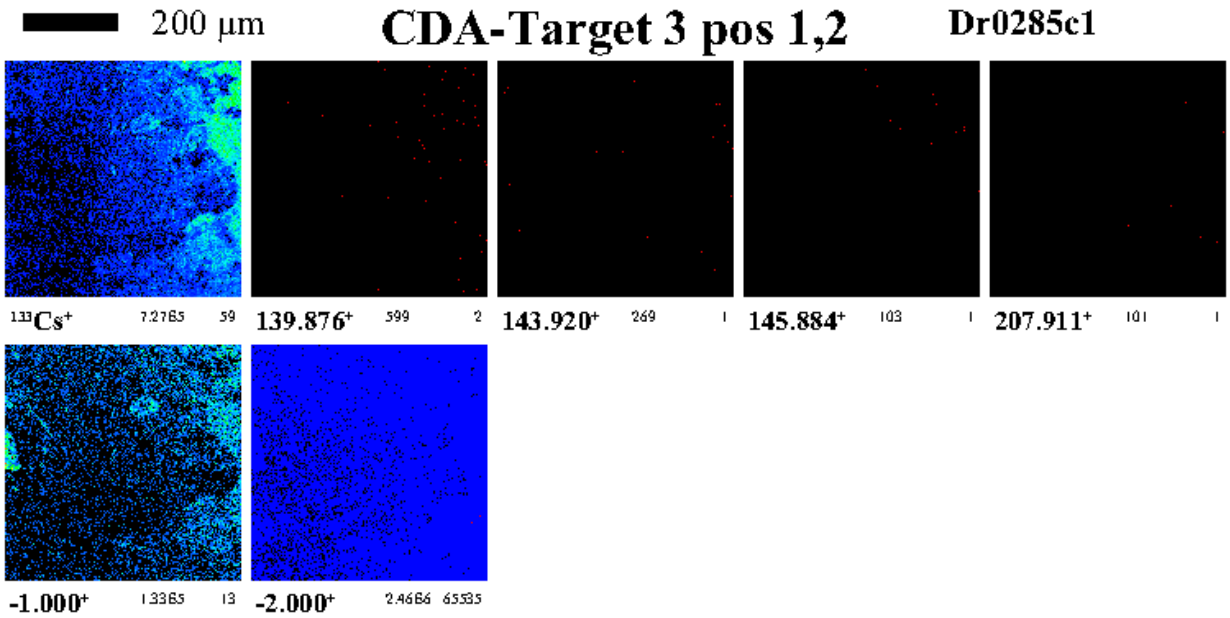
200 µm
CDA-Target 3 pos 1,2
Dr0285c1
133Cs+ 7.2785 59
139.876+ 599 2
143.920+ 269 1
145.884+ 103 1
207.911+ 101 1
-1.000+ 1.3385 13
-2.000+ 2.4686 65535

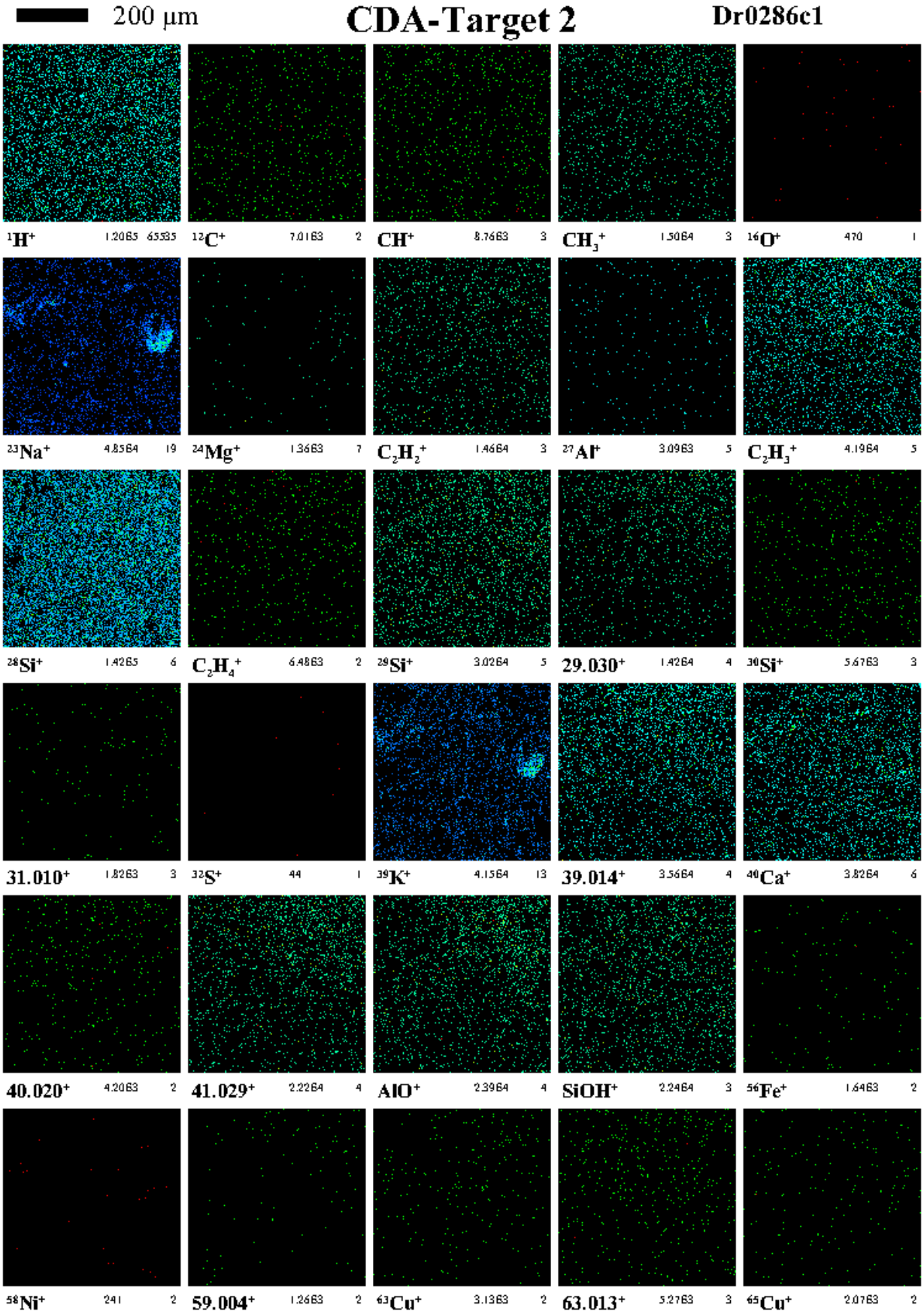
200 µm
CDA-Target 2
Dr0286c1
1H+ 1.20E5 65535
12C+ 7.01E3 2
CH+ 8.76E3 3
CH3+ 1.50E4 3
16O+ 470 1
23Na+ 4.85E4 19
24Mg+ 1.36E3 7
C2H2+ 1.46E4 3
27Al+ 3.09E3 5
C2H3+ 4.19E4 5
28Si+ 1.42E5 6
C2H4+ 6.48E3 2
29Si+ 3.02E4 5
29.030+ 1.42E4 4
30Si+ 5.67E3 3
31.010+ 1.82E3 3
32S+ 44 1
39K+ 4.15E4 13
39.014+ 3.56E4 4
40Ca+ 3.82E4 6
40.020+ 4.20E3 2
41.029+ 2.22E4 4
AlO+ 2.39E4 4
SiOH+ 2.24E4 3
56Fe+ 1.64E3 2
58Ni+ 241 2
59.004+ 1.26E3 2
63Cu+ 3.13E3 2
63.013+ 5.27E3 3
65Cu+ 2.07E3 2

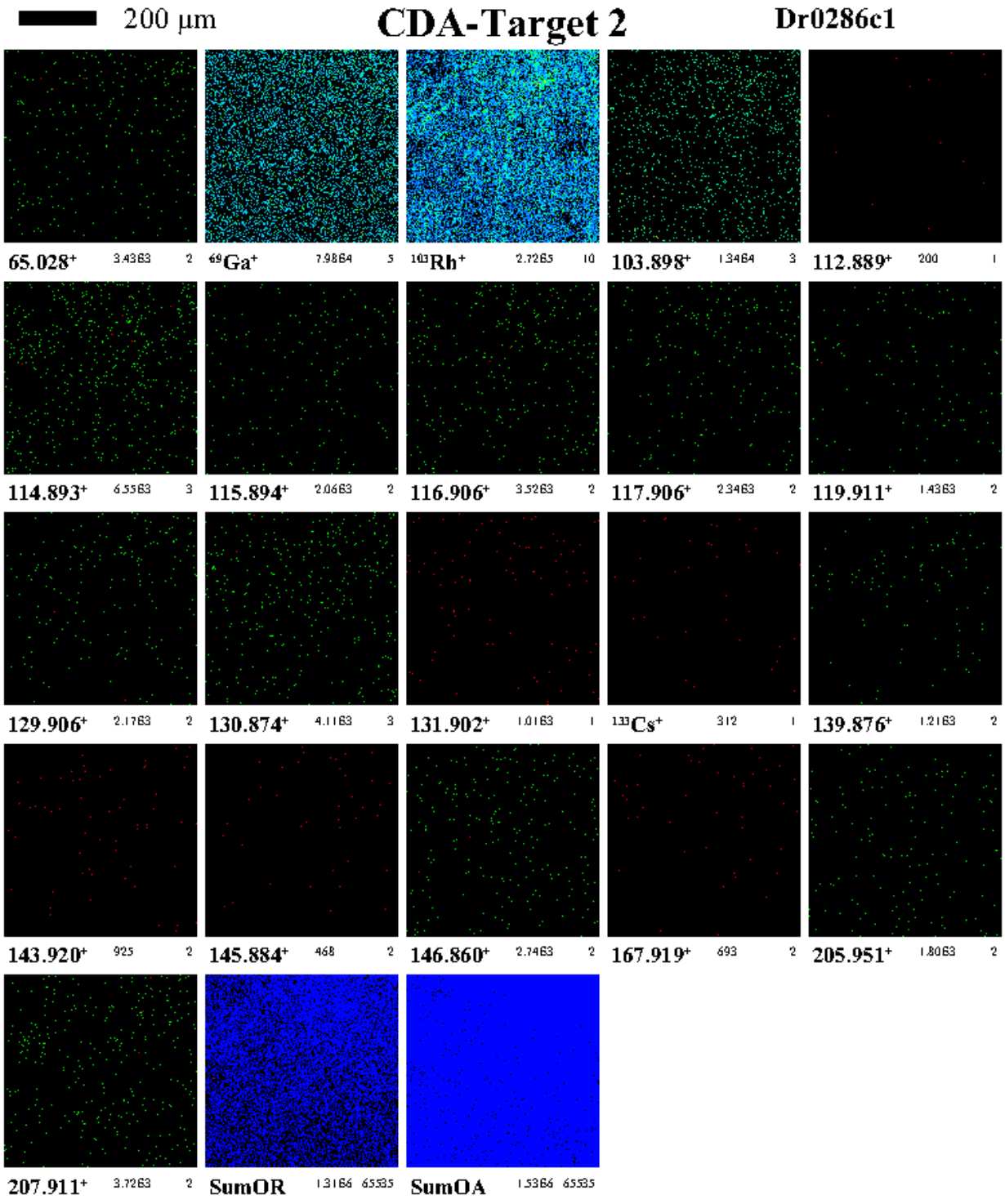
200 µm
CDA-Target 2
Dr0286c1
65.028+ 3.4363 2
69Ga+ 7.9864 5
103Rh+ 2.7265 10
103.898+ 1.3464 3
112.889+ 200 1
114.893+ 6.5563 3
115.894+ 2.0663 2
116.906+ 3.5263 2
117.906+ 2.3463 2
119.911+ 1.4363 2
129.906+ 2.1763 2
130.874+ 4.1163 3
131.902+ 1.0163 1
133Cs+ 312 1
139.876+ 1.2163 2
143.920+ 925 2
145.884+ 468 2
146.860+ 2.7463 2
167.919+ 693 2
205.951+ 1.8063 2
207.911+ 3.7263 2
SumOR 1.3166 65535
SumOA 1.5366 65535

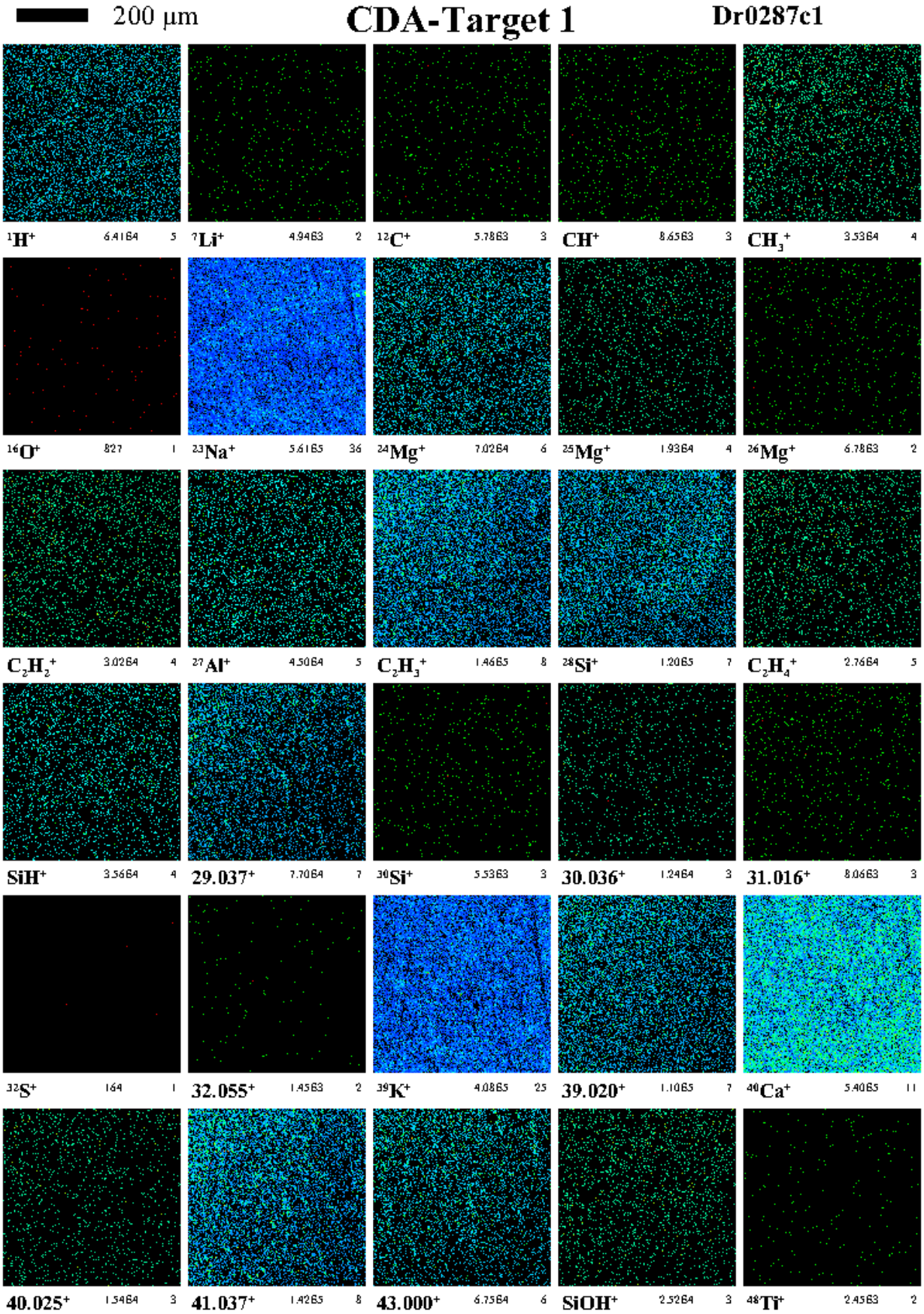
200 µm
CDA-Target 1
Dr0287c1
$^{1}H^{+}$ 6.41E4 5
$^{7}Li^{+}$ 4.94E3 2
$^{12}C^{+}$ 5.78E3 3
CH^{+} 8.65E3 3
CH_3^{+} 3.53E4 4
$^{16}O^{+}$ 827 1
$^{23}Na^{+}$ 5.61E5 36
$^{24}Mg^{+}$ 7.02E4 6
$^{25}Mg^{+}$ 1.93E4 4
$^{26}Mg^{+}$ 6.78E3 2
$C_2H_2^{+}$ 3.02E4 4
$^{27}Al^{+}$ 4.50E4 5
$C_2H_3^{+}$ 1.46E5 8
$^{28}Si^{+}$ 1.20E5 7
$C_2H_4^{+}$ 2.76E4 5
SiH^{+} 3.56E4 4
29.037+ 7.70E4 7
$^{30}Si^{+}$ 5.53E3 3
30.036+ 1.24E4 3
31.016+ 8.06E3 3
$^{32}S^{+}$ 164 1
32.055+ 1.45E3 2
$^{39}K^{+}$ 4.08E5 25
39.020+ 1.10E5 7
$^{40}Ca^{+}$ 5.40E5 11
40.025+ 1.54E4 3
41.037+ 1.42E5 8
43.000+ 6.75E4 6
$SiOH^{+}$ 2.52E4 3
$^{48}Ti^{+}$ 2.45E3 2

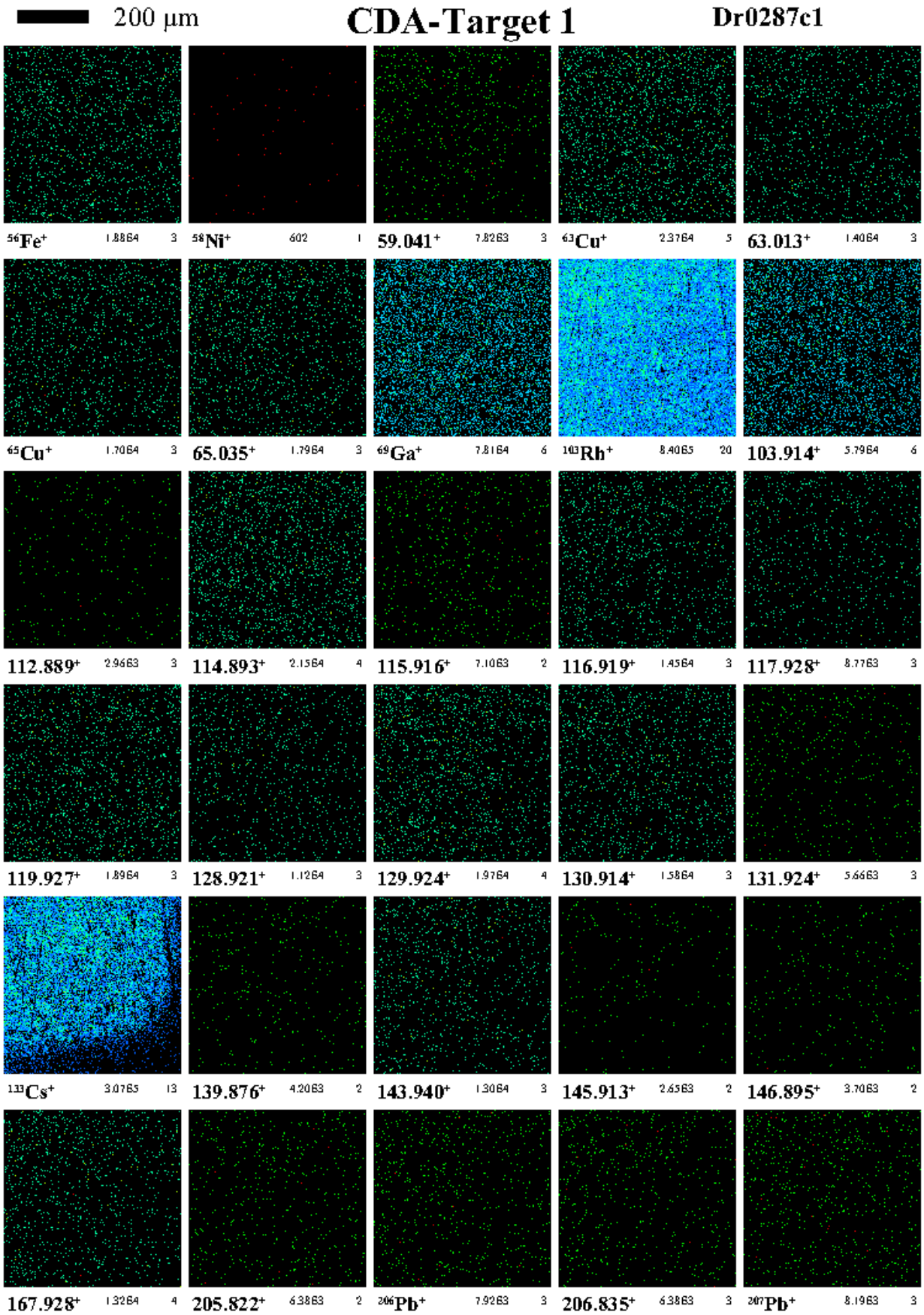
200 µm
CDA-Target 1
Dr0287c1
56Fe+ 1.88E4 3
58Ni+ 602 1
59.041+ 7.82E3 3
63Cu+ 2.37E4 5
63.013+ 1.40E4 3
65Cu+ 1.70E4 3
65.035+ 1.79E4 3
69Ga+ 7.81E4 6
103Rh+ 8.40E5 20
103.914+ 5.79E4 6
112.889+ 2.96E3 3
114.893+ 2.15E4 4
115.916+ 7.10E3 2
116.919+ 1.45E4 3
117.928+ 8.77E3 3
119.927+ 1.89E4 3
128.921+ 1.12E4 3
129.924+ 1.97E4 4
130.914+ 1.58E4 3
131.924+ 5.66E3 3
133Cs+ 3.07E5 13
139.876+ 4.20E3 2
143.940+ 1.30E4 3
145.913+ 2.65E3 2
146.895+ 3.70E3 2
167.928+ 1.32E4 4
205.822+ 6.38E3 2
206Pb+ 7.92E3 3
206.835+ 6.38E3 3
207Pb+ 8.19E3 3

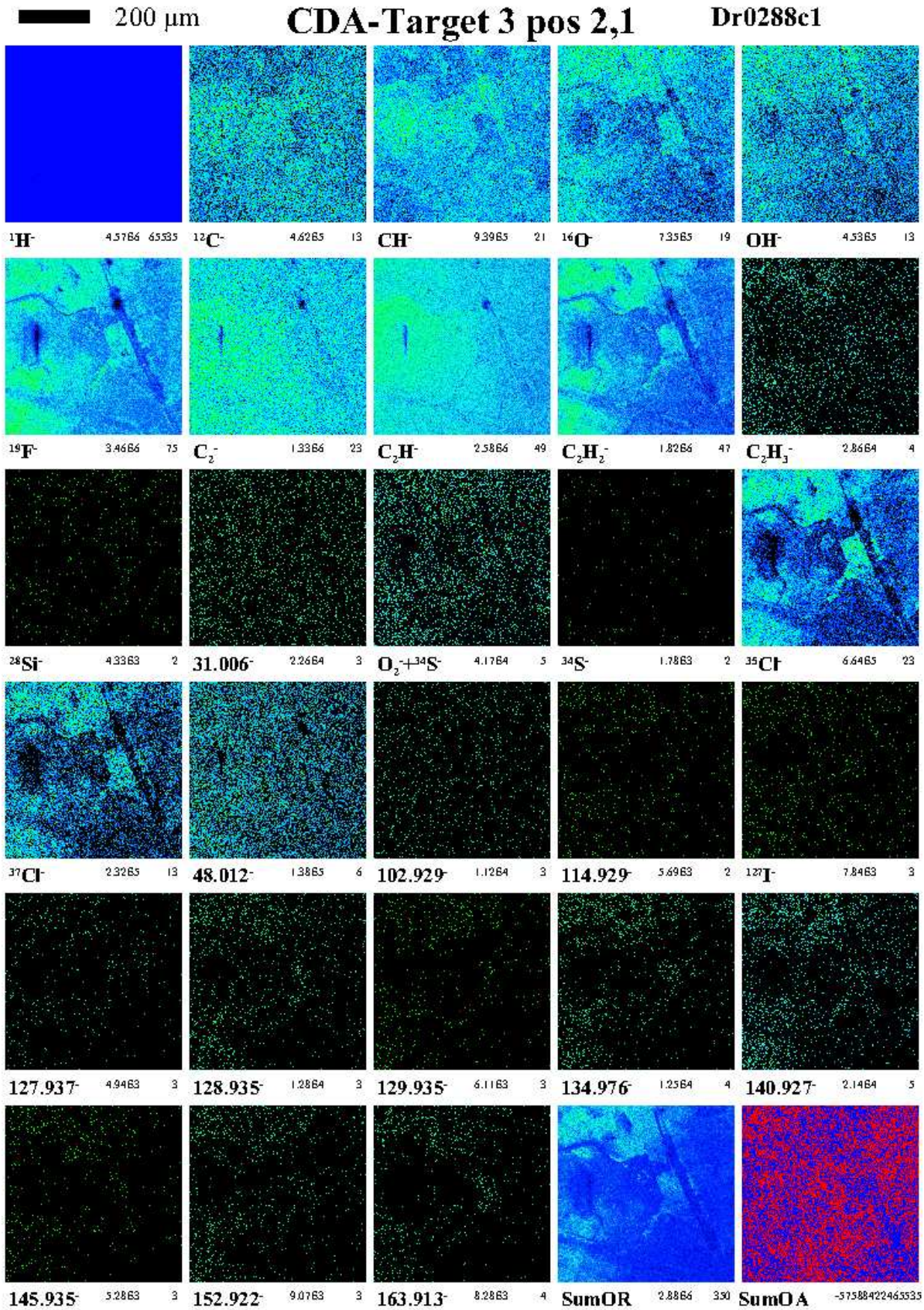
200 µm
CDA-Target 3 pos 2,1
Dr0288c1
1H- 4.5786 65535
12C- 4.6285 13
CH- 9.3985 21
16O- 7.3585 19
OH- 4.5385 13
19F- 3.4686 75
C2- 1.3386 23
C2H- 2.5886 49
C2H2- 1.8286 47
C2H3- 2.8684 4
28Si- 4.3383 2
31.006- 2.2684 3
O2-+34S- 4.1784 5
34S- 1.7883 2
35Cl- 6.6485 23
37Cl- 2.3285 13
48.012- 1.3885 6
102.929- 1.1284 3
114.929- 5.6983 2
127I- 7.8483 3
127.937- 4.9483 3
128.935- 1.2884 3
129.935- 6.1183 3
134.976- 1.2584 4
140.927- 2.1484 5
145.935- 5.2883 3
152.922- 9.0783 3
163.913- 8.2883 4
SumOR 2.8886 350
SumOA -575884224655535

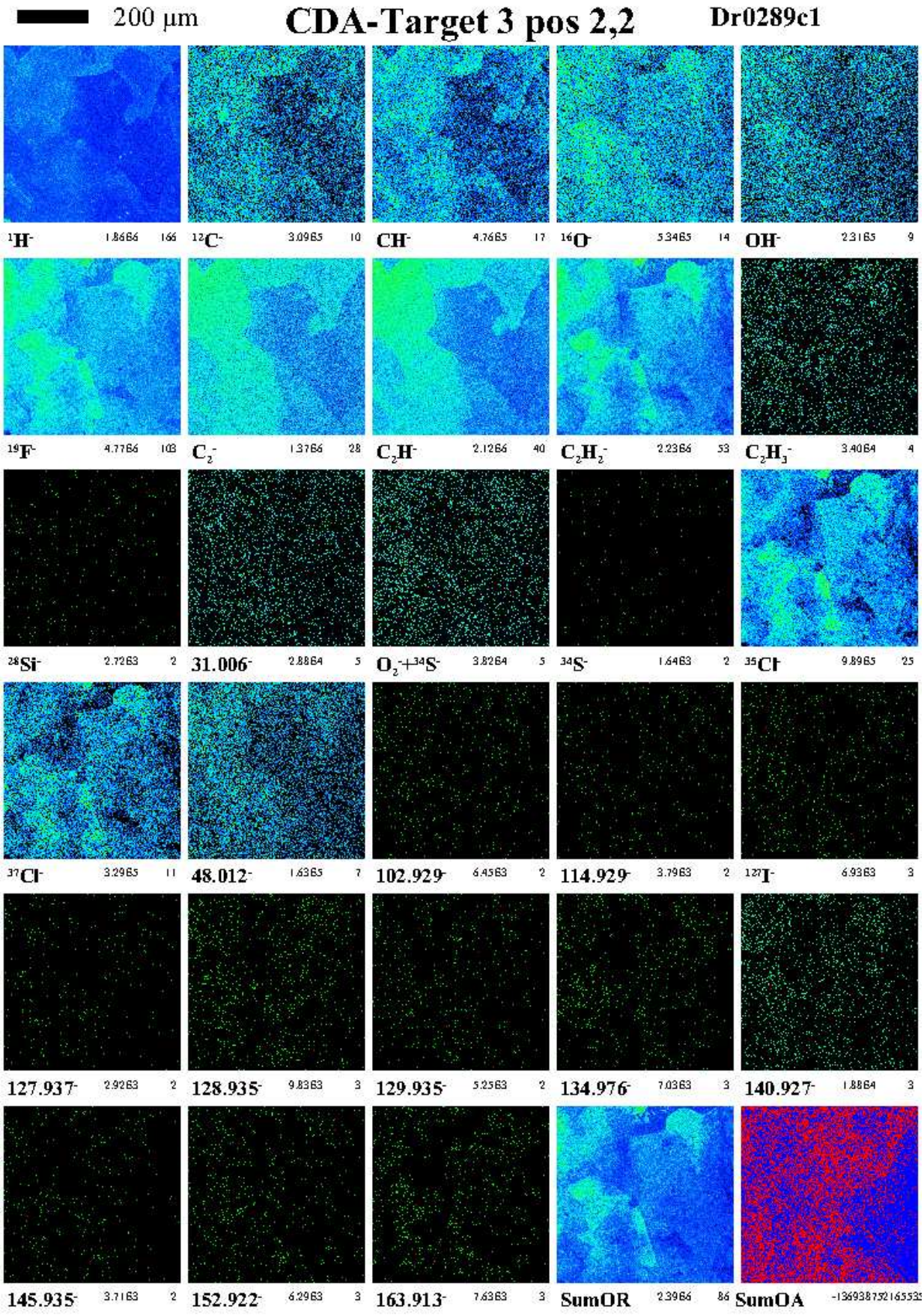
200 µm
CDA-Target 3 pos 2,2
Dr0289c1
1H- 1.86E6 166
12C- 3.09E5 10
CH- 4.76E5 17
16O- 5.34E5 14
OH- 2.31E5 9
19F- 4.77E6 103
C2- 1.37E6 28
C2H- 2.12E6 40
C2H2- 2.23E6 53
C2H3- 3.40E4 4
28Si- 2.72E3 2
31.006- 2.88E4 5
O2-+34S- 3.82E4 5
34S- 1.64E3 2
35Cl- 9.89E5 25
37Cl- 3.29E5 11
48.012- 1.63E5 7
102.929- 6.45E3 2
114.929- 3.79E3 2
127I- 6.93E3 3
127.937- 2.92E3 2
128.935- 9.83E3 3
129.935- 5.25E3 2
134.976- 7.03E3 3
140.927- 1.88E4 3
145.935- 3.71E3 2
152.922- 6.29E3 3
163.913- 7.63E3 3
SumOR 2.39E6 86
SumOA -1369387521655

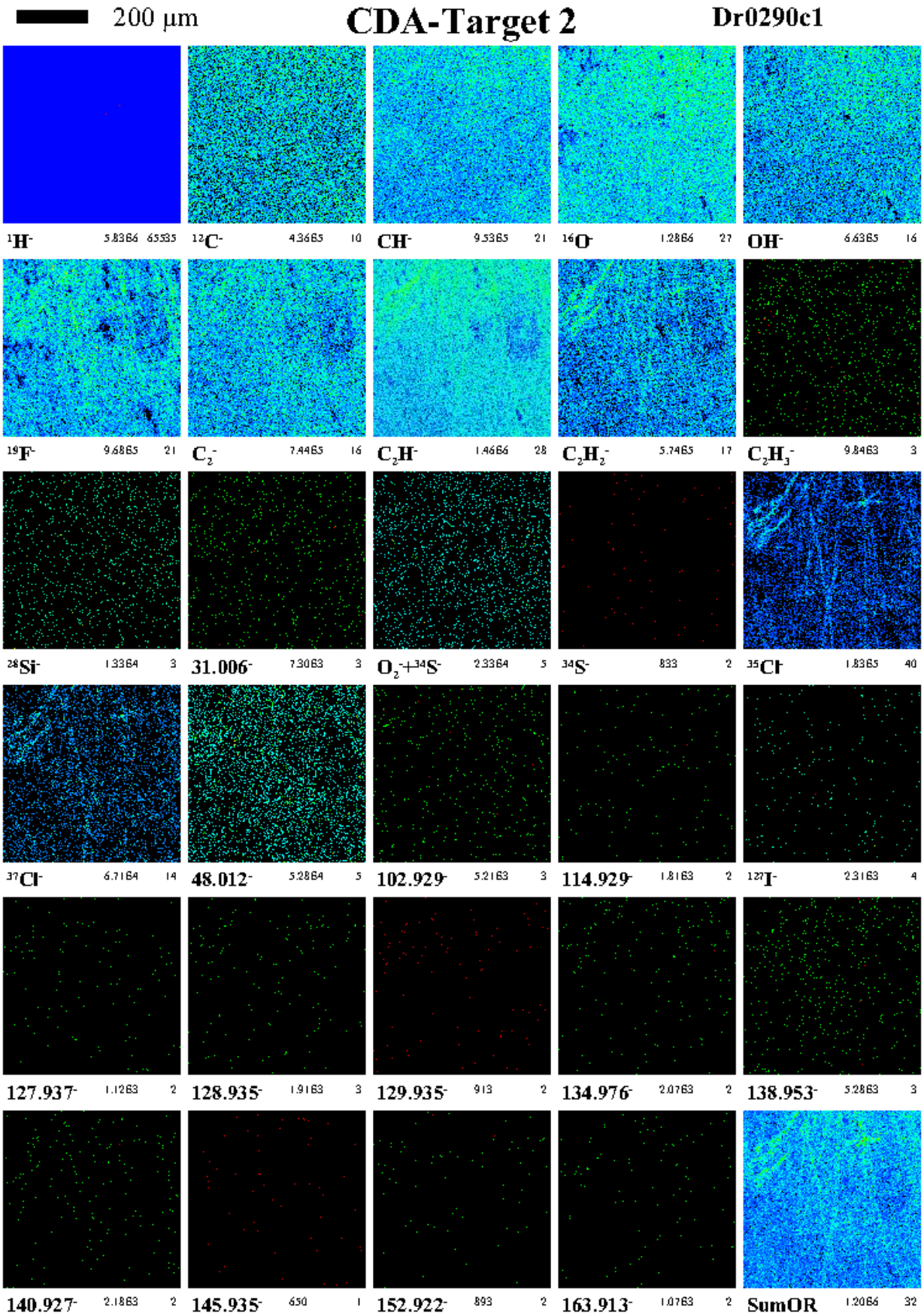
200 µm
CDA-Target 2
Dr0290c1
1H- 5.8386 65535
12C- 4.3685 10
CH- 9.5385 21
16O- 1.2886 27
OH- 6.6385 16
19F- 9.6885 21
C2- 7.4485 16
C2H- 1.4686 28
C2H2- 5.7485 17
C2H3- 9.8483 3
28Si- 1.3384 3
31.006- 7.3083 3
O2-+34S- 2.3384 5
34S- 833 2
35Cl- 1.8385 40
37Cl- 6.7184 14
48.012- 5.2884 5
102.929- 5.2183 3
114.929- 1.8183 2
127I- 2.3183 4
127.937- 1.1283 2
128.935- 1.9183 3
129.935- 913 2
134.976- 2.0783 2
138.953- 5.2883 3
140.927- 2.1883 2
145.935- 650 1
152.922- 893 2
163.913- 1.0783 2
SumOR 1.2086 32

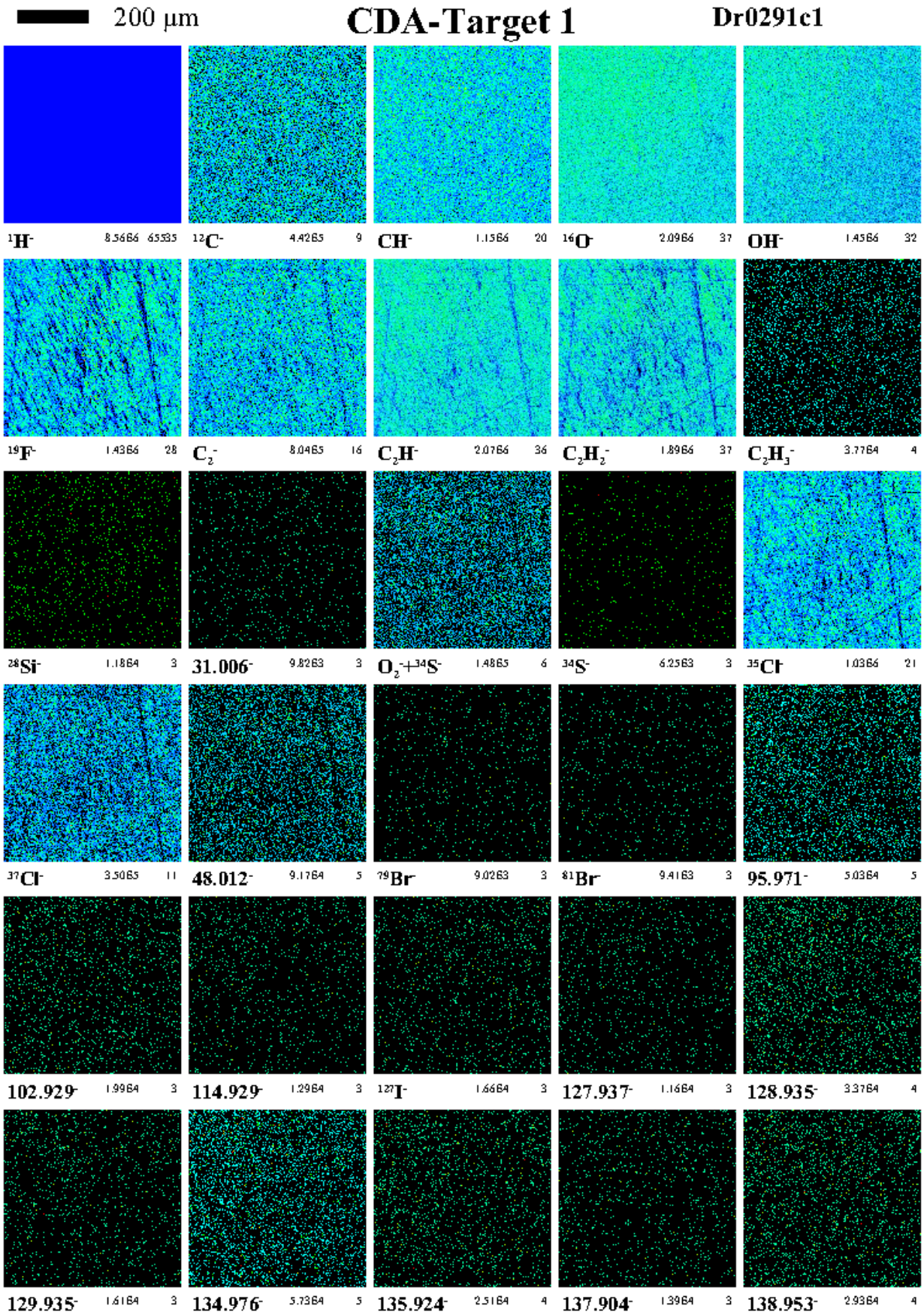
200 µm
CDA-Target 1
Dr0291c1
1H- 8.5686 65535
12C- 4.4265 9
CH- 1.1586 20
16O- 2.0986 37
OH- 1.4586 32
19F- 1.4386 28
C2- 8.0465 16
C2H- 2.0786 36
C2H2- 1.8986 37
C2H3- 3.7784 4
28Si- 1.1884 3
31.006- 9.8263 3
O2-+34S- 1.4885 6
34S- 6.2563 3
35Cl- 1.0386 21
37Cl- 3.5085 11
48.012- 9.1764 5
79Br- 9.0263 3
81Br- 9.4163 3
95.971- 5.0384 5
102.929- 1.9984 3
114.929- 1.2984 3
127I- 1.6684 3
127.937- 1.1684 3
128.935- 3.3784 4
129.935- 1.6184 3
134.976- 5.7384 5
135.924- 2.5184 4
137.904- 1.3984 3
138.953- 2.9384 4

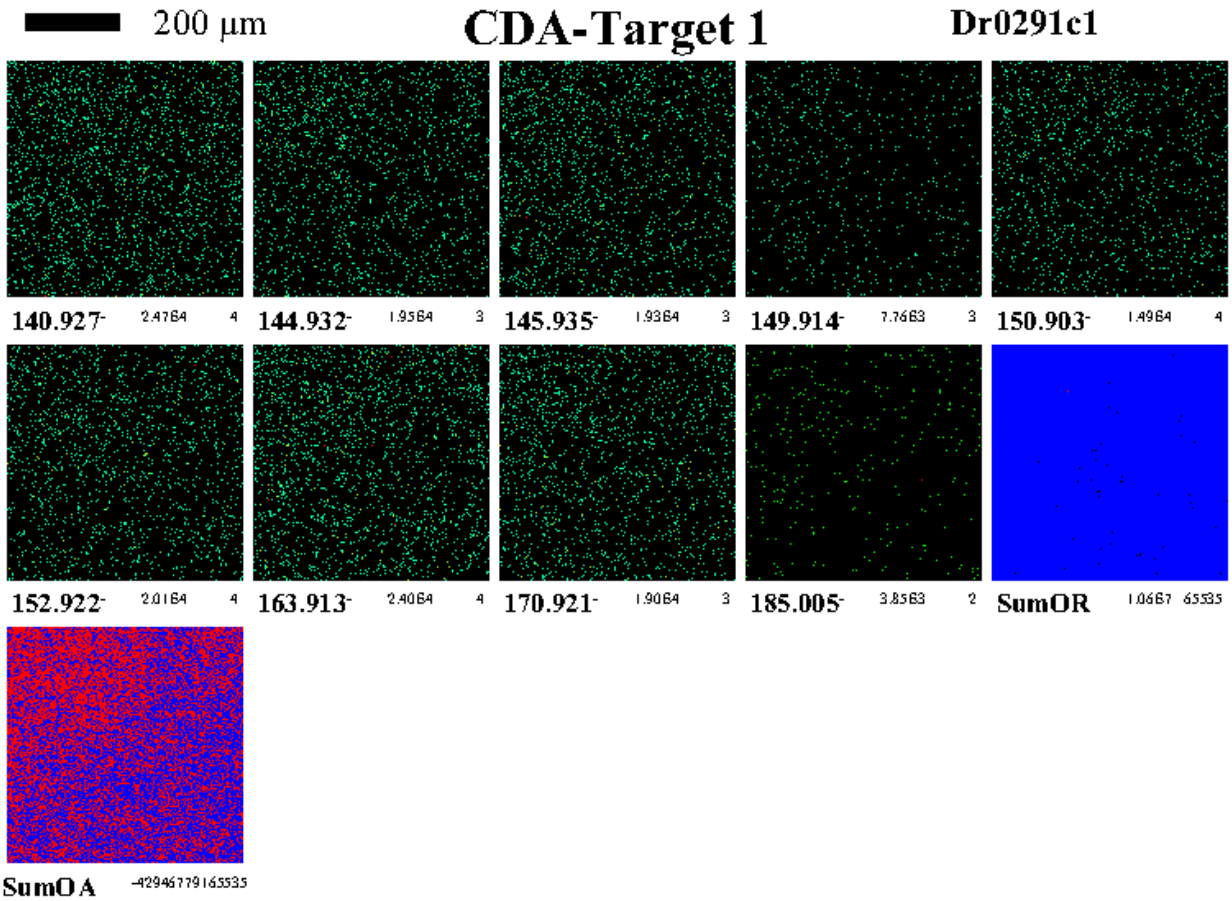
200 µm
CDA-Target 1
Dr0291c1
140.927- 2.4764 4
144.932- 1.9564 3
145.935- 1.9364 3
149.914- 7.7663 3
150.903- 1.4964 4
152.922- 2.0164 4
163.913- 2.4064 4
170.921- 1.9064 3
185.005- 3.8563 2
SumOR 1.0667 65535
SumOA -4294677916535535

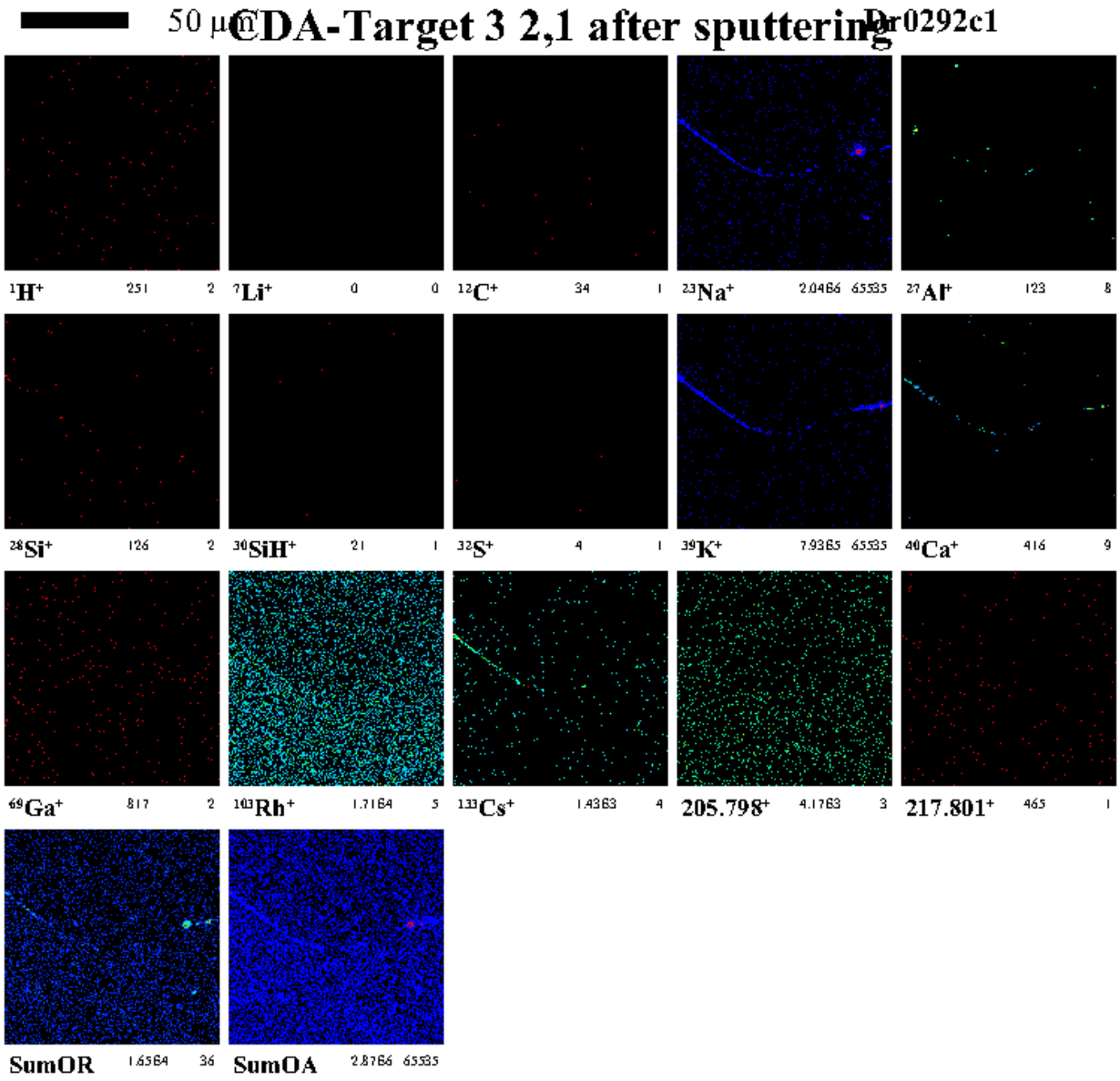
50 µm
CDA-Target 3 2,1 after sputtering
Dr0292c1
1H+ 251 2
7Li+ 0 0
12C+ 34 1
23Na+ 20486 65535
27Al+ 123 8
28Si+ 126 2
30SiH+ 21 1
32S+ 4 1
39K+ 79365 65535
40Ca+ 416 9
69Ga+ 817 2
103Rh+ 17164 5
133Cs+ 14363 4
205.798+ 41763 3
217.801+ 465 1
SumOR 16564 36
SumOA 28766 65535

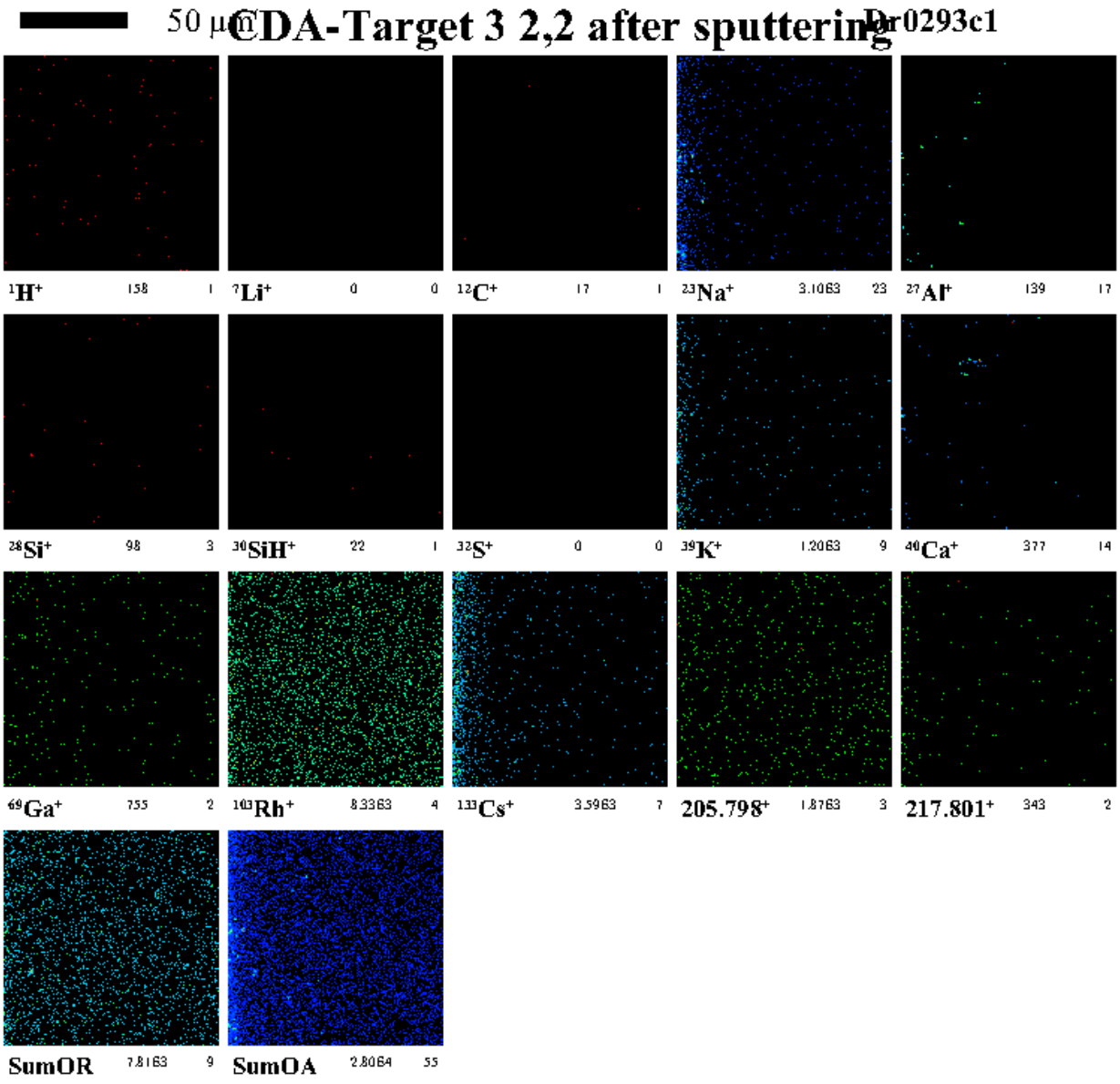
50 µm
CDA-Target 3 2,2 after sputtering
Dr0293c1
1H+ 158 1
7Li+ 0 0
12C+ 17 1
23Na+ 3.1063 23
27Al+ 139 17
28Si+ 98 3
30SiH+ 22 1
32S+ 0 0
39K+ 1.2063 9
40Ca+ 377 14
69Ga+ 755 2
103Rh+ 8.3363 4
133Cs+ 3.5963 7
205.798+ 1.8763 3
217.801+ 343 2
SumOR 7.8163 9
SumOA 2.8064 55

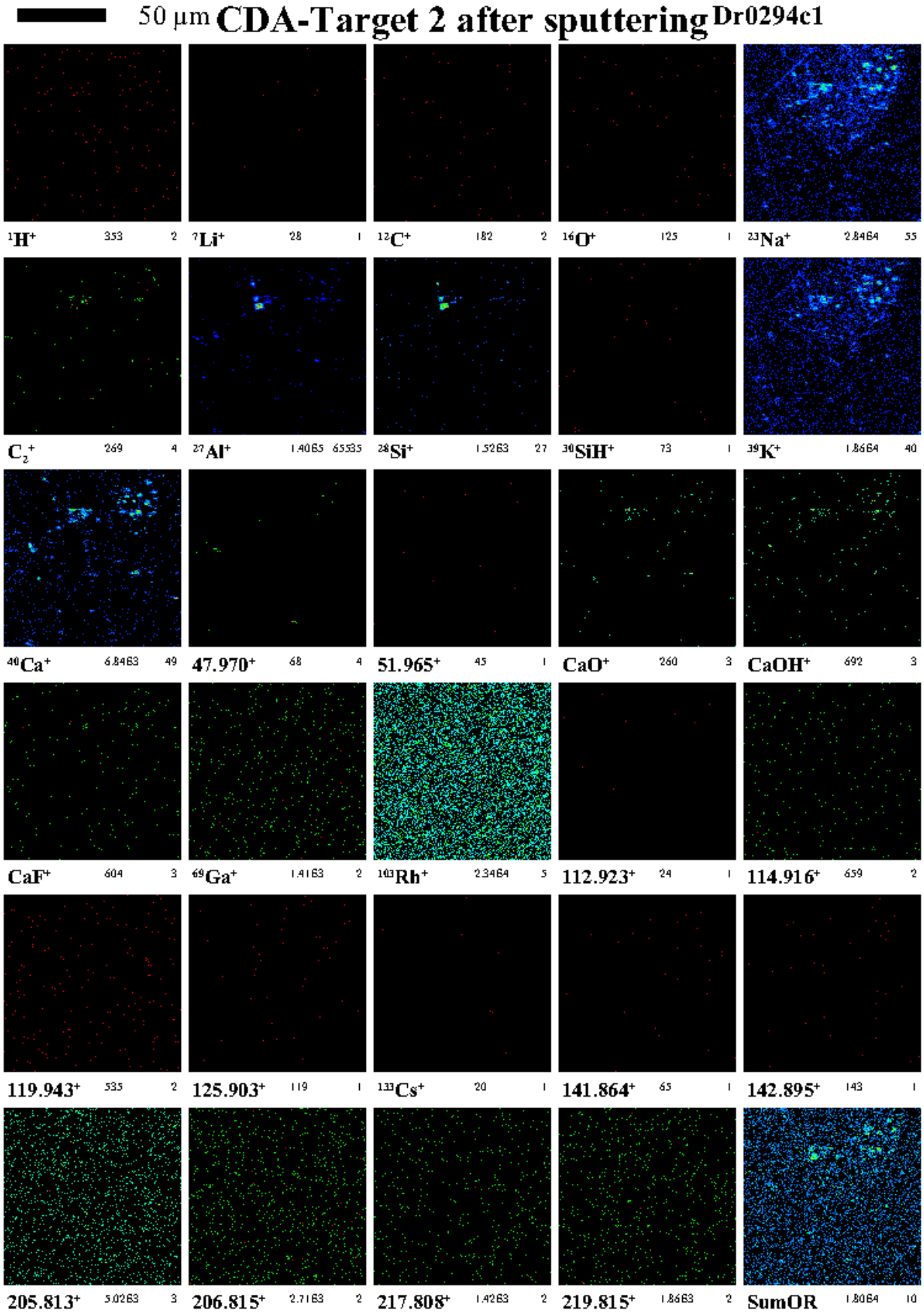
50 µm CDA-Target 2 after sputtering Dr0294c1
1H+ 353 2
7Li+ 28 1
12C+ 182 2
16O+ 125 1
23Na+ 2.8464 55
C2+ 269 4
27Al+ 1.4065 65535
28Si+ 1.5263 27
30SiH+ 73 1
39K+ 1.8664 40
40Ca+ 6.8463 49
47.970+ 68 4
51.965+ 45 1
CaO+ 260 3
CaOH+ 692 3
CaF+ 604 3
69Ga+ 1.4163 2
103Rh+ 2.3464 5
112.923+ 24 1
114.916+ 659 2
119.943+ 535 2
125.903+ 119 1
133Cs+ 20 1
141.864+ 65 1
142.895+ 143 1
205.813+ 5.0263 3
206.815+ 2.7163 2
217.808+ 1.4263 2
219.815+ 1.8663 2
SumOR 1.8064 10

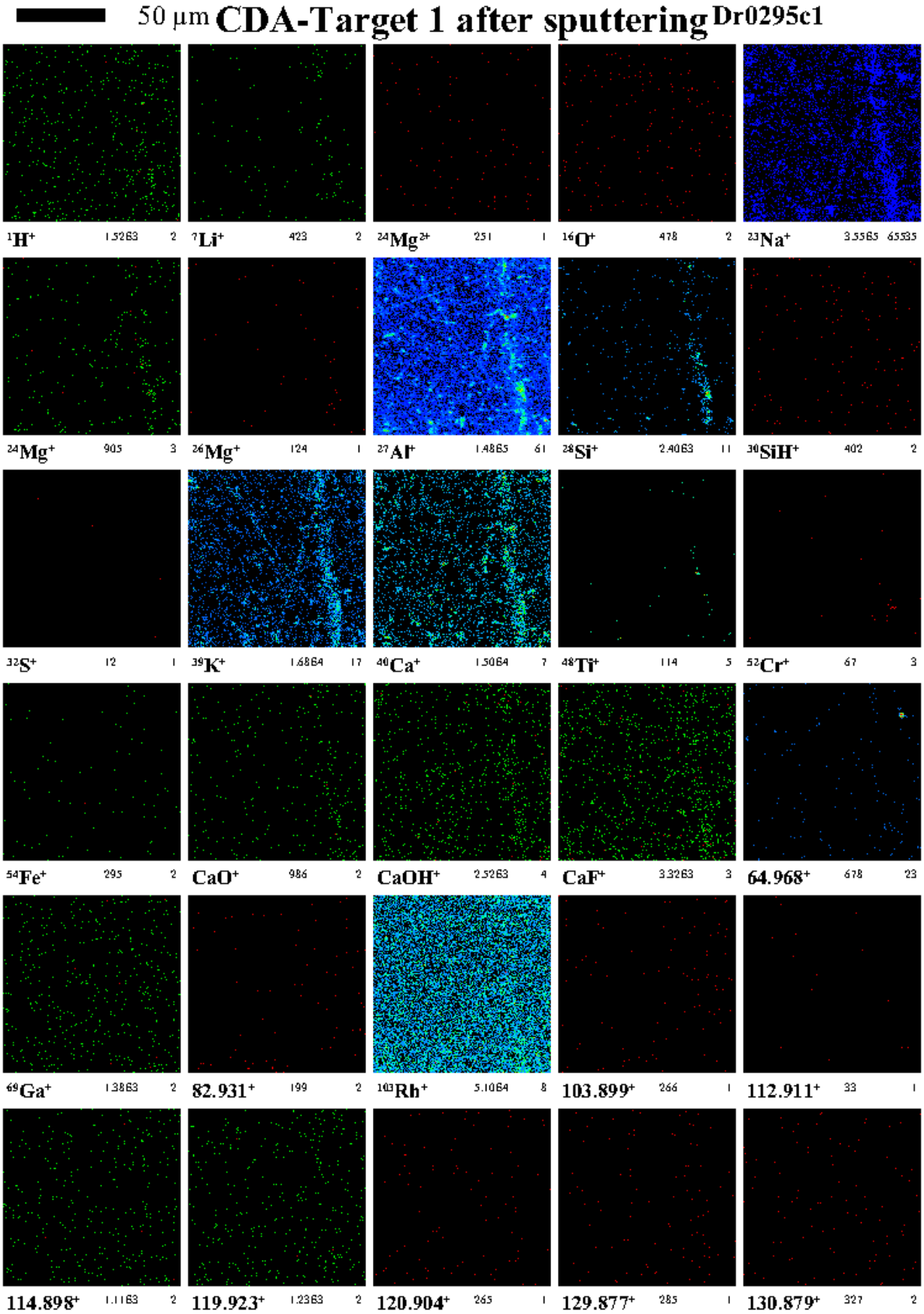
50 µm CDA-Target 1 after sputtering Dr0295c1
1H+ 1.5263 2
7Li+ 423 2
24Mg2+ 251 1
16O+ 478 2
23Na+ 3.5565 65535
24Mg+ 905 3
26Mg+ 124 1
27Al+ 1.4865 61
28Si+ 2.4063 11
30SiH+ 402 2
32S+ 12 1
39K+ 1.6864 17
40Ca+ 1.5064 7
48Ti+ 114 5
52Cr+ 67 3
54Fe+ 295 2
CaO+ 986 2
CaOH+ 2.5263 4
CaF+ 3.3263 3
64.968+ 678 23
69Ga+ 1.3863 2
82.931+ 199 2
103Rh+ 5.1064 8
103.899+ 266 1
112.911+ 33 1
114.898+ 1.1163 2
119.923+ 1.2363 2
120.904+ 265 1
129.877+ 285 1
130.879+ 327 2

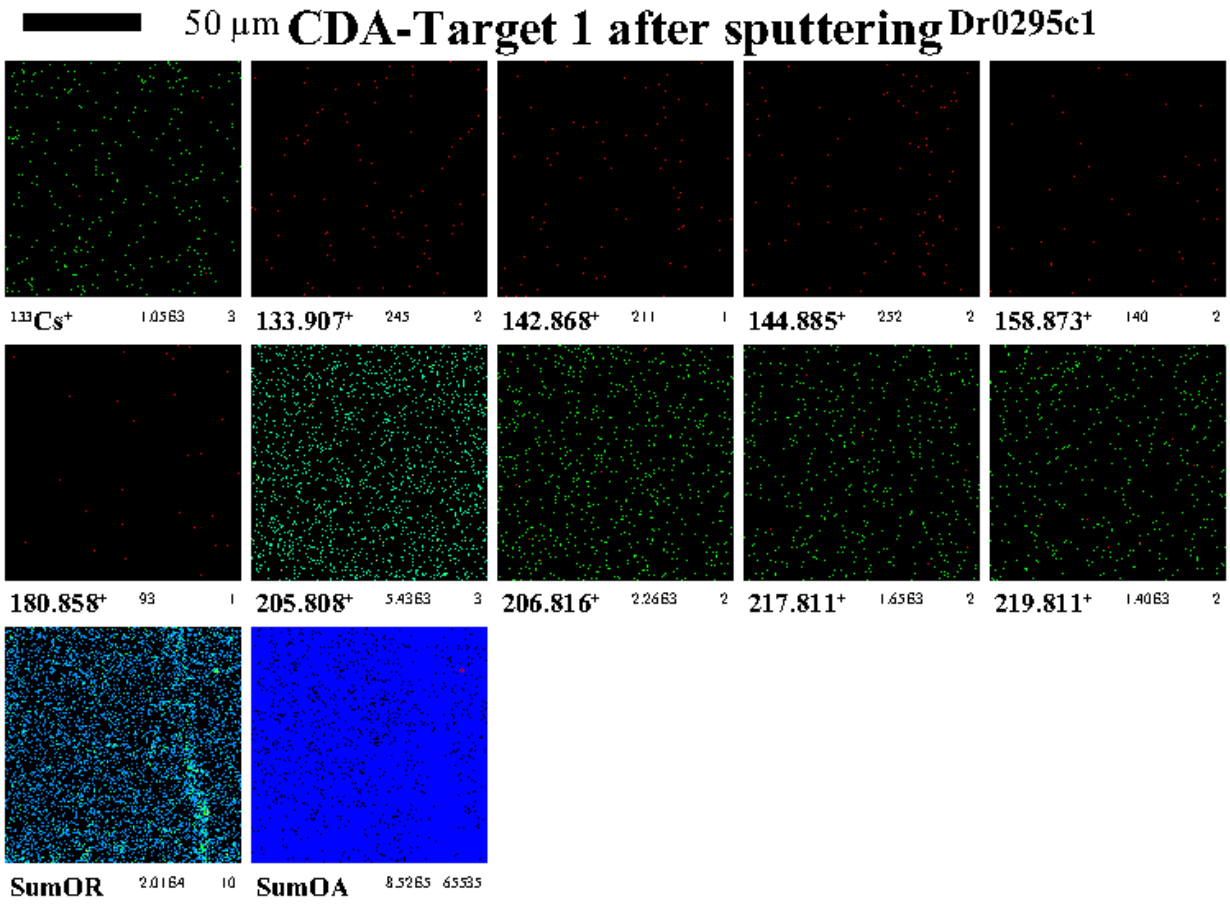
50 µm
CDA-Target 1 after sputtering
Dr0295c1
133Cs+ 1.0563 3
133.907+ 245 2
142.868+ 211 1
144.885+ 252 2
158.873+ 140 2
180.858+ 93 1
205.808+ 5.4363 3
206.816+ 2.2663 2
217.811+ 1.6563 2
219.811+ 1.4063 2
SumOR 2.0164 10
SumOA 8.5265 65535

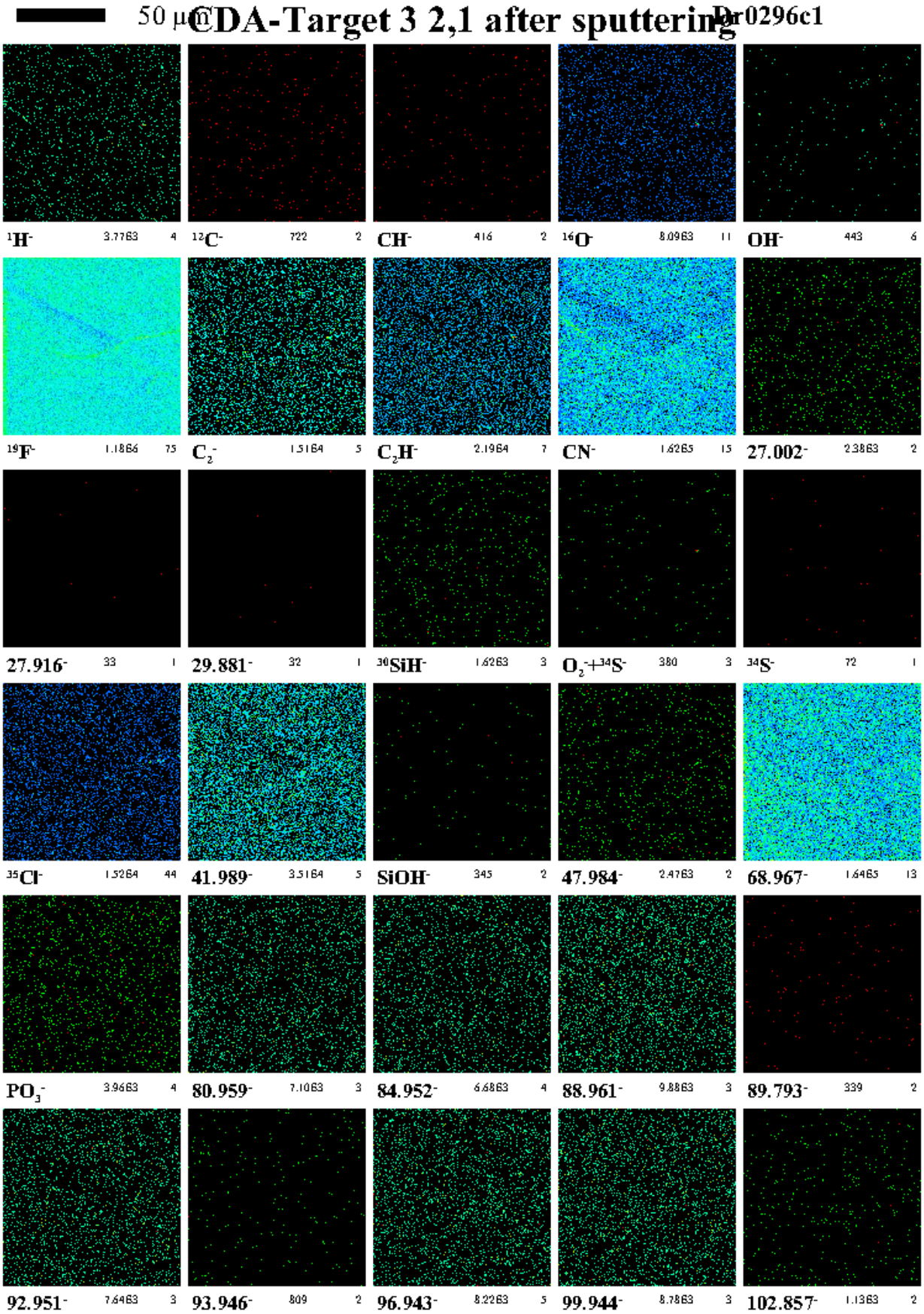
50 µm
CDA-Target 3 2,1 after sputtering
Dr0296c1
1H- 3.7763 4
12C- 722 2
CH- 416 2
16O- 8.0963 11
OH- 443 6
19F- 1.1866 75
C2- 1.5164 5
C2H- 2.1964 7
CN- 1.6265 15
27.002- 2.3863 2
27.916- 33 1
29.881- 32 1
30SiH- 1.6263 3
O2-+34S- 380 3
34S- 72 1
35Cl- 1.5264 44
41.989- 3.5164 5
SiOH- 345 2
47.984- 2.4763 2
68.967- 1.6465 13
PO3- 3.9663 4
80.959- 7.1063 3
84.952- 6.6863 4
88.961- 9.8863 3
89.793- 339 2
92.951- 7.6463 3
93.946- 809 2
96.943- 8.2263 5
99.944- 8.7863 3
102.857- 1.1363 2

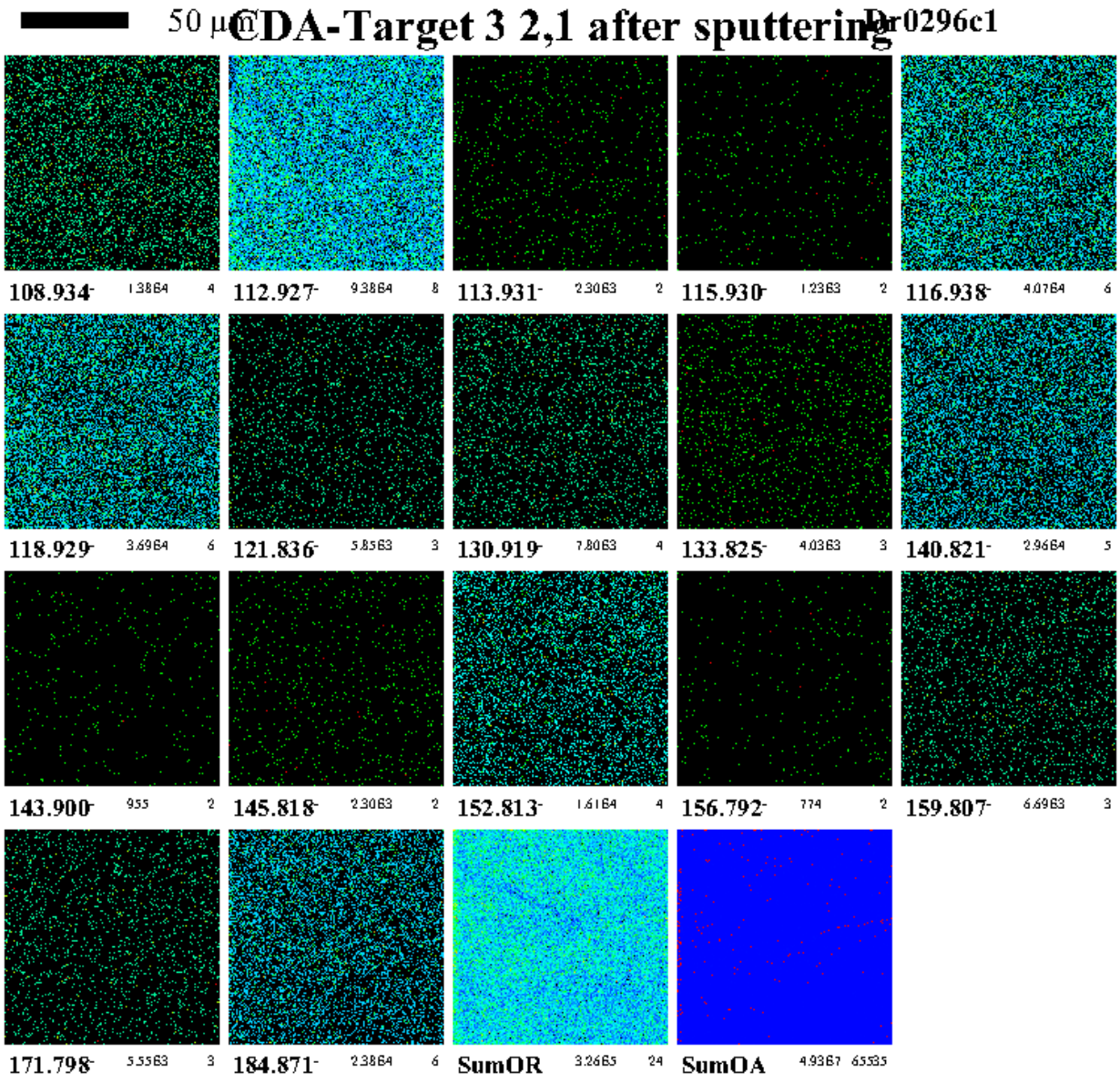
50 µm
CDA-Target 3 2,1 after sputtering
Pr0296c1
108.934- 1.3864 4
112.927- 9.3864 8
113.931- 2.3063 2
115.930- 1.2363 2
116.938- 4.0764 6
118.929- 3.6964 6
121.836- 5.8563 3
130.919- 7.8063 4
133.825- 4.0363 3
140.821- 2.9664 5
143.900- 955 2
145.818- 2.3063 2
152.813- 1.6164 4
156.792- 774 2
159.807- 6.6963 3
171.798- 5.5563 3
184.871- 2.3864 6
SumOR 3.2665 24
SumOA 4.9367 65535

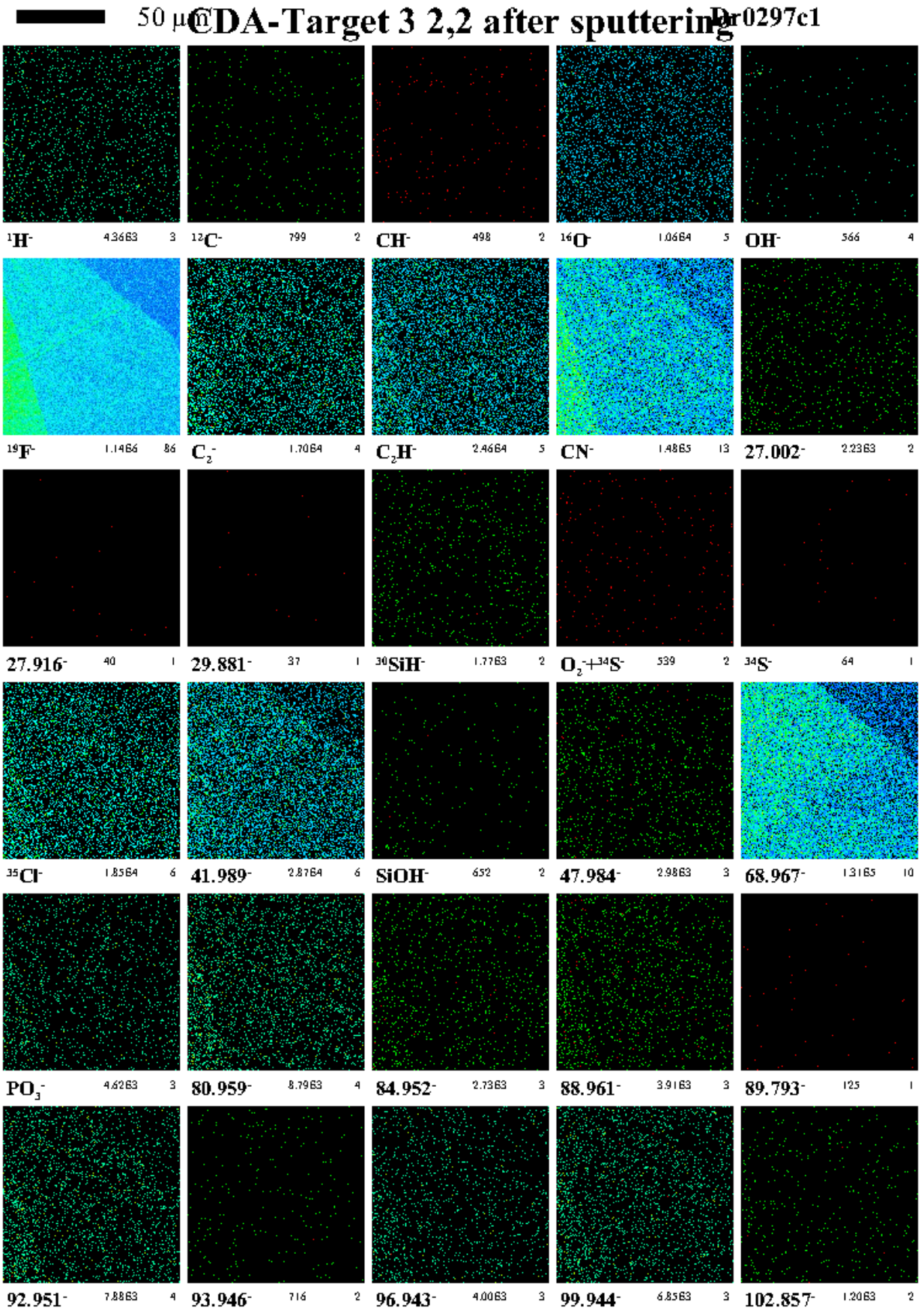
50 µm
CDA-Target 3 2,2 after sputtering
Dr0297c1
1H- 4.36E3 3
12C- 799 2
CH- 498 2
16O- 1.06E4 5
OH- 566 4
19F- 1.14E6 86
C2- 1.70E4 4
C2H- 2.46E4 5
CN- 1.48E5 13
27.002- 2.23E3 2
27.916- 40 1
29.881- 37 1
30SiH- 1.77E3 2
O2-+34S- 539 2
34S- 64 1
35Cl- 1.85E4 6
41.989- 2.87E4 6
SiOH- 652 2
47.984- 2.98E3 3
68.967- 1.31E5 10
PO3- 4.62E3 3
80.959- 8.79E3 4
84.952- 2.73E3 3
88.961- 3.91E3 3
89.793- 125 1
92.951- 7.88E3 4
93.946- 716 2
96.943- 4.00E3 3
99.944- 6.85E3 3
102.857- 1.20E3 2

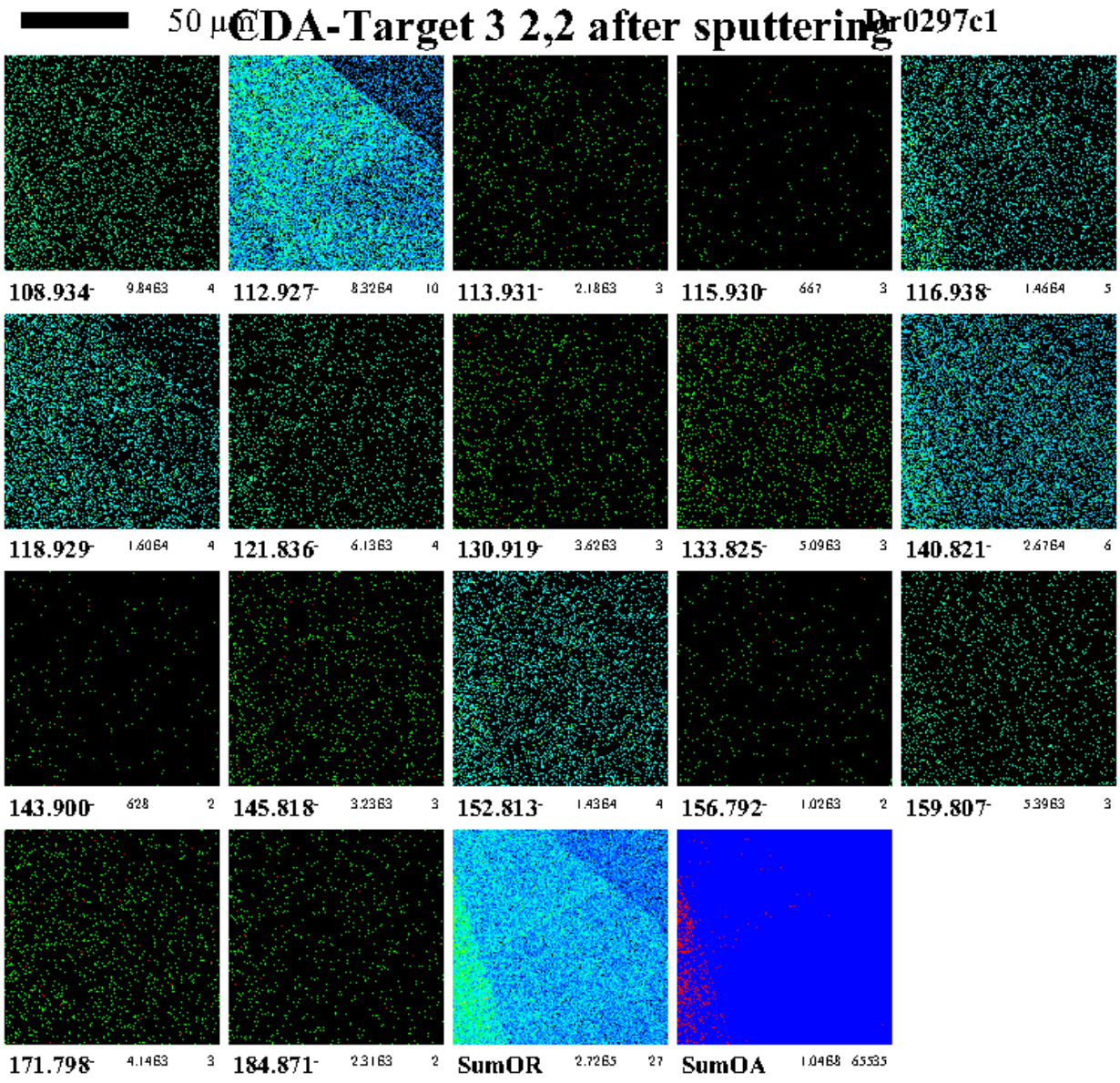
50 µm
CDA-Target 3 2,2 after sputtering
Dr0297c1
108.934- 9.8463 4
112.927- 8.3264 10
113.931- 2.1863 3
115.930- 667 3
116.938- 1.4664 5
118.929- 1.6064 4
121.836- 6.1363 4
130.919- 3.6263 3
133.825- 5.0963 3
140.821- 2.6764 6
143.900- 628 2
145.818- 3.2363 3
152.813- 1.4364 4
156.792- 1.0263 2
159.807- 5.3963 3
171.798- 4.1463 3
184.871- 2.3163 2
SumOR 2.7265 27
SumOA 1.0468 65535

50 µm CDA-Target 3 2,2 after sputtering Pr0298c1

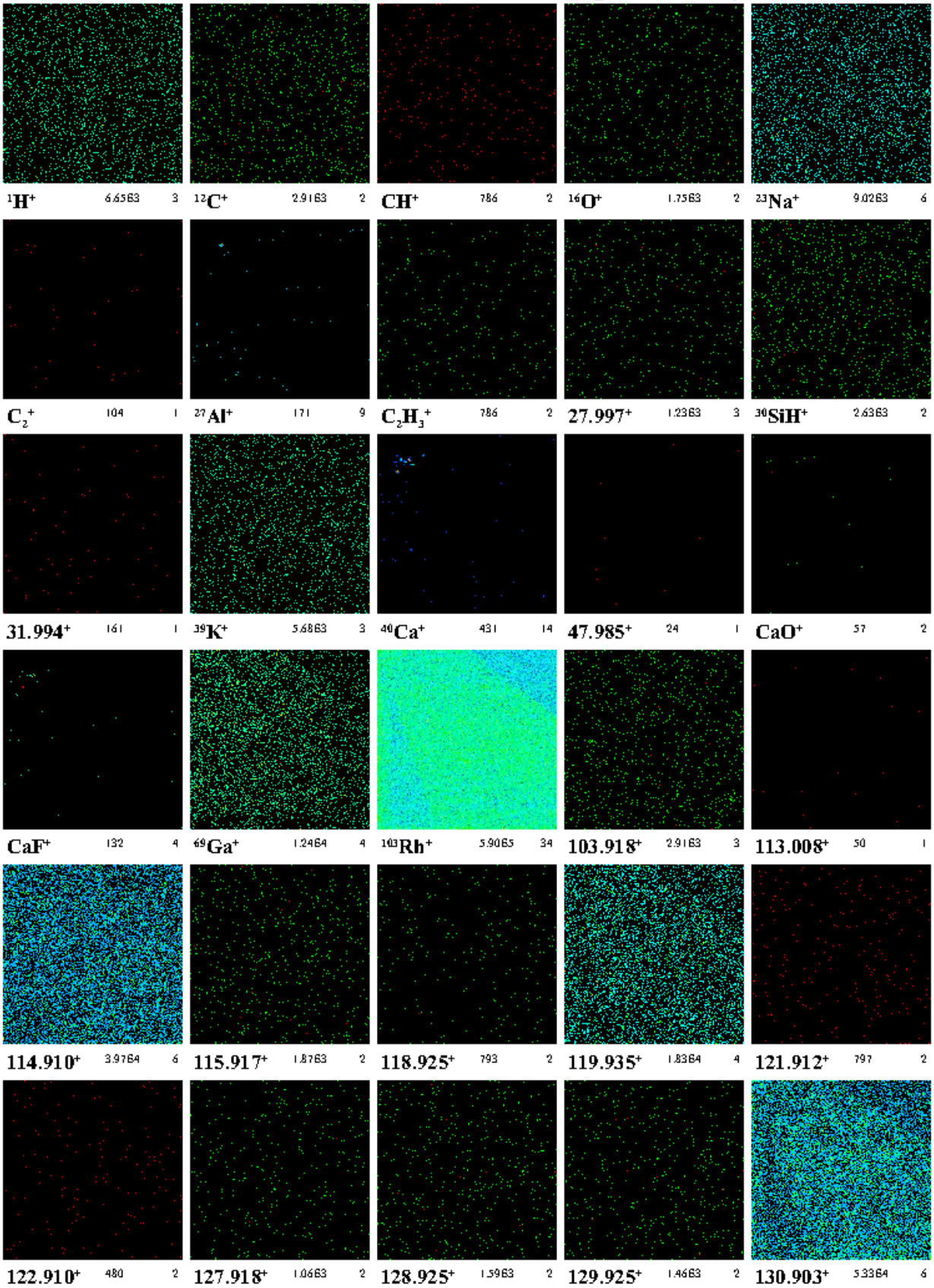

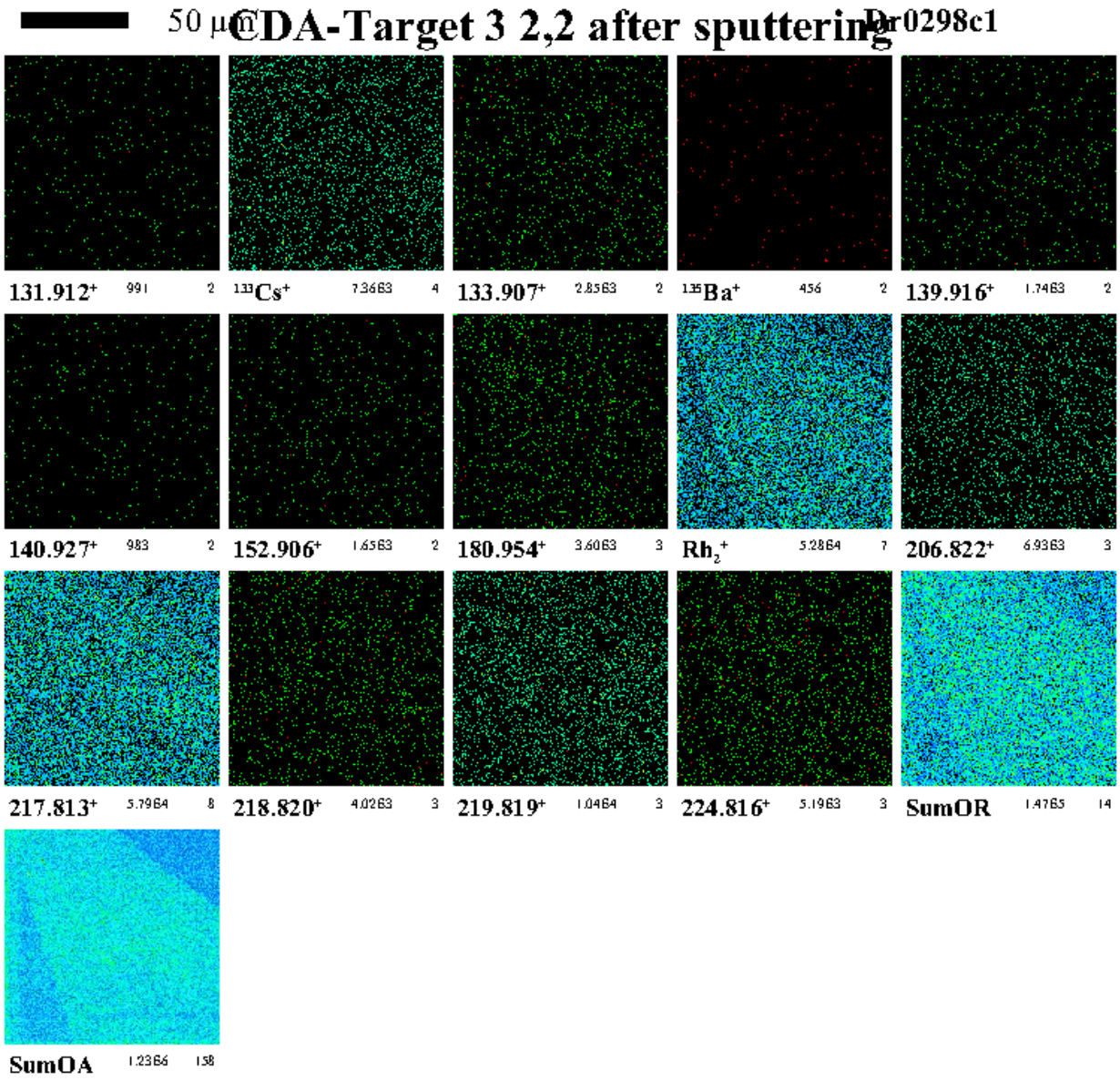
50 µm
CDA-Target 3 2,2 after sputtering
Dr0298c1
131.912+ 991 2
133Cs+ 7.3663 4
133.907+ 2.8563 2
135Ba+ 456 2
139.916+ 1.7463 2
140.927+ 983 2
152.906+ 1.6563 2
180.954+ 3.6063 3
Rh2+ 5.2864 7
206.822+ 6.9363 3
217.813+ 5.7964 8
218.820+ 4.0263 3
219.819+ 1.0464 3
224.816+ 5.1963 3
SumOR 1.4765 14
SumOA 1.2366 158

50 µm CDA-Target 3 2,1 after sputtering Pr0299c1

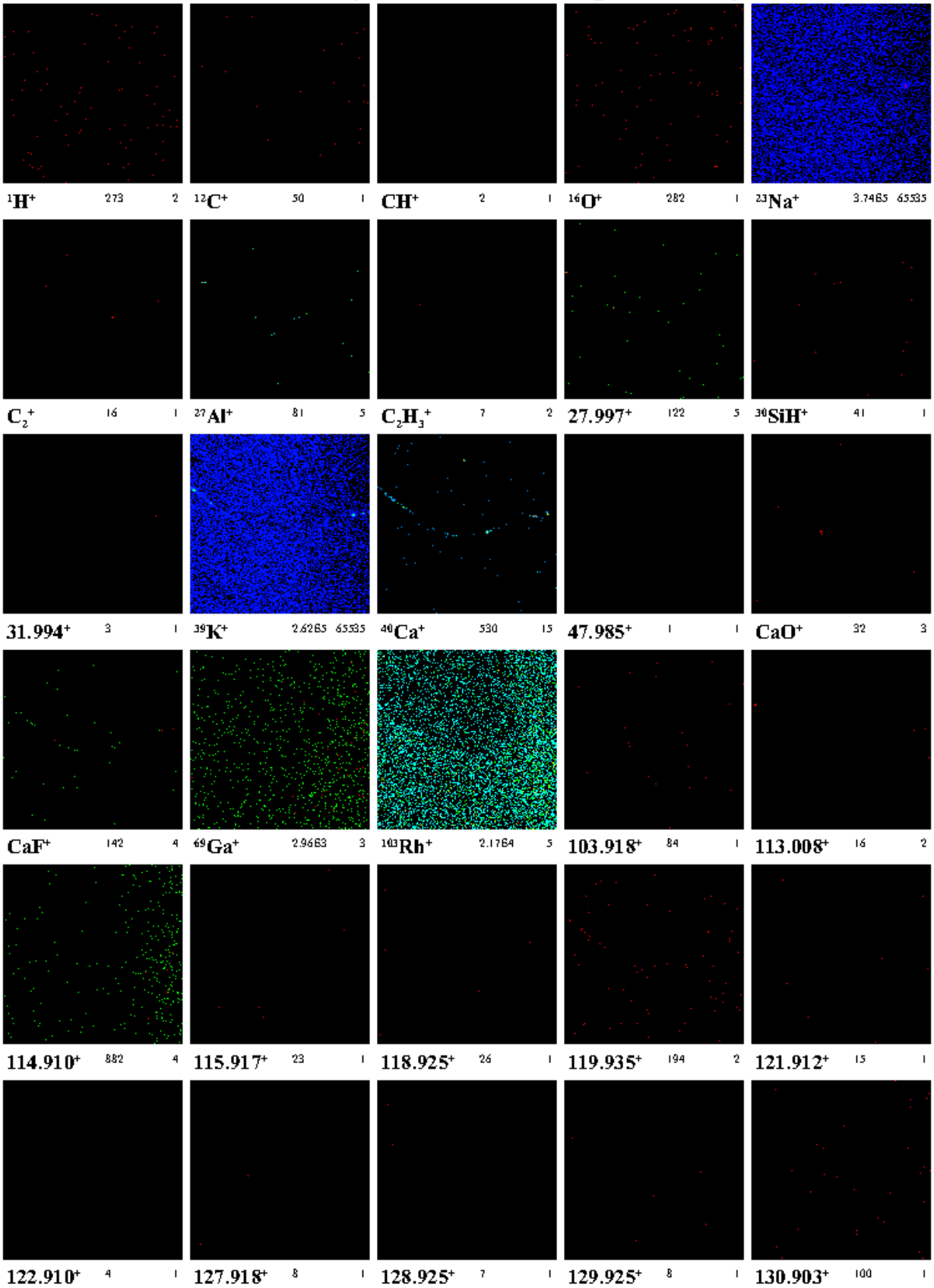

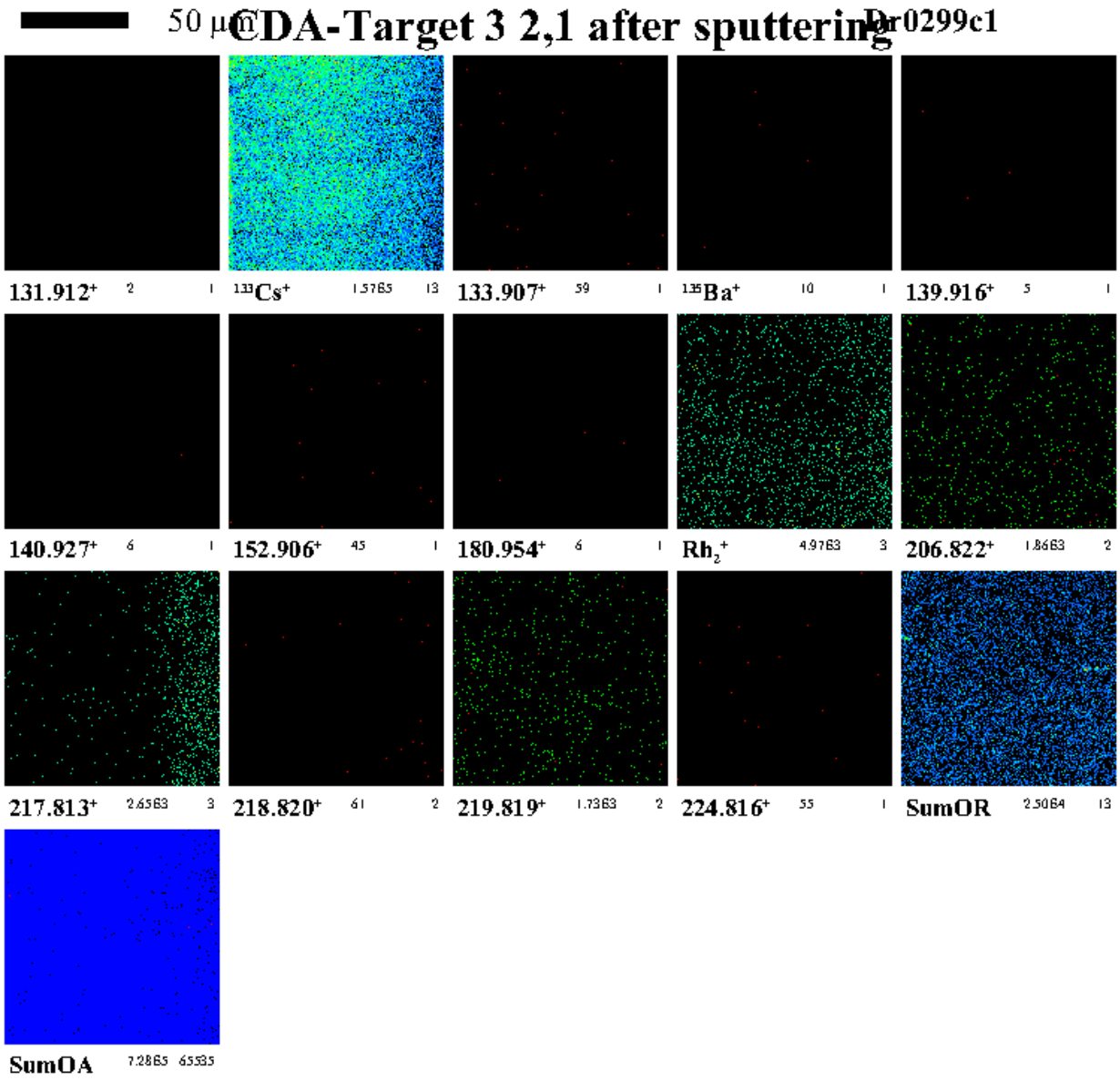
50 µm
CDA-Target 3 2,1 after sputtering
Pr0299c1
131.912+ 2 1
133Cs+ 1.5763 13
133.907+ 59 1
135Ba+ 10 1
139.916+ 5 1
140.927+ 6 1
152.906+ 45 1
180.954+ 6 1
Rh2+ 4.9763 3
206.822+ 1.8663 2
217.813+ 2.6563 3
218.820+ 61 2
219.819+ 1.7363 2
224.816+ 55 1
SumOR 2.5064 13
SumOA 7.2863 65535

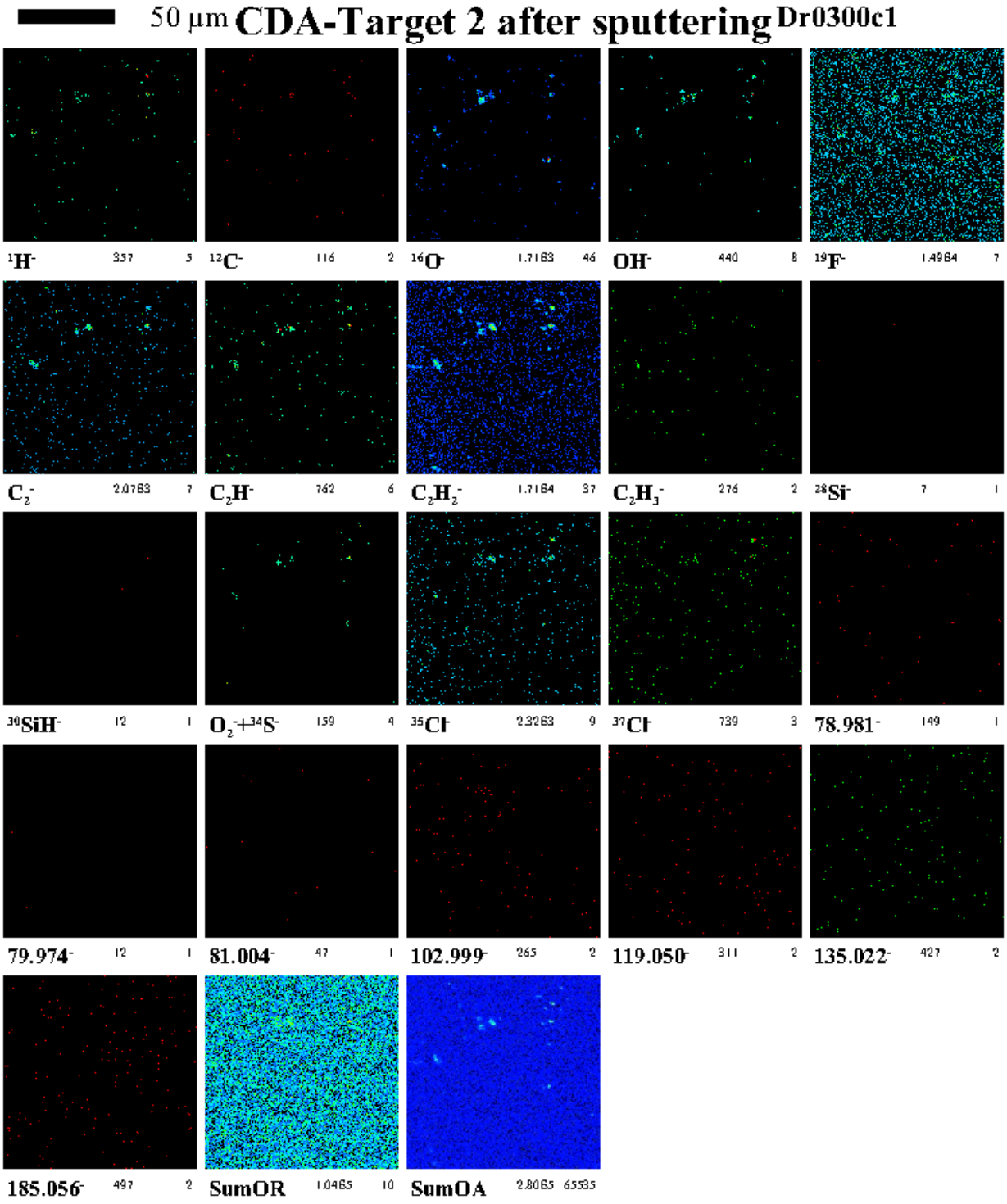
50 µm
CDA-Target 2 after sputtering
Dr0300c1
$^{1}H^{-}$ 357 5
$^{12}C^{-}$ 116 2
$^{16}O^{-}$ 1.7163 46
OH^{-} 440 8
$^{19}F^{-}$ 1.4984 7
C_2^{-} 2.0763 7
C_2H^{-} 762 6
$C_2H_2^{-}$ 1.7164 37
$C_2H_3^{-}$ 276 2
$^{28}Si^{-}$ 7 1
$^{30}SiH^{-}$ 12 1
$O_2^{-}+^{34}S^{-}$ 159 4
$^{35}Cl^{-}$ 2.3263 9
$^{37}Cl^{-}$ 739 3
78.981^{-} 149 1
79.974^{-} 12 1
81.004^{-} 47 1
102.999^{-} 265 2
119.050^{-} 311 2
135.022^{-} 427 2
185.056^{-} 497 2
SumOR 1.0465 10
SumOA 2.8065 65535

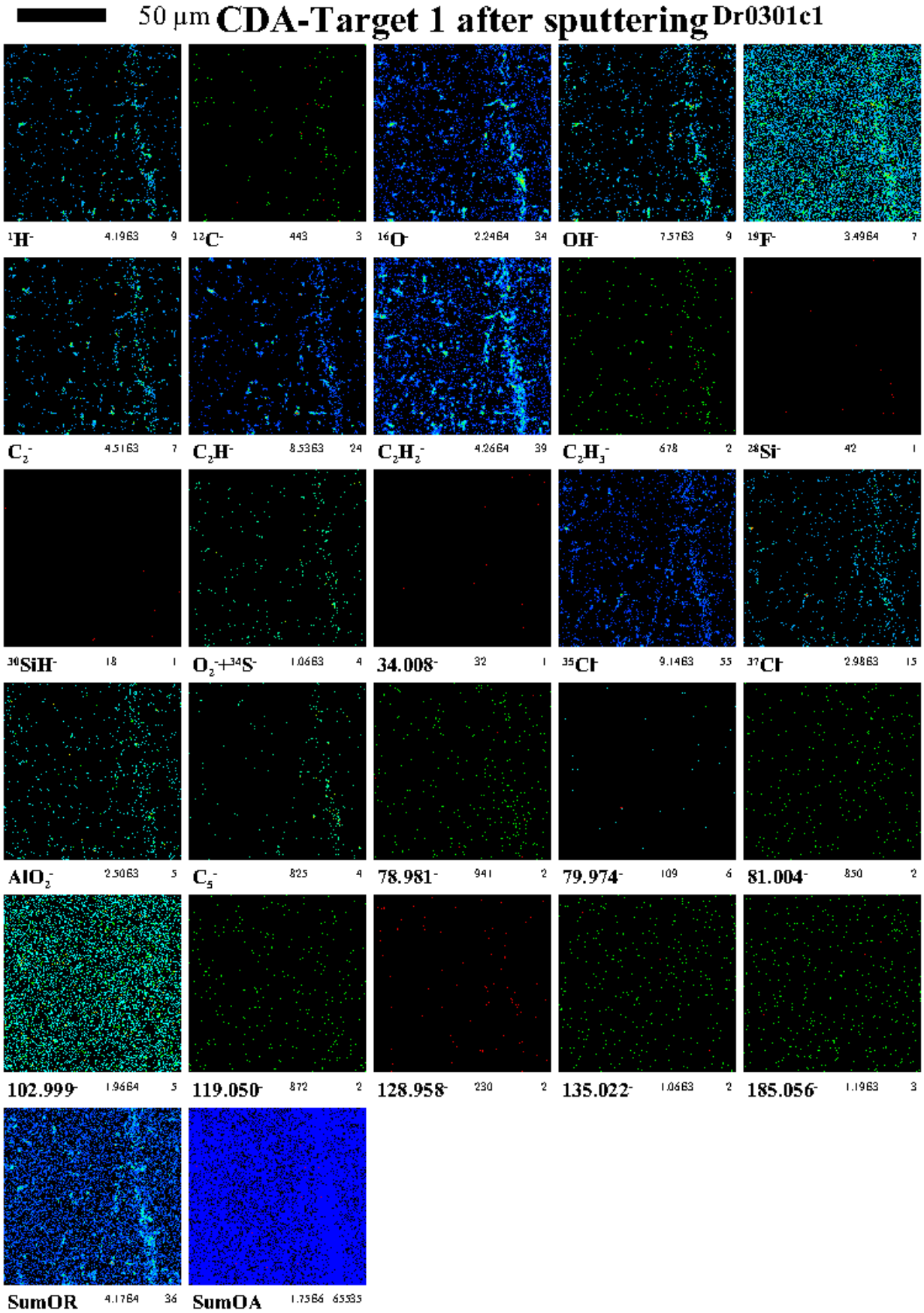
50 µm CDA-Target 1 after sputtering Dr0301c1
1H- 4.1963 9
12C- 443 3
16O- 2.2464 34
OH- 7.5763 9
19F- 3.4964 7
C2- 4.5163 7
C2H- 8.5363 24
C2H2- 4.2664 39
C2H3- 678 2
28Si- 42 1
30SiH- 18 1
O2-+34S- 1.0663 4
34.008- 32 1
35Cl- 9.1463 55
37Cl- 2.9863 15
AlO2- 2.5063 5
C5- 825 4
78.981- 941 2
79.974- 109 6
81.004- 850 2
102.999- 1.9664 5
119.050- 872 2
128.958- 230 2
135.022- 1.0663 2
185.056- 1.1963 3
SumOR 4.1764 36
SumOA 1.7566 65535

Bibliography

Adamczyk, B., Bederski, K., and L. Wojcik 1988. Mass Spectrometric Investigation of Dissociative Ionization of Toxic Gases by Electrons at 20-1000 eV. *Biomedical and Environmental Mass Spectrometry* **16**, 415–417.

Altobelli, N., Kempf, S., Landgraf, M., Srama, R., Dikarev, V., Krüger, H., Moragas-Klostermeyer, G., and E. Grün 2003. Cassini between Venus and Earth: Detection of interstellar grains. *JGR* **108(A10)**, 7–1.

Atterer, M. 1959. *Gmelins Handbuch der anorganischen Chemie, Silicium, 8.Auflage*. Deutsche chemische Gesellschaft, Verlag Chemie GmbH, Weinheim.

Bar-Nun, A., Dror, J., Kochavi, E., and D. Laufer 1987. Amorphous water ice and its ability to trap gases. *Phys. Rev. B* **35**, 2427–2435.

Baum, W. A., Kreidl, T., Westphal, J. A., Danielson, G. E., Seidelmann, P. K., Pascu, D., and D. G. Currie 1981. Saturn's E ring. *Icarus* **47**, 84–96.

Bosh, A. S., Olkin, C. B., French, R. G., and P. D. Nicholson 2002. Saturn's F Ring: Kinematics and Particle Sizes from Stellar Occultation Studies. *Icarus* **157**, 57–75.

Brown, R. A. 1974. Optical line emission from Io. In *IAU Symp. 65: Exploration of the Planetary System* pp., 527–531.

Brown, R. H. and 24 colleagues, 2006. Composition and Physical Properties of Enceladus' Surface. *Science* **311**, 1425–1428.

Brownlee, D. E. and 173 colleagues, 2006. Comet 81P/Wild 2 Under a Microscope. *Science* **314**, 1711–1716.

Brownlee, D. E. and J. Kissel 1990. In *The composition of dust particles in the environment of comet Halley*, Comet Halley: Investigations, Results, Interpretations. Vol. 2: Dust, Nucleus, Evolution.

Burnett, D. S., McNamara, K. M., Jurewicz, A. J. G. and Woolum, D. S. Molecular Contamination on Anodized Aluminum Components of the Genesis Science Canister. In *36th Annual Lunar and Planetary Science Conference*, p. 2405.

Burns, J. A., Lamy, P. L., and S. Soter 1979. Radiation forces on small particles in the solar system. *Icarus* **40**, 1–48.

Burns, J. A., Showalter, M. R., Hamilton, D. P., Nicholson, P. D., de Pater, I., Ockert-Bell, M. E., and P. C. Thomas 1999. The Formation of Jupiter's Faint Rings. *Science* **284**, 1146–1150.

Calaway, M. J., Burnett, D. S., Rodriguez, M. C., Sestak, S., Allton, J. H. and Stansbery, E. K. Decontamination of Genesis Array Materials by UV Ozone Cleaning. In *38th Annual Lunar and Planetary Science Conference*, p. 1627.

Conrath, B. J., Gautier, D., Hanel, R. A., and J. S. Hornstein 1984. The Helium abundance of Saturn from Voyager measurements. *APJ* **282**, 807–815.

Cuzzi, J. N., Lissauer, J. J., Esposito, L. W., Holberg, J. B., Marouf, E. A., Tyler, G. L., and A. Boishchot 1984. Saturn's rings - Properties and processes. In *Planetary Rings* (R. Greenberg and A. Brahic Eds.) pp. 73–199. University of Arizona Press, Tuscon.

Dougherty, M. K., Khurana, K. K., Neubauer, F. M., Russell, C. T., Saur, J., Leisner, J. S., and M. E. Burton 2006. Identification of a Dynamic Atmosphere at Enceladus with the Cassini Magnetometer. *Science* **311**, 1406–1409.

Eichhorn, G. 1976. Analysis of the hypervelocity impact process from impact flash measurements. *Planet. Space Sci.* **24**, 771–781.

Eichhorn, G. 1978. Primary velocity dependence of impact ejecta parameters. *Planet. Space Sci.* **26**, 469–471.

Esposito, L., Cuzzi, J., Holberg, J., Marouf, E., Tyler, G., and C. Porco 1984. In *Saturn*, pp. 463–545, The University of Arizona Press.

Fegley, B. and M. Y. Zolotov 2000. Chemistry of Sodium, Potassium, and Chlorine in Volcanic Gases on Io. *Icarus* **148**, 193–210.

Flandes, A. 2004. Dust escape from Io. *Geophys. Res. Let.* **31**, L16802

Fukai, Y. 2005. *The Metal-Hydrogen System: Basic Bulk Properties*. 2nd rev. and updated ed. by Y. Fukai. Berlin: Springer, 2005.

Galli, A., Wurz, P., Barabash, S., Grigoriev, A., Lundin, R., Futaana, Y., Gunell, H., Holmström, M., Roelof, E. C., Curtis, C. C., Hsieh, K. C., Fedorov, A., Winningham, D., Frahm, R. A., Cerulli-Irelli, R., Bochsler, P., Krupp, N., Woch, J. and Fraenz, M. 2006. Direct Measurements of Energetic Neutral Hydrogen in the Interplanetary Medium. *APJ* **644**, 1317–1325.

Geissler, P. E. 2005. Volcanic Plumes and Plume Deposits on Io. In *36th Annual Lunar and Planetary Science Conference*, p. 1875.

Giese, B., Neukum, G., Roatsch, T., Denk, T., and C. C. Porco 2006. Topographic modeling of Phoebe using Cassini images. *Planet. Space Sci.* **54**, 1156–1166.

Göller, J. R. and E. Grün 1989. Calibration of the Galileo/Ulysses dust detectors with different projectile materials and at varying impact angles. *Planet. Space Sci.* **37**, 1197–1206.

Görlich, M., Lura, F., Stropahl, G. and Siewert, F. 1999 Application of Various Analytical Methods for the Characterisation and Failure Analysis with the Manufacture of a High Purity Rhodium-Target for the CDA/CASSINI (SM98-130/361). *Spacecraft Structures, Materials and Mechanical Testing*. ESA Special Publication **428**, 399–404, Kaldeich-Schürmann, 1999.

Goldsworthy, B. J., Burchell, M. J., Cole, M. J., Armes, S. P., Khan, M. A., Lascelles, S. F., Green, S. F., McDonnell, J. A. M., Srama, R., and S. W. Bigger 2003. Time of flight mass spectra of ions in plasmas produced by hypervelocity impacts of organic and mineralogical microparticles on a cosmic dust analyser. *A&A* **409**, 1151–1167.

Graps, A., Grün, E., Svedhem, H., Krüger, H., Horányi, M., Heck, A., and S. Lammers 2000. Io as a source of the jovian dust streams. *Nature* **405**, 48–50.

Grün, E. and Pailer, N. and Fechtig, H. and Kissel, J. 1980. Orbital and physical characteristics of micrometeoroids in the inner solar system as observed by HELIOS 1. *Planet. Space Sci.* **28**, 333–349.

Grün, E., Fechtig, H., Giese, R. H., Kissel, J., Linkert, D., Maas, D., McDonnel, J., Morfill, G., Schwehm, G., and H. Zook 1992a. The Ulysses dust experiment. *A&A*

Supl. Ser. **92**, 411–423.

Grün, E., Fechtig, H., Hanner, M., Kissel, J., Lindblad, B.-A., Linkert, D., Maas, D., Morfill, G., and H. Zook 1992b. The Galileo dust detector. *Space Science Review* **60**, 317–340.

Grün, E., and 22 collegues 1993. Discovery of Jovian dust streams and interstellar grains by the Ulysses spacecraft. *Nature* **362**, 428–430.

Grün, E., and 21 collegues 1996. Constraints from Galileo observations on the origin of Jovian dust streams. *Nature* **381**, 395–398.

Hamilton, D. and J. Burns 1993. Ejection of dust from Jupiter's gossamer ring. *Nature* **364**, 695–699.

Hamilton, D. P. and J. A. Burns 1994. Origin of Saturn's E ring: Self sustained, naturally. *Science* **267**, 550–553.

Hansen, C. J., Esposito, L., Stewart, A. I. F., Colwell, J., Hendrix, A., Pryor, W., Shemansky, D., and R. West 2006. Enceladus' Water Vapor Plume. *Science* **311**, 1422–1425.

Henry, C. A. 2002. An Introduction to the Design of the Cassini Spacecraft. *Space Science Reviews* **104**, 129–153.

Hillier, J. K., Green, S. F., McBride, N., Altobelli, N., Postberg, F., Kempf, S., Schwanethal, J. P., Srama, R., McDonnel, J. A. M., and E. Grün 2007a. Interplanetary dust detected by the Cassini CDA Chemical Analyser. *Icarus* **190**, 643–654.

Hillier, J. K., Green, S. F., McBride, N., Schwanethal, J. P., Postberg, F., Srama, R., Kempf, S., Moragas-Klostermeyer, G., McDonnell, J. A. M., and E. Grün 2007b. The composition of Saturn's E ring. *MNRAS* **377**, 1588–1596.

Hillier, J. K., McBride, N., Green, S. F., Kempf, S., and R. Srama 2006. Modelling CDA mass spectra. *Planet. Space Sci.* **54**, 1007–1013.

Horányi, M., Morfill, G., and E. Grün 1993a. Mechanism for the acceleration and ejection of dust grains from Jupiter's magnetosphere. *Nature* **363**, 144–146.

Horányi, M., Morfill, G., and E. Grün 1993b. The dusty ballerina skirt of Jupiter. *J. Geophys. Res.* **98**, 21245–21251.

Horányi, M. 2000. Dust stream from Jupiter and Saturn. *Phys. of Plasmas* **7(10)**, 3847–3850.

Hornung, K. and J. Kissel 1994. On shock wave impact ionization of dust particles. *A&A* **291**, 324–336.

Hornung, K., Malama, Y., and K. Kestenboim 2000. Impact Vaporization and Ionization of Cosmic Dust Particles. *Astrophys. and Space Sci.* **274**, 355–363.

Jacobson, R. A. 2000. The Orbits of the Outer Jovian Satellites. *AJ* **120**, 2679–2686.

Juhász, A. and M. Horányi 2002. Saturn's E ring: A dynamical approach. *JGR (Space Physics)* **107**, 1–10.

Jurac, S. 2001. Saturn's E ring and the Production of the Neutral Torus. *Icarus* **149**, 384–396.

Jurac, S., Johnson, R. E., and B. Donn 1998. Monte Carlo Calculations of the Sputtering of Grains: Enhanced Sputtering of Small Grains. *APJ* **503**, 247–252.

Kargel, J. S. 2006. Enceladus: Cosmic Gymnast, Volatile Miniworld. *Science* **311**, 1389–1391.

Keller, L. P. and 23 colleagues 2006. Infrared Spectroscopy of Comet 81P/Wild 2 Samples Returned by Stardust. *Science* **314**, 1728–1731.

Kempf, S., Srama, R., Horányi, M., Burton, M., Helfert, S., Moragas-Klostermeyer, G., Roy, M., and E. Grün 2005a. High-velocity streams of dust originating from Saturn. *Nature* **433**, 289–291.

Kempf, S., Srama, R., Postberg, F., Burton, M., Green, S. F., Helfert, S., Hillier, J. K., McBride, N., McDonnell, J. A. M., Moragas-Klostermeyer, G., Roy, M., and E. Grün 2005b. Composition of Saturnian Stream Particles. *Science* **307**, 1274–1276.

Kempf, S., Beckmann, U., Moragas-Klostermeyer, G., Postberg, F., S. R., Economou, T., Schmidt, J., Spahn, F., and E. Grün 2007. The E ring in the vicinity of Enceladus I: Spatial distribution and properties of the ring particles. *Icarus* in press.

Kissel, J., Brownlee, D. E., Buchler, K., Clark, B. C., Fechtig, H., Grün, E., Hornung, K., Igenbergs, E. B., Jessberger, E. K., Krueger, F. R., Kuczera, H., McDonnell, J. A. M., Morfill, G. M., Rahe, J., Schwehm, G. H., Sekanina, Z., Utterback, N. G., Volk, H. J. and Zook, H. A. 1986a. Composition of comet Halley dust particles from Giotto observations. *Nature* **321**, 336–338.

Kissel, J., Sagdeev, R. Z., Bertaux, J. L., Angarov, V. N., Audouze, J., Blamont, J. E., Buchler, K., Evlanov, E. N., Fechtig, H., Fomenkova, M. N., von Hoerner, H., Inogamov, N. A., Khromov, V. N., Knabe, W., Krueger, F. R., Langevin, Y., Leonasv, B., Levasseur-Regourd, A. C., Managadze, G. G., Podkolzin, S. N., Shapiro, V. D., Tabaldyev, S. R. and Zubkov, B. V. 1986b. Composition of comet Halley dust particles from VEGA observations. *Nature* **321**, 280-282.

Kissel, J. and F. R. Krüger 1987. The Organic Component in Dust from Comet Halley as Measured by the PUMA Mass Spectrometer on Board VEGA 1. *Applied Physics A* **326**, 301–317.

Knabe, W. 1983. *Masssenspektrometrische Untersuchung der Ionenbildung beim Einschlag schneller Staubteilchen. Ph.D. thesis*, Heidelberg University.

Krueger, F. R. 1996. Ion formation by high- and medium-velocities dust impacts from laboratory measurements and Halley results. *Advances in Space Research* **17**, 71–75.

Krüger, H., Geissler, P., Horányi, M., Graps, A., Kempf, S., Srama, R., Moragas-Klostermeyer, G., Moissl, R., Johnson, T., and E. Grün 2003. Jovian dust streams: A monitor of Io's volcanic plume activity. *Geophys. Res. Let.* **30**, 3-1–3-4.

Krüger, H. 2003. *Jupiter's Dust Disc, An Astrophysical Laboratory*. Shaker-Verlag, Aachen.

Krüger, H., Graps, A., Flandes, A., Forsyth, R.J., Hamilton, D.P. Horányi, M., E. Grün 2006. Ulysses jovian latitude scan of high-velocity dust streams originating from the jovian system. *Planet. Space Sci.* **54**, 919–931.

Küppers, M. and N. M. Schneider 2000. Discovery of Chlorine in the Io torus. *Geophys. Res. Let.* **27**, 513–516.

Kuhn, S. 2002. *Hochgeschwindigkeitsmessungen am Staubbeschleuniger mit der CDA - Flugersatzeinheit. Diploma thesis*, Heidelberg University.

Landgraf, M. 2000. Modeling the motion and distribution of interstellar dust inside the heliosphere. *JGR* **105**, 10303–10316.

Landgraf, M., Krüger, H., Altobelli, N., and E. Grün 2003. Penetration of the heliosphere by the interstellar dust stream during solar maximum. *Journal of Geophysical Research (Space Physics)* **108**, 5–1.

Lavila, P. 2002. *Analyzing Time-of-Flight Spectra of CDA*. Research report, Max Planck

Institut für Kernphysik.

Lellouch, E., Paubert, G., Moses, J. I., Schneider, N. M., and D. F. Strobel 2003. Volcanically emitted sodium chloride as a source for Io's neutral clouds and plasma torus. *Nature* **421**, 45–47.

Lellouch, E., Strobel, D. F., Belton, M. J. S., Summers, M. E., Paubert, G., and R. Moreno 1996. Detection of Sulfur Monoxide in Io's Atmosphere. *Astrophysical Journal* **459**, L107–L110.

Lissauer, J. J. and R. G. French 2000. HST High-Resolution Backscatter Image of Saturn's G Ring. *Icarus* **146**, 12–18.

Lura, F. 1997. *Cassini CDA/TDT Schlussbericht*. Technical report, DLR GmbH, Berlin-Adlershof.

Matson, D. L., Castillo, J. C., Lunine, J., and T. V. Johnson 2007. Enceladus' plume: Compositional evidence for a hot interior. *Icarus* **187**, 569–573.

Mendillo, M., Wilson, J., Spencer, J., and J. Stansberry 2004. Io's volcanic control of Jupiter's extended neutral clouds. *Icarus* **170**, 430–442.

Mendillo, M. and Laurent, S. and Wilson, J. and Baumgardner, J. and Konrad, J. and Karl, W. C. 2007 The sources of sodium escaping from Io revealed by spectral high definition imaging. *Nature* **448**, 330–332.

Moore, C., Zhang, J., Goldstein, D. B., Varghese, P. L., and L. Trafton 2003. Modeling of Particulates and Condensates in Io's Pele-type Volcanic Plumes. In *Lunar and Planetary Institute Conference 34.*, Abstract 2102.

Moses, J. I., Zolotov, M. Y., and B. Fegley 2002a. Alkali and Chlorine Photochemistry in a Volcanically Driven Atmosphere on Io. *Icarus* **156**, 107–135.

Moses, J. I., Zolotov, M. Y., and B. Fegley 2002b. Photochemistry of a Volcanically Driven Atmosphere on Io: Sulfur and Oxygen Species from a Pele-Type Eruption. *Icarus* **156**, 76–106.

Murray, C. D. and S. F. Dermott 1999. *Solar system dynamics*. Cambridge University Press, 1999.

Na, C. Y., Trafton, L. M., Barker, E. S., and S. A. Stern 1998. NOTE: A Search for New Species in Io's Extended Atmosphere. *Icarus* **131**, 449–453.

Neugebauer, R. 2001. *Auf der Spur des Ursprungs und der Evolution von Sekundärionen aus ION-Festkörper-Stößen. Ph.D. thesis*, Frankfurt a.M. University.

Nicholson, P. D., Showalter, M. R., and L. Dones 1996. Observations of Saturn's ringplane crossing in August and November. *Science* **272**, 509–516.

Ockert-Bell, M. E., Burns, J. A., Daubar, I. J., Thomas, P. C., Veverka, J., Belton, M. J. S., and K. P. Klaasen 1999. The Structure of Jupiter's Ring System as Revealed by the Galileo Imaging Experiment. *Icarus* **138**, 188–213.

Palumbo, M. E. and Ferini, G. and Baratta, G. A. 2004. Infrared and Raman spectroscopies of refractory residues left over after ion irradiation of nitrogen-bearing icy mixtures. *Advances in Space Research* **33**, 49–56.

Porco, C. C. and 24 colleagues, 2006. Cassini Observes the Active South Pole of Enceladus. *Science* **311**, 1393–1401.

Posner, A. 1995. *Untersuchung von Flugzeit-Massenspektren im Rahmen der Kalibirierung des Cosmic Dust Analyzer Detektors fr die Cassini-Mission. Diploma thesis*, Heidelberg University.

Postberg, F., Kempf, S., Srama, R., Green, S. F., Hillier, J. K., McBride, N., and E. Grün 2006. Composition of jovian dust stream particles. *Icarus* **183**, 122–134.

Postberg, F., Hillier, J. K., Kempf, S., Srama, R., Green, S. F., McBride, N. and E. Grün 2007. The E-ring in the vicinity of Enceladus II: Probing the moon's interior - the composition of E-ring particles. *Icarus* in press.

Poulet, F., Cruikshank, D. P., Cuzzi, J. N., Roush, T. L. and French R. G. 2003. Compositions of Saturn's rings A, B, and C from high resolution near-infrared spectroscopic observations. *A&A* **412**, 305–316.

Reber, O. 1997. *Bestimmung der Energie- und Winkelverteilung von Primärionen beim Einschlag von Hochgeschwindigkeits-Mikrometerpartikeln auf Oberflächen und deren Anwendung auf Einschlagssensoren an Bord interplanetarer Raummissionen*. *Ph.D. thesis*, Heidelberg University.

Roatsch, T., Wählisch, M., Scholten, F., Hoffmeister, A., Matz, K.-D., Denk, T., Neukum, G., Thomas, P., Helfenstein, P., and C. Porco 2006. Mapping of the icy Saturnian satellites: First results from Cassini-ISS. *Planet. Space Sci.* **54**, 1137–1145.

Schaefer, L. and B. Fegley 2005. Alkali and halogen chemistry in volcanic gases on Io. *Icarus* **173**, 454–468.

Schaefer, L. and B. J. Fegley 2005b. Predicted Abundances of Carbon Compounds in Volcanic Gases on Io. *APJ* **618**, 1079–1085.

Schmidt, J., Brilliantov, N., Spahn, F., and S. Kempf 2007. The Icy Breath of the Giant: Formation of Enceladus' Dust Plume. *Nature*. in press.

Schneider, N. M., Park, A. H., and M. E. Küppers 2000. Spectroscopic Studies of the Io Torus during Galileo Encounters: Remote Plasma Diagnostics and the Detection of Cl^{++}. *Bulletin of the American Astronomical Society* **32**, 35.03.

Seidelmann, P. K., Abalakin, V. K., Bursa, M., Davies, M. E., de Bergh, C., Lieske, J. H., Oberst, J., Simon, J. L., Standish, E. M., Stooke, P., and P. C. Thomas 2002. Report of the IAU/IAG Working Group on Cartographic Coordinates and Rotational Elements of the Planets and Satellites: 2000. *Celestial Mechanics and Dynamical Astronomy* **82**, 83–111.

Shi, Z., Ford, J. V., Wei, S., and A. W. Castleman, Jr. 1993. Water clusters: Contributions of binding energy and entropy to stability. *J. Chem. Phys.* **99**, 8009–8015.

Showalter, M. R., Burns, J. A., Cuzzi, J.N., and Pollack, J.B. 1985. Discovery of Jupiter's "gossamer" Ring. *Nature* **316**, 526–528.

Showalter, M. R., Cuzzi, J. N., and S. M. Larson 1991. Structure and particle properties of Saturn's E ring. *Icarus* **94**, 451–473.

Showalter, M. R., Burns, J. A., de Pater, I., Hamilton, D. P., and M. Horanyi 2003. Recent Hubble Observations of Jupiter's Ring System. *AAS/Division for Planetary Sciences Meeting Abstracts* **35**.

Spahn, F., Albers, N., Hörning, M., Kempf, S., Krivov, A. V., Makuch, M., Schmidt, J., Seiß, M., and M. Sremčevic 2006a. E ring dust sources: Implications from Cassini's dust measurements. *Planet. Space Sci.* **54**, 1024–1032.

Spahn, F. and 15 colleagues, 2006b. Cassini Dust Measurements at Enceladus and Implications for the Origin of the E Ring. *Science* **311**, 1416–1418.

Spahn, F., Thiessenhusen, K.-U., Colwell, J. E., Srama, R., and E. Grün 1999. Dynamics of dust ejected from Enceladus: Application to the Cassini dust detector. *JGR* **104**,

24111–24120.

Spencer, J. R. and N. M. Schneider 1996. Io on the Eve of the Galileo Mission. *Annual Review of Earth and Planetary Sciences* **24**, 125–190.

Spencer, J. R., Pearl, J. C., Segura, M., Flasar, F. M., Mamoutkine, A., Romani, P., Buratti, B. J., Hendrix, A. R., Spilker, L. J., and R. M. C. Lopes, 2006. Cassini Encounters Enceladus: Background and the Discovery of a South Polar Hot Spot. *Science* **311**, 1401–1405.

Spencer, J. R., Stern, S. A., Cheng, A. F., Weaver, H. A., Reuter, D. C., Retherford, K., Lunsford, A., Moore, J. M., Abramov, O., Lopes, R. M. C., Perry, J. E., Kamp, L., Showalter, M., Jessup, K. L., Marchis, F., Schenk, P. M. and Dumas, C., 2007. Io Volcanism Seen by New Horizons: A Major Eruption of the Tvashtar Volcano. *Science* **318**, 240–243.

Srama, R. 2000. *Vom Cosmic-Dust-Analyzer zur Modellbeschreibung wissenschaftlicher Raumsonden*. *Ph.D. thesis*, Technische Universität München.

Srama, R. and 43 colleagues, 2004. The Cassini Cosmic Dust Analyser. *SSR* **114**, 465–518.

Stephan, T. 2001. TOF-SIMS in cosmochemistry. *Planet. Space Sci.* **49**, 859–906.

Strom, R. G. and N. M. Schneider 1982. Volcanic eruption plumes on Io. In *Satellites of Jupiter* pp. 598–633.

Stübig, M. 2002. *New insights in impact ionization and in time-of-flight mass spectroscopy with micrometeoroid detectors by improved impact simulations in the laboratory*. *Ph.D. thesis*, Heidelberg University.

Tardy, J., Poitevin, J. M., and G. Lemperiere 1981. Glow discharge mass spectrometry of silicon DC sputtering in argon-hydrogen . *Journal of Physics D* **14**, 339–346.

Tack 1992. *Test report 101 3 L001*. Technical report, Heraeus GmbH, Hanau.

Thomas, N. 1996. High resolution spectra of Io's neutral potassium and oxygen clouds. *A&A* **313**, 306–314.

Tian, F., Stewart, A. I. F., Toon, O. B., Larsen, K. M., and L. W. Esposito 2007. Monte Carlo Simulations of water vapor plumes on Enceladus. *Icarus* **188**, 154–161.

Timmerman, R. 1989. *Ladungsemmission bei Einschlägen schneller Mikroteilchen auf Wassereis*. *Ph.D. thesis*, Heidelberg University.

Timmermann, R. and E. Grün 1991. Plasma emission from high velocity impacts of microparticles onto water ice. In *IAU Colloq. 126: Origin and Evolution of Interplanetary Dust* pp. 375–377, ASSL.

Tokar, R. L., Johnson, R. E., Hill, T. W., Pontius, D. H., Kurth, W. S., Crary, F. J., Young, D. T., Thomsen, M. F., Reisenfeld, D. B., Coates, A. J., Lewis, G. R., Sittler, E. C., and D. A. Gurnett 2006. The Interaction of the Atmosphere of Enceladus with Saturn's Plasma. *Science* **311**, 1409–1412.

Velotta, R., Di Girolamo, P., Berardi, V., Spinelli, N., and M. Armenante 1994. Kinetic-energy distributions of charged fragments from CO_2 dissociative ionization. *Journal of Physics B Atomic Molecular Physics* **27**, 2051–2061.

Waite, J. H., Combi, M. R., Ip, W.-H., Cravens, T. E., McNutt, R. L., Kasprzak, W., Yelle, R., Luhmann, J., Niemann, H., Gell, D., Magee, B., Fletcher, G., Lunine, J., and W.-L. Tseng 2006. Cassini Ion and Neutral Mass Spectrometer: Enceladus Plume Composition and Structure. *Science* **311**, 1419–1422.

Wang, Y. S., Tsai, C. H., Lee, Y. T., Chang, H. C., Jiang, J. C., Asvany, O., Schlemmer, S., and D. Gerlich 2003. Investigations of protonated and deprotonated water clusters using a low-temperature 22-pole ion trap. *J. Phys. Chem. A* **107**, 4217–4225.

Wehry, A. and I. Mann 1999. Identification of β-meteoroids from measurements of the dust detector onboard the ULYSSES spacecraft. *A&A* **341**, 296–303.

Wolf, A. A. 2002. Touring the Saturnian System. *SSR* **104**, 101–128.

Wong, M.-H. 2004. Groundbased near-IR spectroscopy of Jupiters main ring. In *AAS/Division for Planetary Sciences Meeting Abstracts* **36**

Wipf, H. 2001. Solubility and Diffusion of Hydrogen in Pure Metals and Alloys. *Physica Scripta Volume T* **94**, 43–51.

Zhang, J., Goldstein, D. B., Varghese, P. L., Trafton, L., Moore, C., and K. Miki 2004. Numerical modeling of ionian volcanic plumes with entrained particulates. *Icarus* **172**, 479–502.

Zolensky, M. E. and 65 colleagues 2006. Mineralogy and Petrology of Comet 81P/Wild 2 Nucleus Samples. *Science* **314**, 1735–1739.

Zolotov, M. Y. and B. Fegley 2000. Volcanic Degassing of Hydrogen Compounds on Io. In *Lunar and Planetary Institute Conference Abstracts*, p. 1186.

Zook, H., Grün, E., Baguhl, M., Hamilton, D., Linkert, G., Liou, J.-C., Forsyth, R., and J. Phillips 1996. Solar wind magnetic field bending of Jovian dust trajectories. *Science* **274**, 1501–1503.

Acknowledgements

To my PhD committee: Prof. Drs. Eberhard Grün, Matthias Bartelmann, Priv.-Doz. Drs. Mario Trieloff and Harald Krueger.

To my tutor Sascha Kempf who guided my work with great spirit and competence. I'm grateful to - again - Eberhard Grün and Ralf Srama who always found time for fruitful discussions.

Special thanks go to Jon Hillier, who gave valuable input as THE other CDA-spectrum-guy and tirelessly proofread this thesis and my publications.

To Anna Mocker and Thomas Stephan for the initial evaluation of the TOF-SIMS data. To Klaus Hornung, Mario Trieloff and Marianne Görlich, who comprehensively answered all my questions regarding the impact ionisation process, mineralogy and CDA contamination, respectively.

To Simon Green and Neil McBride for their valuable input as co-authors.

To Uwe who, besides the calculations of possible Type III - particle trajectories, contributed as an unfailing source of good mood. Jessica and all other members of the Cosmic dust group who always were good company and created a supportive and warm work environment.

Warm thanks to Gabi and "Kommagöttin" Sabo (who wasn't really challenged this time) for moral encouragement and proofreading, and last but not least to my parents for their unshakeable support.